THE UNIVERSITY *of* EDINBURGH

SCHOOL OF CHEMISTRY

THE UNIVERSITY OF EDINBURGH

Adsorbents for the Removal of Organic and Inorganic Contaminants from Water

Thesis submitted for the degree of Doctor of Philosophy by:

Panos Kolyvakis

Supervisor: Neil B. McKeown

2022

Acknowledgements

First and foremost, I would like to thank my supervisor, Professor Neil McKeown, for his guidance and support throughout my doctorate research years, and professor Michael Shaver for considering me as a candidate for the position, and for his guidance during my undergraduate project and PhD. I am grateful to my parents Nikos and Annita, and my sister Jenny for dealing with my stress issues over the phone and managing to help me with my work without having any understanding of the science behind it.

I would also like to thank my friends from Athens; Christos Kal, Agrafiotis Klis, Pat, Lexy and Vros for being the best group of friends I could ever ask for, and my flatmates Sofia, Pakkos and Andreas for turning my Edinburgh flat into a very destressing and relaxing atmosphere. A big thanks goes to Sofia Luton for being the best (and loudest) flight company I could ask for; and for her marvellous ability to help out with muddy situations.

Special thanks go to everyone in the McKeown group, especially the PDRAs Dr Richard Malpass Evans, Dr Bibiana Comesana Gandara, Dr Marolino Carta (now a lecturer) & Dr Gracia Bezzu, Dr Aggelos Stamos & Dr John Tobin additionally, I want to thank the PhD students Khairul, Kimia, Sandy, Emily, ChunChun, Richard & Hannah for making lab 29 a very friendly and pleasant working environment. Hector, Laura, Padraig, and Maria are also included. Special thanks also go to all technical staff at the UoE, Juraj and Lorna from the NMR facility, Logan and Alan from mass spectrometry and Lorna Eades from the ICP facility. I would also like to thank everyone from the university stores Mark, Tim, and Simon (thanks for the great chats Simon). I should also thank Red Bull caffeinated beverages for sponsoring my late-night writing sessions.

Finally, I would like to thank ICL for funding, and my industrial supervisor Nick Sutherland for his guidance.

Lay summary

The presence of pollutants in drinking water carries devastating environmental and public health effects. It is estimated that more than 0.78 billion people around the globe do not have accessible water resources, therefore suffering from major health problems. These may be caused by the presence of waterborne bacteria and other microorganisms as well as chemical pollutants of both organic and inorganic nature. The water treatment processes that have been employed in chemical pollutant removal include precipitation, ion exchange, membrane filtration, reverse osmosis, and electrochemical treatment. Most of the quoted water treatment methods carry significant operational costs, and removal by adsorption onto porous materials is often preferred due to its low-cost and high efficiency.

For the removal of organic contaminants by adsorption, the most common material of choice is industrial Granular Activated Carbon (GAC). Owing to its hydrophobicity and largely microporous structure, GAC generally demonstrates high affinity for most organic contaminants, with the exception of certain Emerging Groundwater Contaminants (EGCs), which have been recently detected in high concentrations in surface and ground waters. EGCs commonly originate from agricultural, industrial and municipal sources and their presence in groundwaters carries serious health and environmental risks. Owing to their moderately polar physicochemical properties, EGCs are difficult to remove from water using conventional water treatment processes. The low adsorption capacities of GAC for certain agricultural EGCs, such as the molluscicide metaldehyde, render its use ineffective in traditional water treatment systems.

Inorganic contaminants, such as toxic heavy metal ions, also pose a serious threat to the public health if present in drinking water in concentrations higher than the proposed regulatory limits. Acute and chronic exposure to toxic heavy metals like cadmium, lead, chromium & arsenic is well-known to cause devastating health effects. Even though physiological effects vary with respect to the identity of the

heavy metal as well as the degree and route of exposure, common adverse health effect include severe toxicity to the central nervous system, organs, as well as the immune system. As in the case of organic contaminants, adsorption is frequently preferred in water remediation from metal ions due to its high efficiency and low cost. Owing to the extremely high toxicity of heavy metals as well as severity of the problem in developing nations, there is a clear need for the development of new cost-effective methods and materials that could be used in aqueous metal removal. Additionally, the development of a full understanding of the adsorption mechanisms facilitating metal uptake from aqueous media is of particular importance as it will stimulate the development of better water treatment technologies.

Conclusively, the development of practical and inexpensive methods and materials for the removal of organic and inorganic pollutants from water is of vital importance for the water industry. The research efforts presented herein describe the development of synthetic porous materials that show great potential to be used as adsorbents in water treatment, due to their low cost and simplicity in synthesis and purification. Hypercrosslinked materials (HCPs) derived from the inexpensive triphenylbenzene (TPB) aromatic unit were found through batch equilibrium, kinetic and column experiments to display excellent adsorptive properties for the molluscicide metaldehyde. Additionally, Ion exchanging materials with high affinity for lead (II) ions were derived from different sulfonation routes of HCPs, and their lead (II) uptake properties were explored. These ion exchangers exhibited extensive catalytic activity in aqueous metaldehyde degradation and the subsequent conversion of the degradation products acetaldehyde and ethanol.

Abstract

The molluscicide metaldehyde has been frequently detected in ground and surface waters in concentrations exceeding the 0.1 μg L^{-1} EU regulatory limit, as industrial Granular Activated Carbon (GAC) has been proven inadequate in achieving efficient removal by adsorption. In the present work, Chapter 3.1 describes our research efforts to identify better adsorbents for metaldehyde. Several HCPs and Polymers of Intrinsic Microporosity (PIMs) were synthesised and tested for their metaldehyde adsorptive properties through batch equilibrium experiments. Upon comparison to benchmark adsorbents, a cost-effective HCP based on the TPB aromatic monomer, polymerised in the presence of $AlCl_3$ and DCM, was identified as an excellent candidate for aqueous metaldehyde removal. Novel externally crosslinked analogues of the material were found to display enhanced adsorptive properties, and this was shown by gas adsorption data to be due a result of higher meso and macroporosities, which result in efficient intraparticle mass transport of metaldehyde to the micropores. Solid-state ^{13}C NMR spectroscopy confirmed that the externally crosslinked networks contained a higher degree of alkyl-based linking units, in comparison to TPB-DCM for which Scholl coupling was prevalent. Further aqueous experiments including isotherm studies, adsorption kinetics and Rapid Small Scale Column Tests (RSSCTs) for the novel network derived from TPB & trimethylorthoformate (TMOF) crosslinker are discussed in Chapter 3.2. The overall findings suggest an exceptional maximum adsorption capacity for metaldehyde q_{max} = 125.00 ± 6.03 mg L^{-1}, as determined from the Langmuir model, very fast kinetics following pseudosecond order kinetics with K_2 = 0.15 ± 0.02 mg^{-1} g min^{-1}, and excellent efficiency in RSSCTs, with 2500 column volumes of 0.5 mg L^{-1} metaldehyde-spiked water purified before breakthrough. Regeneration of the adsorbent thermally, and via solvent wash were shown to be possible but were not fully investigated. Pre-polymerisation modification of the TPB unit by the introduction of methoxy and hydroxy substituents was found to negatively affect the porosity and metaldehyde uptake of the materials produced, whereas no significant differences were observed for

fluorine substituents. A magnetically responsive nanocomposite of TPB-HCP and functionalised magnetite particles was synthesised successfully and retained high metaldehyde affinity.

Chapter 3.3 describes that synthesis of sulfonated HCPs and PIMs, through post-polymerisation modification routes, based on acetylsulfuric acid (ASA) and sulfuric acid/triflic anhydride (SA-TfA). The materials were characterised by SS ^{13}C NMR, TGA and IR, which confirmed successful sulfonation, and the ion-exchange capacity (IEC) was determined by Boehm titration methods. The degree of sulfonation was found to greatly enhance Pb^{2+} uptake properties, despite the significant decreases in pore volumes and BET surface areas. Highly sulfonated adsorbents based on TPB, triptycene (tryp) and dibenzomethanopentace (DBMP) units, with IECs ranging between 4.2-6.5 mmol g^{-1}, were found to achieve similar removal efficiencies approaching 99% at initial Pb^{2+} concentration of 160 mg L^{-1} and adsorbent dose of 1 mg mL^{-1}. Isotherm studies on the DBMP-DCM/SA-TfA modified adsorbent further demonstrated the high affinity of the material for Pb^{2+}, with the dataset showing a satisfactory fit for both Freundlich and Langmuir models, and excellent fit to the Dubinin-Astakov model, suggesting that a chemisorption process is prevalent. This was further supported by the Langmuir separation factor, as well as the observed shifts in Pb^{2+}-induced sulfonic acid vibrational wavenumbers.

Chapter 3.4 investigates the degradation of metaldehyde using the derived sulfonated adsorbents, through batch-type GC-MS and NMR experiments. A fast decline in the kinetics of the process was attributed to the narrow pore size distribution of TPB-DCM/ASA, in addition to the strong binding of metaldehyde degradation products to the material, which compete with metaldehyde for the catalytic sites. The breakdown of metaldehyde to acetaldehyde was observed by NMR, which showed additional conversion of acetaldehyde to a variety of products. The presence of paraldehyde, acetic acid, formic acid, acetone, CO_2 was observed in addition to poly(oxymethylene) glycol chains of various lengths. At high contact times, the presence of alkanes, olefins and various other unidentified compounds was confirmed by the ^{1}H-^{13}C HSQC spectrum. It is speculated that the conversion is likely proceeding through aldol condensation to form acetaldol which forms crotonaldehyde upon dehydration, however,

the high complexity of the redox conversion cycle did not allow for full mechanistic determination. The versatile catalytic activity of the adsorbent TPB-DCM/ASA is recognised and should be further investigated.

Abbreviations

AO	Amidoxime
ASA	Acetylsulfonic acid
ATR	Attenuated Total Reflectance
BET	Brunauer, Emmett and Teller (BET) model
C_0	Initial Concentration (mg L^{-1})
C_e	Concentration at Equilibrium (mg L^{-1})
$CHCl_3$	Chloroform
COSY	Correlation Spectroscopy
D-A	Dubinin-Astakov model
DBMP	Dibenzomethanopentacene
DCE	1,2-Dichloroethane
DCM	Dichloromethane
DMF	Dimethylformamide
DMM	Dimethoxymethane
DMSO	Dimethyl Sulfoxide
DPA	Diphenylanthracene
D-R	Dubinin- Radushkevich
EA	Ethanoantracene
EBCT	Empty Bed Contact Time (min)
EOCs	Emerging Organic Contaminants
EtOH	Ethanol
GAC	Granular Activated Carbon
GC	Gas Chromatography
HCPs	Hyper crosslinked Polymers
HPB	Hexaphenylbenzene
HSQC	Heteronuclear Single Quantum Coherence
Hz	Hertz
ICP	Inductively Coupled Plasma
IEC	Ion Exchange Capacity (mmol g^{-1})
IR	Infra-red
IUPAC	International Union of Pure and Applied Chemistry
J	Coupling constant (in Hz)
k_1	First Order rate constant
k_2	Second order rate constant
K_F	Freundlich constant ((mg g^{-1} (L $mg^{-1})^{1/n}$))
K_L	Langmuir constant (L mg^{-1})
LOD	Limit of Detection
LOQ	Limit of Quantitation
MAS	Magic Angle Spinning
MeOH	Methanol
MS	Mass Spectrometry
MMG-1	Ethane-1,1-diol
MMG-2	Poly(oxymethylene) glycol, with n = 2
MMG-3	Poly(oxymethylene) glycol, with n = 3
mmol	millimole(s)
MOF	Metal Organic Frameworks
n	Heterogeneity parameter
NB	Nitrobenzene

Abbreviations

NIST	National Institute of Standards and Technology
NL-DFT	Non-Linear Density Functional Theory
NMR	Nuclear Magnetic resonance
NOESY	Nuclear Overhauser Enhancement Spectroscopy
OES	Optical Emission Spectroscopy
OMIM	Organic molecule of Intrinsic Microporosity
P/P_0	Partial Pressure
PAC	Powdered Activated Carbon
PFO	Pseudofirst Order Kinetic Model
PIMs	Polymers of Intrinsic Microporosity
PSO	Pseudosecond Order Kinetic model
PTFE	Polytetrafluoroethylene
q_e	Adsorption capacity at equilibrium (mg g^{-1})
q_{max}	Maximum adsorption capacity (mg g^{-1})
q_t	Adsorption capacity at time t (mg g^{-1})
K_L	Langmuir Separation factor
RSD	Relative Standard Deviation
RSSCTs	Rapid Small Scale Column Tests
SA	Sulfuric Acid
S_{BET}	BET surface area (m^2 g^{-1})
SBF	Spirobifluorene
SBI	Tetramethylspirobisindane
SIM	Single Ion Monitoring
SPE	Solid Phase extraction
SS	Solid State
STDV	Styrene Divinyl Copolymer
TB	Tröger's base
TCT	Trichlorotriazine
TfA	Triflic anhydride
TFA	Trifluoroacetic Acid
TGA	Thermogravimetric analysis
THF	Tetrahydrofuran
TIC	Total Ion Count
TLC	Thin Layer Chromatography
TMOC	Tetramethyl orthocarbonate
TMOF	Trimethyl orthoformate
TMSCS	Trimethylsilyl chlorosulfonate
TP	Triphenylene
TPB	Triphenyl benzene
TPB-F	1,3,5-tris-(2-fluorophenyl) benzene
TPB-OH	1,3,5-tris-(2-hydroxyphenyl) benzene
TPB-OMe	1,3,5-tris-(2-methoxyphenyl) benzene
Triflyl	Trifluoromethane sulphonyl
Tryp	Triptycene
V_{micro}	Micropore volume (cm^3 g^{-1})
V_t	Total pore volume (cm^3 g^{-1})
δ	Chemical Shift (in ppm)
$\Sigma\chi^2$	Chi Squared Error Function

Table of contents

1. Introduction

The presence of pollutants in water is known to carry devastating adverse effects to human health and has the potential to disrupt or destroy environmental ecosystems.[1] Water treatment technologies receive a lot of research attention aiming to improve current processes and minimise cost of treatment, therefore pursuing the ultimate goals of providing clean water to the public whilst mitigating the environmental impacts of human activity. Despite the complexity of remediation processes and the high variability of engineering designs implemented industrially on water treatment, drinking water treatment plants typically rely on a filtration step which may assist in the removal of both suspended particles and dissolved organic contaminants. The most common adsorbent used in filter media, granular activated carbon (GAC),[2,3] has been recently proven to be ineffective in removing certain EGCs, such as the molluscicide metaldehyde.[4] Additionally, the semi-persistent nature of metaldehyde, along with its extensive use in crop protection has occasionally resulted in high concentrations in surface waters, raising major concerns.[5] There is therefore a clear need for the development of novel porous materials which could replace conventional adsorbents while maintaining competitive synthetic and operational costs. Similarly, inorganic heavy metal pollutants also carry significant environmental and public health hazards,[6-8] and historically the extensive use of lead (II) has resulted in high environmental concentrations and often chronic exposure originating from contaminated water consumption. Heavy metals such as arsenic and lead are a primary concern in developing nations.[9] Typically, sulfonated resins which can remove metals such as lead (II) by ion exchange, are widely employed in industry, however many aspects of the sulfonation route and its effects on the resin porous structure remain overlooked. The present work focuses on the development and characterisation of sulfonated resins for the aqueous removal of lead (II) and examines their catalytic activity in the degradation of the organic contaminant metaldehyde.

1.1 Organic and Inorganic Groundwater and Surface water Contaminants

1.1.1 Emerging organic contaminants

Recently, more frequent testing of surface waters accompanied with advances in analytical techniques have shown an increase in the presence of EGCs in aqueous environments.[4] This has occasionally resulted the detection of EGCs in drinking water, in concentrations much higher than the regulatory limits imposed by the EU.[10] The term 'emerging' describes newly synthesized chemicals, or compounds that have been present in the environment, but their environmental persistence has only recently been elucidated.[11] EGCs commonly originate from agricultural, industrial and municipal sources. Pharmaceuticals, personal care products, perfluorinated compounds and endocrine disruptors are all examples of EGCs, and their presence in groundwaters carries serious risks to both the environment and public health.[5] There is a significant number of agricultural chemicals (Figure 1.1.1a) that can be classified as EGCs. These are commonly used as pesticides, herbicides or molluscicides.

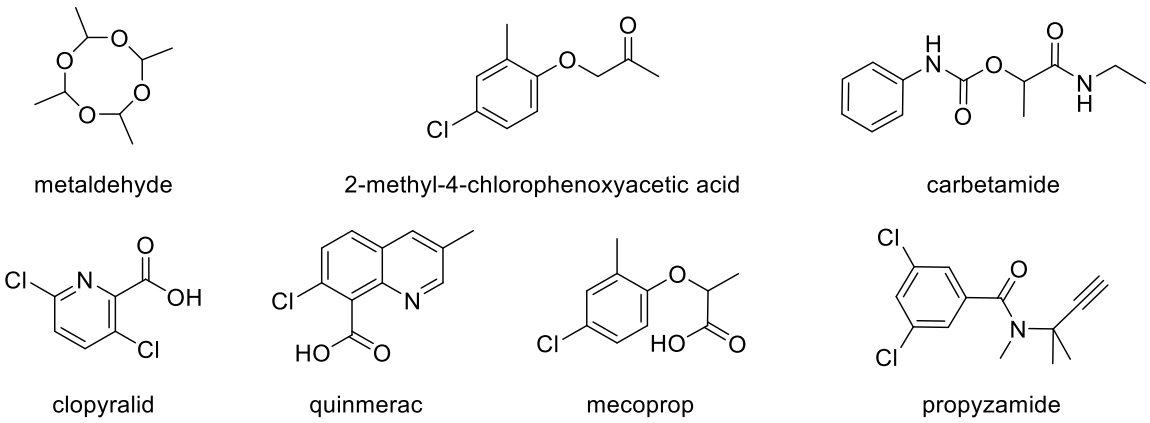

Figure 1.1.1a: Chemical structures of several EGCs.

Owing to their moderately polar physicochemical properties, such contaminants are difficult to remove from water using conventional water treatment processes. GAC is the most common industrially-used adsorbent for the removal of organic contaminants from water.[2] This is due to its high hydrophobicity and largely microporous structure,[3] which facilitates high removal efficiency for a large variety of

organic contaminants. However, the low adsorption capacities of GAC for certain agricultural EGCs have rendered its use ineffective in traditional water filtration systems. As a result, there have been several cases of water tests failing to comply with the EU water quality standards.[12]

1.1.2 Metaldehyde as an emerging pollutant of concern

Table 1.1.2a: Physicochemical properties of metaldehyde.[16]

Chemical structure	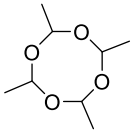
Molar mass	176.21 g mol^{-1}
CAS number	108-62-3
IUPAC name	2,4,6,8-Tetramethyl-1,3,5,7-tetraoxocane
Boiling point	112 to 115 °C
Water solubility	0.188 g L^{-1} (20 °C)
Log (octanol/water) partition coefficient	0.12 (20 °C)

Metaldehyde is a potent molluscicide which is used in 80% of the slug pellets globally.[12] The use of metaldehyde aids in the effective control of molluscs in agriculture, and prevents the loss of valuable crop products which would bare significant economic consequences.[13] In the UK, 1298 tonnes of metaldehyde were used during the period 2008-2011.[12] It has been estimated that lack of control against molluscs in the UK would cost up to £ 100 million per year in lost crop products.[13] Metaldehyde-containing slug pellets are typically applied in the fields during winter-autumn periods when the molluscs thrive in the wet conditions. Following its use, metaldehyde degrades to acetaldehyde which decomposes further to release water and carbon dioxide. Its half-life in soil varies between 3 - 223 days, depending on environmental conditions.[14] In addition, metaldehyde demonstrates a low organic carbon-to-water partition coefficient (Table 1.1.2a), which renders it highly mobile in soil.[15] The

moderately high polarity of metaldehyde also makes it difficult to remove using conventional water treatment processes. Industrial granular activated carbon (GAC) has been found to adsorb only low amounts of metaldehyde (13 mg g^{-1}),[16] although adsorptive capacities may vary significantly based on the AC synthetic route and biomass starting material. Consequently, metaldehyde has been detected in surface waters in concentrations exceeding the 0.1 µg L^{-1} EU regulatory limit for an individual pesticide.[10] Concentrations as high as 8 µg L^{-1} were recorded in the River Thames, during the August-October period in 2012.[1] A study investigating environmental data collected from surface waters over the period 2008 - 2011 in the UK, found that the peak concentrations of metaldehyde were often orders of magnitude higher than the proposed regulatory limit.[17]

Metaldehyde is classified by the World Health Organization as a 'moderately hazardous' pesticide.[12] It is shows moderate toxicity to most organisms. It is known to cause irritation to mammalian mucous membranes, throat, skin, and respiratory tract. Acute exposure to metaldehyde may result in seizures, tremors, salivation, hyperthermia and vomiting.[18] The lethal dose LD_{50} for metaldehyde is species-dependent, with estimates of 500 and 207 mg kg^{-1} for dogs and cats, respectively.[19,12] Metaldehyde poisoning in pets is very common, due to the formulation of the metaldehyde-containing tablets which also contain bait to attract molluscs.[18] Even though the exact mechanism of mammalian toxicity is unknown, it is believed to arise from metaldehyde, rather than its degradation product acetaldehyde.[20] Upon ingestion, studies have shown that the acidic environment of the stomach is unable to fully hydrolyse metaldehyde prior to intestinal adsorption.[21] When metaldehyde enters the bloodstream it can cross the blood-brain barrier to act on the gamma-aminobutyric acid (GABA) system, which inhibits neuronal excitation.[19] Reduced activity of the mammalian GABA-ergic system is commonly associated with convulsions.

With several reports of water treatment systems failing to keep metaldehyde below the drinking standards imposed by the EU, metaldehyde has recently emerged as a pollutant of concern.[4] Several

efforts have been made to develop phenolic-resin carbons,[5] that show improved adsorption capacities over the conventional GACs. However, such materials are limited by the long carbonization and activation methods which typically require very high temperatures. End-of-pipe destruction methods have also shown potential for metaldehyde removal. Anglian Water currently operates a plant that uses membrane filters and a UV/H_2O_2 oxidation technology to remove metaldehyde from the River Trent. Despite the high efficiency of this method, it requires the use of hazardous hydrogen peroxide as well as a constant supply of electricity which is associated with high costs.[22] Introducing such plants all across the Anglian Water supply region, would come with an additional £17 million per annum as operational costs, and an increase of 21% to the overall customer's bill.[12]

Due to its high wildlife toxicity as well as environmental persistence, the UK government has recently imposed a ban for the outdoor use of metaldehyde in pest control, starting in March 2022.[23]

1.1.3 Inorganic contaminants: lead (II) as a water pollutant

Lead is a highly poisonous metal which affects multiple biological functions and organs, with the nervous system being the most affected. Due to its unique physicochemical properties such as ductility, malleability and corrosion resistance lead has been used extensively in human history.[24] Interestingly, lead toxicity is believed to be a main reason for the collapse of the Roman empire.[25] Romans are known to have used lead pipes in their water system and the compound lead (II) acetate as a wine sweetener. In the modern world lead (II) continues to pose serious threats to environmental ecosystems and the public health, as extensive research has shown that long term exposure to lead is associated to lower mental performance, learning disabilities and behavioural problems.[24] Current issues persist from non-replaced lead piping coupled with the ability of water to gradually dissolve lead, often referred to as ''plumbosolvency''.[26]

Lead poisoning mainly occurs via the ingestion of lead-contaminated food or water although other sources such as dust, lead-based paint and contaminated soil may be responsible. Upon ingestion, lead is readily absorbed into the bloodstream and causes severe adverse effects on the cardiovascular system, the central nervous system, the immune system and kidneys. [27] An important factor underlying lead toxicity is its high stability in the 2+ oxidation state, which makes lead ions able to interfere with natural biological processes.[24] Specific biochemical effects of Pb^{2+} ions in the body include its potent and selective activity for voltage dependent Ca^{2+} channels.[28] Additionally, lead poisoning causes microcytic anemia via the inhibition of ferrochelatase and porphobilinogen synthase enzymes, ultimately resulting in the ineffective formation of heme synthesis.[29] Lead is also able to cause biological damage through oxidative stress pathways.[30]

The continuous use of lead in combination with its high stability in the environment therefore results in bioaccumulation, causes severe environmental issues, and poses a great risk for the public health. Consequently, the extensive use of lead has been discontinued in many countries of the world,

however, it is still used in developing countries in industries related to metal refining, smelting, painting, and car repair.

The presence of lead (II) presence in drinking water can therefore have catastrophic effects. There have been several reports of lead-induced intoxication in Nigeria and Senegal which have caused significant adverse developmental and other health effects in adults and children.[31,32] Due to the devastating health effects of lead, the EU standard in drinking water is 10 μg L^{-1},[33] and in the US, the environmental protection agency has set a limit of 15 μg L^{-1}.[34]

The most common water treatment processes conventionally used to remove lead and other toxic heavy metal ions include chemical precipitation, chemical coagulation, membrane filtration, ion exchange, electrochemical methods and adsorption.[35] Amongst them, adsorption of lead onto carbonaceous porous materials is considered to be an effective simple and economically-viable method.[35]

Adsorption is particularly effective at low concentrations and offers flexibility in its design and operation. [36] Furthermore, owing to the reversibility of the adsorption process the material can be regenerated and reused. Several factors affect the efficiency of heavy metal ion removal using adsorbents and these include the temperature of the system, empty bed contact time, adsorbent dose as well as the adsorbate concentration.[37] The physicochemical properties of the adsorbent and adsorbate are also of critical importance, as the adsorbent efficiency relies on the strength of the adsorbent-adsorbate interactions at the surface of the material.

Carbon nanotubes (CNTs) and their derivatives have been extensively researched as potential adsorbents in Pb^{2+} removal. Owing to their highly hydrophobic nature, CNTs are traditionally used for the removal of nonpolar organic contaminants. However, their high porosity also allows for adsorption of polar and ionic species.[36] The low selectivity for specific contaminants observed in the case of CNTs can be improved through several modification routes. A novel alumina-coated CNT (Figure 1.1.3a),

showing excellent adsorptive capacity for Pb^{2+} was synthesised by Gupta and coworkers.[38] The authors used nitric acid to oxidise a multi-walled CNT and coated the functionalised surface using aluminium oxide. The coating of the surface was found to greatly increasing the polarity of the surface, consequently increasing the affinity of the material for lead ions.

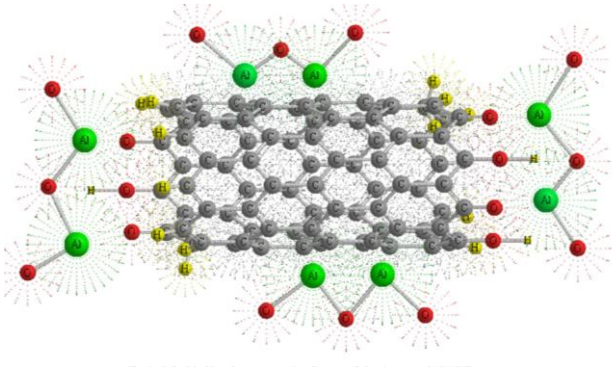

Figure 1.1.3a: 3D representation of alumina-coated CNT used in the removal of Pb^{2+} ions from water.[38]

Another type of functionalised CNTs include a polyacrylamide/CNT composite, with the amide groups of the acrylamide greatly contributing to favourable interactions with the lead ions therefore increasing removal efficiency.[39] In general, the presence of heteroatoms with non-bonding electrons significantly favours lead adsorption, due to their contribution towards electrostatic interactions with the ionic species. This is supported by a study from Yu and coworkers who showed that lead (II) adsorption was enhanced with increasing oxygen content in O_2 plasma-oxidized CNTs.[40] Research extends to the functionalisation of CNTs using amine-containing reagents such as tris(2-aminoethyl)amine.[41] The presence of amine moieties at the surface of CNTs significantly increase the adsorption capacity for lead (II), while simultaneously decreasing the contact time necessary to achieve equilibrium.

Significant research efforts in lead removal from water also include modified graphene and graphene oxide adsorbents. Due to the high accessibility of the external surfaces of graphene, rapid adsorption of lead ions occurs resulting in high adsorption efficiency. [42] This can be further increased through the incorporation of chemical functional groups that increase the polarity of graphene. Deng and coworkers prepared an electrochemically- produced graphene-based adsorbent in the presence of potassium

hexafluorophosphate.[43] An exceptional adsorptive capacity of 406.6 mg g^{-1} was demonstrated for Pb^{2+} and this was attributed to the presence of negative PF_6^- groups onto the surface of the graphene. The deposition of metals/ metal oxides onto graphene sheets has also been explored as a method of enhancing lead (II) affinity. Ren and coworkers prepared a graphene/MnO_2 composite via the reaction of graphite oxide with $KMnO_4$, under MW radiation.[44] XPS and FT-IR studies showed that the enhanced adsorption of lead ions could be attributed to the presence of favourable interactions with the hydroxyl groups at the surface of the modified adsorbent.

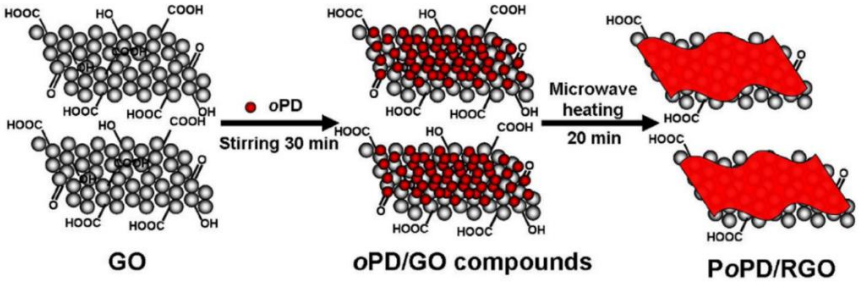

Figure 1.1.3b: MW-assisted functionalisation of GO using poly(o-phenylenediamine).[36]

Chemical modifications of graphite adsorbents are often expensive to perform and require sophisticated equipment. Reduced graphene oxide (rGO) adsorbents can be produced easily via the reduction of graphene oxide (GO) with an appropriate reagent (e.g. sodium borohydride, hydroquinone) and their functionalisation is straightforward, as they already contain a significant level of chemical functionalities on their surface.[36] In a study from Yang and coworkers, a one-step MW-assisted synthesis of a poly(o-phenylenediamine)/reduced graphene oxide composite (Figure 1.1.3b) was reported to show an exceptional maximum adsorptive capacity of 228 mg g^{-1}, as calculated from the Langmuir model.[45] A reusable nanocomposite synthesised from the functionalisation of rGO using thiacalix[4]arenetetrasulfonate was synthesised by Liu *et al.*[46] The heteroatom-containing functionalities on the surface of rGO were reported to participate in strong electrostatic interactions with Pb^{2+} ions in solution, ultimately resulting in metal-ligand complex formation.

HCPs have been widely researched due to their high potential in the removal of organic contaminants from water, due to their low cost and high BET surface areas. The latter is of great importance, since as previously mentioned, the adsorption performance for a specific contaminant is increased as the adsorbent pore size and contaminant molecular size of the contaminant approach similar values. The ionic Van der Waals and hydrated radii for Pb^{2+}, are approximated as 1.19 Å & 2.65 Å, respectively.[47] These values ultimately fall within the microporous region meaning that HCPs can demonstrate good efficiency in the removal of metal ions such as Pb^{2+}, Hg^{2+}, Ag^{+} & Bi^{3+}.[48] The sorption of metal ions onto DVB-hypercrosslinked polystyrene networks is believed to be a consequence of the formation of π-complexes between the cations and the aromatic rings at the pores of the polymer. Additionally, HCPs can be appropriately modified using polar functional groups to enhance their wettability and ion adsorption efficiency. This is demonstrated by the sulfonic acid-modified HCPs synthesised by Li and coworkers who employed a direct sulfonation route using acetylsulfonic acid, to produce an adsorbent with high potential for the aqueous toxic metal ion removal. [47]

1.2 Porous materials

Porous materials are characterised by the intrinsic presence of cavities, interstices, or channels within their microstructure. Porous materials can be naturally occurring, synthetic, or a combination of both. The structural voids they contain are known as pores and their size dictates whether the material is classified, according to IUPAC (International Union of Pure and Applied Chemistry), as microporous (< 2 nm), mesoporous (2- 50 nm) , or macroporous (> 50 nm).[49]

Additionally, pores can be classified as ''closed'' (**a** in Figure 1.2a) and ''open'' (**b, c, d, e** & **f** in Figure 1.2a), according to whether or not they are accessible by an external fluid.[50] When a pore is closed, it does not affect the internal surface area or porosity of a material, but can influence macroscopic properties such as its overall bulk density. Open pores are accessible to external fluid probes and therefore possess an opening to the material's surface. They actively contribute to the internal surface area and porosity.

The shape of a pore can also be of interest. Some are cylindrical (**c** & **f** in Figure 1.2a) and others spherical (**b** in Figure 1.1a). Pores can have one opening (**b** & **f** in Figure 1.1a) or may penetrate the entire material (**e** in Figure 1.1a).

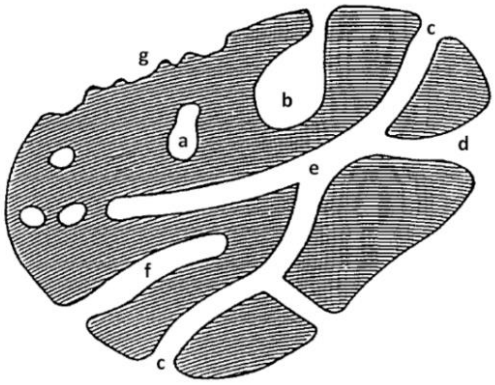

Figure 1.2a: Types of pores found in a porous material.

The volume of the pores of a solid divided by its total nominal volume represents porosity, and is usually expressed as a percentage.[51] Additionally, porosity has a direct impact on the physical, chemical

and mechanical properties of a material.[52] Specifically, the physical properties such as the thermal conductivity, density and strength are influenced by porosity and controlling a materials porosity is therefore of great importance.[50] Porous solids have found applications in sound absorption, heat insulation, energy management and electrical applications.[53] Specifically, microporous materials are particularly useful in gas and vapour separation, catalysis, optoelectronic applications and separation technology.[54] Their abundant small pores and high internal surface areas have resulted in their extensive use as adsorbents, in industry and research, for the removal of pollutants from water.[54]

1.2.1 Microporous materials

Microporous materials have recently received great research attention due to their abundant small pores (< 2 nm), which can interact with small molecules.[55] They can be completely amorphous, or crystalline materials. Crystallinity refers to long-range order within the material's microstructure, which results in the generation of pores of similar nature and size. The most prominent examples of such materials are zeolites,[56] Covalent Organic Frameworks (COFs) [57] and Metal Organic Frameworks (MOFs).[58]

Amorphous materials have highly disordered microstructure, containing pores of various sizes and shapes. Typical examples include Activated Carbons (ACs), Hyper Crosslinked Polymers (HCPs) as well as polymers with high internal free volume such as polymers of intrinsic microporosity (PIMs).[59]

Microporous materials have been widely researched as fluid adsorbents in gas storage and separation, catalysis, as well as water purification.[60,61]

1.2.2 Activated Carbons

ACs are a group of carbonaceous materials that typically possess high porosity and moderate to high internal surface areas, of up to 2000 m^2 g^{-1}.[62] They are characterised by a highly amorphous carbon-based structure and consist of graphene-like sheets which are interconnected randomly to form a porous network structure (Figure 1.2.2a).[63] The pore size distributions found in different types of ACs extend from the microporous to the macroporous region. They are used in a wide range of industrial and domestic applications. Examples include their use as adsorbents in water purification and desalination, medical applications and air purification.[64] The annual production of AC has been estimated to be approximately 100000 tonnes.[65]

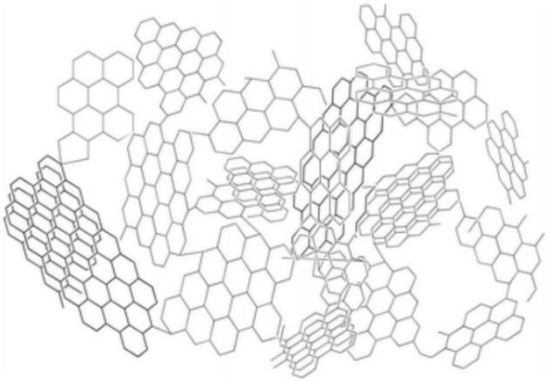

Figure 1.2.2a: Representation of the structure of AC .[68]

The synthesis involves two main stages.[66] The first step of the manufacturing process is the carbonisation of biomass-derived starting materials such as cellulose and wood chips at a temperatures of 500 – 800 °C, and under a stream of an inert gas.[67] During the process, elements like oxygen and hydrogen, are removed from the organic matter through pyrolytic decomposition. This results in the production of a material containing carbon-based graphite crystallites.[63,68] The arrangement of these is irregular, and results in interstices which are formed between them. The temperature of carbonisation as well as the rate of heating, strongly influence the properties and quality of the final material.

Following carbonisation, the carbon produced contains tar-like substances which accumulate in the pores of the material resulting in blockage. The process of removing those chemicals is called activation.

In physical activation, the carbonised material is subjected to high temperatures of 800-1100 °C, and under the presence of oxidising gases such as carbon dioxide, atmospheric air or steam.[69] The oxidising environment in combination with the high temperature result in the opening of the pores, achieving activation. This method is inexpensive, but is limited by the long activation time and high energy consumption.[69] In addition, carbons obtained from physical activation may still contain a large amount of bitumen, which lowers the porosity and adsorbent efficiency. Consequently, chemical activation is often preferred.

Chemical activation is a pre-carbonisation step, and involves the saturation of the biomass starting material with oxidising and dehydrating chemicals (e.g. phosphoric acid).[70] The main mechanisms of activation are believed to include dehydration, depolymerisation and redistribution of cellulosic biomaterials.[71] Following impregnation, the material is dried and subjected to high temperatures of 400-900°C. The activated carbon is finally purified after multiple washings with water to remove the activating agents.[65] In comparison to physical activation, this method of manufacture requires lower temperatures for shorter processing times, and results in higher yields.[72] The chemical activators typically used include acidic or basic reagents such as phosphoric acid, [73] zinc (II) chloride, [74] potassium carbonate, [75] sodium hydroxide[76] or potassium hydroxide.[77] Less common reagents include phytic acid [78] and sulfuric acid. [79] The activator of choice is known to directly affect the morphology of the network as well as the Brunauer-Emmett-Teller (BET) surface area and porosity. The introduction of functional groups on the carbon surface can also be achieved by chemical activation. For instance, alkali metal hydroxides are known to introduce positive charges on the carbon adsorption sites, therefore increasing affinity for negatively charged substrates. [80]

Examples of phosphoric acid activated ACs, derived from several biomass precursors are listed in Table 1.2.2a along with their corresponding synthetic activation temperatures, BET surface areas, total pore volumes, synthetic yields, as well as maximum adsorption capacities for the removal of the organic dye methylene blue from water.

Table 1.2.2a: ACs derived from different precursors and their BET surface areas, total pore volumes & adsorptive capacities for the dye methylene blue.

Biomass precursor	T (°C)	S_{BET} (m^2 g^{-1})	V_t (cm^3 g^{-1})	Yield	q_{max} (mg g^{-1})
Rice Straw[81]	450	522	0.55	51.9	109.1
Cotton cake[82]	450	584	0.298	29.8	250
Coffee grounds[83]	450	925	1.190	48	394
Date palm pits [84]	450	952	1.38	41	455
Eucalyptus [85]	500	1239	1.109	26	427
Vetiver roots[86]	600	1272	1.19	48	394
Peach stones[87]	500	1393	0.689	41.8	362

As previously mentioned, the starting material and synthesis conditions very strictly influence the properties of the carbon produced. This becomes apparent as we compare the first four rows, which are derived via carbonisation/activation at 450 °C from various biomass sources. The resulting yields, total pore volumes and BET surface areas are notably different. Due to methylene blue being a small molecule adsorbate, the maximum adsorptive capacities for the different carbons are somewhat related to their BET surface areas. Highly microporous carbons with high BET surface areas are generally better at adsorbing small molecule contaminants from water, due to the abundance of small pores which display similar cavity size with the molecule of interest. The carbon derived from data palm pits demonstrates an excellent adsorptive capacity of 455 mg g^{-1} for methylene blue,[84] despite having a lower BET surface area compared to ACs derived from eucalyptus or peach stones. Despite the importance of the BET surface area in the adsorption process, several other factors play a major role including material hydrophilicity, presence of mesopores for efficient adsorbate transport as well as the presence of functional groups. Chemically activated carbons have been widely researched for the targeted removal of organic contaminants from water. Examples include ciprofloxacin,[88]

acetaminophen,[89] ibuprophen,[90] paracetamol,[91] phenol,[92] and tetracycline.[93] Research also extends to the aqueous removal of inorganic species. Designer activated carbons have been reported to show excellent maximum adsorptive capacities for metal ions such as cadmium,[94] lead(II),[95] zinc (II),[96] nickel (II) [97] and chromium (VI).[98]

As previously mentioned, there are numerous starting materials that can be used to manufacture activated carbons and the synthesis method and parameters strongly influence the porosity and properties of the material produced. Consequently, extensive research has shown that is possible to produce carbons which show higher affinity for specific substrates of interest. However, the synthesis can often be complex as it requires sophisticated equipment and is energetically intensive. Additionally, the by-products formed by the pyrolytic decomposition of organic matter greatly contribute to greenhouse gas emissions, and the resultant materials show high stability and exhibit no biodegradation following their disposal. In addition, the reduced affinities of ACs for certain EGCs, have resulted in extensive research aiming to develop of alternative synthetic adsorbents for water treatment applications.[99–101]

1.2.3 Hyper Crosslinked Polymers

The term ''hypercrosslinked polymers'' refers to a class of materials which have recently experienced significant research developments due to their ease of synthesis, diverse and simple synthetic and functionalisation strategies as well as the vast availability of inexpensive starting reagents.[101–103]

The synthesis of HCPs typically employs Friedel-Crafts chemistry which results in the formation of fast and irreversible linkages between the monomeric units, resulting in predominantly microporous structures.[102] HCPs generally demonstrate high BET surface areas, high thermal stability as well as exceptional capacities for organic solvents and dyes.[104] Consequently, HCPs have shown potential to be used as industrial adsorbents, as they compete with GAC, both in terms of performance and operational cost.[102] Owing to the substantial number of available aromatic monomers there is a broad diversity of materials that can be produced using a synthetically easy Lewis acid-mediated polymerization. Literature also extends to functionalised, heteroatom-containing monomers being incorporated in HCPs.[103]

1.2.3.1 Post-crosslinking of polystyrene-type chains

The first HCPs, first reported by Davankov,[105–107] were based on polystyrene/ divinylbenzene copolymers which were swollen in appropriate organic solvents (e.g. dichloroethane), and were subsequently crosslinked in the presence of a Lewis acidic catalyst.[108] Specifically, the process involves the dissolution or swelling of the polystyrene chains in a solvent medium, along with a multifunctional crosslinker and catalyst. The swelling process results in the formation of free volume between the chains. The fast and irreversible electrophilic crosslinking reaction results in the formation of strong linkages between phenyl rings of adjacent chains, forming a network which retains a confined and rigid conformation upon solvent removal.[109] The net result of the process is the transformation of solvent-swollen polystyrene into a porous material with low density of packing (Figure 1.2.3.1a).

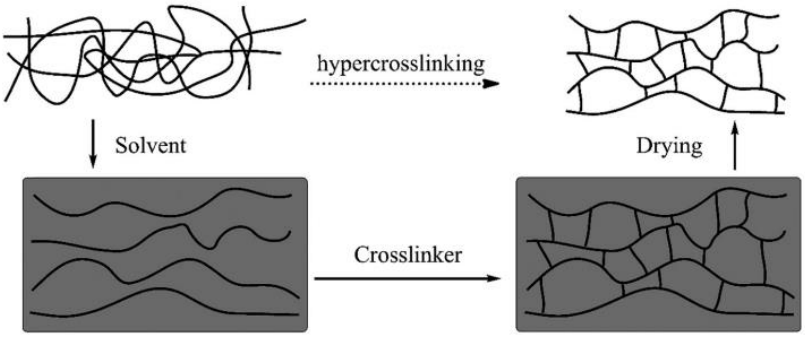

Figure 1.2.3.1a: Schematic representation of crosslinking of swollen polystyrene-type polymers.[102]

The morphology and properties of the network produced will be strictly dependent upon the nature of the crosslinking unit as well as the polystyrene-type precursor. An example of crosslinking of chloromethylated polystyrene is shown in Figure 1.2.3.1b. The very first crosslinkers of choice involved multifunctional halogenated compounds such as tetrachloromethane,[110] monochlorodimethyl ether,[111] dichloroxylene (DCX) and tris-(chloromethyl)-mesitylene.[112]

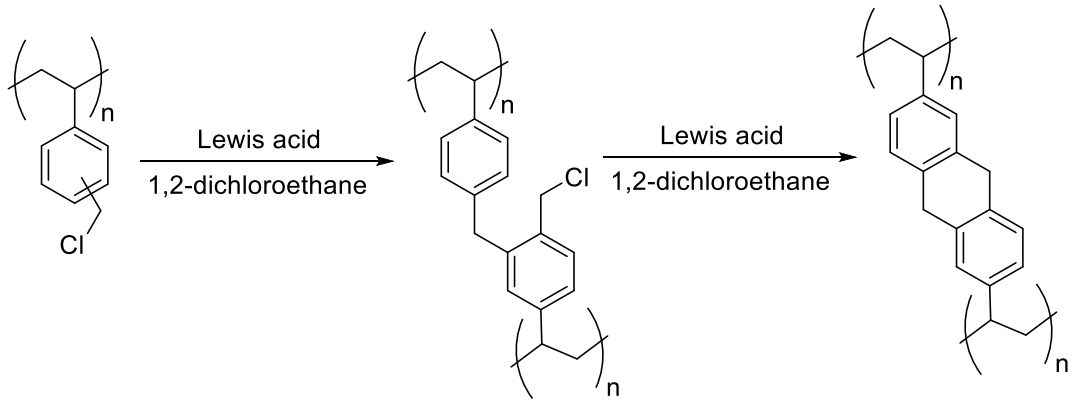

Figure 1.2.3.1b: Crosslinking of halogenoalkane-functionalised polystyrene chains in the presence of Lewis acid.

In general, multi-halogenoalkanes represent the simplest crosslinking units that have been used up to date.[109] The crosslinking process typically involves the conversion of chloromethyl-/ methoxymethane-substituents into direct methylene linkages, through simple Friedel-Crafts chemistry (Figure 1.2.3.1c).[102]

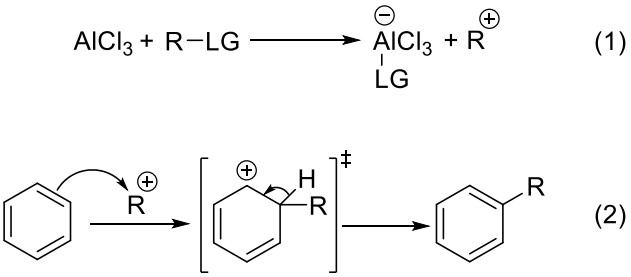

Figure 1.2.3.1c: Mechanism of $AlCl_3$-catalysed Friedel-Crafts alkylation. [102]

The polymerization reaction follows an electrophilic aromatic substitution (S_EAr) reaction mechanism.[102] In the presence of a Lewis acid, halogen or methoxy leaving groups originating from the solvent or crosslinking group, can dissociate to generate a transient carbocation species.[113] This carbocation is then attacked by an aromatic unit to form a second intermediate with disrupted aromaticity.[114] Aromaticity is regained by the loss of a hydrogen ion to produce the final alkylated product. The polymerization takes place in the presence of multifunctional alkyl halide monomers which can repeatedly undergo S_EAr reactions, facilitating the knitting of aromatic units to produce a polymeric structure.

These first ''Davankov resins'' described were based on post-crosslinking strategies and have been extensively researched, and have stimulated the development of modified crosslinking strategies to produce HCPs.[101]

1.2.3.2 Polycondensation of aromatic monomers

Direct condensation reactions of small rigid aromatic monomers were widely attempted following the development of Davankov resins. [102] One of the first self-condensation synthetic strategies came with Cooper and co-workers, who used aromatic blocks such as DCX, BCMBP and BSMBP (Figure 1.2.3.2a) to produce HCPs in a one-pot fashion. [115,116] In the presence of a Lewis acid, the chloromethyl functionalities present in the aromatic blocks mentioned are converted into crosslinking rigid methylene linkages, resulting in the homopolymerisation-derived formation of HCPs, which showed with permanent microporosity and specific surface areas of up to 1874 $m^2\ g^{-1}$. The apparent surface

area and pore size of the networks were highly dependent upon the reaction conditions and monomer ratios.

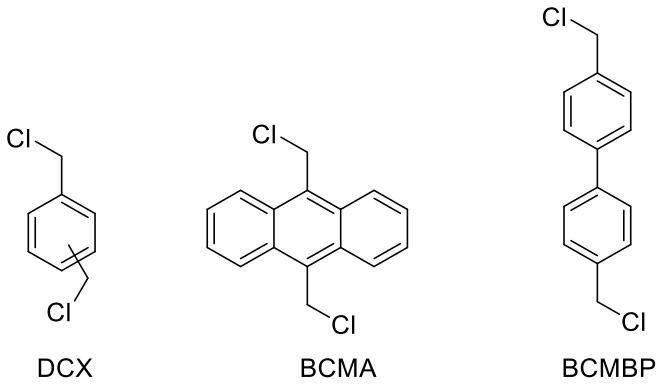

Figure 1.2.3.2a: Chemical structures of monomers used in HCP synthesis via direct condensation methods.[115,116]

Schwab and coworkers realised that the BCMBP unit can also be used as a crosslinker in the polymerisation of other aromatic monomers such as 9-9'-spirobi(fluorene), fluorene, dibenzothiophene and dibenzofuran (Figure 1.2.3.2b). The resulting materials showed high porosity and BET surface area excess of 1800 $m^2 g^{-1}$.[117]

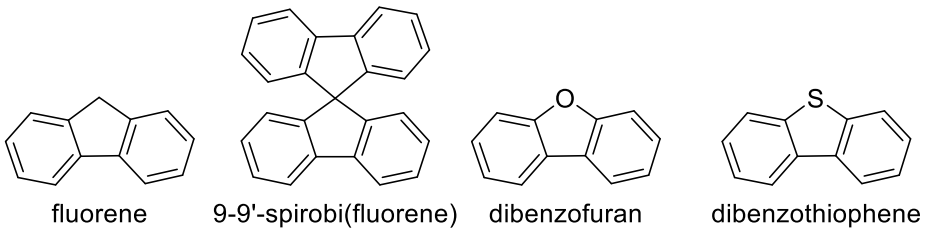

Figure 1.2.3.2b: Chemical structures of monomers used in HCP synthesis by Schwab *et al.*[117]

In a more recent study, networks based on a triphenylamine monomer and the crosslinker DCX were prepared using Friedel Crafts chemistry in the presence of $FeCl_3$ as the Lewis acid.[118] The degree of crosslinking was reported to be directly related to the specific surface areas and pore diameters obtained for the materials produced.[102] This finding supports that the properties of HCPs can be ''tailored'', by the choice of appropriate monomer and crosslinker molecules, as well as the relative ratio. This is further supported by Chen at al. who synthesised porous polymers derived from the crosslinkers BCMPBP and DCX, as well as the monomers ferrocene, tryp and heterocyclic carbazole.[119]

There were apparent differences in the porosities of the materials synthesized, with the crosslinker DCX producing materials of higher porosity than the crosslinker BCMBP. This was attributed to the shorter size of the DCX crosslinking unit, which ultimately generates smaller pores.[119]

A study from Liu et al. examined polymerisation of several aromatic building blocks with the crosslinker tribromomethylbenzene in the presence of the catalysts $FeCl_3$ and $AlCl_3$. A BET surface area of 1783 m^2 g^{-1} was reported for the polymer derived from TPB, while the catalyst $AlCl_3$ resulted in higher material porosities compared to anhydrous $FeCl_3$.[120] The self-condensation polymerisation technique, can be applied to more complex systems as showed by Chaikittisilp et al. who used benzyl chloride-functionalised siloxanes to produce siloxane cages with ultrahigh surface areas of up to 2500 m^2 g^{-1}.[121]

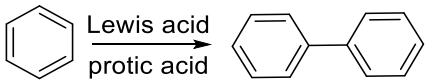

Figure 1.2.3.2c: Scholl coupling in the presence of a Lewis acid and a protic acid.

A study from Luo and coworkers, showed that the polymerisation of aromatic hydroxylated monomers (e.g. 1,4-benzenedimethanol) in the absence of a crosslinker, resulted in the formation of porous polymers.[122] Following this work, the crosslinker-free synthesis of HCPs received more research attention. A synthetic approach based on Scholl coupling is demonstrated by Tan and coworkers, who produced a series of HCPs using various aromatic building blocks without the use of an external crosslinker.[123] The Scholl coupling reaction (Figure 1.2.3.2c) allows for the formation of direct aryl-aryl bonds between the aromatic units through the elimination of aryl hydrogens.[124] In their study, the strong Lewis acid $AlCl_3$ was used to mediate the successful polymerisation of both electron-rich and electron-poor aromatic monomers were polymerised. However, the degree of polymerisation as well as the yield was dependent on specific monomer activities for the Scholl coupling reaction. [102] Using the industrially attractive and simple synthetic method based on Scholl coupling, wide range of materials was produced and several applications including gas storage and catalysis were proposed.[123]

Li et al. used the monomers tetraphenylsilane, tetraphenylmethane and tetraphenylgermane to produced HCPs of moderately high BET surface areas via the Scholl coupling reaction.[125] McKeown and coworkers, used a wide range of commercially available and inexpensive monomers to produce HCPs. [126] A very high BET surface area of up to 2500 m^2 g^{-1} was achieved reproducibly from TPB, DCM and $AlCl_3$. In this example, the crosslinking is a product of direct aryl-aryl Scholl coupling links, as well as Friedel-Crafts alkylation ''methylene'' links originating from the DCM solvent. Solid state ^{13}C-NMR was used to successfully confirm the presence of the methylene bridges in the insoluble HCP networks. [126] A variety of porous materials, derived from aromatic networks such as tryp, TPB, spirobifluorene, biphenyl, hexaphenylbenzene, triphenylene and tetraphenylporphyrin were obtained (Figure 1.2.3.2d).

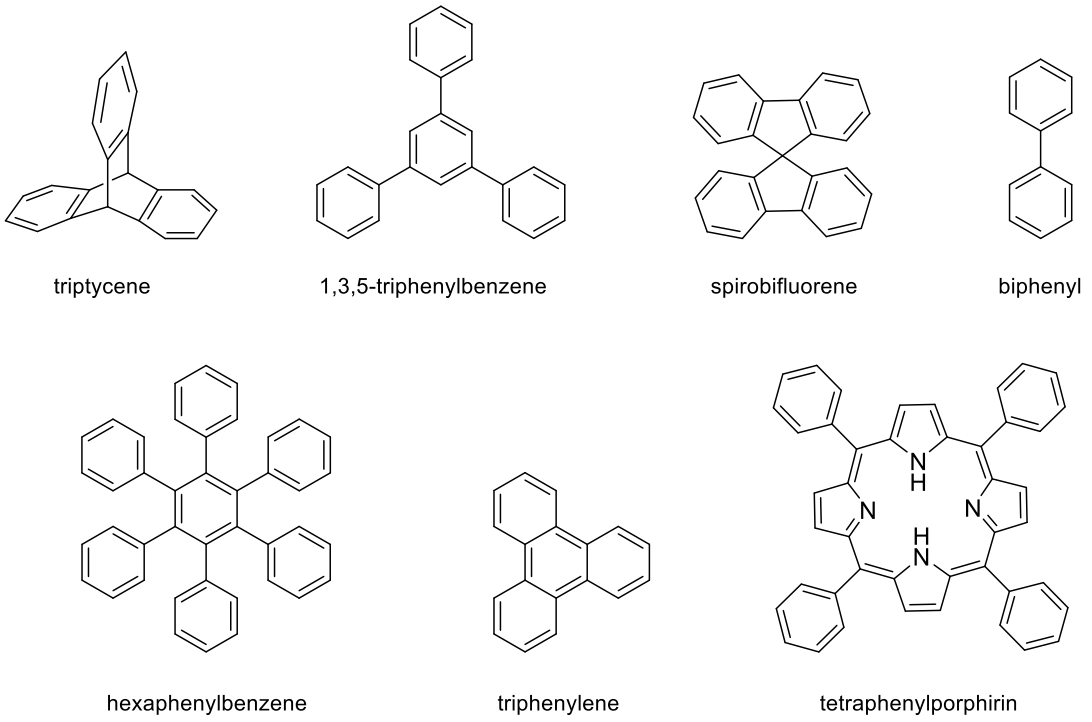

Figure 1.2.3.2d: Aromatic monomers used in HCP synthesis.[87]

1.2.3.3 Other crosslinking strategies

The Scholl coupling-type synthesis of HCPs is limited by the longer reaction time as well as the generation of large volumes of toxic HCl gas, limiting the industrial applicability of the materials produced.[102] Additionally, the formation of direct aryl-aryl linkages which results from Scholl synthesis is often not the crosslinking unit of preference.

A common strategy used to provide control over the polymerization was proposed by Tan and co-workers, and employs the use of external crosslinking molecules.[127] They used the crosslinker dimethoxymethane (DMM) to polymerise several aromatic units such as biphenyl and benzene (Figure 1.2.3.3a). This method resulted in materials that are crosslinked primarily through ''methylene'' links. This is due to the highly reactive crosslinker DMM, which is known to facilitate the generation of large amounts of carbocations in the reaction mixture and ultimately results in the production of single methylene linkages between the aromatic units.[127] Due to this process being kinetically faster than Scholl coupling and other competing reactions, the polymer is composed of primarily crosslinker-mediated linkages. An important consequence of using the external crosslinker DMM instead of chloromethyl groups, is that methanol is eliminated instead of the toxic HCl gas, making this route of synthesis more industrially attractive. [102]

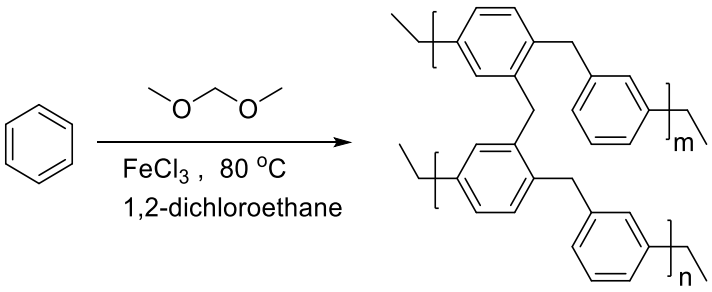

Figure 1.2.3.3a: Synthesis of HCP from benzene, using dimethoxymethane as an external crosslinker.[89]

There are various crosslinkers that have been used in the literature and they all contain two, or more good leaving groups.[102,128] The properties of the HCP produced, strictly depend on the choice of the external crosslinker & aromatic monomer as well as their relative ratio. In other words, the porosity

and surface area of the network are a consequence of the crosslinking degree of the polymer.[101] As an example, the HCP produced from the polymerisation of benzene shows much higher BET surface area when *3 eq.* of DMM is present, compared to an equimolar amount of benzene to DMM.[127]

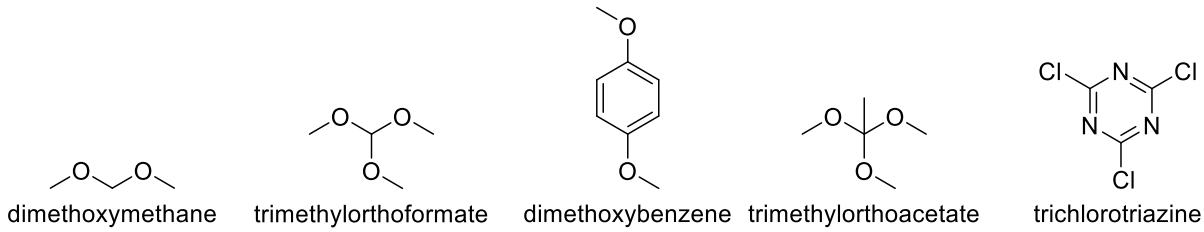

Figure 1.2.3.3b: Crosslinkers typically used in the formation of HCPs.[90-93]

The synthetic strategy based on external crosslinking provides a cost-effective route for the production of porous materials. In addition to DMM, several other crosslinkers have been used including glyoxic acid,[129] 1,4-dimethoxybenzene,[130] trichlorotriazine,[128] trimethylorthoformate, & trimethylorthoacetate (Figure 1.2.2.3b). [131] Research also extends to the synthesis of HCPs derived from heterocyclic aromatic monomers. Examples include the simple heterocyclic molecules thiophene, furan and pyrrole, [103] as well as other fused ring heterocyclics such as benzothiophene,[132] carbazole [119] and dibenzofuran.[132]

1.2.3.4 HCP magnetic nanocomposites

The combination of HCPs with inorganic magnetic agents produces a magnetically responsive composite which possesses porosity and high BET surface area. Iron oxide (Fe_3O_4) is a common material of choice, due to its wide availability and ease of incorporation into material composites.

Tan et al. designed a synthetic route for magnetic polymer composites, which involves an emulsion polymerisation of styrene/ divinylbenzene reagents in the presence of Fe_3O_4 nanoparticles, followed by Friedel Crafts external crosslinking using DMM.[133] Importantly, the authors were able to control the average size of composite particles by varying the amount of emulsifier present. The resulting composite material was successfully used in the removal of organic contaminants from water.

Specifically, an adsorptive capacity of 53.3 mg g^{-1} was obtained for phenol, and the material could be recovered from the sample matrix via the application of an external magnetic field. Ma and coworkers reported an acid-resistant composite produced from the functionalisation of Fe_3O_4 particles with vinyltriethoxysilane, followed by subsequent polymerisation (Figure 1.2.3.4a).[134] The resulting material demonstrated excellent adsorptive capacity for p-nitrophenol and high reusability and robustness.

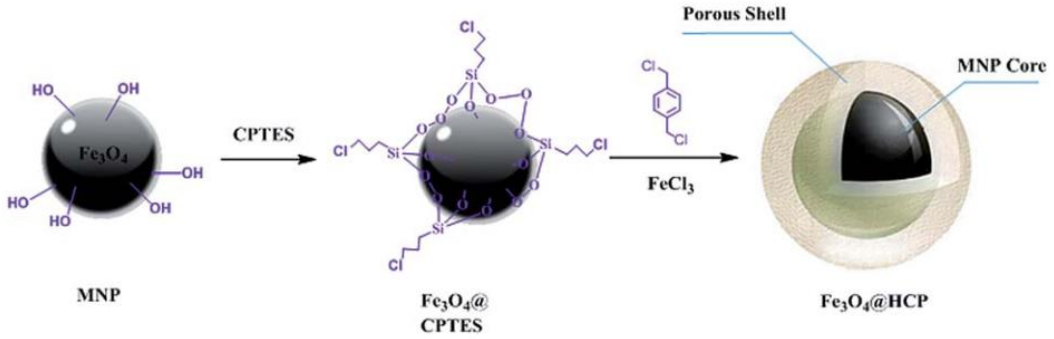

Figure 1.2.3.4a: Magnetic HCP nanocomposite synthesised by Ma *et al.* [134]

Pan and coworkers proposed an alternative functionalisation route of Fe_3O_4, using chloropropyltriethoxysilane.[135] The reagent reacts with the hydroxyl moieties on the surface of the magnetite particles and the functionalisation ultimately results in the incorporation of alkyl chloride functionalities, which can participate in Friedel Crafts reactions. During the polymerisation in the presence of DCX and $FeCl_3$ as the acid catalyst, the porous polymer is built on the outer shell of the magnetite particle forming a composite that possesses high porosity as well as magnetic properties. The resulting particles demonstrated a BET surface area of 770 m^2 g^{-1} and excellent adsorptive capacities for organic dyes such as basic fuchsine and methyl orange.[135]

1.2.3.5 HCPs as adsorbents for water purification

HCPs have been identified to have excellent potential as adsorbents in wastewater treatment, solid phase extraction, organic vapour adsorption as well as chromatographic analysis.[101] Due to their predominantly microporous nature, HCPs can adsorb contaminants from water both on their surface but also in the inner pores, with the transport of substrates occurring through active channels present throughout the structure. This greatly increases the adsorptive capacity for aqueous contaminants and enhances the kinetics of the adsorption process. [100]

Huang et al. synthesised various hypercrosslinked resins via the copolymerisation of several aromatic building blocks and divinylbenzene.[136] Through a series of studies they found that the polarity and porosity of the adsorbents could be adjusted according to the choice of copolymeric precursors and their crosslinking density.[136] The adsorption efficiency of HCP nanoparticles, produced from crosslinking of swollen styrene/divinylbenzene polymers in a Davankov-type synthesis, were investigated by Ouyang et al.[137] The polymers showed high adsorption efficiency towards aromatic molecules such as benzene, ethynylbenzene and toluene.[137] The authors were also able to use the material as a solid phase microextraction adsorbent for the detection of PAHs in real environmental water samples. Li and coworkers successfully incorporated β-cyclodextrin molecules into an HCP network using a Lewis acid-mediated polymerisation route.[138] The hydrophobic interior of β-cyclodextrin contributes to the high affinity of the material produced for a wide variety of aromatic organic contaminants from aqueous media. Interestingly, adsorption of contaminants was found to occur both in the interior of the cyclodextrin moieties as well as at the pores of the HCP network. Impregnation of the material with gold particles resulted in high catalytic activity for the conversion of 4-nitrophenol to 4-aminophenol. [138]

The use of HCPs in water treatment also extends to inorganic contaminants. Heteroatom containing polymers have successfully been used in research for the aqueous removal of heavy metal ions. Li and

coworkers prepared a series of microporous HCPs which were functionalised with sulfonic acid groups, in a post-polymerisation modification method.[47] The materials retained their microporous structure and porosity after sulfonation, and displayed excellent adsorptive capacities for Cu (II), Pb (II), Cr (III) and Ni (II) ions. Triazine and thiophene functionalised polymers, prepared using DMM as the crosslinker, have been reported to demonstrate a high adsorptive capacity for Cu(II) of up to 98 mg g^{-1}, despite the material's low BET surface area of 255 m^2 g^{-1}.[102] The affinity of the material for highly polar copper ions is a consequence of the abundance of nitrogen and sulphur heteroatoms present within the porous structure.

1.2.4 Polymers of Intrinsic microporosity

1.2.4.1 The concept of intrinsic microporosity

In non-porous polymers, the intermolecular interactions between polymer chains result high packing efficiency, minimising the internal free volume of the material. This high packing efficiency is a consequence of high rotational and conformational freedom of chains which allows them to adopt complementary shapes during the packing process. Conversely, if the organic backbone of the polymeric chains is rigid and does not allow efficient packing, then the material is expected to display porosity. The concept of inefficient packing is demonstrated by Organic Molecules of Intrinsic Microporosity (OMIMs). Such molecules possess large contorted and rigid structures which are unable to pack efficiently in space. [139] An example of such molecule (Figure 1.2.4.1a) was reported by McKeown et al. and was derived by the S_NAr reaction between 4,4'-dicyanooctafluorobiphenyl and 2,3-dixydroxytriptycene.

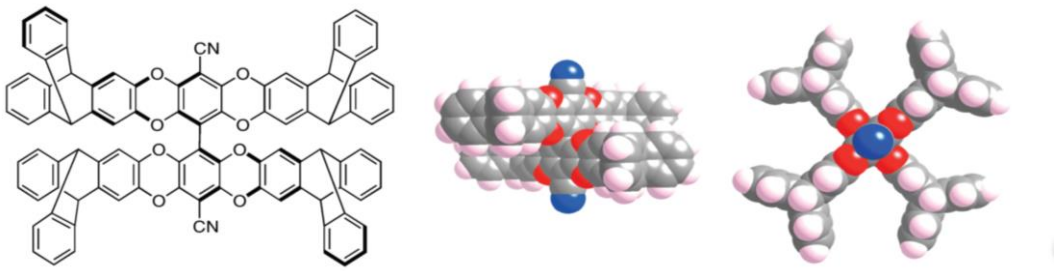

Figure 1.2.4.1a: Chemical structure and 3D representation of an OMIM.[139]

The material produced displayed a BET surface area of 600 $m^2 g^{-1}$, and the porosity solely arises from the 'awkward' packing of the molecules in the solid state.[139] The synthesis and design of OMIMs arises from mathematical studies conducted by Jiao et al. [140] It was found that the packing efficiency (Φ) of a 3D ''superball'' represented by the Cartesian coordinates:

$$|x_1|^{2p} + |x_2|^{2p} + |x_3|^{2p} \leq 1$$

decreases as a function of the deformation parameter p. The deformation of a sphere (p = 1), such that p > 1, causes the surfaces of the object to become convex until the object reaches a perfect cube with p approaching infinity. If 0.5 < p < 1, the sphere changes to an octahedron, with the phases becoming concave at p < 0.5. [141] As p approaches 0, the concavity of the shape increases and the object becomes a 3D ''cross''.[140]

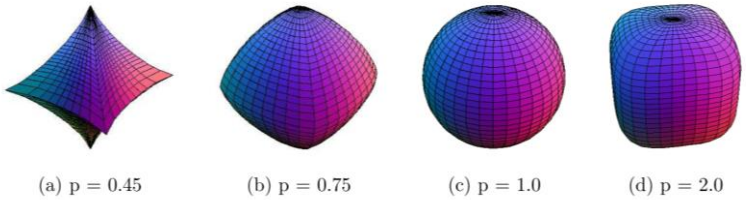

Figure 1.2.4.1b: Representation of ''superballs'' with several deformation parameter p values

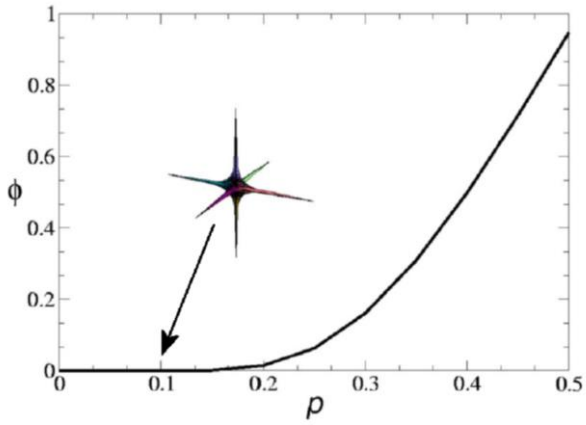

Figure 1.2.4.1c: Packing efficiency Φ as a function of the deformation parameter p.

A plot of the packing efficiency against the deformation parameter (Figure 1.2.4.1c) for values of p < 0.5, shows that as the concavity of the object increases, the packing efficiency decreases and approaches 0 for p → 0. Consequently, the present mathematical model explains why OMIMs display low packing efficiency in the solid state and outlines the importance of high molecular concavity in the generation of material with high intrinsic porosity.

The concept of OMIMs can be applied to polymers by polymerising appropriately functionalised OMIMs to produce a material which displays high internal free volume. As in the case of OMIMs, this is a direct consequence of the concavity of the molecular constituents, which ultimately results in irregular folding and packing of chains. [142]

1.2.4.2 Intrinsic microporosity in polymers

Polymers of Intrinsic Microporosity (PIMs) are a class of highly rigid polymers consisting of interconnected rings with largely restricted conformational and rotational freedom of polymeric chains which disallow efficient packing. This 'intrinsic microporosity' is a result of the generation of 'a continuous network of interconnected intermolecular voids, which forms due to the shape and rigidity of the component macromolecule. The first polymer of this class was reported by McKeown and coworkers in 2004 and was synthesised via the S_NAr substitution reaction between tetrafluoroterephthalonitrile (TFTPN) and 5,5',6,6'-tetrahydroxy-3,3,3',3'-tetramethyl-1,1'-spirobisindane (SBI), in a step-growth polymerisation route (Figure 1.2.4.2a).[59] The resulting microporous polybenzodioxin polymer displayed high BET surface area of up to 850 m^2 g^{-1} and demonstrated high solubility in common laboratory solvents such as chloroform and THF, which allowed for membrane preparation through solution casting. [59]

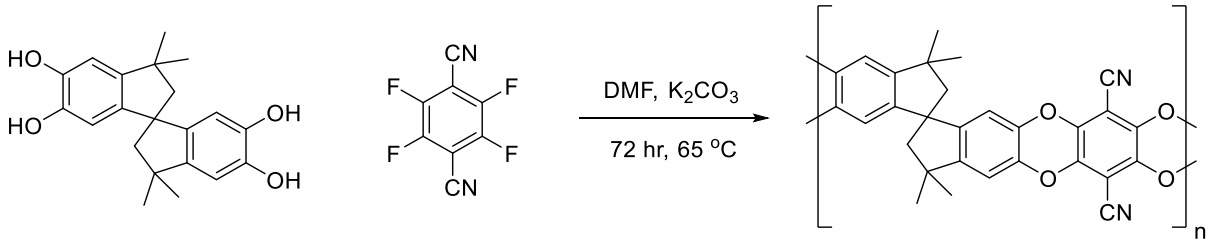

Figure 1.2.4.2a: Synthesis scheme of PIM-1 via an aromatic nucleophilic substitution route.

PIM-1 is easy to synthesise in high molecular weight (>200,000 g mol^{-1}) and displays high chemical stability and moderate thermal stability.[143] In addition, the solution processability and high affinity for

gasses such N_2, CO_2, CH_4 and O_2 are desirable material properties in gas storage and gas separation applications.

Since the synthesis of PIM-1, extensive research has resulted in the development of several polymers which display intrinsic microporosity arising from the restricted conformational and rotational freedom of their constituent monomers. The main routes of synthesis of PIMs include the benzodioxin formation reaction (as explained for PIM-1) ,[144] Tröger's base formation[145] and polyimide formation.[146]

1.2.4.3 Polybenzodioxins

As previously mentioned, the synthesis polybenzodioxins relies on the reaction of equimolar amounts of a bis-catechol and a tetra-halogenated monomer of choice. The S_NAr substitution takes place in the presence of a polar aprotic anhydrous solvent, such as dimethylformamide, to which a base is added initiating the reaction. The reaction mixture is heated to moderate temperatures for several days to ensure completion. The polybenzodioxins are composed of fused rings and can therefore be characterised as ''ladder'' polymers, or ''semi-ladder'' polymers when a spirocentre is incorporated in the structure.

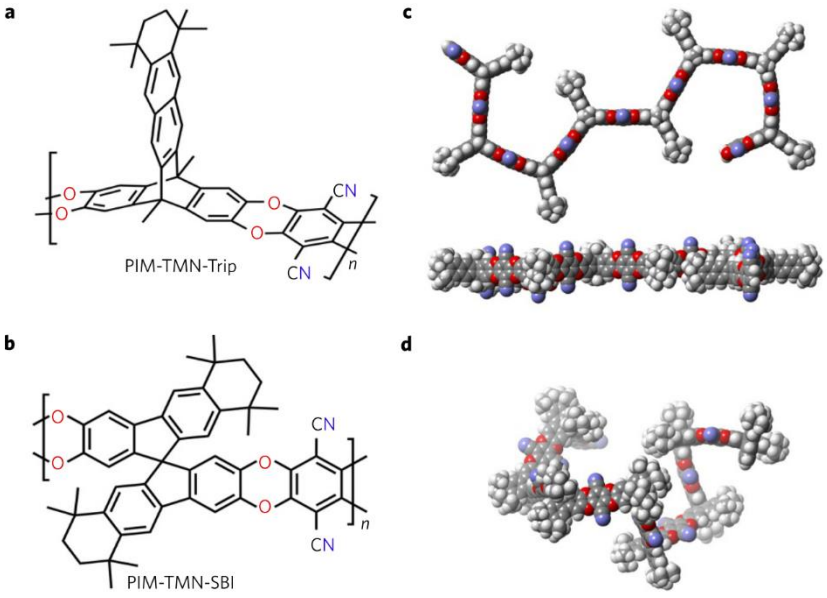

Figure 1.2.4.3a: Molecular structures of the polymers PIM-TMV-Trip (**a**) and PIM-TMN-SBI (**b**) and their 3D conformations (**c** & **d**).[147]

Extensive research on polybenzodioxin PIMs has resulted in the development of materials with exceptional microporosity and excellent potential for applications in gas separation membranes. PIM-TMN-Trip and PIM-TMN-SBI (Figure 1.2.4.3a), published in 2017 by Neil McKeown et al., are noteworthy examples of polybenzodioxane PIMs, as they exhibit ultrapermeability and high selectivity for several gas pairs of interest.[147] Experimental and computational data showed that the materials possess a high amount of internal fractional free volume (approx. 0.309). The ultrapermeability arises from the inefficient packing of 2D chains containing bulky chemical groups, pendant to the polymeric backbone.[147]

1.2.4.4 Tröger's base PIMs

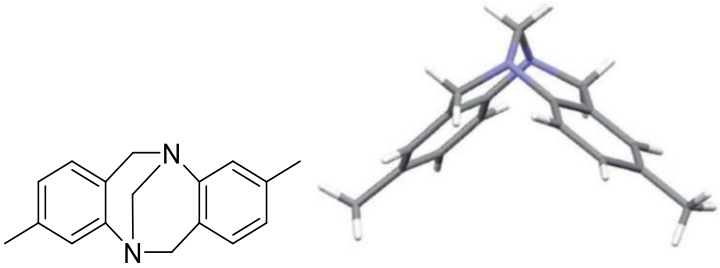

Figure 1.2.4.4a: Chemical structure (left) and 3D representation (right) of Tröger's base.

Julius Tröger synthesised a bicyclic compound in 1887, via the acid-mediated condensation of 4-methylaniline with formaldehyde.[148] The structure remained unknown until it was investigated by Spielman, 50 years after its first synthesis.[149] It consists of fused aromatic rings which contain basic nitrogen atoms connected via a methylene bridge (Figure 1.2.4.4a).[150] The structure possesses high rigidity and concavity, properties that make it a successful candidate in PIM formation.

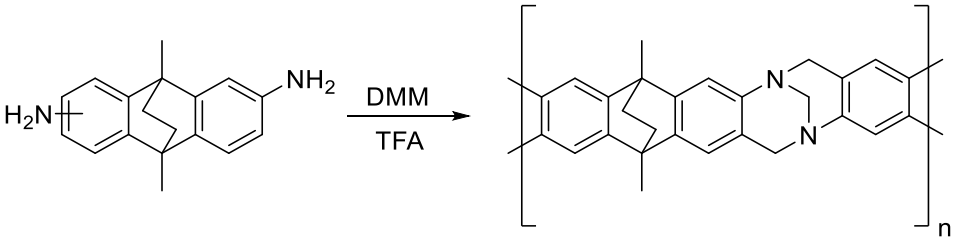

Figure 1.2.4.4b: Synthetic scheme of EA-TB.[151]

The first PIM based on the Tröger's base molecular unit was published in 2013 by McKeown et al., and was based on a polycondensation polymerisation reaction of 2,6(7)-diamino-9,10-dimethylethanoanthracene in trifluoroacetic acid (TFA) and dimethoxymethane (DMM) (Figure 1.2.4.4b), which acts as the ''methylene supplier'' (Figure 1.4.3b).[151] The ethanoanthracene- Tröger's base (EA-TB) polymer displayed very high surface area of 1050 m^2 g^{-1} due to the high rigidity and the presence of multiple contortion sites present in the TB and ethanoanthracene cores.

1.2.4.5. PIMs as adsorbents for water purification

PIMs are solution processable and can easily be cast into films and are therefore mainly recognised for their high potential in gas adsorption and separation membranes. As a relevant example, a poly-benzodioxane PIM based on the polymerisation of a spirobifluorene-based catechol unit was first reported by McKeown *et al.* in 2012 as a membrane-forming solution processable material for gas separation applications.[152] Similarly to other PIMs, the PIM-SBF material displays high BET surface area and exceptional adsorption properties for gases, however owing to its intrinsically hydrophobic nature, displays weak activity in aqueous solution.

There is very limited research for the use of PIMs in the removal of organic and inorganic contaminants from water. Their high hydrophobicity does not allow efficient wettability of the material surface and renders them ineffective in the removal of contaminants from aqueous media, especially in the case of highly polar toxic metal ion contaminants such as Pb^{2+}. Recent research efforts have focused on the functionalisation of PIM-SBF and EA-TB using a variety of functionalities, aiming to increase material

affinity for hydrophilic substrates of interest.[153,154] Significant attention has been received by the use of hydrophilic membranes to selectively separate ions in energy storage devices. PIMs modified using sulfonic acid, amidoxime and other functional groups have also recently found applications in aqueous metal uptake, [47,154,155] however only very limited research exists examining their potential in water treatment.

2. Background theory and analytical techniques

2.1 Determination of surface area and porosity

The determination of the surface area of a classical well-defined object is trivial and requires physical measurements of the material's dimensions. However, when the system of study is a microporous material which possesses internal surface area, the measurement becomes harder to obtain. There are a number of approaches that have been used to quantify internal surface areas of porous materials and these include mercury porosimetry,[156] as well as optical methods.[157] The most widely used approach requires the use of gas adsorption experiments. This technique relies on the reversible physisorption of gases onto a material surface, to quantify the overall surface area. Since the adsorbate possesses a specific cross-sectional area upon adsorption, the surface area of a material can be estimated based on the volume of gas adsorbed.[158] The gas of choice for the determination of surface area is typically the inert gas nitrogen, although gas like carbon dioxide, argon, hydrogen, and krypton have been used.

The process of adsorption can be represented via a thermodynamic equilibrium in which the fluid molecules (X), interact with free surface sites (S) to form adsorbed gas sites (SX).

$$X + S \underset{k_d}{\overset{k_a}{\rightleftharpoons}} XS$$

The position of the equilibrium is a function of the relative stabilities of the occupied and unoccupied sites, as well as the pressure and temperature. [158] The surface coverage of the system (θ) is the fraction of the sites occupied divided by the total number of sites available. The adsorption/ desorption isotherm represents a variation of θ at a constant volume and varying pressure (P/P_0).

2.1.1 Langmuir model

The first isotherm model proposed by Langmuir,[159] assumes that the adsorption process happens on identical adsorption sites on the surface of the adsorbent without any interaction between adsorbent molecules. It is important to note that the Langmuir model accounts for a monolayer of adsorbed molecules, ignoring any potential multilayer formations on the surface. The equation proposed by Langmuir is as follows:

$$q_e = q_m \frac{K_L C_e}{1 + K_L C_e} \quad \text{(eq2.1.1a)}$$

Where q_m (mg g^{-1}), is the number of molecules adsorbed, and C_e (mg dm^{-3}) is the equilibrium concentration of adsorbate molecules. K_L (dm^3 mg^{-1}) is the Langmuir constant, with q_{max} representing the maximum adsorption capacity.[160]

2.1.2 Freundlich model

The first description of multilayer heterogeneous adsorption came with Freundlich, who proposed the equation:

$$q_e = K_F \, C_e^{\,1/n} \quad \text{(eq2.1.2a)}$$

Where q_m and Ce are as previously described and K_F (mg g^{-1} (L $mg^{-1})^{1/n}$)) is the Freundlich constant. The Freundlich exponent is represented by n which is an indicator of the surface heterogeneity and reflects the intensity of adsorption. [159]

2.1.3 Brunauer, Emmett and Teller (BET) model

Brunauer, Emmett and Teller, in 1938, proposed a modified theory based on Langmuir's model that allows for multilayer adsorption. Their theory involves the following assumptions:

1) Adsorption of molecules onto a surface can occur to an infinite layer number.
2) Adsorption layers cannot interact.

3) The Langmuir model can be applied to each layer, individually.

The equation derived using the assumptions above is as follows:

$$n = \frac{n_m CP}{P_0 - P\left(1 + \frac{(C-1)P}{P_0}\right)} \quad \text{(eq2.1.3a)}$$

And can be rearranged in the form:

$$\frac{P/P_0}{n\left(1 - P/P_0\right)} = \frac{1}{n_m C} + \frac{C-1}{n_m C}\left(P/P_0\right) \quad \text{(eq2.1.3b)}$$

Where n represents the amount of gas adsorbed at relative pressure P/P_0 and n_m is the amount of gas in one monolayer. P_0 and C are the saturation pressure and BET constant, respectively. The parameter C changes exponentially with the monolayer adsorption energy and dictates the shape of the material's isotherm.[161] It is represented by:

$$C = \exp\left(\frac{E_1 + E_L}{RT}\right) \quad \text{(eq2.1.3c)}$$

The heat of adsorption for the first adsorption layer is represented by E_1, and for the higher layers by E_L.

The expression eq2.1.3b is in linear form, and therefore plotting $P/n(1-P/P_0)$ against P/P_0, should produce a linear graph. Experimentally, the curve deviates from linearity for high P/P_0, and this is due to multilayer adsorption occurring as the partial pressure approaches saturation pressure for the adsorbent gas. In lower P/P_0, however, linearity is observed. Experimentally, when P/P_0 is in the range of 0.05-0.35, the linearity allows for the intercept (c) and gradient (m) to be calculated from the plot.[162] The amount of gas adsorbed in a monolayer (n) and the BET constant (C) can be expressed as follows:

$$n = \frac{1}{m + c} \quad \text{(eq2.1.3d)} \qquad C = \frac{m}{c} + 1 \quad \text{(eq2.1.3e)}$$

The BET surface area, S_{BET} ($m^2\ g^{-1}$) for a material is given by:

$$S_{BET} = \frac{n\ N_A \sigma}{M\ V_{STP}} \quad \text{(eq2.1.3f)}$$

Where V_{STP} represents the molar volume (22.414 L) of the adsorbate gas ambient temperature and pressure (P = 1 atm and T = 273.15 K), M is the mass of the sample, N_A is the Avogadro's number ($6.022 * 10^{23}\ mol^{-1}$), while σ expresses the cross-sectional area of the adsorbate gas.[162] For diatomic nitrogen gas, this parameter equates to approximately 16.2 $Å^2$.[163]

Based on the background theory explained, the surface area analyser instrument automatically calculates the specific BET surface area of a porous sample, as well as other parameters such as the total and micropore volumes, V_t ($cm^3\ g^{-1}$) & V_{micro} ($cm^3\ g^{-1}$).[164] The BET method is a very powerful tool that can be used to compare properties of porous materials, however it is important to note that the value of surface area obtained using this method is an estimation, and usually deviates from the actual value. This is due to the error in weighing the sample, as well as micropore filling effects which contribute to the overestimation of the BET surface area.[165] Additionally, the size of the adsorbate gas greatly influences the shape of the isotherm and the surface area determined, therefore the compatibility of the gas probe may vary with respect to the nature of the adsorbate system.

2.1.4 Types of isotherms

An isotherm plot represents the amount of gas adsorbed against the partial pressure of the adsorbate gas. According to IUPAC, there are six individual types of isotherms as shown in Figure 2.1.4a.[166] In a type I isotherm (Figure 2.1.4a) the amount of gas adsorbed approaches a specific value, as P/P_0 approaches unity. Microporous materials typically show a type I isotherm since they exhibit high gas uptake at low P/P_0. Types II & III are characteristic of predominantly macroporous materials in which multilayer adsorption occurs at high partial pressures. The adsorbent-adsorbate interactions are higher in type II than type III, and this is reflected on the difference in the shape of the curves at low partial

pressures.[166] Mesoporous materials show isotherm types IV & V which are characterised by both mono- and multilayer adsorption. The stepwise build-up of several adsorbent layers is apparent on the type VI isotherm. There are many reported systems, however which cannot be classified into any of the standard isotherm types.

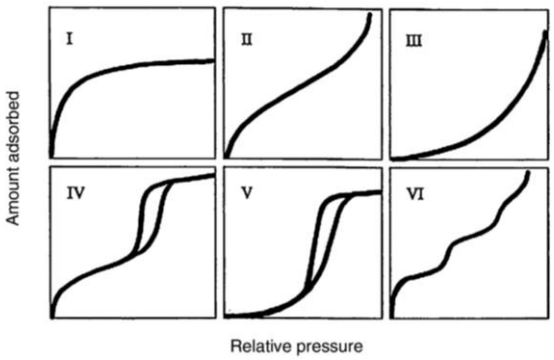

Figure 2.1.4a: Common types of gas adsorption/desorption isotherms.[166]

2.2 Quantitative analytical techniques

2.2.1 Gas chromatography-mass spectrometry

Chromatography is a technique that is used widely used to separate multicomponent mixtures to their constituents.[167] The basic principles of operation include a stationary phase and a mobile phase carrying the mixture. As the different species travel through the stationary phase, they separate according to their distinct molecular characteristics.[168] Ultimately, the analytes demonstrate different degrees of interaction with the stationary phase which results in deviations in the time each component spends in the system. The interaction types include affinity, adsorption, or partition. Mass spectroscopic detection of the effluent compounds results qualitative and/or quantitative identification.

Since the introduction of the first commercially-available GC-MS instrument in 1967,[169] the analytical technique has found several applications in forensic and criminal investigations,[170] clinical toxicology,[171] environmental monitoring,[167] pharmaceutical and industrial applications.

2.2.1.1 Gas chromatography

In the GC compartment the stationary phase consists of a chromatographic column. This capillary column is typically a combination of polysiloxane/ divinylbenzene polymer.[172] The mixture of compounds is introduced in the column at high temperature via the injector. Types of samples include gases, biological or soil sample extracts. GC analysis is typically performed in samples of relatively low molecular weight, and with reasonable volatility and thermal stability.[172] The most common types of injections are either split or splitless. In a split injection, the split valve on the autoinjector remains open during injection resulting in only a fraction of the analyte entering the column. This is particularly useful when analysing concentrated samples, as it dilutes the amount of compound/solvent entering the column, also reducing contamination from chemicals originating from the injection septum. During a splitless injection, the venting valve remains closed, and all the analyte enters the column. Splitless injection is typically used for quantitative analysis of low concentration samples as the analytical

sensitivity is greatly improved. As the high temperature injection pushes the volatile analytes onto the GC column with the aid of an inert carrier gas (e.g. He), their differing affinities for the stationary phase result in separation.[169] The temperature of the column is finely controlled by an oven compartment and is typically programmed to increase as the run progresses, facilitating analyte separation.

2.2.1.2 Mass spectrometry

The separation of different molecular fragments prior to detection is achieved by the ion analyser that the MS is equipped with. There is a high versatility in the types of analysers used in GC-MS instruments with quadrupole, time-of-flight (TOF) and ion-trap analysers being the most common ones. The mass analyser is responsible for directing fragments of a specific m/z value to the detector at a given time. To construct a mass spectrum the analyser scans the selected m/z range several times per second. The separated m/z ion beams are detected using an electron multiplier detector which amplifies the signal and feeds the information into a computer which generates the mass spectrum. Individual components of a mixture are therefore first separated in the GC column, and then identified according to their mass spectra. The integrated areas of each separate peak represent the relative proportion of each component present in the mixture.

2.2.1.3 GC-MS method development

GC-MS instruments are capable of performing a full scan of m/z (mass-to-charge ratio) for a selected range or/and selective ion monitoring (SIM) for specific ion fragments.[173] The full scan analysis is used to obtain all the peaks in a mass spectrum and is used for unknown compound identification. The software automatically compares specific m/z values and isotope patterns to a library of existing reference mass spectra. In the SIM analysis, only selected peaks characteristic of a specific compound is monitored. The main advantage of SIM over the full scan method is a significant reduction in the limit of detection (LOD). More scans are taking place per second for the selected m/z values of interest in SIM analysis than in full scan.[167] SIM analysis is therefore fast and efficient but offers less information

than full scan. Qualitative data for compound identification typically requires full scan, while quantitation of low concentration samples of a known compound is achieved by SIM. Additionally, several parameters need to be optimised in quantitative or qualitative analytical methods. These include the injection temperature, temperature gradient of the oven, choice of chromatographic column, ion source/ interface temperature, monitoring of molecular fragments, detector voltage and others.[169]

Due to the complicated nature of GC-MS instruments, the performance can change according to environmental fluctuations, or the ageing of the instrumental electronic and mechanical components.[169] Calibrations and routine checks should be performed regularly and according to procedures supplied by the manufacturer.

2.2.2 Inductively Coupled Plasma-Optical Emission Spectroscopy

After its introduction in the mid-1970s, inductively Coupled Plasma - Optical Emission Spectroscopy (ICP-OES) has been extensively used for the analytical metal determination in a variety of samples.[174] It offers time-efficient, simultaneous qualitative or quantitative multi-element analysis, robustness and high detection capacity.

The technique employs the use of highly energised plasma, produced using a stream of argon passing through an electromagnetic field of high frequency.[175] The plasma temperatures can reach up to 10000 K, resulting in electronic excitation of the analyte components upon introduction of the sample. Following excitation of the inductively coupled plasma, optical radiation occurs as a consequence of the sample elements returning to their electronic ground states.[176] The emitted radiation is directed, through a monochromator, to the detector which converts the spectral line intensity to an electrical signal. The monochromator compartment is responsible for delivering a specific wavelength to the detector, at a given time. Qualitative analysis involves scanning for a range of wavelengths generating

a metal-specific spectrum, while quantitative analysis relies on the proportionality of the analyte concentration and measured signal intensity.[177]

ICP-OES offers low detection limits in metal quantitation with values approaching the ng ml^{-1} level, as well as excellent reproducibility (RSD = 1-2%) without the use of an internal standard.[176]

2.2.3 Analytical considerations

The validation of an analytical method prior to obtaining quantitative and qualitative data is of great importance. The parameters that should be considered include accuracy, precision, recovery, selectivity, sensitivity, and reproducibility.

The accuracy of the method describes the discrepancy of the mean result to the true value. Replicate analysis of known concentration samples of the analyte is performed with a minimum of five runs per concentration. The % deviation of the real and determined concentrations should be a maximum of 15%. In general, a lower deviation represents higher method accuracy. [178]

The precision of the method relates to the relative deviations shown in multiple runs for a specific homogeneous sample of known concentration. The acceptable values of relative standard deviation (RSD) of typically less than 15%.[179]

Analyte recovery refers to the relative proportion of the analyte detected, against the true concentration of the original sample, prior to sample work-up and preparation. In other words, recovery is related to sample extraction efficiency. The percentage of analyte recovery does not necessarily need to be close to 100%, but it should be consistent within samples. The % value can be derived by comparing analytical data for extracted samples against unextracted standards. [180]

Quantitative detection of analytes relies on the construction of a calibration curve using standard solutions of known concentrations. The curve represents a relationship between instrument response and analyte concentration and may be used to determine concentrations of unknown samples. The

standards and unknowns should always be prepared in the same matrix and the range of concentrations of the standards should be chosen carefully according to the concentration range expected for the unknown samples. [169] The calibration curve is generated using least squares regression method and evaluated using the correlation coefficient (R^2), which should be greater than 0.995.[181]

Quantitative analysis also requires the determination of the limits of detection (LOD) and quantitation (LOQ) based on the method used. A common analytical method for obtaining these limits is on the basis of the signal-to-noise ratio.[182] The LOQ can be approximated as ten times the magnitude of the signal to noise ratio while the LOD should approximate to three times S/N. Noise is described as the fluctuations in the baseline which are a result of variances in the sample injection volume, amount transferred onto the column, ionisation efficiency, ion production and transmission through the analyser. The signal to noise ratio can be expressed as 2H/h, where H is the height of the peak produced by the analyte and h is background noise range.[183] Both quantities are measured with respect to the extrapolated baseline at a distance of 20 times the width of the analyte peak at its half-height.[183]

2.3 Water testing and analysis

2.3.1 Solid-phase extraction of analytes

Despite the advances achieved in chromatographic analytical techniques, sample extraction and preparation remains a crucial pre-analytical step.[184] There are several extraction methods that have been used in the literature and these include liquid-liquid microextraction,[185] stir bar sorptive extraction, [186] microwave-assisted extraction,[187] supercritical fluid extraction,[188] and solid phase extraction.[189] The latter is inexpensive and easy to perform, and is therefore the most common method for the extraction of pesticide from surface and ground water. The process involves the filtration of the aqueous medium through a pre-conditioned adsorbent, designed to selectively capture the analyte. Following adsorption, the analyte can be eluted using an appropriate solvent and analysed using the analytical protocol of choice. SPE is particularly useful in GC-MS analysis, as most chromatographic GC-MS columns show very low tolerance to aqueous samples. Additionally, analysis of environmental water samples with high content in natural organic matter require extraction regardless of the analytical instrument used. Another main advantage of SPE, is that allows for the reduction of the LOD via the pre-concentration of low concentration samples.

There is a wide diversity in the types of commercially available SPE sorbents and the extraction efficiency depends on the adsorbent-analyte compatibility as well as the sample preparation method.

2.3.2 Batch equilibrium studies

A batch equilibrium experiment is the most commonly used method for assessing adsorbent performance for organic and inorganic contaminants from water. [38,79,82,87,160] The technique involves the equilibration of a known weight w (mg) of adsorbent with a contaminant-spiked aqueous solution of concentration C_0 (mg L^{-1}) and volume V (L). The resulting suspension should be continuously stirred or agitated at a constant temperature long contact times, typically 46-48 hrs, to ensure equilibrium

conditions have been reached.[190] Upon equilibrium establishment the suspended adsorbent is removed from the solution, typically by centrifugation or filtration and quantitative analysis of the solution is performed to determine the adsorbate equilibrium concentration C_e (mg L^{-1}). The adsorptive capacity and adsorption efficiency can be calculated using eq2.3.2a & eq2.3.2b, respectively.

$$q_e = \frac{V(C_0 - C_e)}{w} \quad \text{(eq2.3.2a)} \qquad \text{adsorption efficiency (\%)} = \frac{C_0 - C_e}{C_0} \times 100 \quad \text{(eq2.3.2b)}$$

2.3.3 Adsorption isotherm from solution

The solution adsorption isotherm is used to describe the retention of any dissolved aqueous species from solution by the solid surface of the adsorbent, at constant pH and temperature conditions.[191] It can be graphically expressed as the adsorbate amount occupying the sorbent solid surface (q_e), against its residual solution concentration (C_e).

Typically, in the presence of low adsorbate concentrations, high adsorption efficiencies are obtained with efficiency decreasing at increasing concentrations and ultimately plateauing off, as the adsorbent reaches saturation capacity q_{max} (mg g^{-1}). A plot of q_e against C_e for a range of initial concentrations C_0, gives a solution adsorption isotherm, which can give information about the mechanism of the adsorption process as well as the adsorbent-adsorbate interactions.[192] Several models have been used in the literature to gain information about the solution adsorption process and these include the Freundlich and Langmuir models previously introduced for gas adsorption in sections 2.1.1 & 2.1.2, as well as the Dubinin-Radushkevich, Temkin model, Flory-Huggins, and others.[193] For the Freundlich and Langmuir model application in solution adsorption processes, the linearised forms of the proposed equations, eq2.3.2a & eq2.3.2b, have been commonly used due to their simplicity in application. These are shown in the following sections, 2.3.3.1 & 2.3.3.2.

2.3.3.1 Linearised Freundlich model for solution isotherms

As previously discussed, the empirical Freundlich model applies well to adsorbents possessing heterogeneous surfaces, with the adsorption process proceeding to form multilayers of adsorbate onto those surfaces.[194] The Freundlich model assumes a non-ideal adsorption process onto heterogeneous surface, limited availability of adsorption sites, as well as variations of the energy of adsorption between adjacent sites.[195]

The linearised form of the Freundlich solution isotherm, based on eq2.1.2a is expressed as:

$$\log q_e = \log K_F + \frac{1}{n} \log C_e \quad \text{(eq2.3.3.1a)}$$

With q_e & C_e as described above, and K_F (mg g^{-1} (L $mg^{-1})^{1/n}$) and n (dimensionless) being Freundlich constants. The magnitude of the Freundlich parameter n can be obtained from the slope and indicates the degree of surface heterogeneity.[195] If $0 < n < 1$, the adsorption process is favourable, with an unfavourable process demonstrated by $n > 1$.[196] The Freundlich parameter K_F represents material affinity for the adsorbate and could be used as a measure of the adsorption intensity.[196] Despite its widespread use in solution adsorption systems, the linearised equation of the Freundlich model has been observed result in significant error introduction in the values of calculated parameters, in comparison to its linear form.[197]

2.3.3.2 Linearised Langmuir model for solution isotherms

As previously discussed in section 2.1.2, the Langmuir model assumes an even distribution of finite, active sites of equal energy and is strictly suitable for homogeneous adsorption.[193] Adsorption is treated as a fully reversible process, accounting for the adsorbent surface coverage based on adsorption & desorption occurring simultaneously as balanced dynamic equilibrium. Namely, the rate of adsorption

is proportional to the surface fraction available while the desorption is dependent on the surface fraction occupied by the adsorbate.[197]

The linearised form of the Langmuir isotherm expression derived from eq2.1.1a, is:

$$\frac{C_e}{q_e} = \frac{1}{K_L q_{max}} + \frac{C_e}{q_{max}} \quad (eq2.3.3.2a)$$

where K_L (L mg^{-1}) is the Langmuir adsorption constant & q_{max} (mg g^{-1}) represents the maximum adsorption capacity of the adsorbent. A plot of C_e/q_e against C_e for the data obtained gives a straight line with the slope represented by $1/q_{max}$ and the intercept equating to $1/K_L q_{max}$.

The characteristics of the Langmuir model in different initial adsorbate concentrations can be resolved based on the value of the dimensionless separation factor calculated as follows:[198]

$$R_L = \frac{1}{1 + K_L C_0} \quad (eq2.3.3.2b)$$

The value of R_L is indicative of the spontaneity of the adsorption phenomenon, with $R_L > 1$ indicating an unfavourable process, a favourable process when the separation factor is between 0 & 1 and a linear relationship between the initial adsorbate concentration and adsorption capacity when R = 1. Adsorption process irreversibility is indicated by $R_L = 0$.[195] Notably, as in the case of the linearised Freundlich equation, the linear regression method has also been observed to result in significant alterations of the error structure of the isotherm expression.[193]

2.3.4 Adsorption Kinetics

The aqueous adsorption of pollutants relies on various mass transport processes. Initially, film diffusion refers to the transport of adsorbate molecules to the surface of the adsorbent, with the bulk and surface concentration difference acting as the primary thermodynamic driving force.[199] Secondly, intraparticle diffusion involves further transport to the less accessible active sites of the solid adsorbent, through intraparticle transport pores.[200] Finally, adsorption or desorption may occur

between the adsorbent active sites and the adsorbate. Bulk diffusion, involving the transport of adsorbate to the liquid film layer surrounding the solid sorbent particle, is also of particular importance, [201] but its effect on the overall rate may be eliminating by ensuring sufficient agitation. The rate of adsorption is dependent on the slowest step, with adsorption processes most often being limited by film diffusion or intraparticle diffusion.[201] Several kinetic models have been applied to determine the dynamics of adsorption processes, with the pseudo-first order (PFO) & pseudo-second order (PSO) kinetic models most commonly employed.

The PFO kinetic model was first proposed by Lagergren and describes the rate of adsorption being dependent on the rate constant k_1 (s^{-1}), as well as the difference between the adsorbent capacity at equilibrium and at time t (s), q_e-q_t (mg g^{-1}).[199]

$$\frac{dq_t}{dt} = k_1(q_e - q_t) \quad \text{(eq2.3.4a)}$$

Providing that at t = 0, $q_0 = 0$, the integrated form can be obtained as follows:

$$q_t = q_e\left(1 - e^{-k_1 t}\right) \quad \text{(eq2.3.4b)}$$

Taking the logarithm of both sides, followed by mathematical rearrangement results in the linearised expression for the PSO,

$$\ln(q_e - q_t) = \ln q_e - \ln q_t \text{ (eq2.3.4c)}$$

The PSO kinetic model describes the rate of adsorption depending on the second order rate constant k_2, as well as $(q_e\text{-}q_t)^2$.[201] The mathematical expression is as follows:

$$\frac{dq_t}{dt} = k_1(q_e - q_t)^2 \quad \text{(eq2.3.4d)}$$

The integrated PSO model expression is given as follows:

$$q_t = \frac{{q_e}^2 k_2 t}{1 + q_e k_2 t} \quad \text{(eq2.3.4e)}$$

Finally, the linear form can be derived as:

$$\frac{t}{q_t} = \frac{1}{q_e{}^2\, k_2} + \frac{t}{q_e} \quad \text{(eq2.3.4f)}$$

2.3.5 Rapid small scale column tests

The assessment of different adsorbents in terms of their applicability in industrial water purification plants involves a series of tests. Equilibrium batch experiments are usually the first tests performed, and are particularly useful in quantifying the maximum adsorption capacity of an adsorbent to for a particular contaminant of interest.[202] This approach works best for powdered samples and may be used to compare adsorbents of similar particle size distributions but fails to accurately model mass transfer processes in granular adsorbents such as GAC. Traditionally, mass transfer models for GAC samples have been developed but they require several input parameters which are difficult to optimise. Full-scale pilot column tests are a reliable tool in assessing adsorbent performance, but they are expensive and lengthy, as it can take several months to achieve breakthrough. [203]

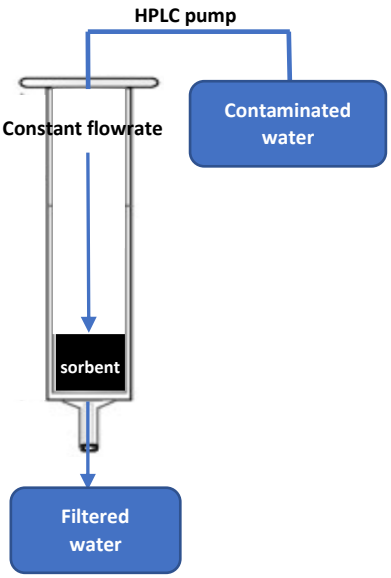

Figure 2.3.5a: Schematic representation of RSSCTs

The RSSCT aims to scale down the mass transfer and thermodynamic phenomena which take place during an adsorption process. A schematic representation is shown in Figure 2.3.5a. As the aqueous medium travels through the porous adsorbent, the solvated contaminant gets adsorbed through pore

diffusion and film diffusion. Initially, adsorption occurs at the external surfaces of the porous material. This creates a concentration gradient between the internal and external surfaces, which causes the substrate to migrate towards the less-accessible pores of the adsorbent. This intraparticle migration is believed to be the rate limiting step of the adsorption process.[204] Importantly, the difference in the concentration gradient between the internal and external surfaces decreases with time, resulting slower adsorption and subsequent detection of contaminant in the effluent water.

The important parameters that should be considered in RSSCTs are as follows: empty bed contact time (EBCT), bed length, average particle size, column diameter, flow rate and the hydraulic loading rate. The empty bed contact time is given by the volume of the bed, V_{bed}, divided by the flowrate Q.

Assessing the similarity between RSSCTs and a full-scale pilot study relies on the following equation:

$$\frac{\mathrm{EBCT_{SC}}}{\mathrm{EBCT_{LS}}} = \frac{[\mathrm{d_{sc}}]^{2-\mathrm{x}}}{[\mathrm{d_{LC}}]^{2-\mathrm{x}}} \quad \text{(eq2.3.5a)}$$

Where LS and SC are the small and large columns, respectively and d represents the adsorbent particle diameter. The relationship depends on the value of the exponent x which can either be 1 or 0. If x=0, the system is modelled using the assumption that the intraparticle diffusivity is independent of the particle size of the adsorbent and remains constant. Conversely, if x=1, a linear relationship is assumed, the diffusivity increases linearly with respect to the sorbent particle size. The principle of operation of RSSCTs relies on the correct design of the small column and the choice of adsorbent particle size and hydraulic loading rate, to mimic full-scale adsorbent performance.[205]

RSSCTs are fast and inexpensive, easy-to-perform in a controlled laboratory conditions, and do not require complementary isotherm and kinetic data to assess adsorbent performance. [204]

3. Results and discussion

3.1 Organic pollutant removal: Adsorbents for metaldehyde

3.1.1 Broad scope batch equilibrium studies

Aiming to identify a good adsorbent for metaldehyde, several HCPs based on a variety of aromatic monomers were synthesised according to modified literature procedures.[126] HCPs were derived from aromatic building blocks such as hexaphenylbenzene (HPB), tryp, diphenylanthracene (DPA), triphenylene (TP) and TPB in solvents such as dichloromethane (DCM), dichloroethane (DCE) or chloroform ($CHCl_3$). Adsorbents were also derived by external crosslinking synthetic strategies, using dimethoxymethane (DMM), trimethylorthoformate (TMOF), tetramethylorthocarbonate and trichlorotriazine (TCT), and all HCP syntheses were mediated by excess $AlCl_3$ as the Lewis acid. A general synthetic scheme, synthetic reagent structures & abbreviations are shown in Figure 3.1.1a.

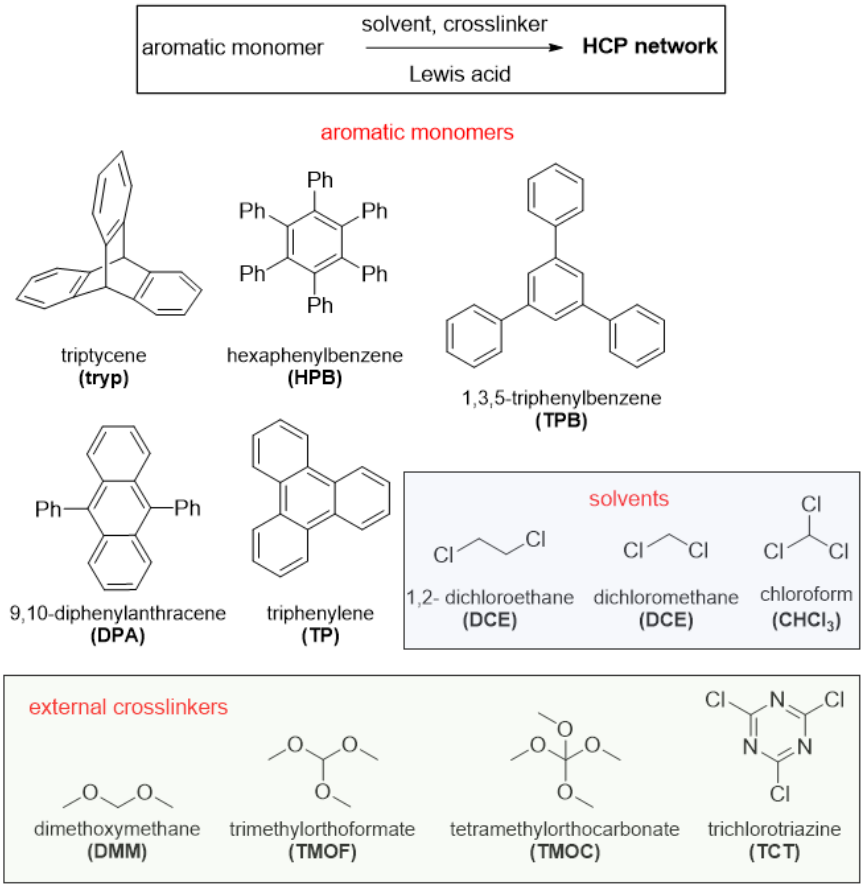

Figure 3.1.1a: General synthetic scheme for HCP syntheses. Chemical structures of aromatic monomers, solvents & crosslinkers are included. Reagent abbreviations are included in brackets.

These majority of these adsorbents were available in the laboratory and were selected based on the well-recognised potential of HCPs as water purification adsorbents. Screening was performed by conducting batch equilibrium studies, according to a standard experimental procedure described in section 5.3.1. Powdered samples (particle size < 100 μm) of adsorbents were incubated for 48 hr at 20 °C using a solution of metaldehyde in ultrapure water, at a concentration 80 mg L^{-1} and a solution pH of 7.4. Providing a narrow particle diameter, an adsorbent-adsorbate contact time of 46 - 48 hours is generally considered sufficient to achieve equilibrium conditions.[190] During adsorbent removal from the aqueous suspensions, the very fine sorbent particle size did not allow for centrifugation, and the adsorbents were removed by filtration through a PTFE 0.22 μm syringe filter. Filtration through the porous PTFE was found to have no effect on the metaldehyde adsorptive capacities obtained. Following SPE, quantitative GC-MS analysis was performed to determine the metaldehyde content of the aqueous filtrates at equilibrium conditions, which allowed for the calculation of equilibrium capacities, using eq2.3.2a. Along with the HCP adsorbents, PIM-1 & EA-TB were also subjected to batch equilibrium conditions. Finally, Darco RTM® powdered activated carbon (PAC) and a lower-grade general purpose granular activated carbon (GAC), were used as benchmarks for comparison.

The results were distributed across a wide diversity of adsorptive equilibrium capacities (Figure 3.1.1b), ranging from 0.1 to 63.3 mg g^{-1}. Upon comparison of the AC adsorbents, it is evident that the capacity for PAC of 33.4 ± 0.1 mg g^{-1} is largely higher than 0.1 ± 0.07 mg g^{-1}, achieved by GAC. This significant difference is likely originating from the particle size and low wettability of the pores at the surface of GAC, which kinetically slow down the adsorption process and limit the intraparticle diffusion processes that are known to facilitate sorption.[206] In addition, with reference to section 1.3, it should be noted that the porous structures and adsorption properties of ACs are highly dependent on the biomass precursor as well as synthetic conditions, and it is therefore not uncommon for different AC samples to display substantial differences in pollutant adsorption efficiencies.[71]

Negligible metaldehyde affinity was demonstrated by the microporous adsorbents PIM-1 and EA-TB, and this was attributed to the intrinsically high hydrophobicity of PIMs, which likely inhibits efficient mass transport of solute into the micropores. Interestingly, both materials have been extensively researched due to their excellent adsorption properties for gas adsorbate molecules, however efficient adsorption from aqueous media has been primarily reported for functionalised analogues with enhanced surface polarity.[155,207] This demonstrates that there exist different requirements for the porous structures and properties for adsorbents,[206] and that these requirements are highly dependent on the phase and the properties of the adsorbate of interest.[208]

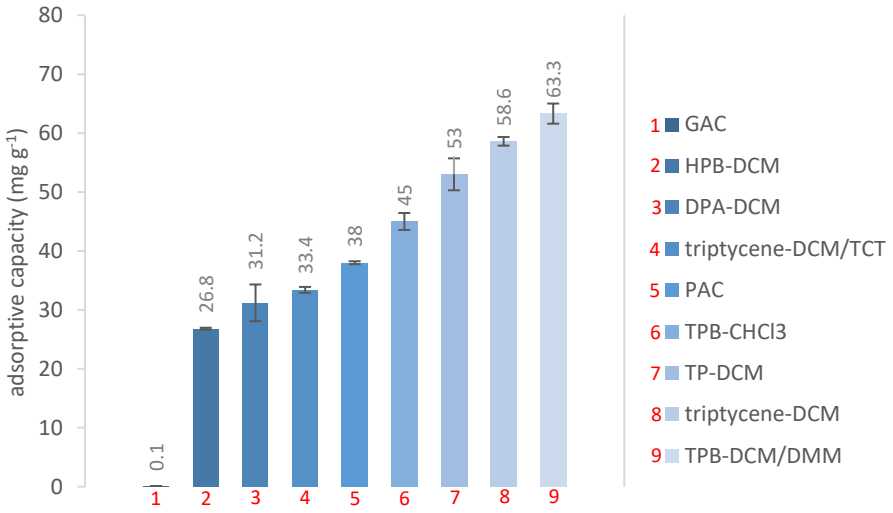

Figure 3.1.1b: Metaldehyde equilibrium adsorption capacities, as determined via batch equilibrium studies. Initial metaldehyde concentration: 80 mg L^{-1} Adsorbent dose: 1 mg mL^{-1}.

The HCP sorbent of lowest performance, HPB-DCM, demonstrated a low affinity for metaldehyde of 26.8 ± 0.2 mg g^{-1}, despite possessing a high BET surface area of 1791 m^2 g^{-1}. Notably, metaldehyde adsorption has been previously reported to be independent of a material's surface area,[16] and a higher dependence on pore size distribution has been observed.[209,210] Examination of the N_2 adsorption isotherm of HPB-DCM confirms that the adsorbent demonstrates high microporosity, with rapid uptake of N_2 occurring at very low partial pressures, with no significant multilayer adsorption occurring. It is therefore concluded that the HPB-DCM is not suitable for solution adsorption applications due to the

absence of sufficient meso and macroporosity, which results in the inaccessibility of the inner micropores by the solution medium.

Networks derived from tryp in DCM as a solvent, were synthesised in the presence and absence of the TCT external crosslinking unit. Despite N_2 gas adsorption data suggesting that crosslinking with TCT does not significantly alter the BET surface area or micropore and total pore volumes, TCT was experimentally found to have a negative impact on metaldehyde affinity. Specifically, tryp-DCM achieved an equilibrium capacity of 58.6 ± 0.7 mg g^{-1}, which decreased to 33.4 ± 0.5 mg g^{-1} when the TCT external crosslinker was used. This could be due to the apparent increase in the polarity of the adsorbent surface, which subsequently increases competition with water for the active sorption sites and results in lower metaldehyde adsorption. An alternative explanation is based on the presence of basic sites on the crosslinker unit, which disfavour metaldehyde binding due to unfavourable secondary interactions between the adsorbate and the surfaces of the pores. Previous literature findings suggest that positively charged or neutral surfaces are required to achieve high metaldehyde adsorption properties.[16] The HCP adsorbents TP-DCM and DPA-DCM show intermediate adsorption equilibrium capacities for metaldehyde.

Exceptional performance was demonstrated by the TPB-DCM aromatic network. The adsorbent reached 63 ± 2 mg g^{-1}, achieving the highest uptake in the broad-scope batch experiment. Interestingly, upon changing the solvent from DCM to $CHCl_3$, the adsorptive capacity significantly decreases significantly to 45 ± 1.5 mg g^{-1}. This is congruent with previous literature findings, suggesting that the properties and performance of the HCPs are largely dependent on the solvent and/or crosslinker of choice, as well as their relative ratio.[100,102] Importantly, the broad scope batch equilibrium experiment was successful at identifying the exceptional adsorptive properties of TPB-DCM for metaldehyde, with the adsorbent achieving a removal efficiency of 80% at an initial concentration of 80 mg L^{-1} and adsorbent dose of 1 mg mL^{-1}.

There is a well-established and significant dependence of the batch method-determined equilibrium adsorption capacity, to several different experimental factors including: adsorbent dose, initial concentration of contaminant, solution pH & adsorbent particle size distribution.[99,191] The considerable effect of adsorbent dose was also demonstrated experimentally, with the equilibrium capacity of TPB-DCM decreasing from 63 ± 2 mg g^{-1} to 42.5 ± 0.2 mg g^{-1}, in response to a change in adsorbent dose, from 1 mg mL^{-1} to 1.6 mg mL^{-1}.

Therefore, comparisons of equilibrium capacities to literature values should be selectively and carefully performed, providing that identical experimental conditions have been used. In the present study, the exceptional affinity of the TPB-DCM adsorbent is demonstrated upon comparison to the PAC sorbent, which achieved a much lower removal efficiency of 47%. It should also be noted that the Darco-type PAC used, is of much higher quality compared to industrial grade GAC commonly used in aqueous organic pollutant removal. This is illustrated by a previous literature study, in which excellent aqueous uptake performance of was achieved using Darco RTM PAC, for a variety of organic dyes.[211]

3.1.1.1 TPB as an inexpensive aromatic monomer for HCP synthesis

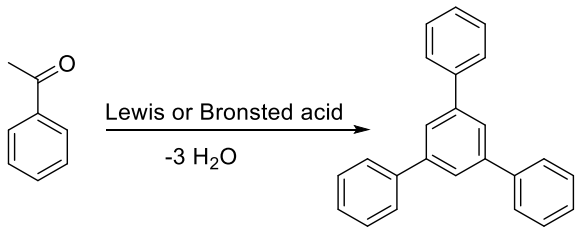

Figure 3.1.1.1a: Synthesis of TPB via the trimerization of acetophenone.

The TPB aromatic building block has been previously considered to be a very attractive and inexpensive precursor for the synthesis of HCPs.[212] TPB can be synthesized via the trimerization of the common, commercially available acetophenone precursor in the presence of a Lewis acid, such as $SiCl_4$,[213] although many available routes involving Brønsted acids are also possible (Figure 3.1.1.1a).[214–220] Due to the nature of the trimerization reaction which generates three water molecules as well as a fully aromatic monomer, the thermodynamically stable product is generally obtained in high percentage

yields. Furthermore, the aromaticity of the molecule allows for easy purification via crystallisation from common solvents, such as ethanol or methanol. Noteworthily, the polymerisation step employs the solvent DCM and the $AlCl_3$ Lewis acid, both being widely available and inexpensive reagents. Due to the exceptional affinity of the TPB-DCM polymer for metaldehyde, as well as the high potential of the TPB aromatic monomer for industrial applications, novel analogues of the network were synthesised and subjected to further testing, to investigate on whether the affinity of the network for metaldehyde could be further improved.

3.1.2 Batch equilibrium studies for TPB-HCPs

Aiming to further increase the adsorption properties of TPB-DCM for metaldehyde, several HCPs based on the TPB aromatic building block were synthesised. This was done in accordance with the well-recognised dependence of HCP properties and porous structures, on the solvent & crosslinker used during synthesis.[101] Different solvents (DCM, DCE & nitrobenzene) as well as crosslinkers (DMM, TMOF & TMOC) were employed. In all syntheses, the concentration of the TPB aromatic monomer was kept constant. The degree of crosslinking was also kept constant, by taking into consideration the number of crosslinking functional groups present in each DMM, TMOF & TMOC.

To assess the validity of the batch equilibrium method, TPB-based adsorbents were screened against PAC as a reference adsorbent. Importantly, small discrepancies were demonstrated for PAC and TPB-DCM with reference to the general scope batch studies (section 3.1.1), therefore demonstrating good reproducibility of the experimental method. A commercially available, hydroxylated styrene-divinyl copolymer (STDV) was also used as a reference. This solid phase adsorbent has found extensive use as a SPE adsorbent of polar pesticides, including metaldehyde,[12] and it was therefore decided to be a good benchmark for comparison. The STDV equilibrium adsorptive capacity for metaldehyde was experimentally determined as 58.3 ± 0.7 mg g^{-1}, outperforming PAC, but showing a significantly lower capacity than all the TPB-based synthetic adsorbents tested.

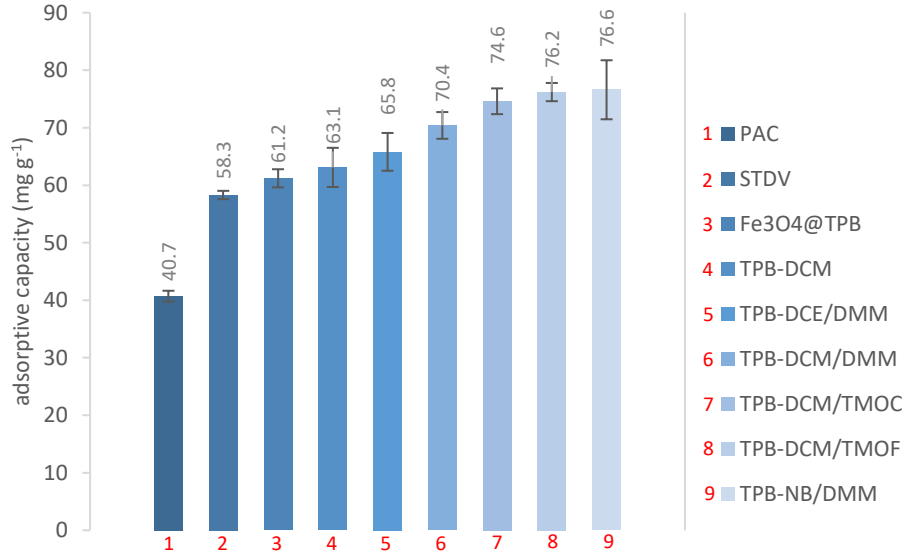

Figure 3.1.2a: Metaldehyde equilibrium adsorption capacities for TPB-HCPs, as determined via batch equilibrium studies. Initial metaldehyde concentration: 80 mg L^{-1} Adsorbent dose: 1 mg mL^{-1}.

Interestingly, the adsorbent TPB-DCM, synthesised in the absence of a crosslinker, was found to demonstrate significantly lower metaldehyde uptake compared to the externally crosslinked TPB-HCPs. Specifically, the presence of DMM as a crosslinking unit was found to enhance metaldehyde uptake in the polymers TPB-DCM/DMM & TPB-DCE/DMM. As shown in Figure 3.1.2a, metaldehyde adsorptive capacities were further improved in the HCPs obtained from DCM and the crosslinkers TMOC & TMOF, as well as the adsorbent derived from NB and DMM. These adsorbents of high performance were determined to absorb almost twice the amount of metaldehyde compared to PAC, with removal efficiencies of approximately 95%.

3.1.3 Characterisation of TPB-HCPs

HCPs have been previously recognised as highly amorphous, difficult to characterise, structurally-elusive materials.[101,221] In an attempt to gain structural information which could be related to the TPB-HCP experimentally determined metaldehyde affinities, N_2 & CO_2 adsorption, SS ^{13}C NMR spectroscopy, Al content determination by ICP-OES, IR spectroscopy and TGA analyses were conducted.

3.1.3.1 Gas adsorption isotherms

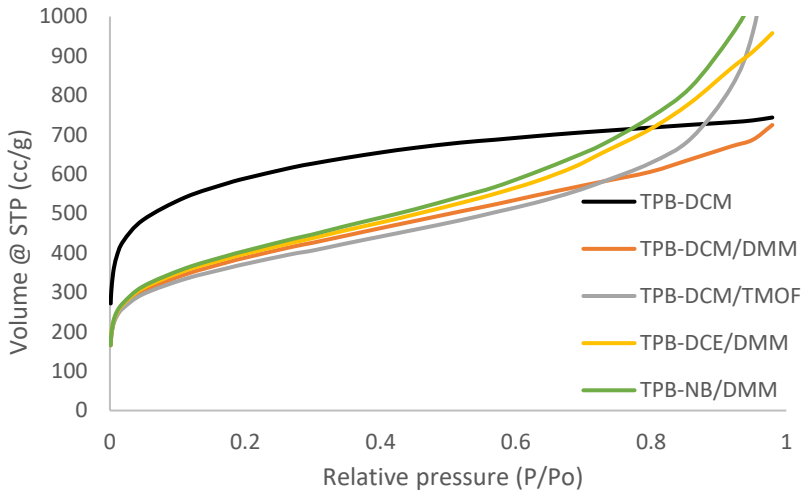

Figure 3.1.3.1a: N_2 adsorption isotherms of TPB-HCPs, at 77 K. The adsorption curve for TPB-DCM/TMOC overlaps with TPB-DCM/TMOF and is omitted. N_2 desorption curves are omitted for clarity.

The N_2 adsorption curve of TPB-DCM at 77 K (Figure 3.1.3.1a), shows that the material is highly microporous with rapid adsorption occurring at low partial pressures and levelling off quickly at increasing partial pressures, owing to multilayer adsorption. The rest of the adsorbents synthesised in the presence of external crosslinkers, all demonstrate very similar N_2 adsorption curves in the microporous and mesoporous regions. These observations are also reflected on the N_2 isotherm-derived data displayed in Table 3.1.3.1a, which demonstrate significant differences in micropore volume and BET surface areas between TPB-DCM and the remaining TPB-derived adsorbents.

Table 3.1.3.1a: Properties of TPB-derived porous polymers. [a] BET surface area derived from N_2 adsorption at 77 K, [b] Micropore volume obtained from N_2 adsorption at P/P_0 = 0.01 & 77 K, [c] Total pore volume obtained from N_2 adsorption at P/P_- = 0.98, 77 K, [d] Total uptake of CO_2 estimated at P = 1 bar and T = 273 K. [e] Equilibrium capacity for metaldehyde, determined from batch experiments at C_0 = 80 mg L^{-1} & adsorbent dose of 1 mg mL^{-1}.

Polymer Abbreviation	SA_{BET} [a] ($m^2\ g^{-1}$)	V_{micro} [b] ($cm^3\ g^{-1}$)	V_{total} [c] ($cm^3\ g^{-1}$)	CO_2 uptake [d] ($mmol\ g^{-1}$)	q_e [e] ($mg\ g^{-1}$)
TPB-DCM	2082 ± 124	0.5	1.2	4.27	63 ± 2
TPB-DCE/DMM	1399 ± 84	0.26	1.5	2.82	66 ± 3
TPB-DCM/DMM	1365 ± 70	0.26	1.1	3.41	70 ± 2
TPB-DCM/TMOC	1300 ± 64	0.26	1.9	3.36	74 ± 4
TPB-DCM/TMOF	1308 ± 62	0.26	1.9	3.40	76 ± 2
TPB-NB/DMM	1426 ± 79	0.26	1.8	2.46	76 ± 5

Specifically, the TPB-DCM polymer consists of a largely microporous structure, as observed from its estimated V_{micro} which is significantly higher than in the externally crosslinked TPB-HCPs. Importantly, the ratio of V_{micro}: V_{total} reveals that an abundance of micropores contributes for approximately 42% of the total pore volume, while the micropore contribution in the externally crosslinked networks ranges between 13 - 23%. With reference to Table 3.1.3.1a, this divergence in adsorbent microporosity is also consistent with the superior CO_2 uptake properties of the highly microporous TPB-DCM, as well as the trend observed in average pore radii estimated for all networks. In summary, owing to its highly microporous structure, TPB-DCM possesses an incredibly high BET surface area of 2082 $m^2\ g^{-1}$, significantly outperforming the externally crosslinked networks; however, the opposite trend is observed in the experimentally determined equilibrium capacities for metaldehyde.

As introduced in Chapter 1.2, efficient adsorption of small molecules of interest typically requires the presence of an abundance of micropores as well as a high surface area available for adsorption.

Nonetheless, the presence of a sufficient number of mesopores is also of critical importance, as pores in the mesoporous and lower macroporous regions are known to mediate adsorbate transport within sorbent network microstructures.[208] The data obtained from N_2 adsorption isotherms of TPB-HCPs suggest an unambiguously higher mesopore presence in the externally crosslinked networks, compared to TPB-DCM. Consequently, the absence of mesopores in TPB-DCM is likely a primary factor limiting its metaldehyde adsorption properties over the rest of the adsorbents, despite its much higher BET surface area.

Additionally, the absence of transport pores is explicitly important if the interactions of the adsorbent surface with the fluid medium are weak and may also depend on the nature of the adsorbate molecule. Specifically for metaldehyde, high aqueous concentrations may allow for the formation of macro-molecular clusters via the H-bond assisted assembly of molecules in solution,[209] and larger pores may assist in the adsorption of those clusters. The importance of adsorbent mesoporosity as well as an absence of a correlation between BET surface area and metaldehyde adsorption properties, have therefore been previously discussed.[16,209,222]

Conclusively, the absence of macro and mesoporosity reduces metaldehyde adsorption by inhibiting the mass transport of metaldehyde to the adsorption sites.[16] The use of an external crosslinking unit such as TMOC or TMOF during the polymerisation of TPB, offers enhanced adsorption performance by introducing additional transport pores within the polymeric microstructure. Such pores may also be introduced by the solvent, and it is likely that the excellent capacity demonstrated by TPB-NB/DMM is associated to the porogenic activity of the NB solvent, which has been previously recognised.[223]

3.1.3.2 ^{13}C SSNMR characterisation

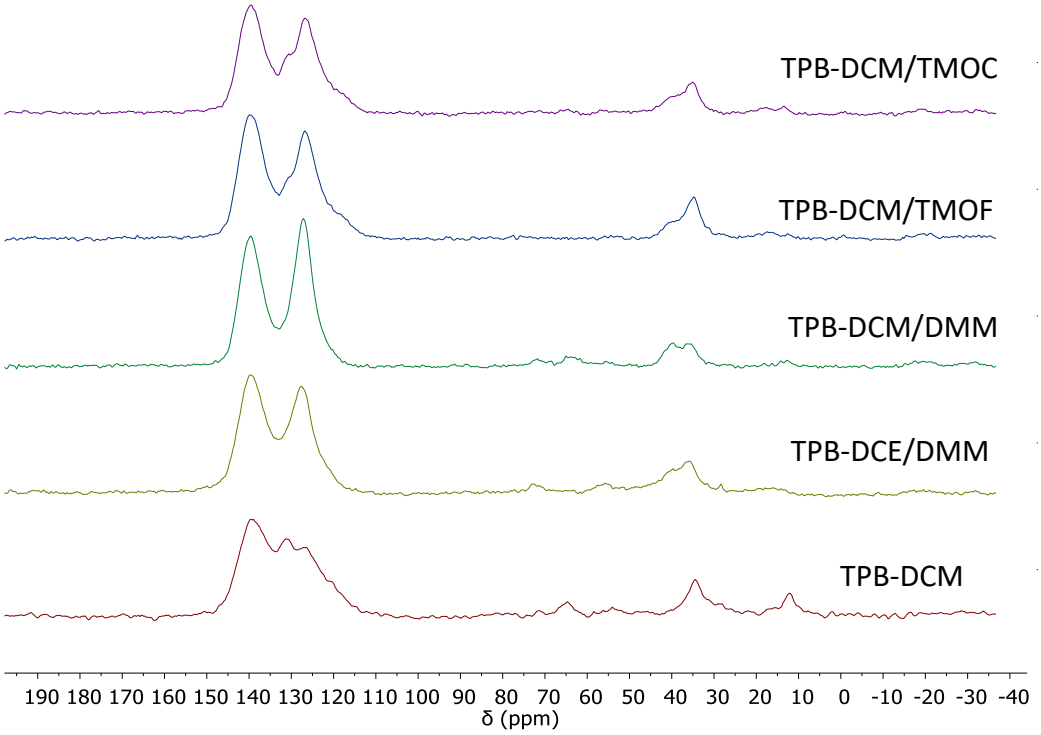

Figure 3.1.3.2a: SS ^{13}C NMR spectra of TPB-HCP adsorbents. Recorded at 300 MHz, spin rate: 12000 Hz.

The SS ^{13}C NMR spectra of all TPB-based adsorbents synthesised using various solvents and crosslinkers, shown in Figure 3.1.3.2a, all display similar features. Broad peaks are present in the aromatic region at δ = 110 - 150 ppm, associated with the aromatic polyphenylene backbone of the networks. Resonances in the region δ = 30-45 ppm are originating from alkyl linking units connecting the aromatic monomers.[224] In principle, the alkyl linking units should primarily be 'methylene' groups, although slight variations in the alkyl carbon chain, as well as singly reacted alkyl units with residual chlorine or methoxy substituents are both likely polymerisation outcomes, and give rise to the smaller peaks in the region δ = 40-75 ppm. Small resonances in that region are observed for all TPB-HCPs, demonstrating that crosslinking of the aromatic TPB units is largely mediated by alkyl groups which originate either from the Friedel-Crafts active DCM solvent, or by the crosslinkers DMM, TMOC and TMOF. The polymers TPB-DCM/TMOC & TPB-DCM/TMOF show identical SS ^{13}C NMR spectra, very similar adsorption properties for the N_2 and CO_2 gaseous probes, as well as similar affinity in the aqueous removal of metaldehyde. This suggests that the crosslinking of three or four aromatic monomers via a single TMOF

or TMOC crosslinker molecule is likely not favoured, due to a large steric barrier and therefore does not occur to a significant extent. The presence of residual unreacted methoxy substituents is therefore possible; however, their presence could not be unambiguously supported by SS NMR due to broad overlapping signals.

Importantly, the quaternary aromatic region 135-45 ppm,[225] appears broader and more intense for TPB-DCM in comparison to the externally crosslinked networks, and the resonance at δ = 30-45 ppm,[224] corresponding to the methylene linking units, emerges as narrower and weaker in intensity. Both observations are a consequence of a higher degree of direct Scholl aryl-aryl couplings present within the microstructure of TPB-DCM, compared to external crosslinker-derived HCPs. As explained in section 1.4.3, the solvent DCM can facilitate the formation of methylene linkages between aromatic units during HCP formation; however, this reaction is kinetically moderate and may allow for the Scholl coupling side reaction to occur at a significant extent. Addition of more reactive, methoxy-containing crosslinkers such as DMM, TMOC and TMOF can therefore reduce Scholl coupling side reactions and generate a material predominantly containing alkyl linkages. This suggestion has been previously made by McKeown *et. al* who also suggested that the higher microporosity obtained in the absence of an external crosslinker may also be related to DCM's activity as a porogen.[126] It is also likely that the shorter aryl-aryl linkages, ultimately generate smaller pores compared to longer alkyl links, simply due to the preferential establishment of smaller distances between interconnected aromatic monomers. This is supported by previous literature findings, suggesting that Scholl coupling synthesis of HCPs generally results in the formation of polymers with narrow pore distribution and high microporosity.[226]

3.1.3.3 Determination of aluminium content for HCP adsorbents using ICP-OES

To determine the aluminium content of the TPB adsorbents synthesized, the materials were dissolved in a mixture of concentrated sulphuric and nitric acid using MW digestion techniques. Following acid digestion, the dissolved solutions were analysed for aluminium using ICP-OES. Interestingly, the aluminium contents for most of the HCPs synthesized were found to be lower than 0.1% by weight, suggesting that metaldehyde removal is due to adsorption onto the polymer surface rather than degradation from any Lewis acidic species trapped within the polymeric network. The network TPB-DCM displayed a much higher aluminium content of 2.3%. This is probably due to the highly microporous structure of the adsorbent of the network which does not allow for efficient removal of aluminium species during the purification process. It is therefore likely that the higher presence of aluminium species may lower the adsorption of metaldehyde due to pore-filling effects, but could potentially enhance metaldehyde degradation at the Lewis acidic sites.[209]

3.1.4 Adsorbents based on functionalised TPB analogues.

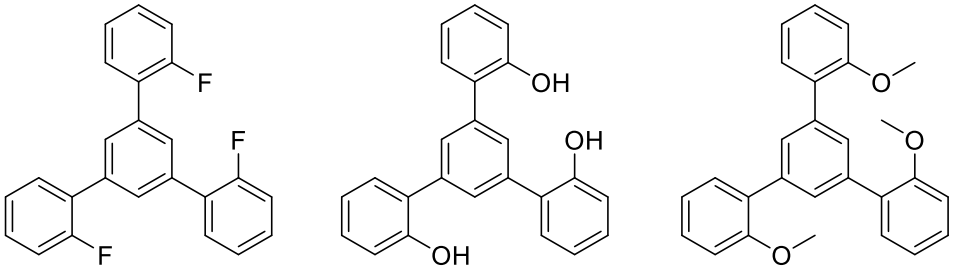

Figure 3.1.4a: Chemical structures of TPB-analogues, functionalised at the 2- positions of the outer aromatic rings.

Due to the high affinity of the TPB-HCP materials for metaldehyde, novel HCPs were also synthesised from functionalised analogues of TPB. The aromatic monomers shown in Figure 3.1.4a, 1,3,5-tris-(2-methoxyphenyl) benzene (TPB-OMe) and 1,3,5-tris-(2-fluorophenyl) benzene (TPB-F) were prepared by the trimerization reactions of the corresponding acetophenone precursors, functionalised in the 2-

position, in the presence of $SiCl_4$. The 1,3,5-tris-(2-hydroxyphenyl) benzene (TPB-OH) was obtained by the demethylation reaction of TPB-OMe, in the presence of BBr_3. The functionalised TPB aromatic monomers were polymerised using the general $AlCl_3$-mediated procedure using DCE as a solvent and DMM as crosslinker, in identical polymerisation conditions as described for TPB-DCE/DMM.

3.1.4.1 Gas adsorption isotherms

Table 3.1.4.1a: Properties of porous polymers derived from functionalised analogues of TPB. [a] BET surface area derived from N_2 adsorption at 77 K, [b] Micropore volume obtained from N_2 adsorption at P/P.= 0.01, 77 K, [c] Total pore volume obtained from N_2 adsorption at P/P.= 0.98, 77 K, [d] Total uptake of CO_2 estimated at P = 1 bar and T = 273 K.

Polymer Abbreviation	SA_{BET} [a] ($m^2\ g^{-1}$)	V_{micro} [b] ($cm^3\ g^{-1}$)	V_{total} [c] ($cm^3\ g^{-1}$)	CO_2 uptake[d] (mmol g^{-1})
TPB-DCE/DMM	1400 ± 50	0.26	1.49	2.82
(TPB-F)-DCE/DMM	1510 ± 83	0.26	2.15	2.21
(TPB-OMe)-DCE/DMM	801 ± 42	0.17	0.61	2.09
(TPB-OH)-DCE/DMM	673± 34	0.16	0.67	1.83

Analysis of the N_2 and CO_2 gas adsorption isotherms data displayed in Table 3.1.4.1a, indicates that all adsorbents demonstrated microporosity. The adsorbent based on non-functionalised TPB possesses high surface area of 1400 $m^2\ g^{-1}$ and a total pore volume of 1.485 ml g^{-1}. Interestingly, polymerisation of the TPB-F monomer yields an adsorbent with slightly higher surface area of 1510 $m^2\ g^{-1}$ and significantly higher total pore volume 2.154 ml g^{-1}. For the adsorbents based on TPB-OMe & TPB-OH, significantly lower BET surface areas of 801 $m^2\ g^{-1}$ & 673 $m^2\ g^{-1}$ were observed. This was in accordance with the total pore volumes which were also significantly reduced for both functionalised aromatic units TPB-OMe & TPB-OH. Despite the moderate BET surface areas of the functionalised (TPB-OMe)-DCE/DMM & (TPB-OMe)-DCE/DMM, a satisfactory CO_2 uptake was maintained, explained by the

presence of polar functionalities which are known to interact strongly with the CO_2 gas probe, resulting in increased heat of adsorption.[132]

Importantly, the morphologies of the networks (TPB-OMe)-DCE/DMM & (TPB-OH)-DCE/DMM, are expected to display significant differences compared to the TPB-DCE/DMM polymer. This is due to the nature of the polymerisation route which employs a highly Lewis acidic $AlCl_3$ species which can strongly coordinate to heteroatoms, such as oxygen and fluorine. In other words, the Lewis acid can act as a template via coordination to such heteroatoms, therefore affecting the pore size distribution, overall porosity, as well as BET surface area. Such properties could also be influenced by substituent effects which can activate or deactivate the aromatic ring towards the electrophilic substitution reaction, which mediates the knitting of aromatic monomers to generate the network. This difference in morphology and properties of the materials produced is thoroughly demonstrated by N_2 & CO_2 isotherm data.

3.1.4.2 ^{13}C SS NMR data

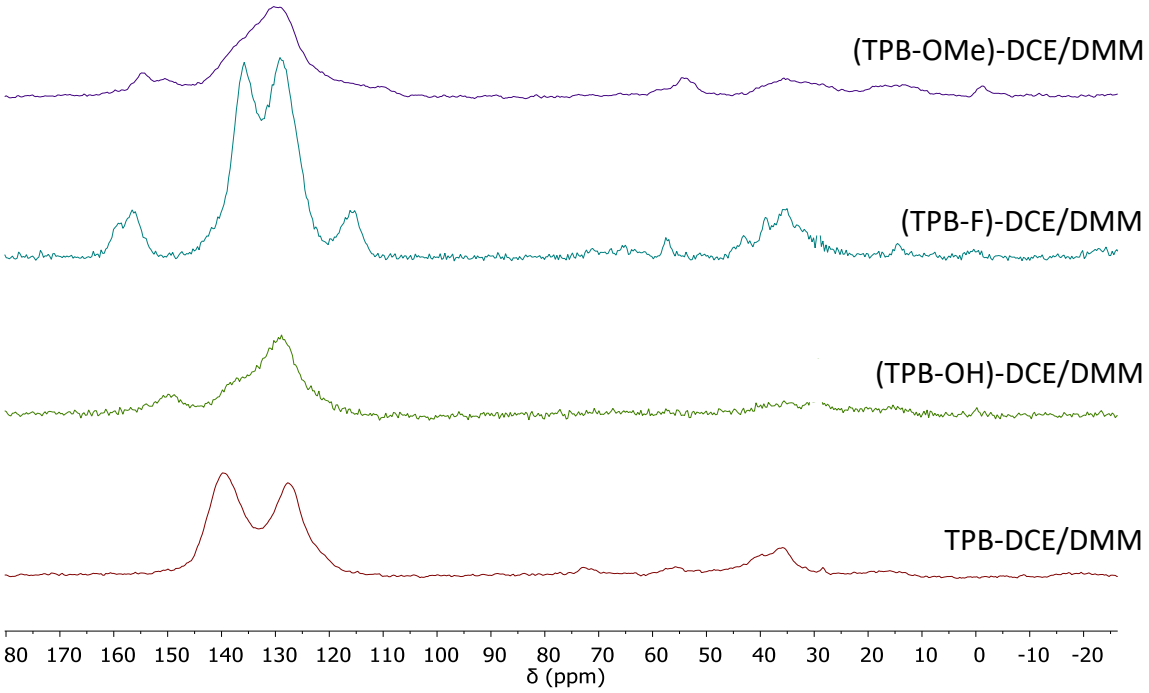

Figure 3.1.4.2a: SS-^{13}C NMR spectra of TPB-HCP adsorbents. Recorded at 300 MHz, spin rate: 12000 Hz.

Upon comparison of the ^{13}C SS-NMR spectra, displayed in Figure 3.1.4.2a, significant differences in the distribution of signals at both the aromatic and alkyl group regions are observed for the functionalised adsorbents. Interestingly, (TPB-OH)-DCE/DMM & (TPB-OMe)-DCE/DMM, show a similar profile with broad and overlapping aromatic resonances in the region δ =105 - 145 ppm. Furthermore, the aromatic carbons attached to the hydroxyl and methoxy functional groups give rise to the signals at 149 ppm and 155 ppm, respectively. A weak resonance is also observed at 155 ppm for (TPB-OMe)-DCE/DMM, suggesting that partial demethylation of the aromatic methoxy functionality has occurred during the Lewis acid-mediated polymerisation. However, residual methoxy substituents are still present within the polymeric structure, as demonstrated by the peak at 54 ppm.

Similarities are also observed in the spectra of the adsorbents TPB-DCE/DMM & (TPB-F)-DCE/DMM, which both show similar broad aromatic resonances, with (TPB-F)-DCE/DMM displaying an additional

peak at δ = 156.5 ppm, which originates from the highly de-shielded aromatic carbon to which the fluorine substituent is attached.

The ^{13}C SS NMR spectra are somewhat consistent with gas adsorption data, showing that the monomers TPB-OH and TPB-OMe result in more amorphous less well-defined structures, likely due to the higher coordinating properties of hydroxyl and methoxy substituents compared to fluorine.

3.1.4.3 Aluminium content determination via ICP-OES

In theory, the presence of Lewis basic substituents on the aromatic building blocks for HCP synthesis could potentially increase the encapsulation of coordinated aluminium-based species within the pores. This was investigated via quantitative analysis of HCP aluminium content using ICP-OES, after acid and MW digestion techniques. The aluminium content for the polyphenylene polymer TPB-DCE/DMM was determined to be very low, approximately 0.09% by weight. Small deviations in aluminium content were observed for (TPB-OMe)-DCE/DMM & (TPB-OH)-DCE/DMM, which contained 0.07% & 0.17% Al, respectively. A significantly higher content was however observed for the polymer (TPB-F)-DCE/DMM, with 1.31% of its total mass originating from trapped aluminium species. The efficiency of aluminium removal from the pores of the polymer during purification is likely dependent on many factors such as the strength of the interactions between Al species and the functionalities present on the polymeric surface, as well as the fraction of mesopores, which are important for effective diffusion and aluminium removal from the micropores. The ICP data suggests that the decrease in BET surface area observed for the polymers (TPB-OMe)-DCE/DMM & (TPB-OH)-DCE/DMM is not due to increased aluminium content, and the Lewis acid-base type coordination during polymerisation, as well as substituent pore filling effects are likely the main contributing factors.

3.1.4.4 Metaldehyde adsorption

In principle, upon introduction of fluorine, methoxy and hydroxy functionalities to the TPB aromatic monomer the polarity of the polymeric networks produced is enhanced. Due to the metaldehyde molecule of interest possessing moderate polarity as well as weak H-bond accepting moieties, in the metaldehyde it was suggested that the functionalisation may lead to better aqueous removal efficiencies. Computational studies have previously shown that metaldehyde interactions with polar functionalities such as carboxylic and hydroxyl functionalities are energetically favourable and therefore may enhance metaldehyde adsorption.[227] In addition, the presence of polar functionalities may result in more efficient polymer swelling when suspended in the aqueous medium, therefore increasing the availability of the adsorbent's surface.

However, subjecting the functionalised materials to batch equilibrium conditions, as described previously, resulted in lower adsorptive capacities compared to the non-functionalised sorbent TPB-DCE/DMM.

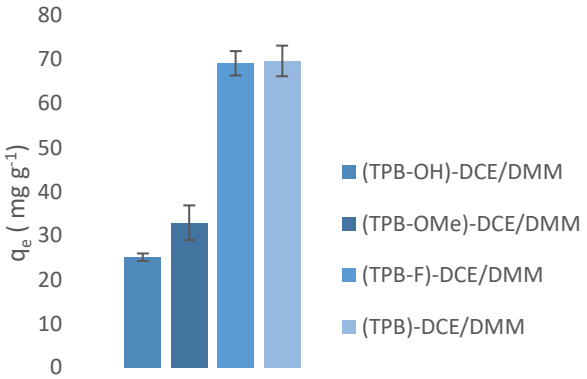

HCP sorbent	q_e (mg g^{-1})
TPB-DCE/DMM	69 ± 5
(TPB-F)-DCE/DMM	69 ± 8
(TPB-OMe)-DCE/DMM	33 ± 1.5
(TPB-OH)-DCE/DMM	25.1 ± 0.9

Figure 3.1.4.4a: Metaldehyde equilibrium adsorption capacities, as determined via batch equilibrium studies. Initial metaldehyde concentration: 80 mg L^{-1} Adsorbent dose: 1 mg mL^{-1}.

As observed in Figure 3.1.4.4a, the functionalised adsorbents produced failed to demonstrate any improvement in aqueous metaldehyde uptake, over the non-functionalised adsorbent. Specifically, the most polar adsorbent derived from the hydroxyl-TPB analogue demonstrated a significantly lower capacity q_e= 25.1 ± 0.9 mg g^{-1}, compared to the TPB-DCE/DMM. The polymer (TPB-OMe)-DCE/DMM also shows a considerably lower affinity for metaldehyde, reaching saturation capacity at q_e= 33 ± 1.5 mg g^{-1}. This reduction could be explained with reference to the gas adsorption data explained in section 3.1.4.1, which indicates significantly compromised pore size distributions and S_{BET} surface areas of the functionalised sorbents in comparison to TPB-DCE/DMM. Specifically, for hydroxy and methoxy functionalised adsorbents, both V_{total} & V_{micro} demonstrate a two-fold decrease over TPB-DCE/DMM, suggesting that pre-polymerisation modification approach has negative effects on the porosity of the materials. It should be however noted that, particularly for adsorbents of high surface polarity, gas adsorption data may not realistically represent an accurate picture of the sorbent porous structure during metaldehyde adsorption, as significant polymer swelling may occur, following suspension of the bulk solid in water.

Alternatively, the substantial increase in the polarity of a surface may result in stronger interactions with the polar aqueous medium, and result in preferential solvation of the active sites, rather than metaldehyde binding.[16]

Finally, the fluorinated adsorbent demonstrated good metaldehyde uptake, owing to its high S_{BET} and good distribution of micro, meso and macropores, as shown by N_2 adsorption data. However, comparted to TPB-DCE/DMM, the fluorinated polymer showed no difference in metaldehyde affinity, to compensate for the significant increase in synthetic route complexity and overall cost. Conclusively, the results reported demonstrate that pre-polymerisation functionalisation of HCPs can often be problematic, as the coordination of Lewis basic functionalities to the Lewis acid catalyst may result in the formation of networks with significantly compromised BET surface areas and porosities.

3.1.5 Magnetically responsive TPB-HCP nanocomposite: Fe_3O_4@TPB-HCP

There are several previous examples of particle-supported HCPs in the literature.[133,228,229] In the present work, a TPB-based HCP was grafted onto functionalised superparamagnetic iron oxide nanoparticles to produce a magnetic nanocomposite which retained high affinity for metaldehyde.

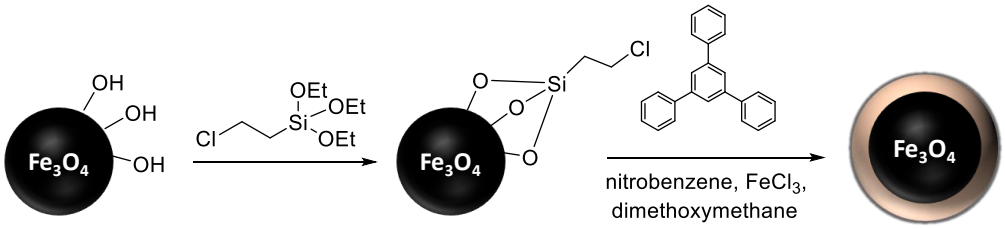

Figure 3.1.5a: Scheme showing the functionalisation of iron oxide nanoparticles,[135] and subsequent polymerisation to form a TPB-HCP magnetic nanocomposite.

The functionalisation of iron oxide nanoparticles using 3-chloropropyltriethoxysilane reagent was performed in DCM and was based on a modified literature procedure, first reported by *Pan et. al*.[135] The synthesis was performed under sonication to prevent Fe_3O_4 particle aggregation, and the final functionalised product was isolated using a magnet and kept under an inert atmosphere to prevent the hydrolysis of the alkyl triethoxysilane functionality. The grafting of the HCP onto the alkyl chloride-functionalised particles was also performed in dilute conditions and under sonication. Specifically, the grafting of the particles with a HCP outer sphere was performed by the Lewis acid mediated polymerisation of TPB, in the presence of nitrobenzene, $FeCl_3$ and DMM. The solvent NB and the milder Lewis acid $FeCl_3$ were used, to eliminate any side reactions that could take place in the presence of chlorinated solvents and the more reactive $AlCl_3$.

Even though the degree of functionalisation is difficult to determine, a TGA comparison of the magnetite, the functionalised magnetite and the final composite material show distinct mass losses at high temperature. Magnetite is stable and experiences mass loss of 5% at 700 °C, associated primarily with loss of moisture from the surface of the particles. The functionalised magnetite and final

composite material show mass losses of 17% & 33%, respectively. Those values are associated with the organic components which will rapidly degrade at high temperatures.

Gas adsorption data for the nanocomposite synthesised show that it retains microporosity with a specific BET surface area of 601 ± 32 $m^2 g^{-1}$, a total pore volume of 0.473 ml g^{-1} and micropore volume of 0.11 ml g^{-1}, as obtained from the N_2 adsorption isotherm at 77 K. Additionally, the maximum CO_2 adsorption of the Fe_3O_4@ TPB-NB/DMM composite, at 273 K, was calculated as 1.02 mmol g^{-1}.

As expected, the porosity and gas adsorption properties of the composite were found to be much lower in comparison to the TPB-HCP synthesised in the absence of the functionalised particles. The synthesis of TPB-NB/DMM was performed under identically dilute conditions, using the same reagents and nitrobenzene as a solvent. The adsorbent demonstrated a surface area of 1426 $m^2 g^{-1}$, total and micropore volumes of 1.826 ml g^{-1} & 0.26 ml g^{-1}, respectively, as well as good CO_2 capacity of 2.46 mmol g^{-1}. The apparent difference between the Fe_3O_4@ TPB-NB/DMM & TPB-NB/DMM originates from the non-porous nature of magnetite particles, which greatly contributes to the mass of the overall composite without contributing to the material's specific surface area.[230] Importantly, both TGA and gas adsorption data suggest that a relatively small amount of the HCP was incorporated onto the surface of the functionalised particles.

The magnetically responsive particles obtained demonstrated a high adsorptive capacity of 61 ± 1.6 mg g^{-1} for metaldehyde, as determined in batch equilibrium studies. This value is slightly lower than for TPB-NB/DMM, with the small difference in metaldehyde uptake being somewhat inconsistent with gas adsorption data obtained for the composite and HCP sorbents. It is speculated, that despite the porous HCP component being present at a relatively low mass percentage, the formation of a thin outer sphere around the Fe_3O_4 particles may result in high intraparticle diffusion efficiency, as most pores of the HCP component are in close proximity to the solution-nanoparticle interface. This would also reduce the requirement for larger transport pores, allowing Fe_3O_4@ TPB-NB/DMM to possess a higher relative

microporosity compared to TPB-NB/DMM. This reduced requirement for metaldehyde bulk diffusion in the composite against TPB-NB/DMM, may account for the nanocomposite displaying higher metaldehyde affinity than expected. However, there exists very limited research on the effect of nanoparticle functionalisation and grafting thickness, with respect to adsorption properties of composite adsorbents from solution. Importantly, the performance of the composite material falls in the lower region of the TPB-based adsorbents previously discussed, but it is higher than PAC & ST-DV adsorbents, and considerably higher than reported for activated carbon adsorbents which typically lie within the region 0.4-50 mg g^{-1}.[196]

Finally, it should be noted that the synthetic route employed in the synthesis of the composite is not industrially attractive as it requires dilute conditions and a sonication bath, and that other methods for magnetic composite syntheses may be preferred for industrial applications.[231]

3.1.6 Summary, aims and objectives

From all materials subjected to batch equilibrium conditions for metaldehyde adsorption from water, the material derived from the TPB aromatic monomer in DCM solvent was of the highest performance. Novel, externally crosslinked analogues of this adsorbent, with higher meso and macroporosities were found to display enhanced metaldehyde affinity, while pre-polymerization modifications on the DCM motif with polar groups were found to be unsuccessful in further increasing metaldehyde capacities. It was decided that due to the simple and inexpensive synthetic routes of the TPB precursor and its polymerisation step, the externally crosslinked adsorbents may show great potential as porous materials that could mediate the aqueous removal of metaldehyde by adsorption. To further evaluate their performance, further water testing was performed in the following Chapter 3.2.

3.2 Further water testing on metaldehyde removal using TPB-HCP adsorbents

In batch equilibrium experiments, discussed in sections 3.1.1 & 3.1.2, the TBP aromatic unit was identified as an industrially attractive and inexpensive building block for the formation of HCP sorbents possessing excellent affinities for metaldehyde. In addition, the presence of an external crosslinking unit was found to facilitate enhanced adsorption properties by resulting in the formation of more meso and macropores, which increase the accessibility of micropores in solution. One of the highest performing adsorbents, namely TPB-DCM/TMOF, was subjected to further analytical testing to assess the suitability of TPB-HCPs in aqueous metaldehyde removal and provide an insight on the mechanisms regulating the adsorption process.

3.2.1 Solution adsorption Isotherm for metaldehyde

The adsorption isotherm experiment was conducted at T= 293 K, by equilibrating polymer samples with metaldehyde aqueous solutions in ultrapure water at an initial concentration range of 4 - 100 mg L^{-1}. The measured pH values of different initial concentrations showed no significant variations and were assumed constant, at pH = 7.4. The adsorbent dose was kept constant at 1 mg ml^{-1} and the amount of metaldehyde remaining after a contact time of 46 hr was quantified using GC-MS, after pre-quantitative SPE. Importantly, all initial metaldehyde concentrations used were standardised against calibration curves of different concentration ranges. This was of particular importance for the most concentrated metaldehyde solutions, where the aqueous solubility of metaldehyde at 20 °C (188 mg L^{-1}),[12] could have resulted in the precipitation of analyte and overestimation of the calculated equilibrium capacity.

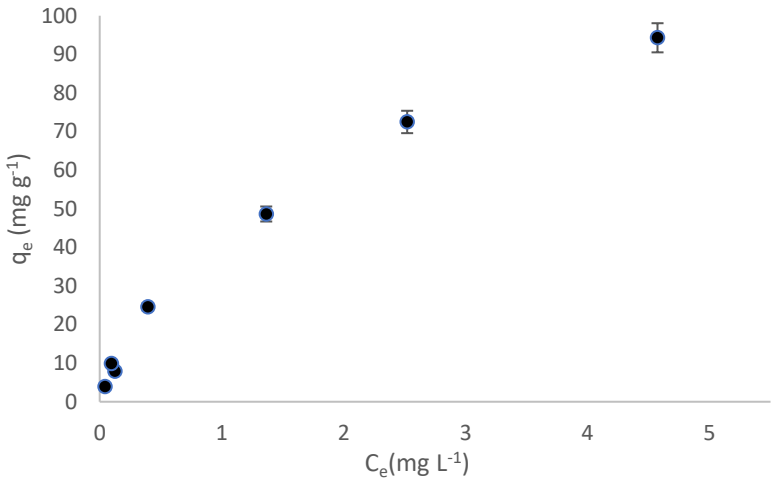

C_0 (mg L^{-1})	Removal (%)
4	98.9
5	98.9
10	98.4
25	98.3
50	97.3
75	96.6
100	94.3

Figure 3.2.1a: Isotherm plot of metaldehyde equilibrium capacity (q_e) against equilibrium solution concentration (C_e), at various initial concentrations (C_0). Percentage removal efficiencies at all concentrations are listed.

As demonstrated in Figure 3.2.1a, the isotherm plot of adsorptive capacities q_e (mg g^{-1}) against equilibrium concentration of metaldehyde, C_e (mg L^{-1}), demonstrates the adsorbent's exceptional affinity for metaldehyde. Specifically, very high adsorption efficiency (~99%) of metaldehyde is observed at low initial concentrations, C_0 = 4 - 10 mg g^{-1}, with the removal efficiency slowly decreasing in higher concentrations as the occupancy of the sorbent active sites increases and the polymer approaches saturation capacity. At the highest metaldehyde concentration of C_0 = 100 mg L^{-1}, a removal efficiency of 94% is observed, corresponding to an experimental adsorptive capacity of 94.4 ± 0.9 mg g^{-1}. Owing to the exceptional adsorptive properties of TPB-DCM/TMOF, the experimental saturation capacity of the sorbent for metaldehyde is likely significantly lower than the theoretical maximum. Obtaining a higher adsorption capacity experimentally is possible but would require changes in the experimental design. Increasing the concentration of metaldehyde above 100 mg L^{-1}, is likely not a suitable approach due to previously mentioned solubility issues, and specifically lowering adsorbent dosage would be most appropriate.

3.2.1.1 Two-parameter adsorption model determination

To further investigate the nature of the adsorption process of metaldehyde, the data was modelled via mathematical fitting, using both the two-parameter, linear and non-linear Freundlich & Langmuir models. Due to its simplicity, linear regression has been extensively used in the literature to analyse adsorption processes and assess the consistency between experimental data and proposed theoretical models.[232] However, the values of calculated model parameters, as well as the statistical correlation coefficients, have been reported to strictly depend on whether the linearised, or non-linear equations are used.[194,195] Significant computational advances have recently resulted in more frequent use of non-linear fitting methods, which have been previously discussed to offer higher accuracy and validity in estimating model parameters as well as statistical correlation coefficients.[193,233] As a result, significant deviations may result based on the choice of mathematical modelling methods, potentially leading to a misjudgement of the best fitting relationship between theoretical models and experimental data.

The issue addressed above is thoroughly demonstrated by Figure 3.2.1.1a, which shows significant changes in the calculated isotherm shapes of the Langmuir & Freundlich models, when linear and non-linear fitting methods are applied.

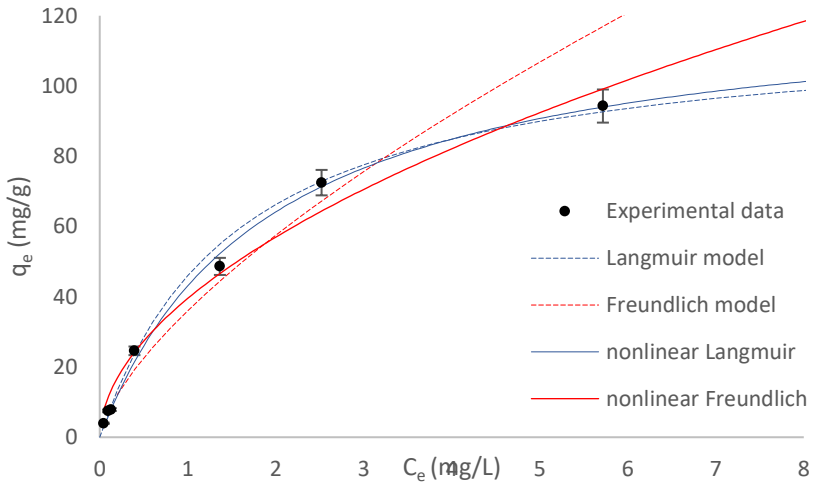

Table 3.2.1.1a: Model parameters determined using linear and nonlinear regression methods for the two parameter isotherms: Langmuir and Freundlich.

Similarly, significant discrepancies are observed for the Langmuir & Freundlich model parameters determined depending on the fitting model employed. All calculated parameters are listed in Table 3.2.1.1a, along with their associated uncertainties.

Figure 3.2.1.1a: Isotherm plot of TPB-DCM/TMOF, for showing experimental data, and the linear and nonlinear Freundlich & Langmuir models calculated using regression methods.

Model parameters		Linear	Non-Linear
Freundlich model	R^2	0.984	0.980
	K_F (mg g^{-1} (L $mg^{-1})^{1/n}$)	36.00 ± 0.17	39.50 ± 2.87
	n	1.48 ± 0.08	1.90 ± 0.2
Langmuir model	R^2	0.988	0.996
	K_L (L mg^{-1})	0.64 ± 0.05	0.52 ± 0.06
	q_{max} (mg g^{-1})	118.00 ± 5.8	125.00 ± 6.03

Derived using the linear method, a very small discrepancy in statistical correlation coefficients R^2 for Langmuir & Freundlich suggests a similar degree of linearity in the dataset mathematical fittings. This may lead to the inaccurate assumption that no preference for either the Langmuir or Freundlich model is observed for the adsorption of metaldehyde onto TPB-DCM/TMOF. This type of consistency with both linear models has been frequently reported in the literature, particularly at low solute concentrations when the adsorption isotherm is often linear. [160]

A contrasting conclusion is observed upon conducting non-linear regression methods to apply the Freundlich & Langmuir models. Specifically, the statistical correlation coefficient R^2 for the Langmuir model is much closer to unity than in the Freundlich model, suggesting that the former is a significantly better predictor of the overall adsorption process. Despite the comparison of R^2 values in model determination being a widespread and practical approach, several authors have reported the requirement of alternative functions of descriptive statistics.[193,194,197,234] Specifically, the χ^2 test has

received significant attention,[194,235] particularly in statistical assessment of nonlinear regression methods, and may be used to evaluate the discrepancy of experimental and theoretical data. The model parameters estimated using the linear and nonlinear Langmuir & Freundlich models were used to calculate $\Sigma\chi^2$ values (using eq 3.2.1.1a), with reference to the 7-point experimental dataset obtained. According to eq3.2.1.1a, good consistency between experimental data and the theoretical model is indicated by low values of $\Sigma\chi^2$.

$$\Sigma\chi^2 = \sum_{n=1}^{n} \frac{(q_e\,(\text{model}) - q_e\,(\text{exp}))^2}{q_e\,(\text{exp})} \qquad (\text{eq } 3.2.1.1a)$$

Table 3.2.1.1b: Calculated values of $\Sigma\chi^2$ for the linear and nonlinear Freundlich & Langmuir models

	Linear	Non-Linear
Freundlich model	7.6	10.4
Langmuir model	1.2	1.3

Upon comparison of the calculated $\Sigma\chi^2$ values, shown in Table 3.2.1.1b, it is evident that there is significant preference for the Langmuir model over the Freundlich, from both linear and nonlinear methods. Importantly, the preference for the Langmuir model is more easily identifiable using nonlinear regression. Notably, examination of χ^2 values for each datapoint may provide valuable information for the consistency of a model at a specific range of initial adsorbate concentration.

3.2.1.2 Explanations concerning the linear Freundlich & Langmuir models

The Freundlich model fails to accurately predict metaldehyde adsorption properties across all initial metaldehyde concentrations used in the experiment. At low initial concentrations, the high affinity of the TPB-DCM/TMOF adsorbent for metaldehyde results in high adsorption efficiency and the resulting high degree of linearity obtained in the plot of q_e against C_e may often produce a statistical correlation coefficient indicative of good data fitting, regardless of which model is used.[233] This effect is observed for metaldehyde adsorption, however detailed statistical analysis of the data shows that the Langmuir model remains prominent, even when the high initial concentration points are omitted from the dataset. Furthermore, appropriate selection of a theoretical model that best describes adsorption behaviour, requires its robustness over an acceptable adsorbate concentration range. Therefore, modelling of the data using the linearised and nonlinear Freundlich models, demonstrates that multilayer adsorption of metaldehyde molecules onto the surface of TPB-DCM/TMOF does not significantly contribute to the overall adsorption process, and that the high statistical correlation coefficient obtained likely originates from the arbitrarily selected metaldehyde initial concentrations.

In contrast, the nonlinear Langmuir model appears to be an excellent predictor of the adsorption of metaldehyde onto TPB-DCM/TMOF, as demonstrated by $R^2 = 0.998$, as well as the calculated values of χ^2, which were found to be close to zero, across all experimental datapoints. Based on the model parameters, the theoretical adsorption capacity of TPB-DCM/TMOF for metaldehyde is estimated as 125.00 ± 6.03 mg g^{-1}, and is amongst the highest capacities reported in the literature up to date. [16,222,227] This result also confirms the previous hypothesis that under experimental conditions of C_0 =100 mg L^{-1} and adsorbent dose of 1 mg mL^{-1}, the HCP adsorbent did not approach its saturation capacity. Additionally, the presence of strong interactions of metaldehyde adsorbate with active sites of the polymeric surface, is demonstrated by the magnitude of $K_L = 0.52 \pm 0.06$ L mg^{-1} which is significantly larger than previous literature work on metaldehyde removal.[16] The separation factor R_L is a

dimensionless quantity, which depends on K_L constant and initial concentration of adsorbate C_0, and is typically used to determine the characteristics of the Langmuir isotherm. The values of R_L for the initial concentration range of C_0 = 4 - 100 mg L^{-1} were found to fall within 0 and 1, indicating a favourable adsorption process.[92] Furthermore, the value of R_L approaches unity at increasing metaldehyde initial concentration, as TPB-DCM/TMOF gradually approaches saturation capacity.

Conclusively, experimental data shows that the adsorption of metaldehyde onto TPB-DCM/TMOF is more consistent with the Langmuir model over the Freundlich, however both models can be most accurately determined using the non-linear regression methods. From a mechanistic perspective, it may seem more logical that the highly amorphous nature of TPB-HCPs may be more consistent with metaldehyde adsorption following the heterogeneous adsorption Freundlich model, as it does not require the even distribution of adsorption sites of identical energy across the surface.[197] Along with several other factors which are known to influence adsorption, adsorbent-adsorbate interactions are dominant in dictating the overall adsorption process.[191] In the case of metaldehyde adsorption onto TPB-DCM/TMOF, π-type interactions are prevalent in driving metaldehyde uptake,[227,236] and the π-rich polyphenylene backbone of the adsorbent may result in the formation of an abundance of adsorption sites with similar energies for metaldehyde binding, therefore improving mechanistic consistency with the Langmuir model. Additionally, it is important to recognise the complexity of the true nature of solution adsorption, which cannot be accurately represented by two-parameter mathematical expressions, such as the Langmuir and Freundlich models. The quote ''all models are incorrect, but some of them are useful'' accurately describes the modelling of adsorption processes,[237] and it is most often the case that the adsorption of solute onto a solid surface occurs via several distinct mechanisms.

3.2.2 Adsorption Kinetics

The adsorbent TPB-DCM/TMOF shows excellent adsorption properties for the aqueous removal of metaldehyde from water in batch equilibrium and solution isotherm experiments discussed in sections 3.1.2 & 3.2.1, respectively. However, both experiments are characterised by long adsorbent-adsorbate contact times (46 - 48 hr) and therefore give no valuable information on adsorption kinetics. The adsorbent's metaldehyde capacity, q_t (mg g^{-1}) at time t (s) was determined at various time points, namely 15 s, 30 s, 60 s, 300 s, 600 s ,1800 s, 50000 s & 108000 s. The experiment was performed at initial metaldehyde concentration, C_0 = 80 mg L^{-1} in ultrapure water, adsorbent dose of 1 mg mL^{-1} and pH = 7.4. Separate sample vials were used for each time point. Kinetic plots of q_t (mg g^{-1}) vs time t (s), are displayed in Figure 3.2.2a for the initial 6-point and full 8-point experimental datasets.

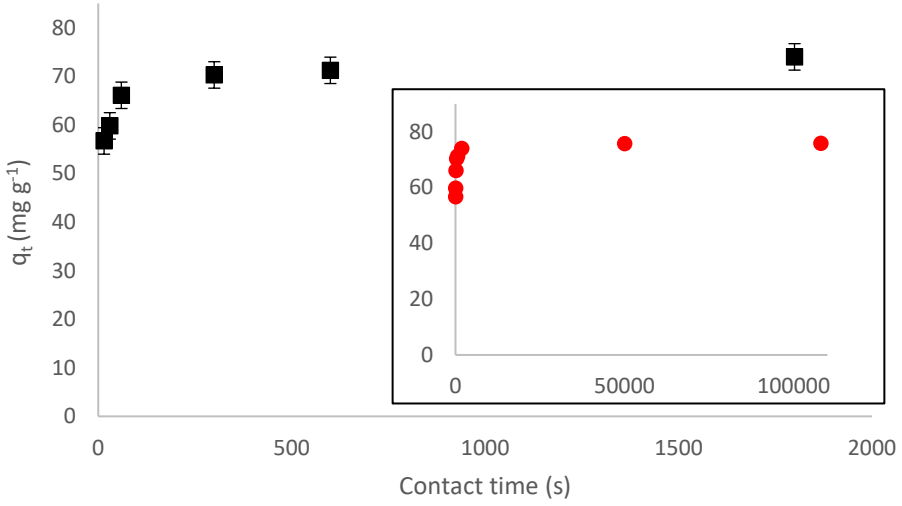

Figure 3.2.2a: Kinetic behaviour of metaldehyde uptake by TPB-DCM/TMOF, determined at 80 mg L^{-1} metaldehyde initial concentration and adsorbent dose of 1 mg mL^{-1}.

The adsorption of metaldehyde onto the surface of TPB-DCM/TMOF was found to occur very rapidly, with 70% of the total metaldehyde removed in the first t = 15 s and with 93% of the total equilibrium saturation capacity reached within 10 mins. At contact times t = 600 s ,1800 s, 50000 s & 108000 s, a very small steady increase is observed for the adsorptive capacity q_t determined. Importantly, the rapid uptake of metaldehyde demonstrated by the TPB-DCM/TMOF, presented difficulties in monitoring the

initial adsorption behaviour. It was decided that equilibration times of t < 15 s, should not be attempted as, at such low contact times, significant relative errors would be introduced in the value of t.

3.2.2.1 Selection of appropriate kinetic models

With reference to previous discussion in section 3.2.1, linear and nonlinear regression methods have also been observed to give significantly different answers in the modelling of kinetics.[199,238,239] Therefore, to get an accurate representation of the metaldehyde adsorption kinetics onto the surface of TPB-DCM/TMOF, the PFO, PSO & Elovich linear and nonlinear kinetic models were used to fit the data, across different sets of datapoints. In addition, the Weber and Morris model was used to explain intraparticle diffusion. Using both regression methods, and in accordance with statistical analysis using the R^2 and χ^2 error functions, the PFO and Elovich models were found to be inconsistent with the experimental adsorption kinetics and are omitted from discussion.

Table 3.2.2.1a: Parameters and error coefficients for the PSO kinetic model, calculated using linear and nonlinear regression methods.

Model parameters		Linear	Non-Linear
PSO	R^2	0.99	0.92
	$\Sigma\chi^2$	23.54	0.48
	q_e (mg g^{-1})	75.7 ± 0.9	73.7 ± 0.9
	K_2 (mg^{-1} g min^{-1})	0.03 ± 0.007	0.15 ± 0.02

Satisfactory agreement was demonstrated by the linear and nonlinear PSO models, while the latter was found to be a much more accurate descriptor of the kinetics of adsorption. This is in agreement with previous literature reporting that the linearisation of the rate expression changes the distribution of errors in the function, consequently altering the calculation of model parameters.[197,238,239] This is largely reflected on the value of the rate constants in Table 3.2.2.1a, with the linear method returning a rate constant five times slower than the nonlinear method.

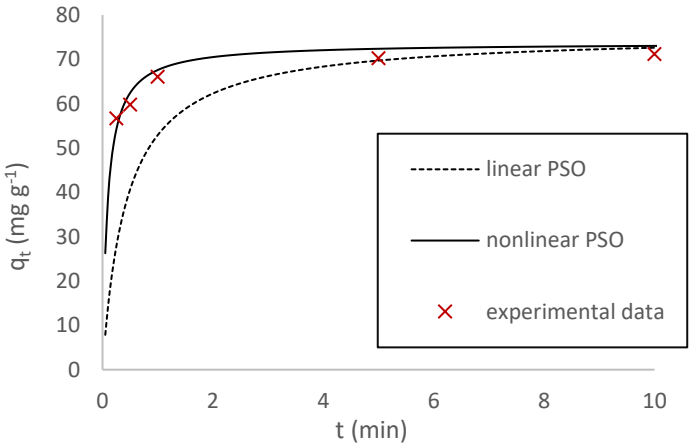

t (min)	Linear	Non-Linear
0.25	14.7	0.114
0.5	6.1	0.116
1	2.6	0.034
5	0.004	0.063
10	0.027	0.046

Figure 3.2.2.1a: Kinetic plot of linear and nonlinear PSO models along with experimental dataset containing the first five points (left). Tabulated χ^2 error values for the linear and nonlinear models (right).

As observed in Figure 3.2.2.1a, the linear regression model is defective at modelling the kinetics of metaldehyde adsorption at low values of t = 0.25 – 1 min. This is thoroughly demonstrated by the initial χ^2 error function values of the linear regression method, which are many orders of magnitude higher than in the non-linear fitting. Interestingly, the χ^2 values approach zero as the adsorption reaches plateau, suggesting that the linearised PSO is good for fitting the experimental data at the linear part of the curve. As the rate constant calculation relies on the initial, nonlinear part of the curve, the linear method is therefore unfit for obtaining an accurate rate constant. Overall, these findings demonstrate the significant disadvantages of using linear regression analysis for non-linear kinetic behaviours, as well as the extensive experimental bias which could arise by selecting a model solely based upon comparisons of R^2 coefficients in linearised models.

3.2.2.2 Explanations concerning the PSO model for metaldehyde adsorption.

Excellent agreement of the experimental data is observed for the linear PSO, with the statistical correlation coefficients approaching better goodness of fit, as higher values of t are omitted from the dataset. This trend represents solid evidence that the PSO model is preferred over the PFO model. The explanation comes from Canzano *et al.*,[240] who demonstrated that datapoints at low contact times are

very important in the determination of a correct model and that the exclusive selection of datapoints close to equilibrium introduces experimental bias favouring the PSO model.

Therefore, the initial adsorption behaviour can be appropriately modelled by the PSO, and the rate constant obtained thoroughly demonstrates the rapid metaldehyde uptake of the TPB-DCM/TMOF adsorbent. With reference to previous studies using the PSO model to characterise the kinetics of metaldehyde adsorption,[222,241,242] the value of k_2 = 0.15 ± 0.02 mg^{-1} g min^{-1} is observed to be exceptionally high, however as previously discussed, direct comparisons to the literature should be performed carefully ensuring identical experimental conditions and regression methods have been employed. In addition, the equilibrium capacity q_e = 73.4 ± 0.9 mg g^{-1} for the adsorbent calculated using the linear PSO, is slightly lower than the experimentally determined equilibrium capacity q_e = 76 ± 2 mg g^{-1}, with their relative discrepancy being within the corresponding calculated errors.

Including adsorbent dose, adsorbate initial concentration and several other factors, the sorbent particle size distribution is a key factor dictating adsorption behaviour. Busquets et al. demonstrated the rapid increase in rate of metaldehyde uptake, when phenolic carbon adsorbent samples of lower particle size distribution were used.[16] it is therefore suggested that the rapid uptake of metaldehyde by the adsorbent TPB-DCM/TMOF is strongly facilitated by the sorbent particle size, which is far less than 100 µm.

Finally, it should be noted that the PSO model is entirely empirical and cannot provide an accurate mechanistic description of the adsorption kinetics, which has led to some authors criticising its validity.[243] From the data and statistical analyses presented herein, the following conclusions can be unambiguously drawn; the TPB-DCM/TMOF adsorbent contains an abundance of active sites which rapidly absorb metaldehyde at very low contact times (t < 60 s), and that the rate slows down as the fractional coverage of those sites increases. As the decrease of unoccupied active sites is directly

accompanied by a decrease in the bulk concentration of metaldehyde, it is likely that the overall adsorption rate is dependent on diffusion phenomena.[199]

3.2.2.3 Weber and Morris intraparticle diffusion model

To investigate upon the mass transfer processes that could potentially be occurring during metaldehyde adsorption onto TPB-DCM/TMOF, the Weber and Morris intraparticle diffusion model was employed.[244] The model relies on a plot of q_t against $t^{1/2}$ to identify linear relationships between the datapoints, although other approaches have also been used.[245] Multilinearity describes the distinct diffusion phenomena affecting the overall rate.

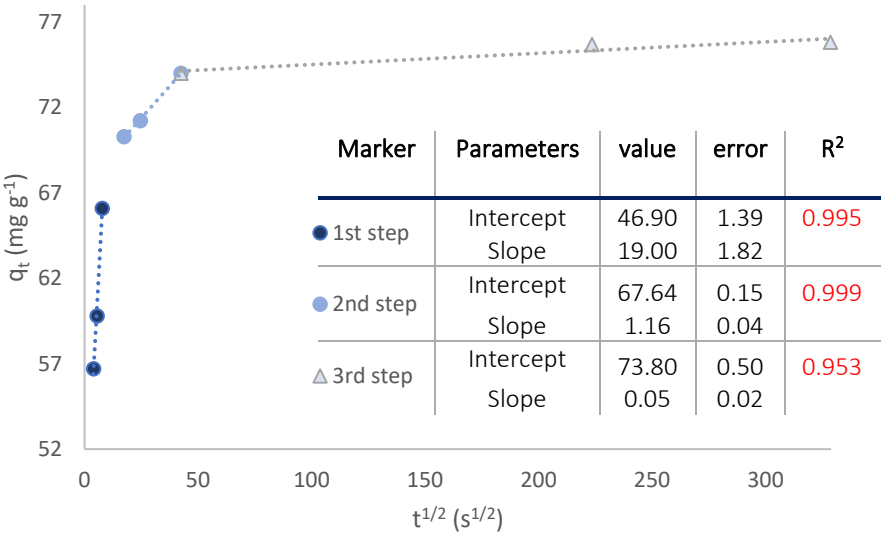

Figure 3.2.2.3a: Weber and Morris intraparticle diffusion model, with the plot of q_t against $t^{0.5}$, identifying three linear steps. Linear regression parameters for each step are listed.

As presented in Figure 3.2.2.3a, the Weber-Morris plot suggests the presence of three kinetic rate-limiting mechanisms. This type of multilinearity been extensively observed in kinetic modelling of organic substrates onto microporous sorbents.[44,245,246,208] Importantly, the final step of the adsorption process; namely the rate of physisorption of metaldehyde onto the active sites, occurs much faster than any mass transfer phenomena and does not contribute to the overall rate of adsorption.[200,201] In fact, kinetic models are most often used to investigate the diffusion path of the adsorbate to reach

active sorption sites. Finally, the bulk diffusion of metaldehyde was also eliminated as a factor dictating adsorption,[247] by ensuring sufficient stirring rate of 1000 rpm.

Consequently, in the 1st linear step of the plot, the rate of adsorption is dependent on external diffusion phenomena, in which the metaldehyde adsorbate molecules diffuse through the boundary layer to reach the surface of TPB-DCM/TMOF. As the surface contains an abundance of active sites, a very high initial uptake rate is observed, with the overall rate showing good agreement with the PSO model. Further influence on the kinetics, arising from the adsorbent particle size, is related to the surface area to volume ratio fraction, [248] which increases with decreasing particle diameter.

As the fractional coverage of the outer particle surface sites increases, the intraparticle diffusion rate gains control of the process, as further adsorption necessitates the redistribution of metaldehyde molecules from the surface to the adsorbent's internal pores. This mass transfer phenomenon is represented by steps 2 & 3, in Figure 3.2.2.3a. Importantly, solution adsorption using microporous materials has commonly been observed to be limited by intraparticle diffusion, as both film diffusion and final are adsorption are frequently both kinetically rapid.[249] Specifically, step 2 is likely associated with the faster diffusion of metaldehyde into macropores and larger mesopores, and is therefore much more rapid than step 3 which represents diffusion into smaller, less accessible pores.[208] In addition, step 3 is approximated to start when the capacity is q_t = 73.99 mg g^{-1} and 92% removal is achieved, which results in the factor q_e-q_t becoming increasingly small, and the magnitude of the driving force for the adsorption process rapidly diminishes.

Intraparticle diffusion mechanisms are separated into pore diffusion and surface diffusion, and the relative contributions of those have been reported to depend on the molecular weight of the adsorbate as well as the porous structure of the sorbent.[206] Although further exploration of the mass diffusion mechanisms is needed to confirm the following hypothesis, it is suggested that the size and molecular weight of metaldehyde is in good compatibility with the pore size distribution of TB-DCM/TMOF.

It can be concluded that, the very rapid uptake of metaldehyde by TPB-DCM/TMOF, is largely a consequence of its porous structure and the small average particle size of the bulk solid. With reference to N_2 adsorption isotherm data, the BET surface area of TPB-DCM/TMOF, S_{BET} = 1308 m^2 g^{-1}, and micropore volume, V_{micro}= 0.26 mL, are sufficiently high to accommodate a high equilibrium capacity for metaldehyde, resulting in 95% removal efficiency. In addition, equilibrium conditions are reached rapidly due to the presence of sufficient macro & mesopores (V_{total} - V_{micro}= 1.64 mL), which are known to facilitate rapid intraparticle diffusion. Finally, the narrow particle size of TPB-DCM/TMOF limits the distance of the particle surface to the inner & less accessible pores, resulting in low bulk diffusion pathways. The small solid particle diameter is also resulting in a high area of contact with the solution medium, further enhancing the kinetics of metaldehyde adsorption.

3.2.3 Rapid Small Scale Column Tests

The RSSCT approach was employed to determine whether TPB-HCPs can efficiently remove metaldehyde at significantly lower initial concentrations compared to previous batch, kinetic and isotherm experiments.

During the experiment, a combination of high hydrophobicity, small bulk sorbent particle size and an abundance of rough surfaces on the outer portions of the particles was assumed to be responsible for the high level of backpressure associated with the filtration of metaldehyde-spiked water, through a packed bed of adsorbent. Specifically, the properties mentioned are speculated to facilitate very efficient packing of the polymer when a hydraulic load is applied. For the highest performing adsorbents TPB-DCM/TMOF and TPB-DCM/TMOC, the hydraulic pressure readings from the HPLC pump often reached pressures of up to 15 bars, causing leaks in the apparatus.

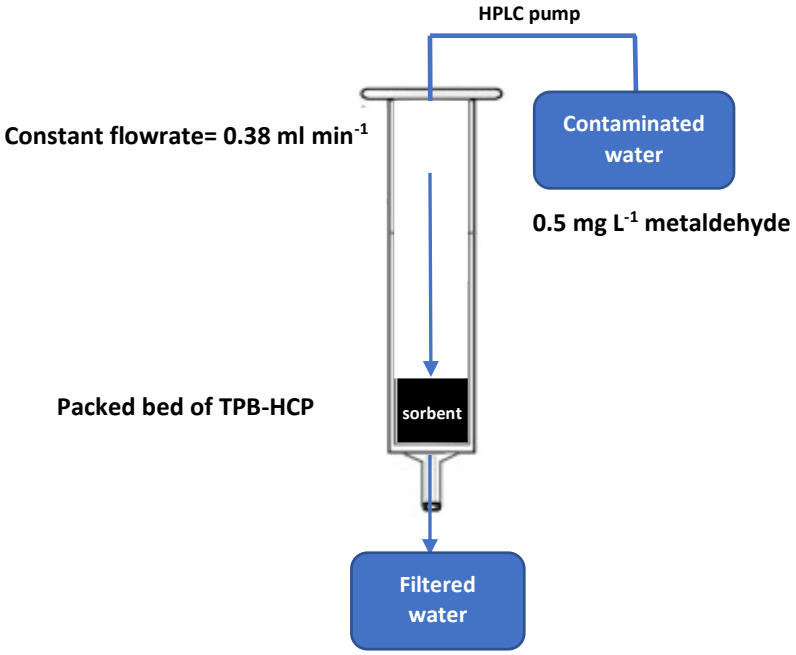

Figure 3.2.3a: Schematic representation of RSSCT using TPB-DCE/DMM. Initial metaldehyde concentration: 0.5 mg L^{-1}, Flowrate: 0.38 ml min^{-1}, Adsorbent amount: 270 mg, Bed volume: 0.9 mL

The polymer TPB-DCE/DMM was identified to demonstrate a stable, reasonably low hydrostatic pressure of 4 bar, and it was selected for the RSSCT. During the RSSCT an HPLC pump was used to continuously pump water through a cartridge packed with 270 mg of polymer TPB-DCE/DMM. Pumps of this type have commonly been used in RSSCTs due to their ability to handle moderately high pressures.[250] The flowrate was kept constant at 0.38 ml min^{-1}, corresponding to a volume of 547.2 ml of water being filtered per day. A schematic representation is shown in Figure 3.2.3a.

The filtration was carried out over a period of 8 days and a total of 4 L of water was filtered. The water was collected in separate 500 mL aliquots which were concentrated onto STDV (1 g /25 mL) cartridges. The cartridges were air-dried using a vacuum manifold and the analyte samples were eluted with DCM and subjected to quantitative analysis, using GC-MS. Detailed analytical method details are present in section 5.3.

Importantly, the pre-concentration of water in the SPE step decreases the method detection limit of metaldehyde to 0.025 µg L^{-1} which is far lower than the EU regulatory limit of 0.1 µg L^{-1}.[10] Upon analysis of GC-MS chromatograms, it was shown that no metaldehyde was present in any of the individual runs. Therefore, slow filtration through the HCP adsorbent corresponding to an empty bed contact time of 2.38 min, resulted in a 20000-fold reduction of metaldehyde concentration, as determined by effluent water analysis. This corresponds to a decrease in metaldehyde from 0.5 mg L^{-1} to lower than 0.025 µg L^{-1}.

The moderate stability of metaldehyde in aqueous solutions suggests that some degradation could have occurred over a week of filtration. Standardisation of the water used in the experiment shows an average metaldehyde content of 0.4 mg L^{-1}, suggesting that metaldehyde degradation of less 20% had occurred over the course of the experiment.

As an alternative method of quantifying the amount of metaldehyde adsorbed by the polymer, the cartridge was removed from the set-up and the polymer was air-dried. Determination of the metaldehyde content was performed by washing the polymer with DCM and then analysing using GC-MS, against a calibration curve. From the total of 2 mg of metaldehyde expected, 1.6 mg was present in the DCM extract, the result being consistent with metaldehyde-spiked water standardization data demonstrating a 20% metaldehyde degradation over a week of filtration. Furthermore, the removal of metaldehyde from the pores of the polymer after filtration can be performed via an organic solvent wash, which has important applications towards adsorbent reusability. In addition, this suggests that TPB-HCP adsorbents could also be potentially useful as SPE sorbents, as they show higher metaldehyde adsorptive capacities than the STDV sorbent commonly used in the solid phase extraction of metaldehyde, and with analyte recovery easily performed via organic solvent elution.

3.2.4 Investigating the breakthrough point for metaldehyde in RSSCTs.

The first RSSCT results demonstrate the exceptional affinity of the TPB-DCE/DMM for metaldehyde-spiked water but do not provide insight on the breakthrough point, at which metaldehyde can no longer be absorbed onto the polymer and will consequently be detected in the effluent water. The RSSCT experiment was therefore optimised and repeated. A custom-made apparatus was made consisting of a steal Swagelok® tube fitting which can be connected to the HPLC pump tube and a threaded PTFE column which could be directly screwed onto the Swagelok. Further description on the experimental apparatus can be found in chapter 5.3.4.

A dried sample of TPB-DCE/DMM was packed in the PTFE column using glass frits and connected to the HPLC pump. Aiming to reach breakthrough within a week of filtration, the amount of adsorbent was reduced to 200 mg, with respect to the previous RSSCT experiment. The column was washed with MeOH for 1 hr followed by ultrapure water, prior to filtration of metaldehyde-spiked aqueous solution at a concentration of 0.5 mg L^{-1}. After filtration through the TPB sorbent, the effluent water was passed through a pre-conditioned SPE cartridge directly, at a flowrate of 0.35 ml min^{-1}. The cartridge contained 1 g of ST-DV polymer with an approximate adsorbent bed volume of 4.17 mL, resulting in a very high empty bed contact time of 11.9 mins for the SPE process. There are several advantages associated with performing SPE under low flowrate/ high empty bed contact time conditions and these include significant increases in analyte recovery and improvement of the quality of the data obtained.[251] In addition, combining the filtration and solid phase extraction of water in one step makes the process easier and faster to execute. The SPE sorbent was replaced every 24 hrs, meaning that 504 ml of water was solid phase-extracted on each cartridge.

The filtration of metaldehyde-spiked water was carried out for a period of 9 days with a total of 4536 ml of water filtered and 9 fractions of 504 ml were extracted onto SPE cartridges. The cartridges were air-dried using a vacuum manifold and the analyte was eluted into 25 ml volumetric flasks.

Noteworthily, preconcentration of a large volume of water and elution with a smaller amount of solvent, greatly improves the overall method sensitivity by a factor of 20. As observed in Figure 3.2.4b, for the first 4 runs no metaldehyde was observed. As previously, due the LOD of the method estimated to be less than 0.025 μg L^{-1}, it can be inferred that for the first 2 L of filtration TPB-DCE/DMM was able to remove metaldehyde from the aqueous medium, rapidly decreasing the concentration far under the EU regulatory limit of 0.1 μg L^{-1}.

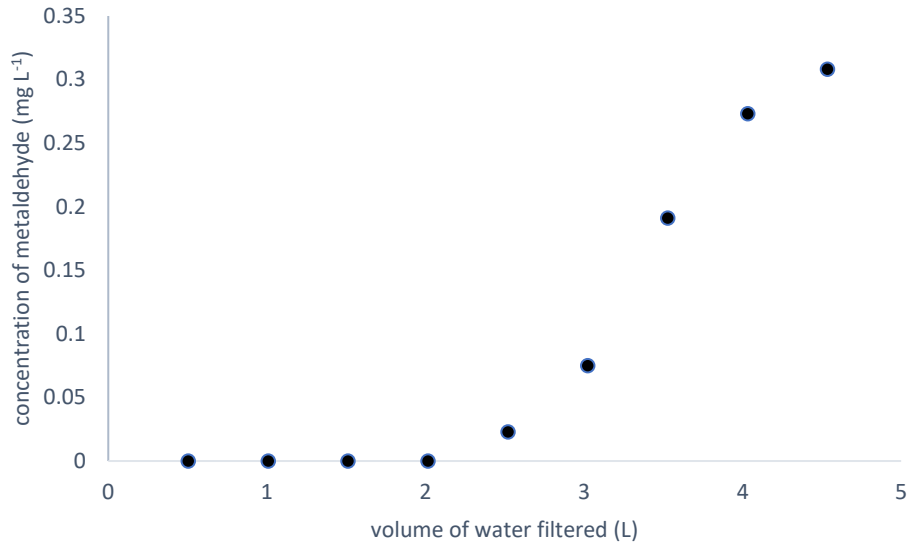

Figure 3.2.4b: Metaldehyde concentration of effluent water, as a function of the total volume filtered through the TPB-DCE/DMM adsorbent bed.

Upon filtration of 2.5 L of metaldehyde-spiked water, metaldehyde is observed in the effluent at a concentration of 0.023 mg L^{-1}, as estimated from the GC-MS chromatogram, using a calibration curve constructed from metaldehyde standards. As expected, the concentration of metaldehyde in the effluent water increases significantly as the RSSCT progresses reaching 0.075 mg L^{-1} at 3 L of filtration, followed by 0.191, 0.273 & 0.308 mg L^{-1} at 3.5, 4 & 4.5 L of filtration, respectively. Noteworthily the concentration rises rapidly and then plateaus off as the concentration of the effluent water approaches the concentration of the metaldehyde spiked water at a concentration of 0.5 mg L^{-1} (Figure 3.2.4b).

The volume of the packed TB-DCE/DMM bed located in the PTFE column was calculated to be approximately 0.8 cm^3, which divided by the flowrate of 0.35 ml min^{-1}, returns a value of 2.4 min for the EBCT. Since metaldehyde was detected in the effluent after approx. 2 L of filtration, it can be concluded that the polymer bed was able to purify over than 2500 column volumes of metaldehyde-spiked water before breakthrough was achieved.

3.2.5 Removal of metaldehyde via thermal regeneration

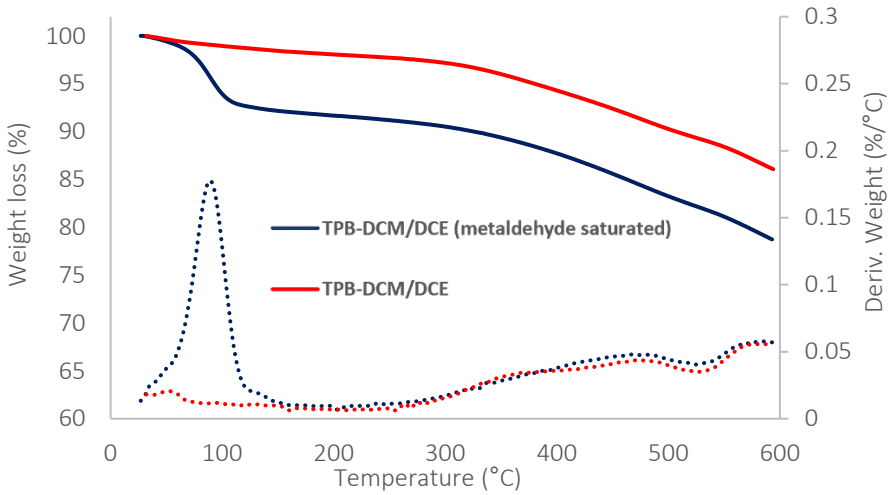

Figure 3.2.5a: TGA profile of TPB-DCM/DCE, & TPB-DCM/DCE saturated with metaldehyde, following batch equilibrium studies. 1st derivative spectra are shown as dotted lines.

Following equilibrium studies, a TPB-based HCP saturated with metaldehyde was filtered and air-dried to remove most of the water. A TGA run was conducted to assess whether metaldehyde can be removed from the pores of the polymer via the application of heat. Metaldehyde is known to be heat sensitive and degrades thermally, resulting in the release of four volatile acetaldehyde molecules. The drop at 89 °C shown by the blue solid line in Figure 3.2.5a represents the subsequent loss of mass in

the sample associated with metaldehyde degradation. A similar mass loss is absent in the red line which represents the reference TGA profile of the same polymeric network. Comparison of the 1st derivative spectra suggests that rate of metaldehyde degradation peaks at 89°C, which is slightly lower than the degradation temperature (commences at 110°C) demonstrated by the TGA of pure metaldehyde. This suggests that the metaldehyde molecules are more prone to degradation when adsorbed onto the polymeric surface compared to it solid form. Due to the high thermal stability of HCPs, for which decomposition commences at temperatures higher than 300°C, their metaldehyde-adsorbing properties likely remain unaffected after thermal regeneration. As all HCP adsorbents were regularly dried in a vacuum oven at 100 °C prior to batch equilibrium, kinetic, isotherm and RSSCT experiments, it is reasonable to suggest that thermal regeneration of HCPs from metaldehyde would not likely be associated with performance loss due to thermal aging of the sorbents. However, HCP adsorbent performance decline following thermal regeneration was not further investigated.

3.2.6 Summary, aims and objectives

The highest performing adsorbent TPB-DCM/TMOF identified through batch equilibrium studies described in Chapter 3.1, was found to display excellent adsorptive capacity for metaldehyde across a wide concentration range. Analysis of isotherm data and modelling using the Langmuir and Freundlich models showed that the non-linearised Langmuir was the best descriptor of the adsorption process, with the values of q_{max}= 125.00 ± 6.03 mg g^{-1} and K_L = 0.52 ± 0.06 L mg^{-1} further supporting the prevalence of excellent adsorption characteristics. The adsorption process was found to occur rapidly at surface of TPB-DCM/TMOF following the PSO model with k_2= 0.15 ± 0.02 mg^{-1} g min^{-1}. In RSSCTs of the adsorbent TPB-DCE/DMM at lower metaldehyde concentration of C_0= 0.5 mg L^{-1}, flowrate= 0.35 ml min^{-1} & EBCT= 2.4 min, 2500 column volumes were purified before breakthrough, with the effluent concentration being lower than 0.025 µg L^{-1}. TGA was used as a novel method of examining thermal removal of metaldehyde from the pores of the polymer and showed that the degradation of metaldehyde at the pores of the polymer occurs at T=89°C, suggesting that the thermal regeneration

of the adsorbent is likely plausible. Based on these findings, it is suggested that the HCP adsorbents based on the TPB motif show excellent potential to be used as inexpensive adsorbents for the removal of the moderately polar metaldehyde from water. Further research is however required to assess their performance using real water samples containing high organic matter, ions and other contaminants, as well as the environmental impact of the TPB and TPB-HCPs synthetic routes in comparison to the currently used activated carbon sorbents. HCP adsorbent regeneration and reusability should also be investigated and compared to conventional industrial water remediation materials.

3.3 Inorganic pollutant removal: Pb (II)

As discussed in section 1.5.3, the presence of Pb^{2+} in drinking water is a well-known threat to the public health. Previous research efforts on the development of adsorbents for Pb^{2+} removal from water are mainly focused on carbonaceous materials such as modified CNTs, AC, GO and reduced GO.[44,95,102] The potential of HCPs in metal adsorption from aqueous media has also been previously recognised.[47,101] Due to the HCP adsorptive properties relying primarily on π-type interactions,[236] the introduction of hydrophilic groups to the polyphenylene structures is a known modification strategy, achieving enhanced sorption properties of polar heavy metal ions.[47,252,253] There are examples of modified HCPs in the literature which have demonstrated excellent adsorption properties for metals such as Cu^{2+}, Cs^{+}, Sr^{2+}, Ni^{2+}, Mn^{3+}, Zn^{2+}, Cr^{3+} & Pb^{2+}.[47,224,252,254] Similar to HCPs, PIMs are also intrinsically hydrophobic, and although they have been widely researched as gas adsorbents, there are only recent examples of modified PIMs, with potential applications in aqueous metal uptake. [47,154,155]

3.3.1 Broad scope batch equilibrium studies for Pb (II) adsorption

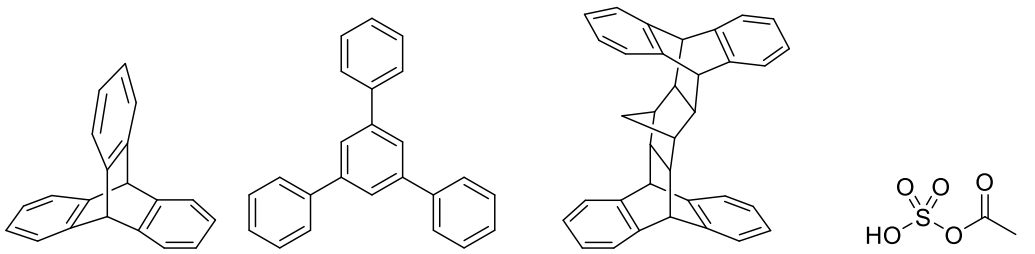

Figure 3.3.1a: Chemical structures of tryp, TPB and DMBP aromatic monomers, and the sulfonating agent ASA.

In the present work, HCPs derived from a variety of aromatic monomers including TPB, tryp and a di-benzomethanopentacene-type unit (DBMP) previously explored within our group (Figure 3.3.1a), were tested for their potential to adsorb Pb^{2+} ions. Batch equilibrium studies were conducted in ultrapure water, spiked with lead (II) nitrate at a concentration of 105 mg L^{-1} Pb^{2+} and a constant adsorbent dose

of 1 mg mL^{-1}. Modified adsorbents, sulfonated via an acetylsulfonic acid (ASA)-based post-polymerisation modification route were also tested. The analytical procedure is described in detail in section 5.4.1, the instrumental method for quantitative analysis using ICP-OES can be found in section 5.3.4, and detailed characterisation of adsorbents is present in section 3.3.3.

The HCP adsorbent derived from the $AlCl_3$-mediated polymerisation of the TPB aromatic unit and the solvent DCM has been extensively discussed in Chapter 3.1, as an inexpensive adsorbent with promising potential for the aqueous removal of metaldehyde. In Pb^{2+} uptake studies, TPB-DCM achieved a satisfactory maximum adsorptive capacity of 17.8 ± 3 mg g^{-1}. Interestingly, the adsorbent significantly outperformed the remainder of the non-modified HCPs, likely due to its high micropore volume, V_{micro} = 0.5 mL g^{-1}, and S_{BET} = 2100 m^2 g^{-1}. With reference to previous discussion on metaldehyde adsorption, the absence of sufficient meso and microporosity of TPB-DCM was found to decrease transport of the organic adsorbate to the micropores; however, this trend is not observed in Pb^{2+} adsorption. This demonstrates that the requirements for the porous structures of adsorbents are highly dependent upon the adsorbate of interest. In the case of Pb^{2+} adsorption the efficiency of internal mass transport phenomena relies on the hydrated and ionic diameters of Pb^{2+} ions, which are 0.802 nm & 0.224 nm, respectively.[255] As both are much smaller than the average diameter of TPB-DCM's micropores, as well as the WDV's diameter of metaldehyde, lower fractional meso & macroporosities are likely required. Adsorption of Pb^{2+} onto the aromatic surface relies on π-cation interactions,[256] and good agreement between pore and adsorbate sizes is likely important for non-modified HCPs. Finally, the moderate Pb^{2+} uptake TPB-DCM is also consistent with ICP-AES data, showing that a much higher Lewis acid-induced aluminium content was present in TPB-DCM, compared to other HCPs of lower microporosity.

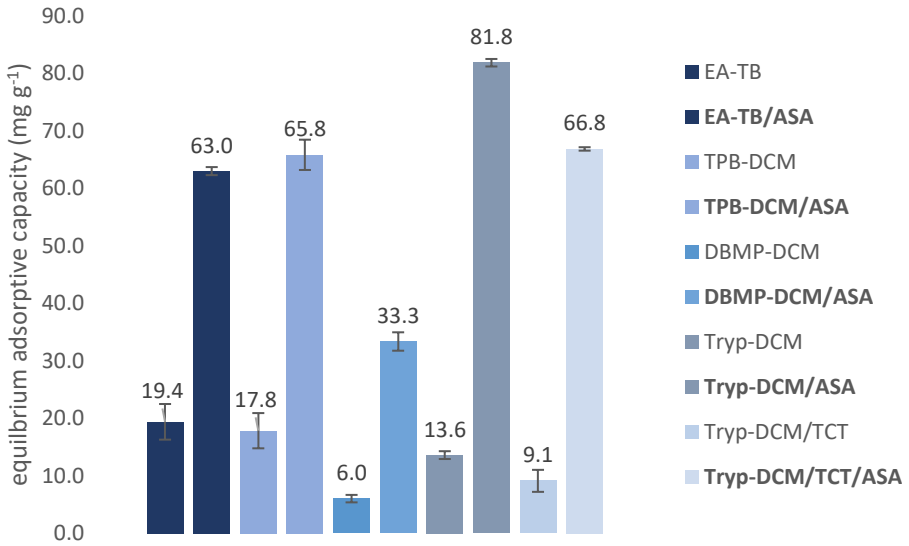

Figure 3.3.1b: Equilibrium adsorptive capacities of several adsorbents and their corresponding sulfonated analogues. Adsorbent dose 1 mg mL^{-1}, Initial Pb^{2+} concentration: 105 mg L^{-1}

As shown in Figure 3.3.1b, upon sulfonation of the DCE-swollen adsorbent using ASA, the adsorption capacity largely increases to 63 ± 2.6 mg g^{-1}, owing to favourable physisorption interactions of the sulphonic acid groups with Pb^{2+} ions. In addition, H^{+}/Pb^{2+} exchange is a possible chemisorption process that has been previously shown to facilitate metal uptake in sulfonic acid 'strong cation' resins, of similar morphology to the modified HCP.[101,224,257]

A similar pattern is observed for the adsorbent derived from the DBMP aromatic unit. The hydrophobic HCP derived from DBMP in DCM was found to only adsorb 6 ± 2 mg g^{-1} of Pb^{2+}, which increased fivefold to 33.3 ± 0.7 mg g^{-1} upon sulphonation. The lower performance of DBMP-DCM/ASA in comparison to TPB-DCM/ASA was attributed to its much lower ion exchange capacity (IEC), as calculated by Boehm titration methods (Figure 3.3.1c).[96] The lower level of functionalisation was due to a lower level of purity in the ASA sulfonating agent. It was decided however that DMBP-DCM/ASA represents a good example of an HCP of moderate IEC and is therefore included in further discussion.

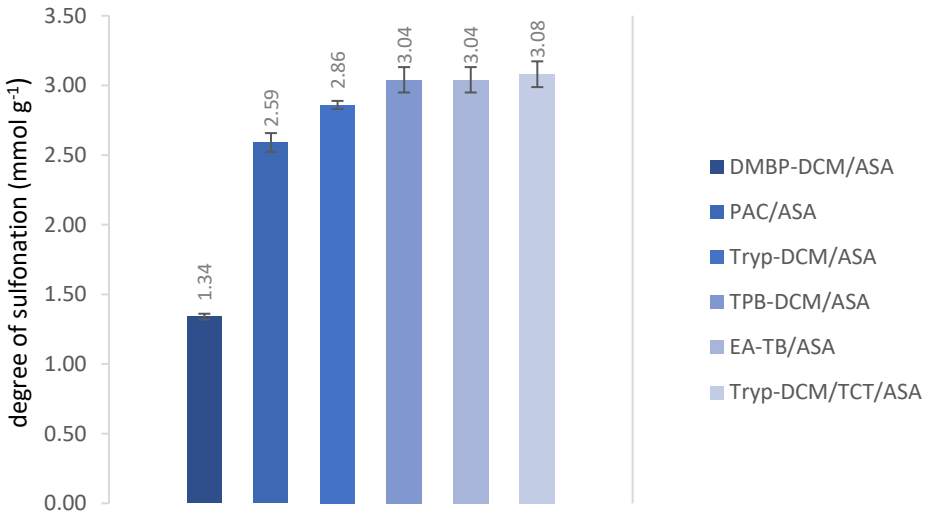

Figure 3.3.1c: IECs of the sulfonated adsorbents tested for Pb^{2+} uptake, determined via Boehm titration.

The HCP polymer derived from the Scholl coupling using tryp and DCM, demonstrated an equilibrium capacity of 13.6 ± 0.4 mg g^{-1}. Interestingly, its sulfonated analogue Tryp-DCM/ASA was identified as the highest performing adsorbent for the removal of Pb^{2+}, achieving a maximum equilibrium capacity of 81.8 ± 0.7 mg g^{-1}, and total removal efficiency of 78%.

The polymer tryp-DCM/TCT synthesized in the presence of TCT as a crosslinker was found to show a decreased Pb^{2+} affinity compared to tryp-DCM, despite the higher number of heteroatoms in its microstructure. However, the presence of TCT during the polymerisation process strongly affects the morphology of the resulting network, and in this is reflected on gas adsorption data which show significant reductions in V_{micro}, V_{total} & S_{BET}, upon incorporation of TCT to the network. It is therefore suggested that the polar triazine crosslinking units likely do not compensate for the loss of Pb^{2+}- binding affinity likely originating from those morphological changes. As expected, the sulfonated analogue tryp-DCM/TCT/ASA exhibits an enhanced adsorptive capacity of 66.8 ± 0.3 mg g^{-1}, however significantly lower than the sulphonated tryp-DCM/ASA.

Interestingly, a PAC sample (Darco RTM® type) was found to display significant affinity for lead (II) and achieved a saturation capacity of 48.3 ± 1.7 mg g^{-1}, indicating that polar groups are present onto the carbonaceous surface. In contrast to the polyphenylene network polymers, sulfonation of PAC was found to decrease the adsorption capacity to 37 ± 1.9 mg g^{-1}, and this was attributed to ASA resulting in alteration or destruction of pre-existing chemical functional groups.

3.3.2 Synthesis of highly sulfonated HCPs

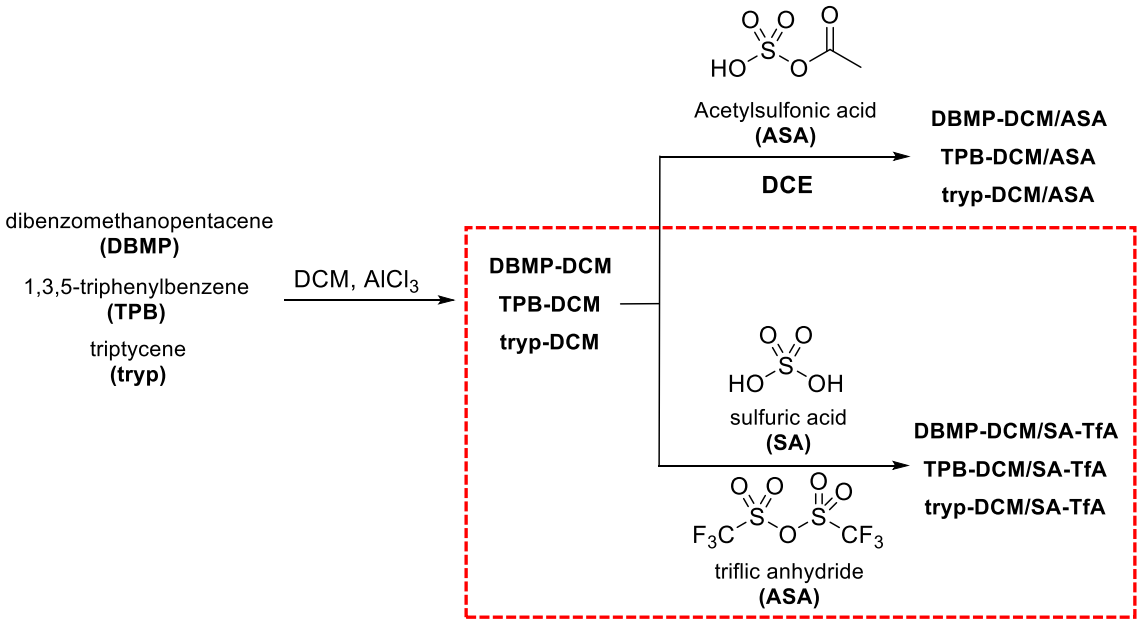

Figure 3.3.2a: Synthesis of DMBP-DCM, TPB-DCM & tryp-DCM and their modification using SA -TfA (highlighted in red dash) and ASA.

Due to the established relationship between the degree of sulphonation of HCPs relative to their adsorptive capacities for Pb^{2+} ions, an alternative sulphonation approach based on triflic anhydride (TfA) and sulphuric acid (SA) was designed to obtain highly polar, multi-functionalised adsorbents (Figure 3.3.2a). Despite the significant level of attention received by sulfonated HCPs and crosslinked polystyrene adsorbents,[47,224,252,258,259] sulfonation routes in the absence of swelling solvents have not been frequently explored, particularly in the case of HCPs.[260,261] Generally, solvent swelling is known to facilitate the expansion of the HCP aromatic framework,[225] and may directly increase the availability of internal surfaces for the electrophilic sulfonation reaction. However, previous research suggests that

the degree of swelling of an HCP, of invariable crosslinking density, is somewhat independent of the nature and polarity of the solvent.[262,263] Upon swelling, a HCP returns to its most thermodynamically stable state, established during network formation, and any steric strain present in the dry state is relieved.[264] The alleviation of strain during network expansion is therefore a more pronounced thermodynamic factor facilitating solvent swelling, and prevails over the solvent-surface interactions.

In addition, the introduction of multiple proximal sulfonic acid groups has been reported to increase the overall acidity,[253] which is a desirable property in strong cation exchange resins. Nonetheless, as the electrophilic sulfonation reaction progresses, it becomes increasingly harder to obtain higher levels of functionalisation and harsh conditions are needed to obtain persulfonated products. Considering these factors, a novel sulfonation approach was attempted, based on a high temperature modification using SA and TfA. Additionally, since solvent swelling typically relies on low boiling point solvents, such as DCE, the modification was performed without solvent swelling, to allow for high temperature synthesis at 250 °C. Importantly, at such high temperatures the viscosity of the reaction mixture significantly decreases,[265] which could allow for sulfonation of the inner surfaces. It was also suggested that sulphonation of the outer layer may occur first, increasing interactions with the highly polar sulphonating agent and consequently further increasing bulk diffusion efficiencies.

The sulfonating reagent mixture SA-TfA was prepared *in situ* from TfA and SA in ice-cold DCE. The solvent was used solely to dilute down the reagents and avoid excess production of heat and was removed prior to HCP sulfonation. The synthetic route was found to be similar to the synthesis of ASA, with the product mixture phase-separating from the DCE solvent upon formation. The general synthetic procedure is present in section 5.2.4.

There are only a few examples in the literature utilising SA-TfA for the sulfonation of porous materials such as MOFs.[266,267] One of the active sulfonation agents may be trifluoromethanesulphonyl (triflyl) sulphonic acid, a molecule analogous to the previously used ASA. However, due to the presence of

highly reactive reagents in the mixture, as well as the tremendously high activity of the triflyl functionality as a leaving group, it is likely that multiple species are present in dynamic equilibria, as in the case of previously reported superacids bearing multiple triflyl functionalities.[268]

Analysis of the mixture was attempted using NMR spectroscopy by comparing the spectra obtained for the TfA and SA precursors. In the SA-TfA ^{1}H-NMR, the peak at δ= 10.73 ppm corresponding to SA, appears as very broad overlapping resonances extending in the region δ= 10.67-11.54 ppm, confirming that several protic species based on sulphur are present. The ^{13}C-NMR spectra of the SA-TfA mixture and TfA both show quartet signals of 1:3:3:1 relative intensity originating from coupling to ^{19}F, in similar chemical shifts of 118.6 & 118.4 ppm, respectively. Importantly, the carbon-fluorine coupling constants for the SA-TfA mixture (J_{C-F} = 317.8 Hz) was found to be slightly lower than for TfA (J_{C-F} = 322.4 Hz). The ^{19}F-NMR spectrum of TfA shows a broad peak at δ= -72.3 ppm, which is slightly shifted to δ= -77.4 in SA-TfA. This shift may be originating by the consumption of TfA to form active sulfonating species in the SA-TfA mixture, but it is also likely that the shift is caused by solution interactions of fluorine atoms with the highly polar sulfuric acid, therefore resulting in a small chemical shift change. Due to the high toxicity and moisture sensitivity as well as highly corrosive nature of the sulfonation reaction mixture, further characterisation was not attempted.

During the sulphonation process, powdered samples of HCPs were added to the acid mixture without swelling in a chlorinated solvent and were left to stir at room temperature for 15 mins. Upon addition of the polymers into SA-TfA, an immediate colour change from light brown to black was observed indicative of rapid sulfonation taking place at the surface of the particles. The black suspensions were intensely heated to 250 ^{o}C for 1 hr and were left to cool before they were poured into water.

Figure 3.3.2b: DBMP-DCM (left) and DBMP-DCM/SA-TfA suspended in water.

HCP polymeric adsorbents based on the aromatic monomers DBMP, tryp and TPB were modified according to the described synthetic route. The modified adsorbents DBMP-DCM/SA-TfA, TPB-DCM/SA-TfA, tryp-DCM/SA-TfA were observed to interact very well with polar solvents. Upon addition of a powdered sample of DMBP-DCM/ SA-TfA to water, a homogeneous suspension quickly formed whereas addition of the parent adsorbent did not form a homogenous suspension (Figure 3.3.2b). This enhanced hydrophilicity was considered desirable, as it may enhance network swelling in water, therefore increasing adsorbate intraparticle diffusion efficiencies, adsorption kinetics and the overall adsorption capacity.[225]

3.3.3 Characterisation of sulfonated adsorbents

3.3.3.1 IECs of ASA- and SA-TfA- modified HCPs

The sulfonation content for all modified adsorbents was determined using a Boehm back-titration procedure. The IEC values are displayed in Table 3.3.3.1a, along with the number of sulphonic acid functionalities per ideal repeating unit & per aromatic ring.

Table 3.3.3.1a: IECs, acid content per ideal repeating unit (RU), and per aromatic ring, calculated for adsorbents tryp-DCM, TPB-DCM & DBMP-DCM modified by ASA and SA-TfA.

	Modification using ASA at 84 °C Swelling solvent DCE			Modification using SA-TfA at 250 °C No swelling solvent		
	IEC (mmol g^{-1})	per RU	Per ring	IEC (mmol g^{-1})	per RU	per ring
tryp-DCM	2.86 ± 0.01	0.98	0.32	4.15 ± 0.01	1.66	0.55
TPB-DCM	3.04 ± 0.02	1.27	0.32	6.5 ± 0.13	3.77	0.94
DBMP-DCM	1.34 ± 0.02	0.7	0.18	-	-	-

As expected, the high temperature SA-TfA reaction produced highly sulphonated adsorbents, with IECs largely increased over the softer ASA method. The IECs for tryp-DCM/ASA & TPB-DCM/ASA are moderate and correspond to the sulfonation of 32% of the aromatic rings, assuming ideal structures were preserved. Much higher IECs are observed for the high temperature SA-TfA-modified materials derived in the absence of a swelling solvent. Notably, the IECs were observed to increase to different extents, with a much higher change obtained for the TPB-based network for which a 94% ring sulfonation was obtained. Other than the synthetic conditions and the choice of sulfonating agent, the degree of functionalisation likely depends on several factors including swelling efficiency in the SA-TfA

mixture & pore size distribution, and it is therefore not clear why a lower sulfonation efficiency was obtained for tryp-DCM/SA-TfA.

For the adsorbent DBMP-DCM/ASA, a very low sulfonation content was achieved due to the presence of residual DCE in the ASA product which resulted in much lower acid concentration during synthesis. For the highly sulfonated adsorbent DBMP-DCM/SA-TfA, the IEC could not be determined via Boehm titration. Following its synthesis, the powder was refluxed several times in different solvents for purification, and filtration from the solvent medium was performed unproblematically on a sintered glass funnel. However, upon reaction of the acidic groups at the surface of the adsorbent with the standard $NaOH_{(aq)}$ solution, filtration of the particles could not be successfully performed. Several methods were attempted including filtration through a 0.22 µm pore diameter syringe filter, filtration through a Celite® plug and centrifugation but were all proven to be ineffective. It is thought that the deprotonation of the surface acidic groups increases the surface charge of the particles causing interparticle electrostatic repulsive interactions to increase, therefore disallowing any aggregation of the particles in solution. Notably, the suspension was left to stand for several days, and no sedimentation was observed, demonstrating an exceptionally high stability. This stability is underlined by the diameter of the adsorbent particles which likely approaches the nanometre region, coupled with the high degree of surface charge which results in intraparticle repulsion and significant particle-solvent interactions with the polar aqueous medium.[269] Despite the unsuccessful IEC quantification of DBMP-DCM/SA-TfA, the above observations are strongly indicative of a very high acid content. Additionally, it is likely that the population of sulfonic acid residues is not uniformly distributed across the particle cross-section, with higher acid contents at the particle surface and lower in the less accessible inner surfaces.

3.3.3.2 SS ^{13}C-NMR

Analysis of carbon-13 NMR spectra for all adsorbents derived from Tryp, DBMP & TPB, compared to their corresponding ASA & SA-TfA analogues, confirms successful sulfonation of the aromatic networks, along with substantial changes in network morphologies. Importantly, similar trends were observed for all three TPB, DBMP & tryp derived networks. Apart from aromatic group sulfonation, both modification routes achieved alterations of the alkyl crosslinking units, and this was reflected by the disappearance of peaks in the alkyl & chloroalkyl region, 10 - 80 ppm, which was additionally accompanied by the appearance of new resonances at approximate shifts of 196, 183 & 168 ppm. The alteration of linking units was observed to a lesser extent in the lower temperature ASA modification, whereas at harsh sulfonation conditions during sulfonation with SA-TfA, almost complete disappearance of alkyl groups is observed. The strongly oxidising high temperature conditions of sulfonation,[263] are likely responsible for the conversion of alkyl and chloroalkyl units to carboxylic acids (δ= 168 - 170 ppm),[270] di-aryl ketones (δ = 196 ppm),[270] with the peak at δ = 182-186 ppm likely associated with either of the two, with a sulfonic acid group present at the *ortho* position of an adjacent ring, as shown in Figure 3.3.3.2b. The oxidation of haloalkyl aromatics,[271] and alkyl aromatics, have been extensively explored in the presence of oxidizing reagents or atmospheric O_2.[272] Importantly, these reactions have been known to occur in the presence of acetic anhydride together with an oxidant,[273] and it is therefore reasonable that the harsh conditions used in the SA-TfA modification resulted in complete oxidation of alkyl linking units. All modified adsorbents obtained using SA-TfA display a single broad resonance in the region 45-55 ppm. For the adsorbents based on DBMP and tryp monomers, there is a significant contribution of this peak from the tertiary alkyl carbons within the aromatic units, with the remainder likely being due to modified alkoxide-based analogues.

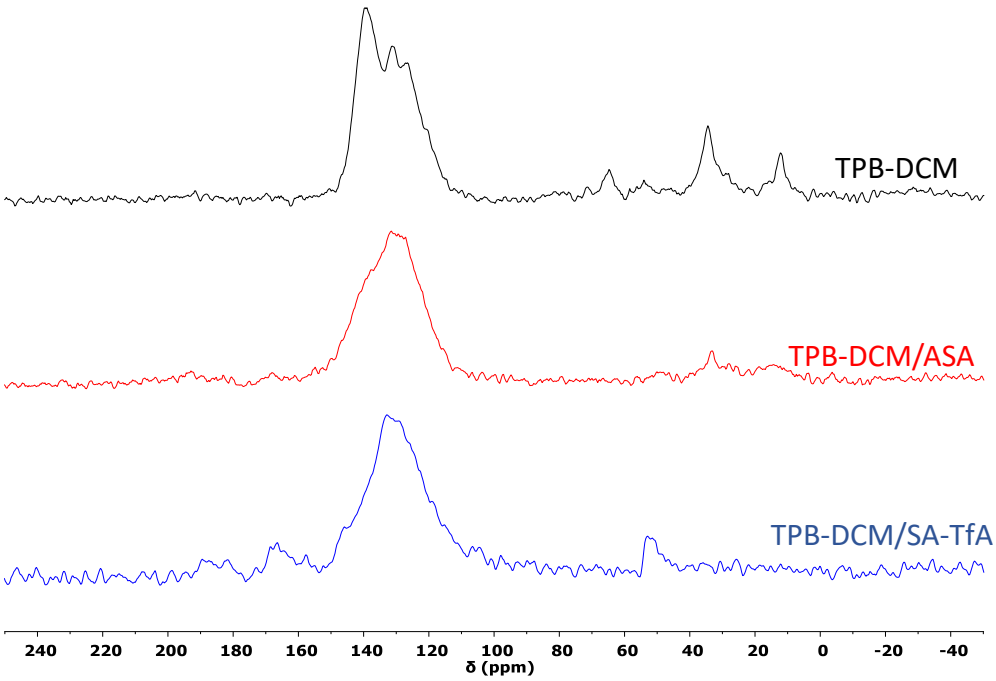

Figure 3.3.3.2a: MAS ^{13}C NMR spectra of TPB-DCM and the sulfonated analogues TPB-DCM/ASA & TPB-DCM/SA-TfA.

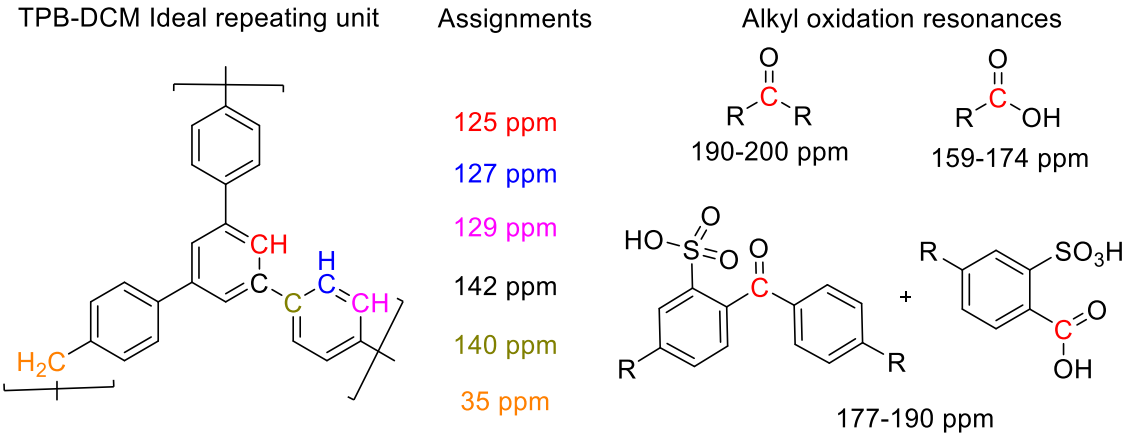

Figure 3.3.3.2b: Expected ^{13}C NMR chemical shifts of TPB-DCM, assuming ideal structure formation(left), Chemical shifts of oxidised alkyl and chloroalkyl moieties in TPB-DCM/ASA & TPB-DCM/SA-TfA (right).

The spectrum of unmodified TPB-DCM displays all expected carbon resonances in the aromatic region, with peaks at 125 ppm, 127 ppm & 129 ppm corresponding to secondary aromatic carbons and peaks at 140 & 142 ppm corresponding to tertiary aromatic carbons (Figure 3.3.3.2b).[225] Noteworthily, the high intensity of the peak at 142 ppm indicates that a high contribution of linking units is additionally originating from aryl-aryl Scholl couplings.[212] Upon sulfonation of TPB-DCM, broadening in the distribution of aromatic resonances is observed (Figure 3.3.3.2a), suggesting an increase in the

amorphous nature of the network and underlying the introduction of several other functional groups, in addition to sulfonic acids. Generally, upon sulfonation, the relative intensities of the tertiary carbons reduce in size and the resonances broaden and move to higher chemical shifts, indicating quaternary carbon formation. As expected, this effect is more pronounced in the harsh conditions of the SA-TfA route and is therefore consistent with the previously discussed IECs. There are new aromatic resonances introduced by sulfonation are observed at approximately 146, 148, 151 & 154 ppm, which are likely associated with highly de-shielded aromatic carbons, *ipso* to protonated and deprotonated sulfonic acid groups.[274]

As observed in Figure 3.3.3.2a, the alkyl region of the parent polymer and the modified analogues also displays significant differences. Upon sulphonation with ASA, the sharp peak present for TPB-DCM at δ= 35 ppm, corresponding to methylene crosslinks, originating from the DCM solvent,[275] decreases in intensity and a small peak indicative of ketone formation is observed. Importantly, peaks corresponding to linking or nonlinking alkyl peaks at 12 & 35 ppm undergo small reductions in intensity, while the peaks 64 & 71 ppm completely disappear. As the latter are associated with aryl alkyl unit bearing residual chlorine substituents, they exhibit reduced stability towards oxidation and therefore do not survive even under the ''softer'' low temperature sulfonation using ASA. In fact, industrial routes for toluene oxidation to the corresponding aldehyde and carboxylic acid, generally rely on a chlorination step prior to oxidation.[276]

The harsh synthetic conditions of TPB-DCM/SA-TfA formation result in a single broad resonance in the region 45-55 ppm, which could be due to a variety of chemical groups. As the oxidation of alkyl groups results in the formation of more reactive aldehydes, carboxylic acids and ketones,[276] further reactions occur during modification. Even though the broad and overlapping resonances of the NMR spectra do not allow for unambiguous identification of specific groups, possible outcomes are shown in Figure 3.3.3.2c.

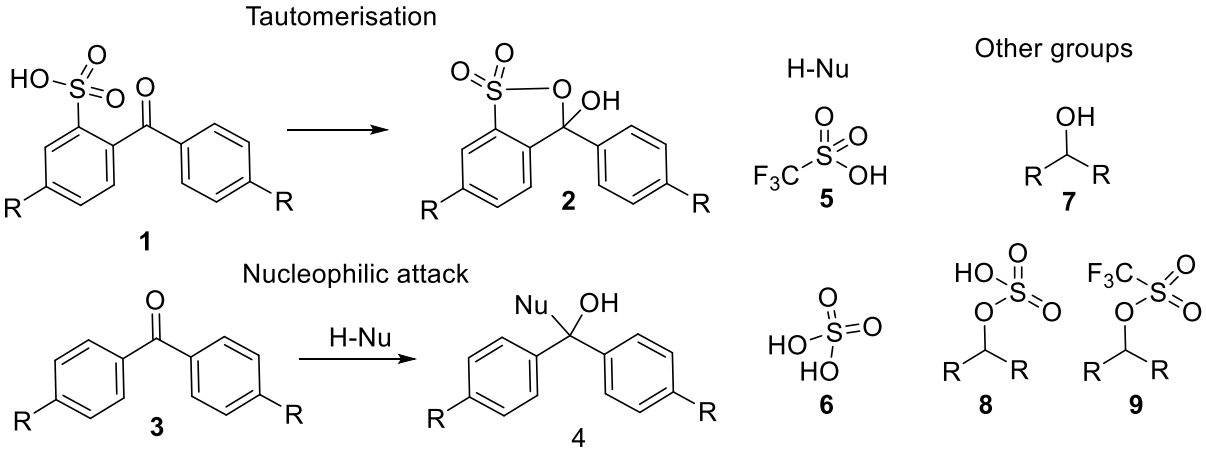

Figure 3.3.3.2c: Possible side reactions occurring during the high temperature modification using SA-TfA.

The formation of **1**, Figure 3.3.3.2c, is likely initiated via sulfonation at the ortho position relative to an alkyl link, which exerts electronic effects favouring electrophilic aromatic substitution at the ortho position.[277] Subsequent oxidation of the alkyl linker results in the formation of the ketone product **1**. The tautomerisation reaction to form **2** has been previously reported to occur at high temperatures (< 200°C),[278] while conversion back to **1** is not observed at room temperature due to the high stability of the cyclic tautomer. This type of tautomerisation may have beneficial effects in the case of sulfonated microporous adsorbents, as it results in increased rigidity of the network structure. However, this type of system remains profoundly unexplored and requires further investigation. Interestingly, the Scholl dehydrogenating coupling reaction has been previously shown to occur in the presence of a strong Bronsted acid and an oxidant,[279] however in this case there exists no evidence for its occurrence. Additionally, the di-aryl ketone **3** can also undergo further modifications, owing to nucleophilic attack by reagents such as **5** & **6** to form the corresponding analogues of **5**. Finally, incomplete oxidation of haloalkyl or alkyl linkages may form **7**, which can undergo further reactions to form products **8** & **9**.

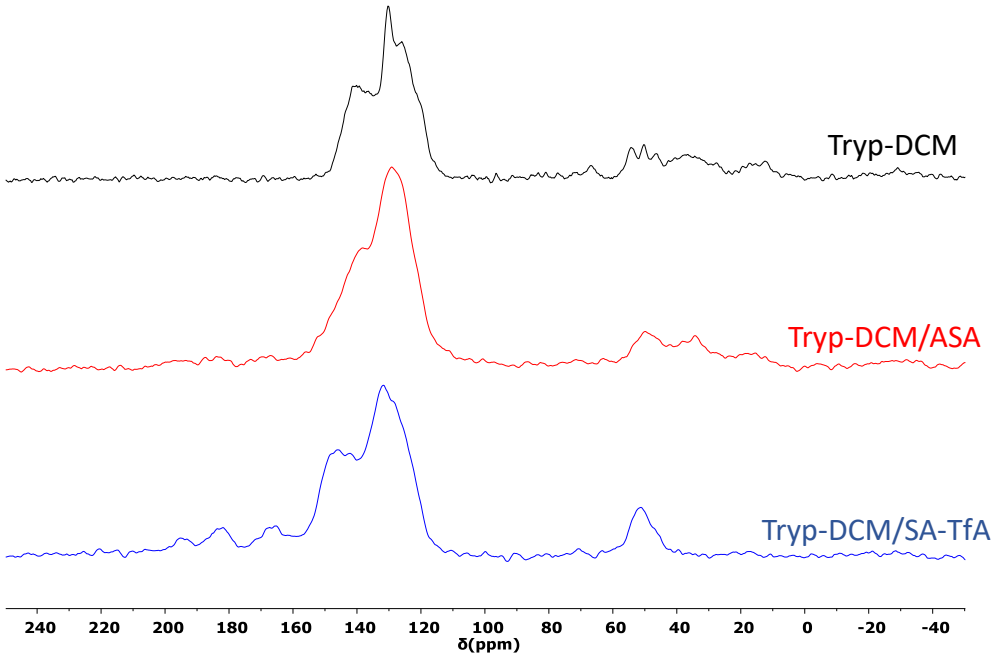

Figure 3.3.3.2d: MAS ^{13}C NMR spectra of tryp-DCM and the sulfonated analogues tryp-DCM/ASA & tryp-DCM/SA-TfA.

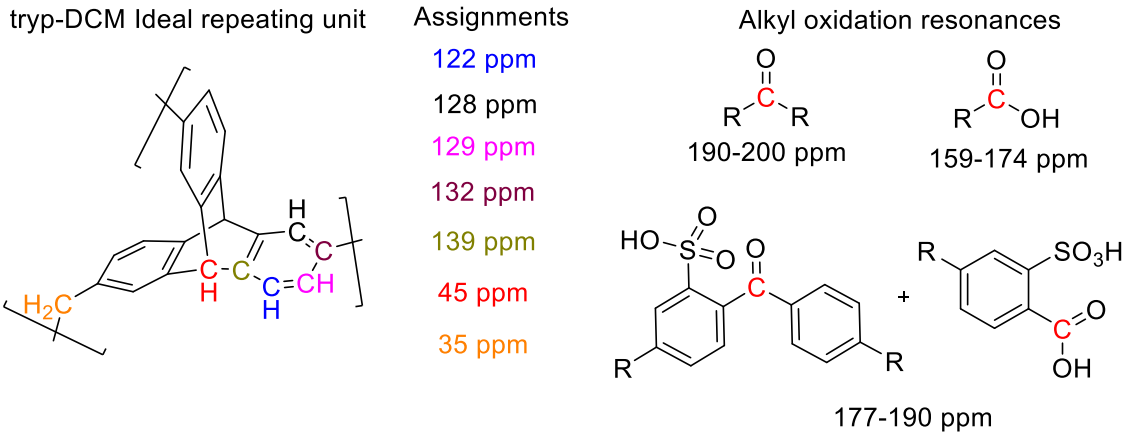

Figure 3.3.3.2e: Expected ^{13}C NMR chemical shifts of tryp-DCM, assuming ideal structure formation(left), Chemical shifts of oxidised alkyl and chloroalkyl moieties in tryp-DCM/ASA & tryp-DCM/SA-TfA (right).

The expected aromatic resonances for tryp-DCM (Figure 3.3.3.2e), appear as a broad signal at 134-145 ppm, corresponding to the six quaternary carbons of the tryp monomer, along with the secondary aromatic carbon region at 115-133 ppm. The quaternary carbons holding the linking units appear as a shoulder peak at 132 ppm. The methylene linking units give rise to a broad resonance at 35 ppm, and a significant number of alkylated products are present at similar shifts, as described previously for TPB-DCM. Soft sulfonation using ASA results in broadening of the aromatic signals with the resonances

extending towards higher chemical shifts, and harder sulfonation using SA-TfA results in further shifts giving rise to previously observed shoulder peaks at 146, 149, 151, and 154 ppm (Figure 3.3.3.2.d). All resonances explained as previously for TPB-DCM, however in this case the oxidised alkyl linking units overlap with the tertiary carbons of the tryp unit.

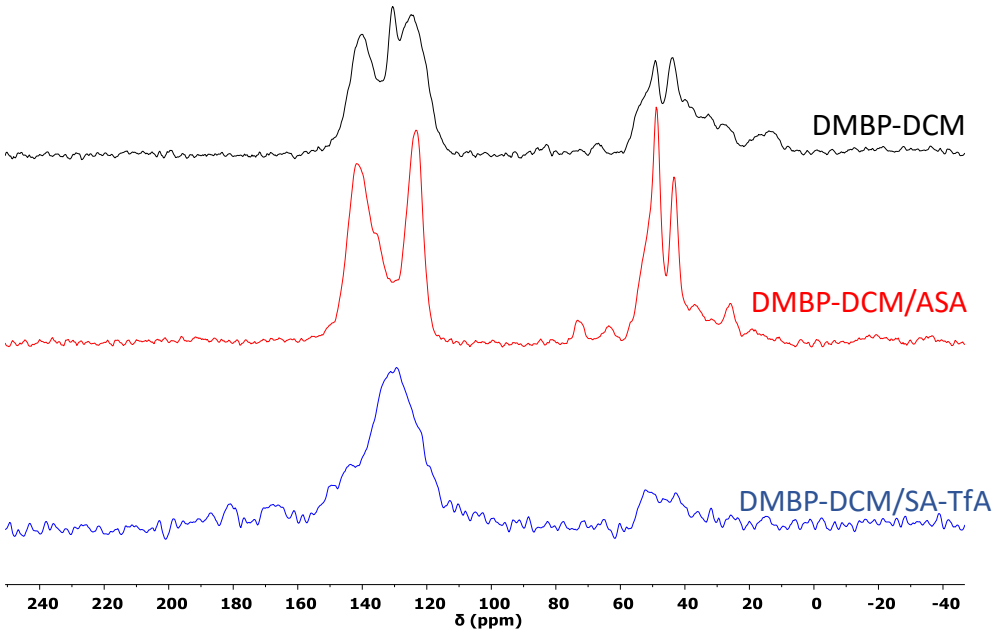

Figure 3.3.2.3f: MAS ^{13}C NMR spectra of DBMP-DCM and the sulfonated analogues DBMP-DCM/ASA & DBMP-DCM/SA-TfA.

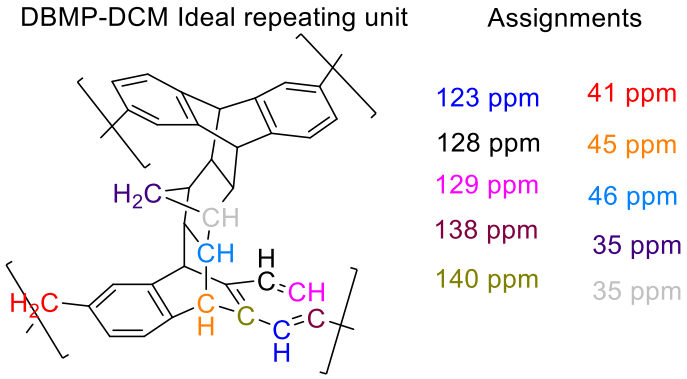

Figure 3.3.2.3g: Expected ^{13}C NMR chemical shifts of DBMP -DCM, assuming ideal structure formation.

As observed in Figure 3.3.2.3f, the aromatic region of DBMP-DCM, corresponding to tertiary aromatic carbons, appears as two broad resonances at 115-128 ppm & 128-134, while the quaternary carbons of the DBMP aromatic unit, in addition to aromatic carbons attached to linking units are observed at

135-147 ppm. Due to a low sulfonation content the adsorbent DBMP-DCM/ASA does not display significant changes. In contrast, DBMP-DCM/SA-TfA alkyl linking unit oxidation is prevalent, and integration of the alkyl peak with respect to the aromatic region shows that the aromatic: alkyl ratio is much lower than expected, which suggests that oxidation has likely occurred at the internal DBMP tertiary alkyl units.

3.3.3.3 Gas adsorption isotherms

As previously reported,[47,224] the BET surface area, micropore & total pore volumes of HCPs decrease rapidly as the degree of sulfonation increases. Noteworthily, in the case of highly polar adsorbents, direct correlations between gas adsorption data and aqueous solution uptake behaviour cannot be established, as the degree of polymer swelling is difficult to predict.[280] A similar behaviour was observed for all modified adsorbents, based on the DBMP-DCM and tryp-DCM. This behaviour is a result of the strong interactions of adjacent sulfonic acid groups, which form clusters to minimise their free energy,[281] therefore resulting in pore collapsing in the dry state. The linking and nonlinking alkyl unit conversion to various polar functionalities, as shown by ^{13}C-NMR, is likely further contributing to this effect. The reductions in pore size could additionally be due to the introduction of additional crosslinks, mainly sulfone bridges,[225] which are known to form in the network structure during the sulfonation procedure. These additional crosslinks have been shown to significantly reduce gas uptake properties as well as the solvent swelling ability of modified carbonaceous materials.[274] Finally, the introduction of bulky -SO_3H groups at the surface and the pores of the polymer may result in pore-filling effects, additionally contributing to decreased BET surface areas.[282]

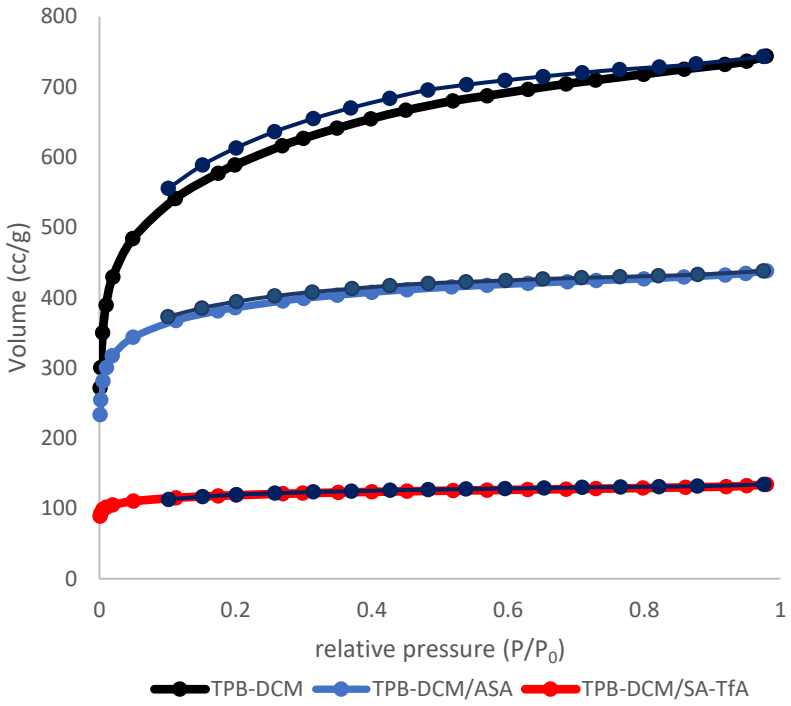

Figure 3.3.3.3a: N_2 adsorption isotherms of TPB-DCM and the sulfonated analogues TPB-DCM/ASA & TPB-DCM/SA-TfA, measured at 77 K.

As demonstrated by Figure 3.3.3.3a, the adsorbent TPB-DCM displays an exceptionally high BET surface area of 2081 $m^2 g^{-1}$ prior to any post-polymerisation modification, which decreases significantly to 1364 $m^2 g^{-1}$ for the ASA-treated sorbent with sulphonation content 3.03 mmol g^{-1}, with a further decrease to 420 $m^2 g^{-1}$ obtained for the SA-TfA-treated adsorbent with sulfonation content of 6.5 mmol g^{-1}. The total pore volume for the materials, obtained from the N_2 isotherms, also follows the same trend, rapidly decreasing from 1.15 $cm^3 g^{-1}$ for TPB-DCM, to 0.68 & 0.21 $cm^3 g^{-1}$ for TPB-DCM/ASA & TPB-DCM/SA-TfA, respectively.

Upon comparison of the N_2 adsorption/desorption isotherms, it becomes apparent that the materials produced after sulfonation have undergone significant morphological changes. The parent adsorbent TPB-DCM adsorbs strongly at low P/P_0 and the adsorption quickly reaches saturation, with this behaviour being indicative of its highly microporous structure. The ASA-modified adsorbent is observed to approach saturation capacity at a lower partial pressure than TPB-DCM, suggesting an overall

reduction in pore size. The same phenomenon is observed for the highly sulfonated TPB-DCM/SA-TfA, which reaches saturation capacity for the N_2 probe gas at a notably low partial pressure and quickly plateaus off, suggesting that multilayer adsorption component does not occur to a significant extent. These observations are consistent with the rapid decrease in micropore volumes arising from higher degrees of functionalisation.

The N_2 desorption behaviour of the material is also significantly altered upon post-polymerisation modifications. A well-defined hysteresis is observed for the parent polymer TPB-DCM, with TPB-DCM/ASA demonstrating a weaker desorption profile and a complete absence of hysteresis demonstrated by the highly sulfonated TPB-DCM/SA-TfA (Figure 3.3.3.3a). This behaviour is either explained by the higher degree of microporosity sulfonated adsorbents which reduces the diffusion kinetics of desorption, or alternatively, due to the presence of polar functionalities which may enhance interactions between N_2 molecules and the surface.

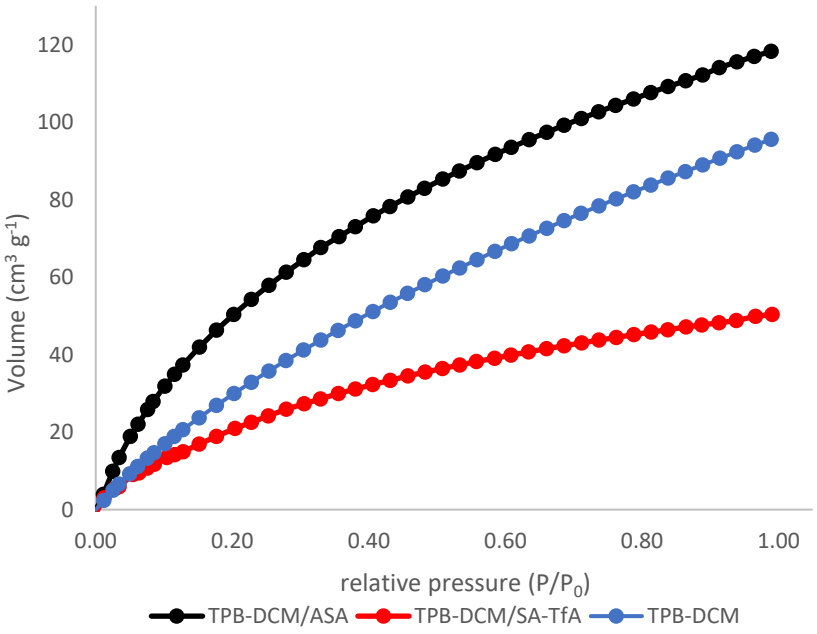

Figure 3.3.3.3b: CO_2 adsorption isotherms of TPB-DCM and the sulfonated analogues TPB-DCM/ASA & TPB-DCM/SA-TfA, measured at 273 K.

The CO_2 adsorption isotherms (Figure 3.3.3.3b), obtained for TPB-DCM and the sulfonated analogues were also found to follow a different trend than in the case of N_2 .The polymer TPB-DCM was synthesised according to a modified literature procedure, and has been previously recognised as an exceptional material for use in carbon capture applications.[126] As a consequence, excellent CO_2 adsorption was observed for TPB-DCM, with a total capacity of 95.53 ml g^{-1}, which corresponds to 4.27 mmol g^{-1}. Interestingly, the modified adsorbent TPB-DCM/ASA significantly surpassed TPB-DCM in terms of CO_2 affinity, demonstrating remarkable adsorption characteristics at both low and high partial pressure, with the maximum CO_2 uptake calculated as 5.28 mmol g^{-1}. This type of enhancement in CO_2 uptake, induced by the introduction of -SO_3H moieties has been explored in previous literature. [283,284] Current findings support that preferential CO_2 adsorption over N_2 can be enhanced via a variety of post- and pre- polymerisation synthetic routes to introduce polar functionalities to the aromatic networks, increasing the interactions of the surface with CO_2 and offering selective adsorption in the CO_2/N_2 gas pair. Despite the limited research on the field, the general understanding is that multiple factors affect a materials CO_2 uptake, and those including pore size distribution, surface area as well as the nature of functionalities and degree of functionalisation.[283] Due to a lower BET surface area, lower pore size and/or higher level of functionalisation, the polymer TPB-DCM/SA-TfA demonstrated a much lower CO_2 uptake than the adsorbents TPB-DCM and TPB-DCM/ASA. Conclusively, there seems to exist a balance between functional group content and the associated BET surface area reduction, however a clear relationship has yet to be identified. [284]

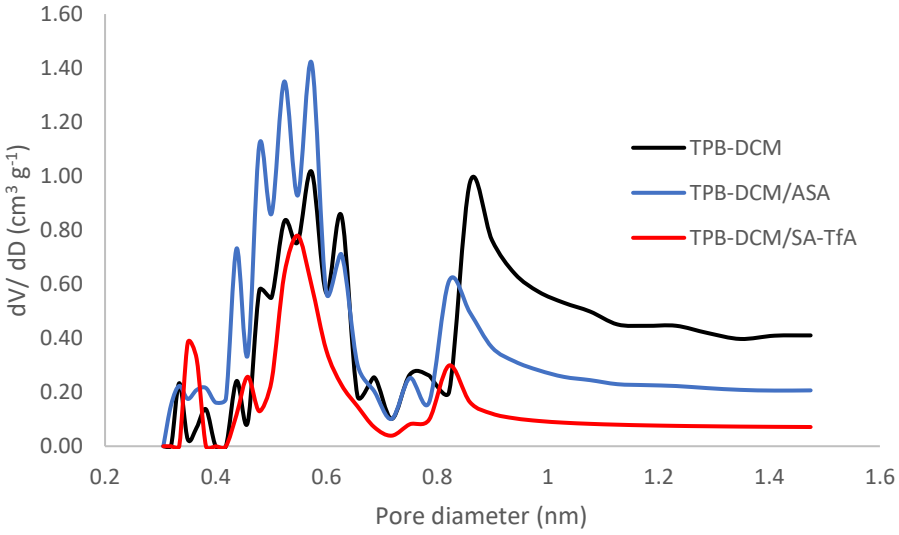

Figure 3.3.3.3c: NL-DFT pore size distributions of TPB-DCM and the sulfonated analogues TPB-DCM/ASA & TPB-DCM/SA-TfA, obtained from CO_2 adsorption isotherms.

The pore size distribution profiles calculated using the NL-DFT method (Figure 3.3.3.3c), also show a decrease in microporosity upon introduction of sulfonic acid groups. The plot of dV/dD against pore width obtained for the polymer TPB-DCM shows a narrow profile with an abundance of micropores of width less than 2 nm. Upon modification using ASA, an overall reduction in pore size is observed, with a higher degree of functionalization resulting in further pore size reduction, as observed for TPB-DCM/SA-TfA.

As previously discussed, the morphological properties of HCPs significantly vary in gaseous and aqueous media, and their adsorption behaviour in aqueous solutions cannot be unambiguously predicted using gas isotherms. Notably, reduction in pore size could likely negatively influence the kinetics of the adsorption process, due to the absence of mesopores which are known to play a major role in intraparticle diffusion rate. [80,159] Due to those kinetic limitations, macroporous sulfonated resins are often preferred for metal adsorption applications.[285]

Table 3.3.3.3a: Gas uptake properties of TPB, DBMP & tryp HCPs, in comparison to their sulfonated analogues modified by ASA & SA/TfA.[a] BET surface area derived from N_2 adsorption at 77 K, [b] Micropore volume obtained from N_2 adsorption at P/P.= 0.01, 77 K, [c] Total pore volume obtained from N_2 adsorption at P/P.= 0.98, 77 K, [d] Total uptake of CO_2 estimated at P = 1 bar and T = 273K. [e] Ion exchange capacity determined via Boehm titration.

Polymer Abbreviation	SA_{BET} [a] ($m^2\ g^{-1}$)	V_{micro} [b] ($cm^3\ g^{-1}$)	V_{total} [c] ($cm^3\ g^{-1}$)	CO_2 uptake[d] ($mmol\ g^{-1}$)	IEC[e] ($mmol\ g^{-1}$)
TPB-DCM	2082 ± 124	0.5	1.2	4.27	0
TPB-DCM/ASA	1364 ± 60	0.36	0.68	4.93	3.04 ± 0.02
TPB-DCM/SA-TfA	420 ± 30	0.14	0.21	2.10	6.5 ± 0.13
DBMP-DCM	1398 ± 51	0.33	0.85	2.42	0
DBMP-DCM/ASA	1319 ± 32	0.28	0.76	2.8	1.34 ± 0.02
DBMP-DCM/SA-TfA	245 ± 11	0.05	0.15	2.01	-
Tryp-DCM	1492 ± 48	0.33	0.85	3.95	0
Tryp-DCM/ASA	515 ± 28	0.16	0.26	2.75	2.86 ± 0.01
Tryp-DCM/SA-TfA	710 ± 31	0.26	0.36	4.24	4.15 ± 0.01

As observed in Table 3.3.3.3a, adsorbent modification of DBMP-DCM using the soft ASA method resulted in a very low IEC, with no significant changes in S_{BET} V_{total} & V_{micro}, and slightly enhanced CO_2 saturation capacity. Conversely, subjecting the material to the harsh conditions of the SA-TfA method resulted in severely compromised pore volume, S_{BET} and slightly decreased CO_2 affinity.

In the case of the sulfonated analogues of tryp-DCM, an anomaly was observed in the obtained gas uptake properties, with tryp-DCM/ASA demonstrating higher porosity than the tryp-DCM/SA-TfA, despite a much lower IEC. Importantly the measurements were repeated twice, and good consistency was achieved between runs. With reference to acquired IR & TGA data, discussed in the following sections 3.3.3.4 & 3.3.3.5, respectively, it is speculated that the low gas uptake properties observed for

tryp-DCM/ASA are likely related to its astounding affinity for water molecules. Specifically, the amount of chemisorbed water in tryp-DCM/ASA is much higher compared to the rest of sulfonated adsorbents, and this is demonstrated by its thermal degradation profile showing a significant % mass loss in the region 140 – 215 °C. Similarly, its IR spectrum demonstrates intense vibrations associated with hydronium ions, in addition to a high population of deprotonated $-SO_3^-$ functionalities. It is therefore likely that a reduction in N_2 adsorption is due to the occupation of the polar surface with chemisorbed water molecules, which at 77 K form a solid layer covering the surface, therefore exerting pore filling effects and reducing the S_{BET} and calculated pore volumes.[286] As tryp-DCM/ASA retains water up to very high temperatures, it is likely that complete moisture removal during drying and degassing procedures is not possible, as a very high enthalpy of hydration results in rapid moisture uptake,[287] which could be occurring as soon as the sample is removed from the degasser apparatus. As shown in table 3.3.3.3a, the adsorbent of higher sulfonation Tryp-DCM/SA-TfA, demonstrated superior N_2 and CO_2 uptake properties despite its higher IEC. Although counterintuitive, the reduction of water uptake with increased sulfonation content has been previously observed,[253] and even though the exact hydration mechanisms remain unexplored, it is likely that interactions between neighbouring polar groups in Tryp-DCM/SA-TfA reduce the overall requirement for hydration. As the affinity for water has been previously reported to be pore size dependent,[288] it is also likely that tryp-DCM/ASA possesses a micropore structure which allows very efficient accommodation of water molecules. Importantly, the adsorbent Tryp-DCM/SA-TfA is observed to demonstrate a good balance between S_{BET} V_{total} & V_{micro} and IEC, which is underlined by excellent CO_2 uptake properties of 4.24 mmol g^{-1}.

3.3.3.4 ATR-IR

Analysis of the IR-spectra of the parent and sulfonated HCPs is consistent with previous literature findings for sulphonated hypercrosslinked polystyrene-divinylbenzene adsorbents.[47] As the acidity of sulfonated adsorbents is likely similar to that of *p*-toluenesulfonic acid which has a pK_a of -2.8,[289] and significantly lower than for the H_3O^+ ion, pKa = -1.7,[290] a large proportion of the functionalities exist as anionic sulfonate moeities, electrostatically attracted to hydronium cations. This is readily confirmed by the IR profiles sulfonated adsorbents, and particularly in the case of the SA-TfA high temperature modification. The asymmetric bending vibration of hydronium ions, H_3O^+, appears as a small peak at 1744 cm^{-1},[291] and neutral water vibrations, often overlapping with other peaks in the region 1676 -1678 cm^{-1},[292] are observed in all modified adsorbents. Noteworthily, exact appearance of water bands depends on the H-bonded network,[291] and formations of complex aggregates $[(H_2O)_nH^+]$ have been previously studied in persulfonated systems.[291,293,294] Such H-bonded clusters have been observed to display highly split OH stretch vibrational regions,[295] similar to the ones observed experimentally. High levels of hydration are further demonstrated by the broad band at 1599 cm^{-1}, to which the H-bonded network is likely contributing.[296]

The presence of broad peaks is explained by the amorphous nature of HCPs which results in incorporation of $-SO_3H$ groups in several different chemical environments, with their interactions with adsorbed water also likely contributing to peak broadening.

With reference to the ^{13}C NMR spectra of sulfonated analogues, the presence of carbonyl-based compounds is confirmed by the region 1550-1730 cm^{-1}, in which strong overlapping vibrations are observed. The sharp peak at approximately 1676 cm^{-1} likely being indicative of di-aryl ketone linking units,[297] and carboxylic acids and other possible analogues (discussed in section 3.3.3.2) also contributing to 1600- 1722 cm^{-1}.[298]

Of particular importance are the peak maxima at approximately 1165 cm^{-1}, observed for all sulfonated adsorbents, which may be indicative of sulfone bridges. In fact, diphenyl sulfones have been previously reported to display a S=O symmetric stretching at around 1164 cm^{-1}, and the introduction of sulfone bridges during polymer sulfonation is a known phenomenon. [225] However, identification of sulfone bridges using IR spectroscopy is difficult to perform unambiguously, as a symmetric SO_2 vibration of the acid is also commonly reported at 1172 cm^{-1}.[225]

Conclusively, interactions between a plethora of various proximal polar groups, complex material hydration and further crosslinking introduced during sulfonation, are all likely responsible for the high complexity observed in the solid-state IR spectra of sulfonated HCPs.

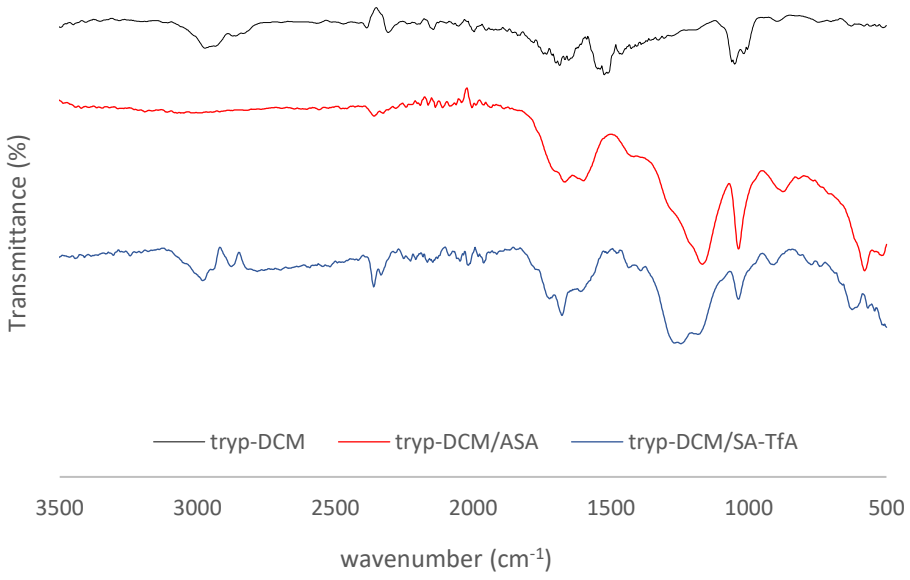

Figure 3.3.3.4a: IR spectra of tryp-DCM and the sulfonated analogues tryp-DCM/ASA & tryp-DCM/SA-TfA.

The IR absorption profile for tryp-DCM (Figure 3.3.3.4a) shows weak vibrations at the region 2981-2918 cm^{-1} & 1056-1002 cm^{-1}, the former associated with symmetrical and asymmetrical -CH_2- vibrational modes originating from the alkyl crosslinking moieties,[47] and the latter from di-substituted aromatic ring vibrations.[299] The adsorbents tryp-DCM/ASA & tryp-DCM/SA-TfA show almost identical IR profiles indicative of the presence of sulphonic acid groups, and potentially other sulphur-based functionalities.

Specifically, 567-619 cm^{-1} corresponds to C-S vibrations,[300] 870-906 cm^{-1} corresponds to a stretching vibration of S-O bond, 1035 cm^{-1} is assigned to the symmetric vibration of the $-SO_3^-$ functionality, [301] and 2200-2600 cm^{-1}, correspond to non-hydrated $-SO_3H$ vibrations.[300,302, 303] A main difference observed in the case of tryp-DCM modified analogues is related to the band SO_3^- band at 1035 cm^{-1}, which is of much higher relative intensity in the ASA-analogue compared to the high temperature SA-TfA method. This is indicative of a higher presence of deprotonated sulfonate moieties, and indirectly indicative of higher levels of adsorbed water. In addition, the band at 1175 cm^{-1} is observed at a notably strong relative intensity in tryp-DCM/ASA,[304] which could be indicative of a significant presence of sulfone bridges,[274,300,305] and in fact many authors have reported a higher formation of sulfone crosslinks upon sulfonation with ASA or chlorosulfonic acid, compared to sulfuric acid.[225,274] Interestingly, the band at 580 cm^{-1} corresponding to C-S vibrations,[300] is also shifted with respect to other sulfonated materials and is of higher intensity, which is also partially suggestive of sulfone formation. It is therefore likely that the increased water affinity of the tryp-DCM/ASA may be related to an increased crosslinking density, originating from the introduction of those bridges.[288] Importantly, a higher presence of sulfone bridges could also account for the S_{BET}, V_{micro} & V_{total}, which for tryp-DCM/ASA were much lower than anticipated.[225]

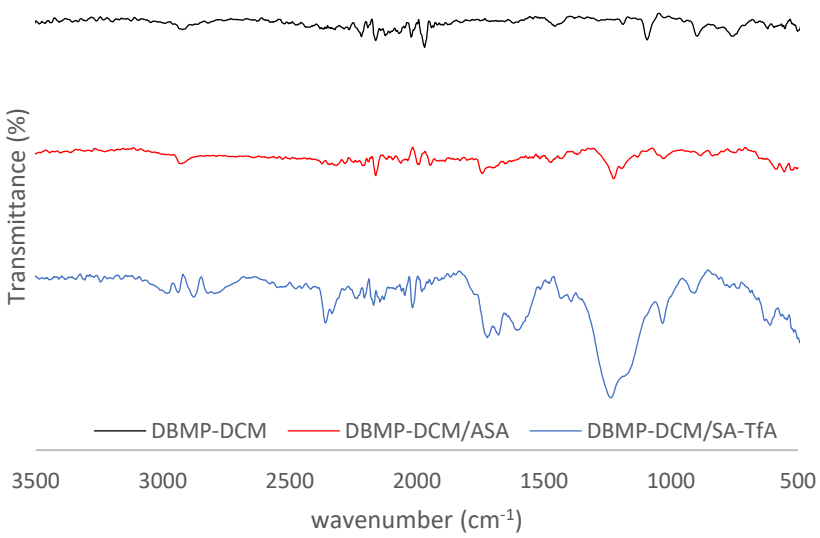

Figure 3.3.3.4b: IR spectra of TPB-DCM and the sulfonated analogues TPB -DCM/ASA & TPB-DCM/SA-TfA.

As observed in Figure 3.3.3.4b, the DBMP-DCM adsorbent shows very weak IR activity, with weak peaks present at 2941 cm^{-1} and 1089 cm^{-1} corresponding to aromatic C-H stretching and bending vibrations, respectively.[299] The IR spectrum of the ASA-modified derivative adsorbent, with low sulfonation content of 1.34 mmol g^{-1} displays similarly weak IR absorbance with broad peaks present at 1222 cm^{-1} & 1022 cm^{-1}, attributed to the presence of sulfonic acids. The high temperature modification using SA-TfA produced a polymer with significantly higher IR activity, explained due to the introduction of a much higher population of polar oscillating groups to the polymeric surface. Peaks corresponding to carbonyl-based oxidised alkyl substituents present at 1590 cm^{-1} & 1714 cm^{-1}, are also of very high relative intensity with respect to the bread peak at 1225 cm^{-1}, which supports the previous hypothesis arising from ^{13}C NMR data, suggesting that oxidation may have taken place internally in the DBMP aromatic units. The same peaks as in the case of modified tryp-based adsorbents are present at slightly shifted wavenumbers, 605 cm^{-1}, 906 cm^{-1}, 1032 cm^{-1}, 1172 cm^{-1}, 1228 cm^{-1}, 1593 cm^{-1}, and are assigned as previously.

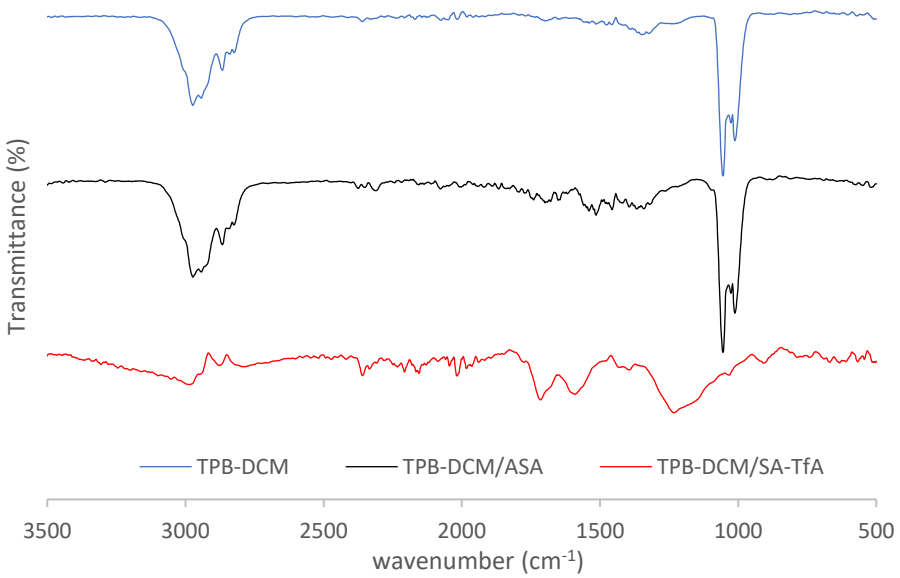

Figure 3.3.3.4c: IR spectra of TPB-DCM and the sulfonated analogues TPB -DCM/ASA & TPB-DCM/SA-TfA.

Prior to modification, TPB-DCM displays strong vibrations at 2972 & 2864 cm^{-1}, in addition to 1053 & 970 cm^{-1}, the former arising from CH vibrations of the aromatic backbone and the latter from aromatic vibrations of disubstituted rings. After treatment of a DCE-swollen sample with ASA at 65 °C, to produce the adsorbent TPB-DCM/ASA, these aromatic vibrations persist in the IR spectrum of the analogue (Figure 3.3.4c). Despite a high sulfonic acid content of 3.03 mmol g^{-1}, in addition to significantly enhanced adsorption of Pb^{2+} demonstrated in batch equilibrium experiments, peaks that can be attributed to sulfonic acid vibrations arise as very weak, compared to the background aromatic vibrations.

In contrast, the IR profile of the adsorbent TPB-DCM/SA-TfA shows that an abundance of $-SO_3H$ groups are present, with very weak aromatic vibrations based on the aromatic scaffold. This suggests that there is a high proportion of acidic groups at the surface of the particles, which supresses any weaker IR activity of the polyphenylene backbone. Since the adsorbent TPB-DCM/SA-TfA was synthesized without swelling in an organic solvent, there is likely a higher population of acidic sites present at the surface of the particles compared to the internal pores, while a more uniform distribution is likely prevalent for TPB-DCM/ASA. Previous research has shown that the separation of functionalised and non-functionalised domains is a common outcome arising from material sulfonation.[306]

3.3.3.5 Thermogravimetric analysis

Similar trends are observed in TGA data for all unmodified adsorbents based on TPB, tryp & DBMP aromatic networks, in comparison to their sulphonated analogues. In most cases, the unmodified polymers showed no significant mass loss under temperatures lower than 270 °C. This is consistent with the excellent thermal stability of HCPs, which did not decrease following sulfonation. For most sulfonated adsorbents, significant percentage mass reductions are observed in the temperature range of 80 - 150 °C, due to the high affinities of the polar surfaces for moisture. Notably, all adsorbents were dried at 120 °C under vacuum prior to TGA acquisition, which suggests that moisture re-adsorption

occurs very rapidly under ambient atmosphere. Interestingly, the water content of sulfonated macroporous resins has previously been shown to decrease with the level of sulfonation;[253] and this is observed upon TGA curve comparison of the ASA- and SA-TfA modified analogues of all TPB-DCM, DBMP-DCM & tryp-DCM. In all three cases, a higher sulfonation degree was associated with lower % water loss observed in the TGA, and with the transitions occurring at higher temperatures and broader temperature ranges compared to the ASA- modified sorbents. For highly sulfonated sorbents, these observations were attributed to lower material pore sizes, which result in inefficient inward and outward diffusion of water molecules into the networks. In addition, as the presence of multiple polar groups increases the binding strength of water to the surface, and mass loss transitions of SA-TfA modified analogues are observed at higher temperatures. It is also important to distinguish between physically bound water, and the disintegration of $-SO_3^- H_3O^+$ pairs, for which much higher temperatures are required to achieve dehydration.[281] Notably, similar degradation products such as SO_2, H_2O & CS_2 are expected for all sulfonated analogues, as identified in previous literature for sulfonic acid containing materials.[307]

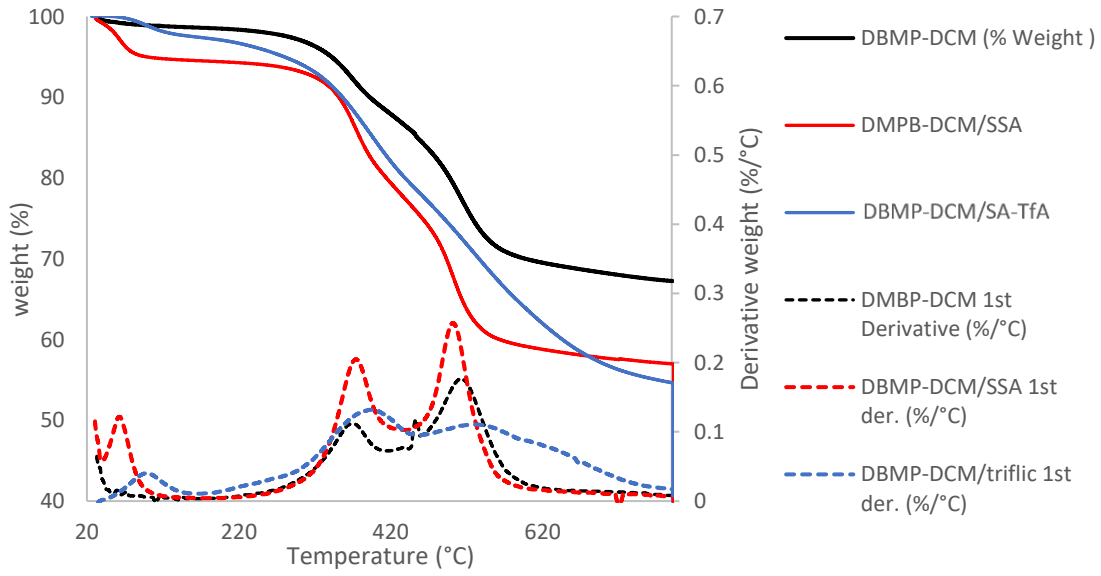

Figure 3.3.3.5a: TGA spectra (% weight) of DMBP-DCM and the sulfonated analogues DMBP-DCM/ASA & DMBP-DCM/SA-TfA (solid lines), 1st derivative spectra (%/ °C) (dotted lines).

The thermal degradation of sulfonic acid groups is associated with the mass loss in the temperature region 300-800 °C, with significant degradation of the polymer aromatic backbone is also occurring simultaneously within the range 300-600 °C. Specifically, the 1st derivative spectrum of DMBP-DCM (Figure 3.3.3.5a) shows two overlapping mass loss transitions at temperatures 360 & 520 °C, associated with the degradation of the aromatic backbone. The degradation mechanisms are dependent on the morphology of the HCP network, therefore slight variations in temperatures are observed for TPB-DCM & tryp-DCM.

In general, at the temperature range 300-600°C, the polymers with lower sulfonation contents are observed to display a more rapid degradation rates, while highly sulfonated polymers lose mass more steadily up to temperatures of 800 °C. This is in agreement with previous literature on sulfonated

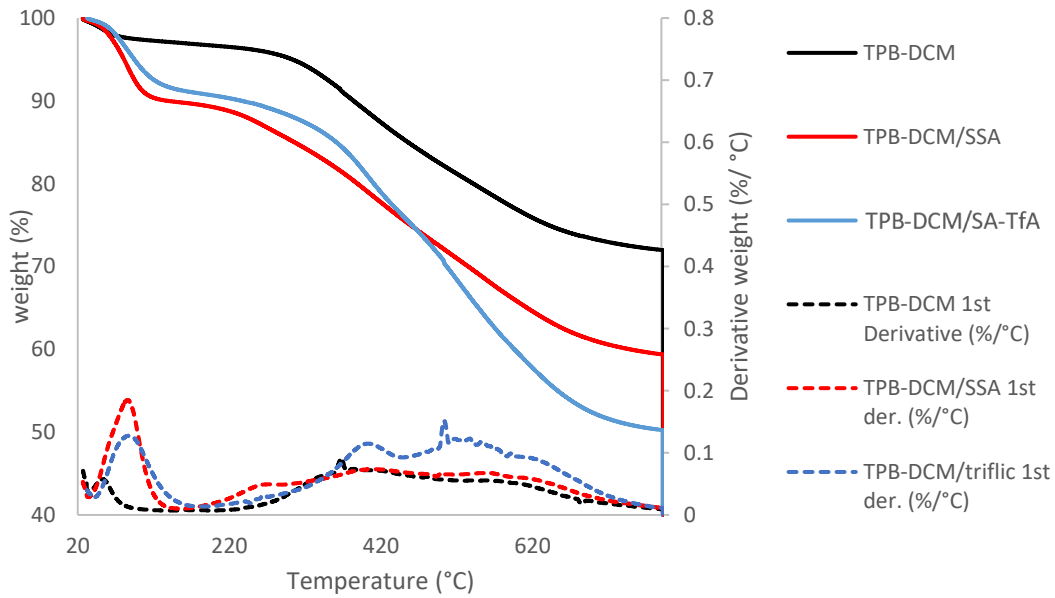

Figure 3.3.3.5b: TGA spectra (% weight) of TPB-DCM and the sulfonated analogues TPB-DCM/ASA & TPB-DCM/SA-TfA (solid lines), 1st derivative spectra (%/ °C) (dotted lines).

polystyrene resins, which suggests increased material thermal stability as a result of higher sulfonation degrees.[253] This is likely a consequence of decreased electron density on the aromatic network, which reduces overall reactivity. Importantly, the total % mass losses at a temperature 800 °C for all SA-TfA modified adsorbents were found to be much lower compared to ASA-HCPs, confirming that the higher temperature SA-TfA method resulted in much higher levels of functionalisation.

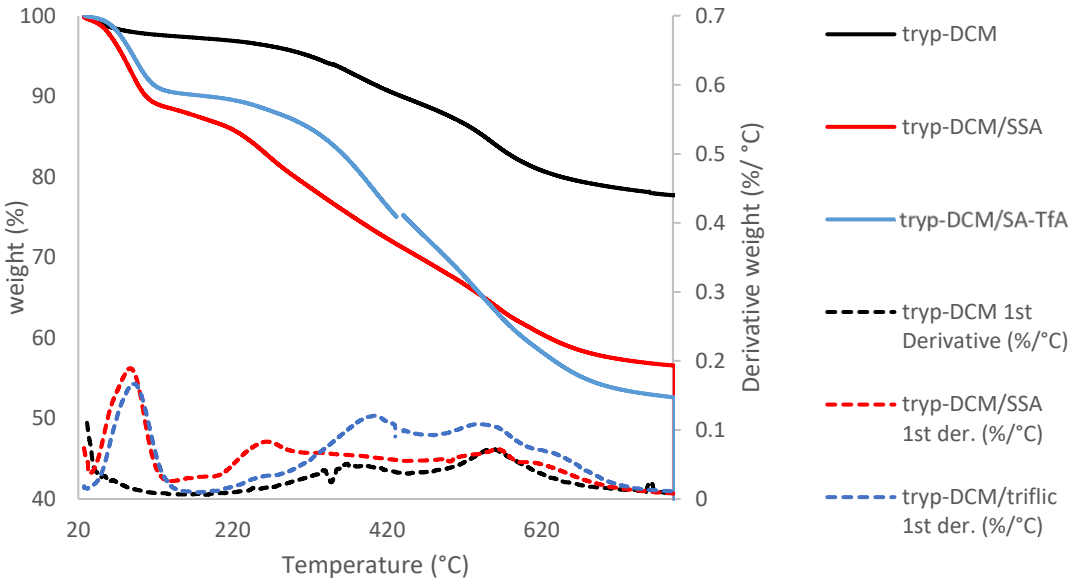

Figure 3.3.3.5c: TGA spectra (% weight) of tryp-DCM and the sulfonated analogues tryp-DCM/ASA & tryp-DCM/SA-TfA (solid lines), 1st derivative spectra (%/ °C) (dotted lines).

Similar trends as described for DBMP-based adsorbents are observed in the case of TPB and tryp polymers, shown in Figure 3.3.3.5b & Figure 3.3.3.5c, respectively. Due to the sulfonic acid degradation occurring simultaneously with polymer backbone degradation, any quantitative information of sulfonic acid content was not possible. In addition, high degrees of sulfonation are observed to significantly enhance the thermal stabilities of the modified adsorbents, with TPB-DCM/SA-TfA, tryp-DCM/SA-TfA & DBMP-DCM/SA-TfA, displaying almost identical % weight loss and 1st derivative spectra profiles, with slight variations in mass loss transition temperatures.

Importantly, in the case of the ASA modification thermal degradations are initiated at much lower temperatures of approximately 215 °C, with highest thermal degradation rates achieved at 272 °C. Even though it is very difficult to explain the thermal degradation properties of each, it is speculated that this reduction in thermal stability may be related to the higher levels of hydration observed for polymers of lower sulfonation. Specifically, previous research suggests a dependence of sulfonic functionality on whether it exists in the protonated or deprotonated form, with the latter most often associated with

lower thermal stability.[308] It is therefore likely that after elimination of physically bound water, for which rate of loss peaks at 80 – 90 °C, chemisorbed water may survive up to 215 °C or higher,[287] at which temperature region the degradation temperature of sulfonate is approached.[308] The presence of residual strongly bound water at such high temperatures is likely responsible for the reduced thermal stability observed, as it disallows re-protonation to form the more thermally stable neutral sulfonic acid. This effect is particularly prominent in the case of tryp-DCM/ASA, which experiences significant mass loss in the region 140 – 200 °C, before the sulfonate degradation commences at 215 °C. The higher level of ionised sulfonate moieties in tryp-DCM/ASA is also confirmed by the relative intensity of the IR band at 1030 cm^{-1}, corresponding to $-SO_3^-$ and previously recognised as the 'ionic marker',[287] which was much higher in comparison to the remainder of the adsorbents. Importantly, a very similar thermal degradation behaviour is discussed in section 3.3.4.1, concerning a Pb^{2+}-saturated sample of DBMP-DCM/SA-TfA.

Finally, the abundance of various functional groups incorporated in the polymeric structures following sulfonation, and particularly when harsh conditions are employed, are expected to affect the degradation properties of the networks. For instance, sulfone bridges have been reported to increase thermal stability,[253] by exerting electron withdrawing effects which disfavour the radical cleavage of the C-S bond.[307] The residues formed after conducting TGA up to 800 °C are likely composed mostly of graphitic type materials with high sulphur content.[309]

3.3.4 Further batch adsorption experiments

All sulfonated adsorbents were tested for Pb^{2+} adsorption at concentrations of 102.8 mg L^{-1} and 160 mg L^{-1} Pb^{2+}. Experimental conditions were kept constant as described previously with adsorbent dose of 1 mg mL^{-1} of solution and equilibration time of 46 hrs. ICP-AES quantitative analysis was performed against a calibration curve.

Table 3.3.4a: % removal and equilibrium capacities of DBMP-DCM/SA-TfA, TPB-DCM/SA-TfA & tryp-DCM/SA-TfA at initial Pb^{2+} concentrations of 102.8 mg L^{-1} & 160 mg L^{-1}, adsorbent dose 1 mg mL^{-1}.

	102.8 mg L^{-1} Pb^{2+}		160 mg L^{-1} Pb^{2+}	
Adsorbent	% removal	q_e (mg g^{-1})	% removal	q_e (mg g^{-1})
DBMP-DCM/ SA-TfA	98.9	101.2	88.8	142.1
TPB-DCM/ SA-TfA	96.6	98.8	84.7	135.5
tryp-DCM/ SA-TfA	98.8	101.1	84.8	135.6

As shown in Table 3.3.4a, at initial Pb^{2+} concentration of 102.8 mg L^{-1} of Pb^{2+}, a removal efficiency of approximately 99% was observed for the modified adsorbents based on the DBMP and tryp aromatic units with a slightly lower Pb^{2+} removal efficiency of 96.6% obtained for the adsorbent based on the TPB aromatic monomer. To further assess the adsorption properties of ASA-modified sorbents, the polymers were also equilibrated at a higher concentration of 160 mg L^{-1} Pb^{2+}. The polymers TPB-DCM/SA-TfA and tryp-DCM/SA-TfA were found to demonstrate excellent removal efficiencies of 84.7 & 84.8% respectively, whereas the adsorbent DBMP-DCM/SA-TfA achieved 88.8%. The experimental maximum equilibrium capacity obtained for DBMP-DCM/SA-TfA was calculated as 142.1 mg g^{-1}, significantly outperforming the ASA-treated sorbents derived at lower temperature, and demonstrating exceptional adsorption properties, with reference to previously explored Pb^{2+}-adsorbing materials.[43,94,95,257]

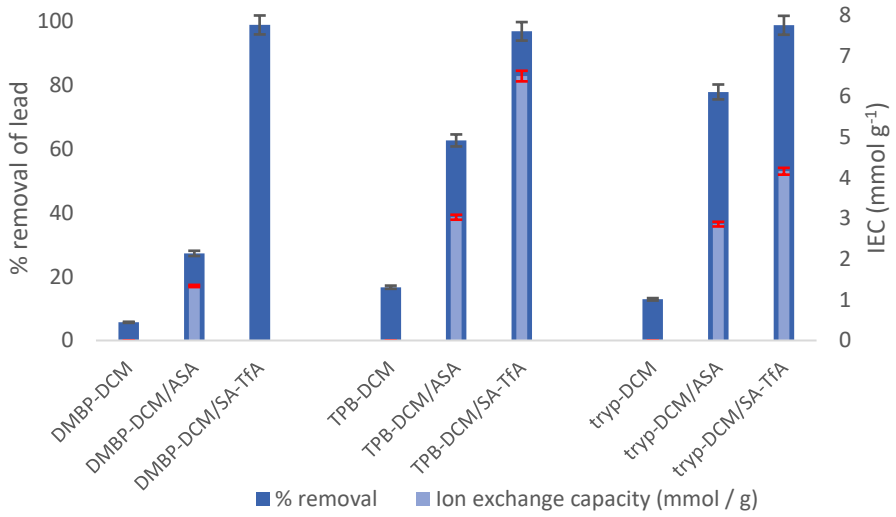

Figure 3.3.4a: % removal and ion exchange capacities of DBMP-DCM, TPB-DCM & tryp-DCM in comparison to ASA- and SA-TfA- modified analogues, at initial Pb^{2+} concentration of 102.8 mg L^{-1} & adsorbent dose 1 mg mL^{-1}. IECs are included.

Figure 3.3.4a summarises equilibrium data (C_0 = 102.8 mg L^{-1} Pb^{2+}), obtained for the sulfonated adsorbents, modified using the ASA and SA-TfA methods. In consonance with previous literature,[225] the degree of sulfonation is observed to be directly related to the affinity of a polymer for cationic lead ions. For all three adsorbents based on TPB, DBMP and tryp, the % removal of lead at concentration of 102.8 ppm is in the region 6 - 16% for the unmodified adsorbents, increases significantly upon modification with ASA, and increases further approaching 99% removal for all SA-TfA modified adsorbents. The similarly high affinity of all three modified networks for Pb^{2+}, suggests that the adsorption process may be independent of the nature and morphology of the parent HCP adsorbent. In other words, it may be that all HCP backbone networks act as aromatic scaffolds which hold the polar groups, and the metal uptake properties are more dependent on the distribution and number of functionalities, rather than the morphology of the parent network. In addition, the similar adsorption capacities obtained for all SA-TfA modified materials suggest that S_{BET}, V_{micro} & V_{macro} are not correlated to a material's performance in terms of metal ion uptake capacity. Importantly, the DBMP-DCM/SA-TfA was identified as the best performing adsorbent, despite its much lower porosity and S_{BET} in comparison to TPB-DCM/SA-TfA & tryp-DCM/SA-TfA, and this is possibly due to a higher level of functionalisation.

3.3.4.1 Studies on the Pb (II)-form of DBMP-DCM/SA-TfA

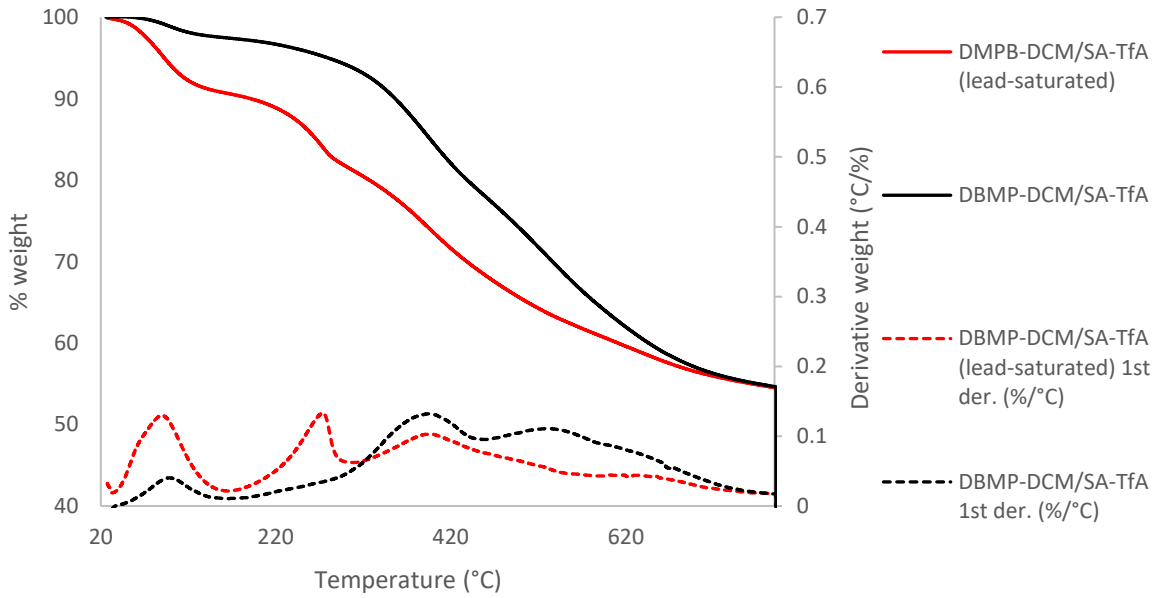

Figure 3.3.4.1a: TGA curves (%) & 1st derivative spectra (%/°C) of DBMP -DCM/SA-TfA, and Pb^{2+}-saturated DBMP -DCM/SA-TfA,, following batch equilibrium studies.

TGA was conducted to compare the degradation properties of the polymer DBMP-DCM/SA-TfA, with a Pb^{2+}- saturated sample obtained following batch equilibrium studies using 160 mg L^{-1} lead (II) nitrate solution (Figure 3.3.4.1a). Following batch equilibrium studies, the adsorbent was recovered by filtration and dried in a vacuum oven at 120 °C to remove excess water. TGA results suggest that the degradation of the adsorbent changes significantly upon Pb^{2+} binding. Firstly, the Pb^{2+} saturated sample holds 8% by mass more water than the original sample, possibly indicating that the Pb^{2+} ions contribute to the hygroscopicity of the adsorbent by increasing surface interactions with the water molecules. The remaining differences are explained in terms of the relative amounts of protonated and deprotonated sulfonic acid residues. In DBMP-DCM/SA-TfA, most of the acids should exist in the H^{+}-form, whereas upon H^{+}/Pb^{2+} ion exchange, the resin consists mainly of sulfonate groups strongly bound to Pb^{2+} ions. A new mass loss transition is identified at 277 °C, marginally overlapping with the main transitions found in the H^{+}-form DBMP-DCM/SA-TfA, at approximately 400 & 535 °C. At T > 320 °C, the rate of degradation

of Pb^{2+}- DBMP-DCM/SA-TfA slows down in comparison to the H^+-form, and a lower percentage mass loss is observed. These observations suggest that the presence of Pb^{2+} lowers the thermal stability of the sulfonated adsorbent and are in complete agreement with results from section 3.4.3.5, where a correlation between chemisorbed water and thermal degradation temperature was suggested. Interestingly, the new transition of Pb^{2+}- DBMP-DCM/SA-TfA at 277 °C, corresponds to approximately 8.8% total mass degradation and is quantitatively consistent with the equilibrium capacity of DBMP-DCM/SA-TfA, determined through batch equilibrium studies as 140.7 mg g^{-1}. As Pb^{2+} is a divalent cation, ion exchange with adjacent acid groups should theoretically result in Pb^{2+} complexation by two $-SO_3^-$ moieties, to form the ionic bridge shown in Figure 3.3.4.1b. The relative amount of sulfonyl moieties calculated based on experimentally determined Pb^{2+} uptake, corresponds to 8.7% of the total mass assuming liberation of SO_2 gas which is known to be the main mass loss mechanism associated with degradation.[307]

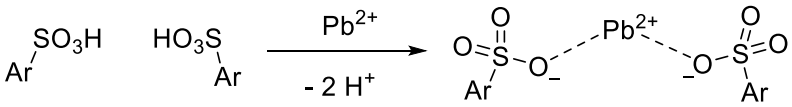

Figure 3.4.4.1b: H^+/ Pb^{2+} exchange resulting in the formation of ionic bridges between adjacent sulfonate groups.

Notably, the effect of cation on the thermal properties of sulfonated materials has been previously studied for sulfonated polystyrene,[307] with ion-exchange sulfonated membranes being a main research focus.[281,310] For the latter, there exist comparative studies on the effect of several counterions to the degradation of the sulfonate moiety,[310] in which the functionality degradation temperature has been suggested to depend on the Lewis acid strength and radius of the cation bound. Generally, multivalent highly Lewis acidic ions usually decrease the thermal stability of the sulfonate moiety, however there are exceptions to this trend, and in the case of Pb^{2+} there exists no relevant literature for comparison. Nevertheless, considering the ionic bridge formation as being dependent on dipole-dipole interactions,

as well as an elastic opposing force arising from the overall conformational restriction, it seems reasonable to suggest higher susceptibility to degradation at lower temperatures.

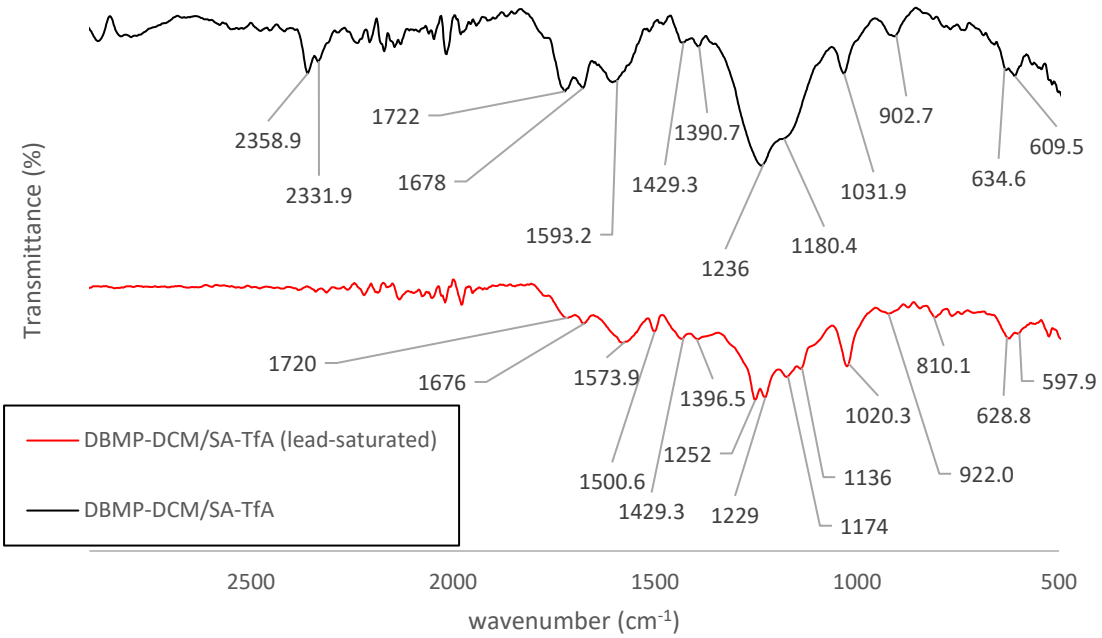

Figure 3.3.4.1c: IR spectra of DBMP-DCM/SA-TfA and its Pb^{2+}-saturated analogue.

As shown in Figure 3.3.4.1c, the IR spectra of the H^+ and Pb^{2+}-forms of the adsorbent DBMP-DCM/SA-TfA also display significant differences. These differences arise from cation influences on the oscillating groups, resulting in polarisation changes.[281] Spectra normalisation was not considered applicable, due to the absence of appropriate vibrational bands. Firstly, bands indicative of anhydrous free SO_3H, are present for the H^+-form in the region 2200-2600 cm^{-1},[303] but disappear upon Pb^{2+} uptake owing to acid deprotonation which facilitates adsorption by ion exchange. In general, much sharper and well-defined peaks were observed for the Pb^{2+}-saturated sample in the 590-1650 cm^{-1} region. Notably, the presence of water molecules within the material likely impacts the oscillating properties of the polar groups, in a similar fashion as reported for sulfonated hydrophilic membranes.[311] As seen previously in TGA studies, the Pb^{2+}-form carries approximately 7% more water than the H^+ form and it is therefore difficult to separate the relative contributions of Pb^{2+} cations and water molecules to the overall spectral changes observed.

The presence of new vibrational stretches may also be attributed to the removal of degeneracy of the sulfonate group, arising from asymmetric Pb^{2+} coordination.[312] In particular, the vibration at 1236 cm^{-1} is split into a doublet at 1252 cm^{-1} & 1229 cm^{-1}, upon Pb^{2+} binding. This band is associated with asymmetric SO_3^- vibrations,[311,312] with the vibrational wavenumber being dependent upon the cation, namely H^+ or Pb^{2+}. A similar splitting pattern is observed for the symmetric S=O vibration of the sulfonate moiety which changes from a shoulder peak at 1180 cm^{-1}, [225] to two well-resolved peaks at 1136 & 1174 cm^{-1}. Peaks corresponding to S=O symmetric vibrations are likely present at 1392 & 1433 cm^{-1}, and in the H^+-form spectrum and appear broader and slightly shifted in the Pb^{2+}-form, at 1395 & 1435 cm^{-1}, the shifts being in good agreement to their asymmetric counterparts.

Of particular importance is the peak at 1032 cm^{-1}, corresponding to symmetric SO_3^- vibrations,[225] which in the Pb^{2+}-form exhibits a significant shift to 1022 cm^{-1}, along with an increase in relative intensity with respect to other bands. The latter is consistent with the conversion of acidic moieties to their ionic forms and indicative of ion-exchange occurrence during Pb^{2+} uptake, but could also be due to a higher water content which allows more sulfonic acid moieties to remain deprotonated, with hydronium ions balancing the charges.[294] Additionally, the S-O stretch at 907 cm^{-1}, also appears broadened at 921 cm^{-1} and a new peak arises at 810 cm^{-1}, likely originating from S-O-Pb vibrations.[296] The peaks at 609 cm^{-1} & 631 cm^{-1} have been previously assigned to C-S,[300,313,314] and upon Pb^{2+} uptake shift to 600 cm^{-1} & 623 cm^{-1}, respectively, suggesting that the C-S bond strength reduces upon cation exchange. As aryl sulfonic acid degradation has been known to proceed via radical cleavage of the C-S bond,[307] this decrease is in agreement with previously explained TGA studies suggesting an overall decrease in thermal stability, induced by Pb^{2+} ions. The complexity of material hydration is further demonstrated by a broad band at 1599 cm^{-1}, also arising from the H-bonded network,[296] which observed to shift to 1580 cm^{-1} likely due to the disruption of the network by the Pb^{2+} ions.

The band associated with the asymmetric bending vibration of the hydronium ion, H_3O^+,[291] 1740 cm^{-1}, and neutral water vibration at 1676-1678 cm^{-1},[292] do not exhibit any shifts in the H^+ & Pb^{2+} cationic

forms. Despite a higher water content, the intensity of the H_3O^+ band does not increase after batch studies, as the bound Pb^{2+} contributes significantly to the balancing of surface charges.

3.3.5 Adsorption solution isotherm for DBMP-DCM/SA-TfA

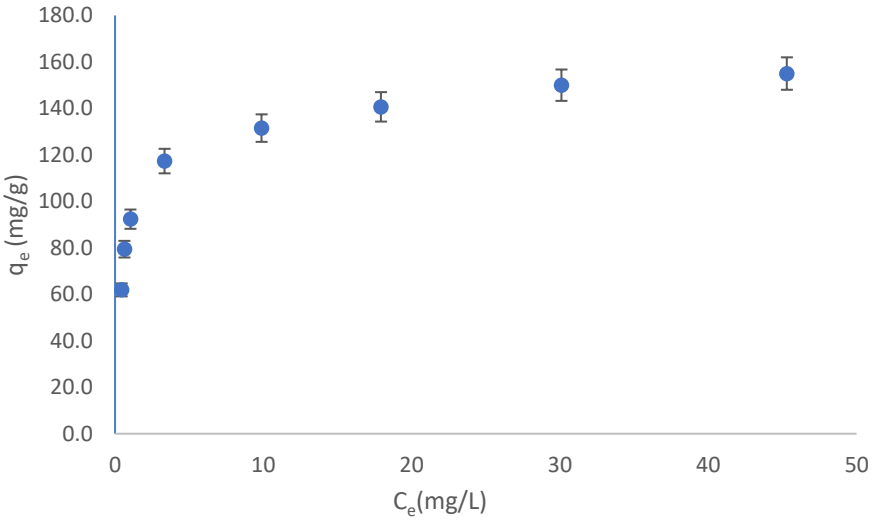

Figure 3.3.5a: Adsorption equilibrium capacity against equilibrium concentration for the adsorbent DBMP-DCM/SA-TfA.

A solution adsorption isotherm for lead (II) was obtained for the polymer DBMP-DCM by equilibrating in several concentrations, in the range 62 - 200.3 mg L^{-1}. The solutions were adjusted to pH = 7.4, if required. The adsorbent dose was kept constant at 1 mg ml^{-1} and the samples were equilibrated for 46 hrs at 293 K. As expected, at low concentrations an exceptional removal efficiency of Pb (II) is observed after equilibration, with approximately 99% efficiency observed in the concentration region 14.3 - 93.4 ppm. Small deviations are likely originating from experimental error; however, the deduced relative standard deviations are in the region 3-7%, indicating good reproducibility of the data. With reference to Figure 3.3.5a, the linearity of the curve for adsorptive capacity against concentration decreases slightly at concentrations 120.7 and 141.4 ppm with a much faster decrease observed in the concentration region 158.6 - 200.3 ppm.

3.3.5.1 Commonly used two-parameter models

Aiming to provide insights on the nature of the adsorption process, several isotherm models were tested to describe the process of aqueous lead ion uptake from DBMP-DCM/SA-TfA. The most used two-parameter Freundlich & Langmuir models displayed interesting fitting characteristics and are therefore discussed herein.

The Langmuir and Freundlich models were used to model the 8-point dataset. With reference to previous isotherm discussion on metaldehyde from section 2.3.3, both linear and nonlinear regression methods were employed. As in the case of metaldehyde adsorption onto TPB-DCM/TMOF, the parameters and shapes of the model isotherm were found to depend upon the regression method used. The plots of the calculated isotherms and the model parameters are shown in Figure 3.3.5.1a and Table 3.3.5.1a, respectively.

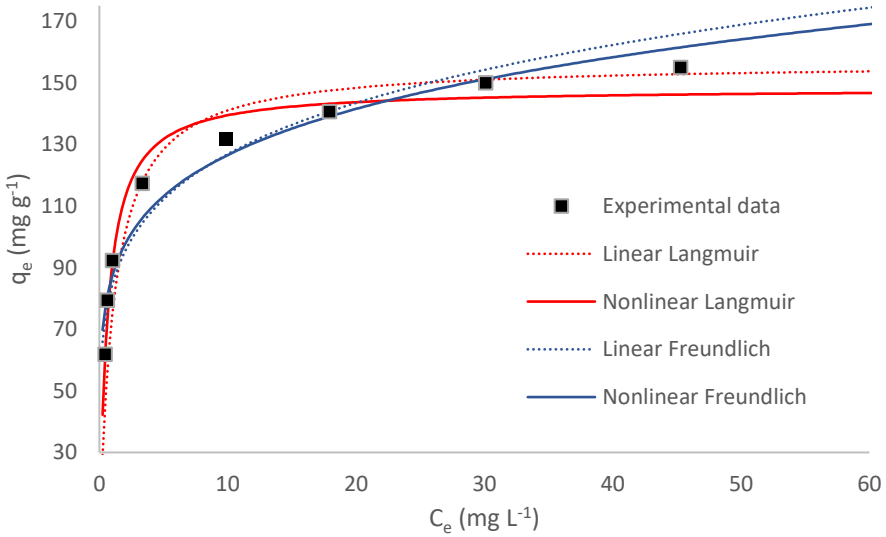

Figure 3.3.5.1a: Linear and nonlinear regression Langmuir and Freundlich curves, together with the experimental dataset.

Table 3.3.5.1a: Linear and nonlinear regression Langmuir and Freundlich parameters, along with the statistical correlation coefficients $\Sigma\chi^2$ & R^2.

Model parameters		Linear	Non-Linear
Freundlich model	R^2	0.928	0.947
	K_F (mg g^{-1} (L $mg^{-1})^{1/n}$)	84.273 ± 5.3	87.26 ± 4.2
	n	5.63 ± 0.8	6.195 ± 0.7
	$\Sigma\chi^2$	5.37	5.16
Langmuir model	R^2	0.999	0.970
	K_L (L mg^{-1})	0.91 ± 0.4	1.6 ± 0.19
	q_{max} (mg g^{-1})	156.5 ± 2.1	148.19 ± 3.47
	$\Sigma\chi^2$	14.51	1.96

Satisfactory agreement was achieved upon modelling the dataset using the linear and nonlinear Freundlich models. For this dataset, the choice of regression method introduces only small discrepancies on the values of the Freundlich parameters n & K_F. Examination of $\Sigma\chi^2$ and individual χ^2 values along the dataset, suggests that the nonlinear method is a slightly better predictor of the adsorption process.

Upon examination of Figure 3.3.5.1a and Table 3.3.5.1a, it is however evident that both the linear and nonlinear regression methods suggest a preference for the Langmuir isotherm. In contrast to the Freundlich model, the linearisation of the Langmuir model was observed to introduce significant discrepancies to the parameters calculated, particularly in the case of the Langmuir constant K_L. Despite the much higher R^2 value demonstrated by the linear Langmuir, the $\Sigma\chi^2$ error coefficient is several times smaller in the nonlinear model as opposed to the linear, therefore demonstrating a much better fitting of experimental data.[235] In addition, statistical analysis of χ^2 values for individual datapoints shows that

the nonlinear model offers uniform error distribution across the entire range, whereas in the linear method very large errors have been introduced at the initial low concentration datapoints.

With reference to sections 2.3.3 & 2.3.4, describing isotherm and kinetic modelling of metaldehyde adsorption, these results demonstrate that the linearisation of non-linear models and subsequent linear regression analysis, does not represent a robust method for modelling data.[197,232,234]

3.3.5.2 Nonlinear Langmuir model

The nonlinear Langmuir model was statistically demonstrated to be a good predictor of the initial adsorption of Pb^{2+} onto DBMP-DCM/SA-TfA, particularly at a Pb^{2+} initial concentration range of 62.3 – 140 mg L^{-1}. Upon inspection of the χ^2 error function for the concentrations 180.1 & 200.3 mg L^{-1}, as well as comparison of Langmuir-determined q_{max}= 148.19 ± 3.47 mg g^{-1} to the experimentally determined maximum capacity q_{max}= 155 ± 2 mg g^{-1}, suggests that at higher initial concentrations a deviation from the Langmuir is observed. Importantly, the linear model is observed to better match the experimental q_{max} value, however the linearisation results in significant underestimation of K_L, accompanied with inaccurate fitting at the initial stage of adsorption.

With reference to previous literature studies utilising a variety of materials for Pb^{2+} uptake,[39,40,96,192] the magnitude of K_L = 1.6 ± 0.19 L mg^{-1} signifies that Pb^{2+} uptake by DBMP-DCM/SA-TfA is associated with a very high energy of adsorption. Additionally, the Langmuir separation factor provides further evidence for the high binding interactions of lead (II) ions with the surface of the modified HCP, as R_L was found to be very close to zero across all initial lead concentrations. Specifically, at C_0 = 62.3 mg L^{-1}, the separation factor is R_L = 0.0099, and a steady decrease to R_L = 0.0031 is observed for the highest initial concentration C_0 = 200.3 mg L^{-1}. Mathematically, R_L displays an asymptomatic behaviour approaching zero as the initial concentration factor approaches infinity. This established behaviour of R_L suggests that the adsorption of Pb^{2+} onto DMBP-DCM/SA-TfA is irreversible.[195] As previously discussed, it is the high content of sulfonic acid functionalities that results in very high Pb^{2+} uptake properties, and this is

demonstrated by the very low experimental uptake capacity, q_{max}= 6 mg g^{-1} obtained for the non-sulfonated DMBP-DCM. In accordance with the values of K_L and R_L, as well as TGA and IR data from section 3.3.4.1, it therefore suggested that there exists a significant dependence of the adsorption process on ion-exchange chemisorption mechanisms, which have been previously shown to be mediated by sulfonic acid functionalities.[224,47]

3.3.5.3 Nonlinear Freundlich model

Satisfactory fitting of the experimental data was demonstrated by the heterogeneous adsorption Freundlich model, with the nonlinear regression method producing correlation coefficients R^2= 0.947 and $\Sigma\chi^2$= 5.16 (χ^2_{corr} = 0.73). With reference to existing literature examining aqueous Pb^{2+} uptake,[41,43,79,315] the calculated Freundlich parameter K_F = 87.26 ± 4.2 (mg g^{-1} (L mg^{-1})$^{1/n}$) indicates very strong binding, and the factor n = 6.195, indicates a highly heterogenous surface, the latter also being consistent with the highly amorphous nature of the modified HCP sorbent. Similar values of n have been observed in modelling Pb^{2+} solution adsorption using amorphous carbonaceous materials in previous literature.[316,315]

3.3.5.4 Conclusions based on the Langmuir and Freundlich models

Conclusively, examination of the dataset across different initial concentration ranges, suggests that at higher initial concentrations of Pb^{2+} the Freundlich model is prevalent over the Langmuir, while the opposite is true for low concentrations of adsorbate. As previously mentioned, it is very often the case that two-parameter isotherm models fail to predict the adsorption behaviour, which is of high complexity, and often depends on via several different mechanisms.

Concerning the adsorption system described herein, there is theoretical evidence from the Langmuir model (R_L=0), suggesting significant chemisorption contribution to the overall adsorption process. This is further supported experimentally by significant IR vibrational shifts in sulfonyl group wavenumbers

(section 3.3.4.1), which were identified according to relevant literature to be a result of Pb^{2+} binding onto the surface of DBMP-DCM/SA-TfA.[47,96,225,317]

3.3.5.5 Isotherm models commonly used for chemisorption.

The Dubinin-Rudushkevich model (D-R) has recently received significant popularity for modelling adsorption based on chemisorption ion-exchange processes,[155,192,224,318,319] and has also been extensively used in modelling of metal uptake using commercially available sulfonated crosslinked ion-exchange resins, of similar morphology to DMBP-DCM/SA-TfA.[320,321] The model was initially developed for gas adsorption, and was later adjusted to allow for application to solution systems.[322] It describes adsorption based on the following equations:

$$q_e = q_{max} e^{\left[-\left(\frac{\varepsilon}{E}\right)^2\right]} \quad \text{(eq3.3.5.5a)} \qquad \varepsilon = RT\ln\left(\frac{C_s}{C_e}\right) \quad \text{(eq3.3.5.5b)}$$

With q_e & q_{max} as previously described, R = 8.134 J K^{-1} mol^{-1} being the universal gas constant, T being the temperature in K. It should be noted that the exponent factor in eq3.3.5.5a should be unitless, therefore the solubility-normalised model contains C_s (mg L^{-1}), representing the aqueous solubility of the specific ion adsorbed.[318] The parameter E (J mol^{-1}) describes the energy of adsorption with the Polanyi potential represented by ε (J mol^{-1}).[323]

The aqueous solubility for the Pb^{2+} ion, C_s = 373350 mg L^{-1},[324] was used to calculate ε. Modelling the experimental dataset using the D-R model was conducted by performing nonlinear regression analysis of a plot of q_e against ε, allowing for calculation of the parameters q_{max} & E, shown in Table 3.3.5.5a.

Table 3.3.5.5a: D-R model parameters, along with the statistical correlation coefficients $\Sigma\chi^2$ & R^2.

Dubinin - Radushkevich model	
R^2	**0.992**
$\Sigma\chi^2$	6.01
q_{max} (mg g^{-1})	288.7 ± 21
E (J mol^{-1})	20489 ± 91

Despite the R^2 factor being very close to unity, the $\Sigma\chi^2$ factor suggests that the model is less suitable than the previously examined Langmuir and Freundlich models. Further analysis shows large deviations between the model and experimental data at equilibrium concentrations higher than 20 mg L^{-1}, and this overestimation of adsorption behaviour is reflected on the value of q_{max}= 288.7 ± 21, which is much larger than the highest experimentally obtained capacity, as well as the theoretical value obtained from Langmuir. This type of overestimation has been previously observed in similar research studies.[320,323,324]

The application of the solubility normalised Dubinin-Astakov (D-A) model, has been proposed by Inglezakis to provide a better approach at modelling similar Pb^{2+}-adsorbing systems based on ACs.[324] In fact, the D-R system originates from the D-A but assumes that the heterogeneity parameter is always n = 2, hence the exponent factor in eq3.3.5.5a, is squared. In the approach used by Inglezakis, the heterogeneity parameter n is calculated from the fitting method, and the value of q_{max} is obtained from experiment. Upon introduction of a correction factor, the following solution-normalised D-A equations are obtained:

$$q_e = q_{max} e^{\left[-\left(\frac{\varepsilon}{\sqrt{2}E}\right)^n\right]} \quad \text{(eq3.3.5.5a)} \qquad \varepsilon = RT\ln\left(\frac{C_s}{C_e}\right) \quad \text{(eq3.3.5.5b)}$$

It was decided that q_{max} = 160 mg g^{-1} for DMBP-DCM/SA-TfA, as that represented the highest capacity experimentally obtained, at a Pb^{2+} concentration of C_0= 250 mg L^{-1}.[324] Upon data modelling and parameter calculations, exceptional fitting characteristics were obtained (Table 3.3.5.5b).

Table 3.3.5.5b: D-A model parameters, along with the statistical correlation coefficients $\Sigma\chi^2$ & R^2.

Dubinin - Astakov model	
R^2	**0.992**
$\Sigma\chi^2$	0.88
n	6.55 ± 0.4
E (J mol^{-1})	24303 ± 300

The statistical correlation coefficients R^2 & $\Sigma\chi^2$ are indicative of excellent consistency between the experimental data and the D-A model. Importantly, comparison of the R^2 values for D-R and D-A models would suggest that both fit the data equally well, however the opposite is true for $\Sigma\chi^2$ which suggests a significantly better fitting relationship for the D-A model. Upon visual inspection of the plot, it is evident that the D-R model fails to predict the Pb^{2+} adsorption behaviour at higher concentrations, and the satisfactory statistical agreement observed is likely coincidental, depending on arbitrarily chosen experimental initial concentrations.

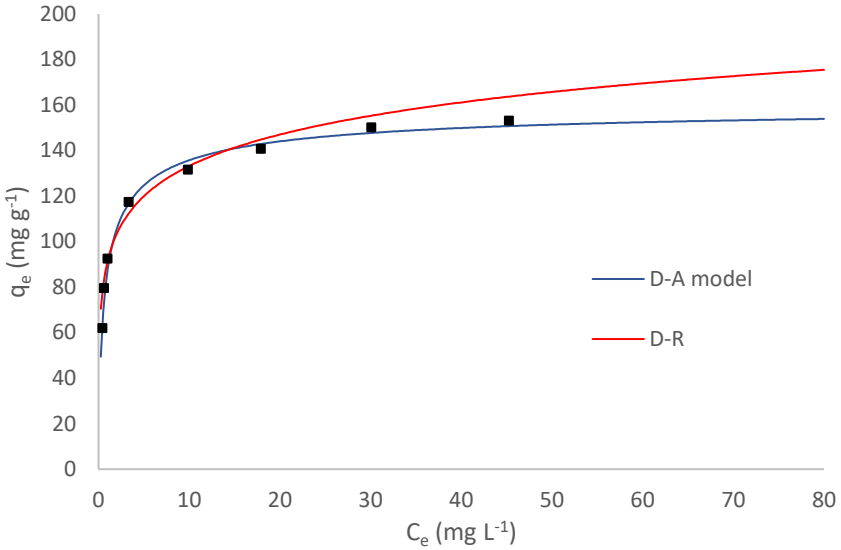

Figure 3.3.5.5a: Calculated D-A & D-R models with reference to experimental data.

As the maximum adsorption capacity can be determined to adequate accuracy by experiment, the use of D-A model to allow for the calculation of a heterogeneity parameter is logical, with this approach ensuring that the model fits well with the higher equilibrium concentration datapoints. Interestingly, the value of n= 6.55 ± 0.4 is consistent with previous carbonaceous adsorbent systems which showed good fitting to the D-A model,[324,325,326] and with relevance to Pb^{2+} adsorption.[324,327] Interestingly, the parameter of n matches that calculated from the Freundlich model, however this is likely coincidental as the Freundlich model is empirical whereas D-A is derived from a theoretical background. Furthermore, the estimated energy of adsorption as calculated from the D-A model as E = 24303 ± J mol^{-1}, is in the range observed in previous literature studies,[324,325,327] and indicates that the adsorption of Pb^{2+} onto DBMP-DCM/SA-TfA relies predominantly on chemisorption.

3.3.6 Adsorption of Pb (II) using sulfonated PIMs

3.3.6.1 EA-TB/ASA

In the current work, ASA-treated EA-TB was found to achieve a 60% total adsorption of Pb^{2+} from equilibrium studies using 102.8 mg L^{-1} Pb^{2+} solution. This equates to a total saturation capacity of 63 ± 0.4 mg g^{-1}, significantly higher than the value obtained for the non-sulfonated adsorbent which reached saturation at 18 ± 3.7 mg g^{-1}.

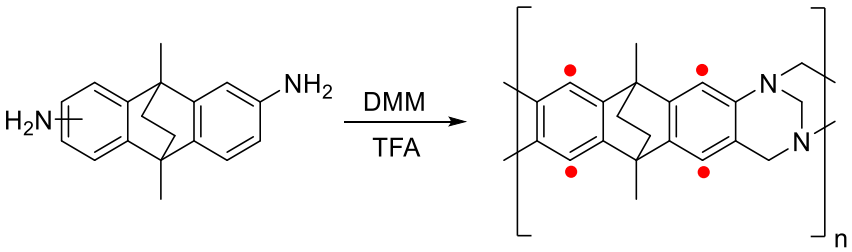

Figure 3.3.6.1a: Calculated D-A & D-R models with reference to experimental data. Possible sulfonation sites are shown in red.

The unique structure of Tröger's base contains basic nitrogen heteroatoms embedded in the 'ladder' backbone. Due to the rigid and contorted structure of TB, the lone pairs on the nitrogen atoms cannot be delocalised onto the aromatic ring as the orientation of the orbital containing the electrons does not align with the π system on the aromatic ring. The basicity of these heteroatoms renders the polymer moderately hydrophilic. Consequently, batch equilibrium experiments determined that there is satisfactory affinity of EA-TB for Pb^{2+} ions, with a saturation capacity of 18 ± 3.7 mg g^{-1}. Like in the case of HCPs, sulfonation of EA-TB increases the polarity and wettability of the material as the sulfonic acid moieties can interact with the aqueous medium and participate in favourable interactions facilitating the adsorption of ions. The IEC was determined via a back titration as 3.04 mmol g^{-1}. Interestingly, when reacted with aqueous sodium hydroxide, the EA-TB/ASA displayed partial solubility in water, with the filtered solution displaying a bright yellow colour. This has likely resulted in the overestimation of the sulphonic acid content of EA-TB/ASA, but likely not with significant discrepancy as only oligomers are

expected to display solubility in water. Theoretically, there are two electron rich aromatic rings per repeating unit and a total of 4 potential sulfonation sites, marked in red in Figure 3.3.6.1a. A sulfonation content of 3.04 mmol g^{-1}, determined by back titration, corresponds to 1.33 -SO_3H units per repeating unit and 0.67 acidic units per benzene ring. Due to the nature of the aromatic sulfonation reaction which yields a sulphonated product deactivated towards additional electrophilic substitution reactions, it is highly unlikely that sulphonation at 83 °C would take place twice in the same ring.[328]

The modified adsorbent EA-TB/ASA was also found to display solubility in solvents like DMSO and DMF, which allowed for solution ^{1}H-NMR spectra acquisition, prior and after sulfonation. Broad peaks indicative of high molecular weight polymeric chains are present for both the parent and sulfonated polymers, suggesting that no significant depolymerisation occurred during the sulfonation process and the Troger's base unit remains intact. As expected, peaks in the aromatic region appear broader and more deshielded for the sulfonated analogue. A copy of the spectra is attached section 7.2 (Appendices Figure 7.2a).

The BET surface area of EA-TB decreases rapidly from 900 $m^2 g^{-1}$ to 12 $m^2 g^{-1}$ upon sulfonation. This is due to the introduced acidic moieties which can interact with the basic nitrogen atoms in the structure, ultimately resulting in the collapse of the pores and decreasing the materials adsorption capacity for the nitrogen gas probe. In the presence of a polar solvent like water, interactions between solvated adjacent polar groups will be minimised, and the size of the pores increases together with the material's accessible surface area. An independence between BET surface area and metal uptake activity may be observed.[47,48] Despite the severely compromised BET surface area obtained upon sulfonation, the material EA-TB/ASA displays moderate CO_2 adsorption properties. Specifically, sulfonation was found to decrease the uptake of CO_2 from 3.24 mmol g^{-1} to 1.78 mmol g^{-1}. Despite this decrease being significant, it does not correlate to the N_2 adsorption data, according to which EA-TB/ASA could be classified as non-porous. There have been several reports in the literature discussing the enhanced CO_2 uptake of materials modified through functionalisation with polar groups including hydroxyl, carboxylic

and sulfonic acid moieties. [284,329] In the case of EA-TB/ASA, the polar -SO_3H and TB functionalities display significant affinity for CO_2, causing the material to partially retain its adsorptive properties whilst N_2 affinity is severely reduced. The established difference in CO_2/N_2 suggests that there may be potential applications of EA-TB/ASA or its analogues, in gas separation and carbon capture applications.

The IR spectrum of the sulfonated analogue compared to the non-modified adsorbent EA-TB, displays several additional peaks associated with the presence of sulfonic acid groups. The broad set of peaks at 2810-3090 cm^{-1} is attributed to OH stretch originating from the -SO_3H groups and possibly from moisture absorbed onto the polar polymeric surface. Peaks indicative of asymmetrical and symmetrical stretching vibrations of the -SO_2- group are present at wavenumbers 1371 & 1207 cm^{-1}. Additionally, the asymmetrical stretch of S-O bonds is observed at 818 cm^{-1} and the sharp peak at 1082 cm^{-1} is originating from SO_3^- assymetric stretching vibrations.[47]

3.3.6.2 PIM-SBF/TMSCS (K^+-form)

During the general scope batch adsorption experiments, modified PIMs synthesized by other members of our research group were also tested for Pb^{2+} adsorption. These include the amidoxime-functionalised AO-PIM-1[155] & AO-PIM-Trip,[147] and the sulfonated adsorbent PIM-SBF/TMSCS, converted to its K^+-form. The amidoxime-functionalised PIMs did not demonstrate significant Pb^{2+} uptake properties and are not discussed further. In contrast, exceptional adsorptive properties were demonstrated by PIM-SBF/TMSCS, synthesised by a sulfonation route employing trimethylsilyl chlorosulfonate (TMSCS), followed by washed with $KCl_{(aq)}$ solution to ensure complete H^+/ K^+ exchange in internal sulfonate moieties. The K^+-form achieved a remarkably high adsorption efficiency of 99.8%, at 105 mg L^{-1} initial Pb^{2+} concentration, corresponding to capacity of 102 ± 0.6 mg g^{-1}. Even though batch studies at higher initial Pb^{2+} concentrations were not conducted, it is evident that the material displays much better adsorptive properties than EA-TB/ASA, and similar to the highly sulfonated sorbents TPB-DCM/SA-TfA, tryp-DCM/SA-TfA & DBMP-DCM/SA-TfA.

In comparison to the SA-TfA modified adsorbents, a much IEC of 1.86 mmol g^{-1} was determined for PIM-SBF/TMSCS via Boehm titration. Generally, the ion exchange process is known to depend on the ion separation factor, represented by the selectivity of the material for Pb^{2+},[330] with respect to the exchanging cation, H^+ or K^+. Even though the specific values of ion selectivity are material-dependent, generalised values suggest that K^+ should bind more strongly to the sulfonate moieties than H^+,[330] which would result in a reduced ion exchange efficiency for the K^+-form. Nevertheless, the efficiency of inward and outward diffusion of charged species in an ion exchanging material depends on a variety of factors including water content, pore size distribution & degree of swelling in water, and all these factors depend strongly on the nature of the cation present.[330] Conclusively, the remarkable Pb^{2+} affinity demonstrated by PIM-SBF/TMSCS for Pb^{2+} remains unclear and requires further investigation.

3.4 Metaldehyde degradation using sulfonated adsorbents

3.4.1 Batch-type degradation experiments: GC-MS analysis

HCPs based on the TPB monomeric unit are extensively discussed in chapters 3.1 & 3.2 due to their exceptional performance in aqueous metaldehyde removal by adsorption. In chapter 3.3, post-polymerisation sulfonation of HCPs was shown through analytical experiments to result in high affinity for metal ions such as Pb^{2+}. The molluscicide metaldehyde is a tetramer of acetaldehyde units, and its degradation is known to occur readily under acidic conditions or thermal treatment. Therefore, a question that arises from the combination of these two different chapters is whether the sulfonated materials could potentially achieve metaldehyde degradation. This type of solid surface-catalysed metaldehyde degradation has been previously reported for acid-containing activated carbon materials.[16,222]

The modified adsorbents EA-TB-ASA, TPB-DCM/ASA & TPB-DCM/SA-TfA were subjected to batch equilibrium conditions as described in section 5.3.1, at an initial metaldehyde concentration of C_0 = 80.7 mg L^{-1}. Equilibration was achieved following a contact time of 46 hrs at two different adsorbent doses, 1 mg L^{-1} and 0.4 mg L^{-1}. The concentration of the remaining metaldehyde was determined using GC-MS quantitative analysis following SPE of analyte.

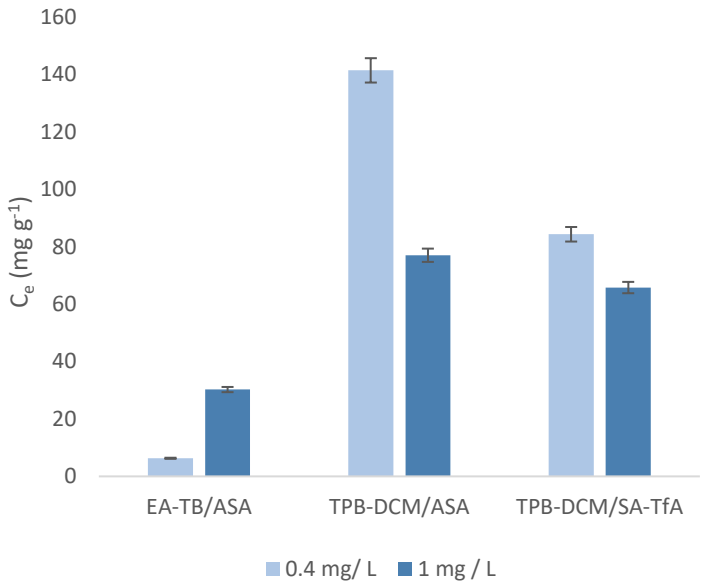

Figure 3.4.1a: Adsorption equilibrium capacities obtained at adsorbent doses of 0.4 & 1 mg /L and initial metaldehyde concentration C_0 = 80.7 mg L^{-1}, for all sulfonated adsorbents tested

The adsorbent EA-TB/ASA was found to remove a small amount of metaldehyde at both adsorbent doses 0.4 & 1 mg L^{-1}, despite the abundance of acidic sites present in its structure (3.04 mmol g^{-1}). Notably, the capacity q_e = 30.24 mg g^{-1} obtained for EA-TB/ASA at adsorbent dose 1 mg L^{-1}, is significantly higher compared to unmodified EA-TB, for which q_e= 8.05 mg g^{-1} was obtained. Upon sulfonation of EA-TB, hydrophobicity is significantly decreased; however, this is also accompanied by dramatic reduction in BET surface area and pore volumes which may limit the surface area accessible to the adsorbate.

Higher removal efficiency was observed for the modified HCPs TPB-DCM/ASA & TPB-DCM/SA-TfA. Interestingly, TPB-DCM/ASA for which IEC = 3.04 mmol g^{-1} was obtained, significantly outperformed TPB-DCM/SA-TfA, despite its much higher acid content of 6.5 mmol g^{-1}. Specifically at 0.4 mg L^{-1} adsorbent dose, removal capacities of 141.29 mg g^{-1} & 84.33 mg g^{-1} were determined for the adsorbents TPB-DCM/ASA & TPB-DCM/SA-TfA, respectively. As previously explained, this difference is likely due TPB-DCM/SA-TfA possessing a significantly compromised BET surface area and pore size reduction which arise from the introduction of excess polar functionalities. This underlines the importance of

mesopores in metaldehyde adsorption, previously discussed in chapter 3.1. It is also logical that sufficient meso and microporosities are important in metaldehyde degradation, as the processes necessitates the efficient transport of the molluscicide to the acidic sites. It is therefore speculated that there must exist a balance between acid content and surface area reduction, for which metaldehyde removal and degradation kinetics are optimal. [209]

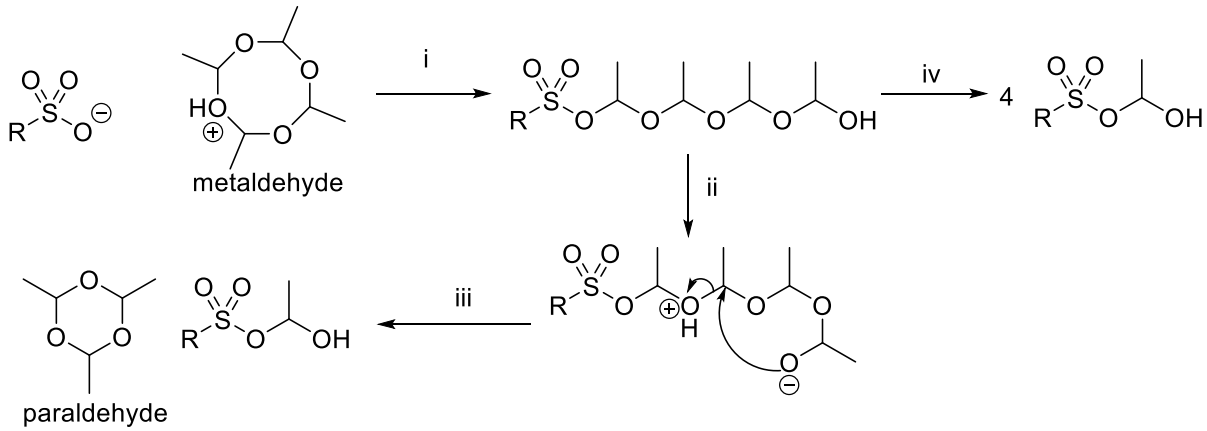

Figure 3.4.1b: **i.** Sulfonic acid-catalysed ring opening of metaldehyde **ii.** Conformational rearrangement of the Poly(oxymethylene) glycol chain **iii** Nucleophilic ring closure to form paraldehyde **iv** Further depolymerisation of the glycol chain.

Metaldehyde degradation using a commercially available, highly sulfonated polymeric resin has been previously reported.[222] The authors proposed a degradation mechanism involving protonation of metaldehyde ether functionalities by the acidic sites, followed by nucleophilic attack of the acidic group and ring opening of the metaldehyde molecule (**i** in Figure 3.4.1b). It was also suggested that subsequent depolymerisation may occur through the attack of adjacent acidic functionalities, reducing the long chain polyether alcohol (**iv** in Figure 3.4.1b). GC-MS data obtained in the present study suggest that the mechanism proposed by Fletcher *et al.* is logical, but other metaldehyde degradation pathways may be possible. Specifically, the GC-MS chromatographs of the solid phase extracted filtrates of TPB-DCM/ASA & TPB-DCM/SA-TfA, confirmed the high presence of paraldehyde, which was detected as a separate peak at t = 8.4 min, and was identified through similarity search using the NIST library.[331] It is therefore suggested that the ring-opened polyether alcohol chain termini could perform intramolecular

nucleophilic attack on the backbone chain, and this attack may result to the formation of the cyclic paraldehyde product as shown in Figure 3.4.1b. Paraldehyde is more thermodynamically stable than metaldehyde and may also form by the trimerization of acetaldehyde at acidic conditions.[332]

Notably, the presence of tetrachloroethene was identified in in the chromatograph, likely formed from the DCM extraction solvent at high temperatures supplied GC compartment. Even though the formation of tetrachloroethene has been previously reported to form from chlorinated solvents,[333] it proceeds via radical intermediates and the exact mechanism of its formation remains unclear. Further examination of the chromatograms revealed the presence of many unexpected compounds identified using NIST mass spectral library.[331] Even though it is very likely that those could have formed under the high temperature GC injection conditions, the structures shown in Figure 3.4.1c demonstrate that the sulfonated adsorbents exhibit extensive catalytic activity. Nevertheless, the quantitative GC-MS method is not a suitable way of obtaining mechanistic details and identifying degradation products, as it relies on a pre-analytical SPE step which may not have captured some of the degradation components, or during which significant changes in analyte composition may have occurred.

volatile components observed before the solvent peak

Figure 3.4.1c: Chemical structures of compounds identified in the chromatograms, following metaldehyde degradation experiments using TPB-DCM/ASA & TPB-DCM/SA-TfA. Identification was performed using the NIST library.

Following metaldehyde degradation experiments, the adsorbent TPB-DCM/ASA was filtered & air-dried and a TGA spectrum was acquired. The % thermal degradation & 1st derivative (%/ °C) spectra of the TPB-DCM/ASA adsorbent are shown in Figure 3.4.1d, together with the corresponding spectra for the unmodified adsorbent TPB-DCM, saturated with metaldehyde.

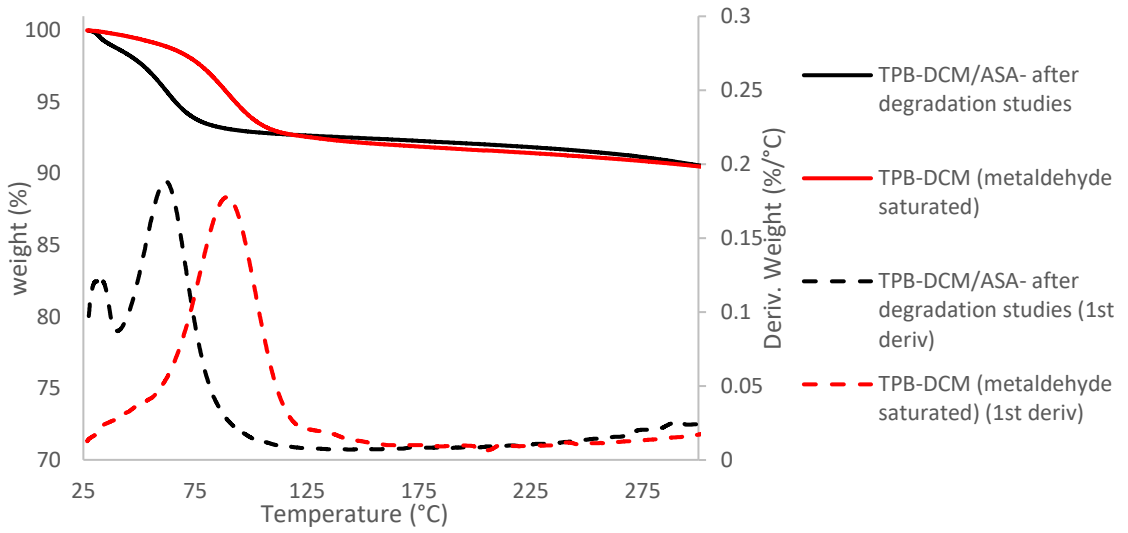

Figure 3.4.1d: TGA analyses of TPB-DCM/ASA following metaldehyde degradation studies in comparison to the non-functionalised TPB-DCM metaldehyde saturated sample.

The degradation profile of the metaldehyde-saturated TPB-DCM sample exhibits significant mass loss at 92.6 °C, associated with metaldehyde conversion to four volatile acetaldehyde monomers. For TPB-DCM/ASA, two distinct losses are observed for T< 80 °C. The first mass loss is clearly observed in the 1st derivative spectrum at T= 35 °C and is associated with the release of a volatile component adsorbed onto the surface of the modified adsorbent. At a higher temperature of T= 63.5 °C, a separate mass loss process is observed, which is likely originating from the thermal loss of sulfonyl ether functionalities arising from depolymerised metaldehyde, as shown in Figure 3.4.1b. It is therefore likely that acetaldehyde binding to the sulfonate moieties of the polymers relies on chemisorption, and that an abundance of metaldehyde degradation products preferentially partition into the pores of the polymeric adsorbent. The high volatility of the component removed at T= 35 °C may lead to the association of that mass loss transition with acetaldehyde, however this should be further confirmed by TGA-MS,[334] as other volatile degradation products may be present. It is also likely that a high proportion of those may have been removed prior to TGA acquisition, during the air-drying process.

3.4.2 Further degradation experiments: NMR studies

The degradation experiment was also conducted in D_2O to gain insights on the mechanism of degradation and identify any intermediates formed. Experimentally, the adsorbent was added to an NMR tube at a dose of 1 mg mL^{-1}, and the concentration of metaldehyde (103 mg L^{-1}) was standardised against dimethyl sulfone as an internal standard. To allow for addition of the adsorbent at such low amounts, a 2 mg mL^{-1} suspension of particles in D_2O was prepared, and the suspension was homogenised by sonication, prior to addition of the solid to the NMR tube using a volumetric pipette. Due to a small particle size and high hydrophilicity, the TPB-DCM suspension in D_2O remained homogeneous during spectrum acquisition and did not result in resonance broadening effects. It is therefore suggested that the present experimental design may be appropriate for studying metaldehyde degradation kinetics, providing that the adsorbent of choice is of similar hydrophilicity and bulk particle size as the TPB-DCM/ASA sorbent discussed herein.

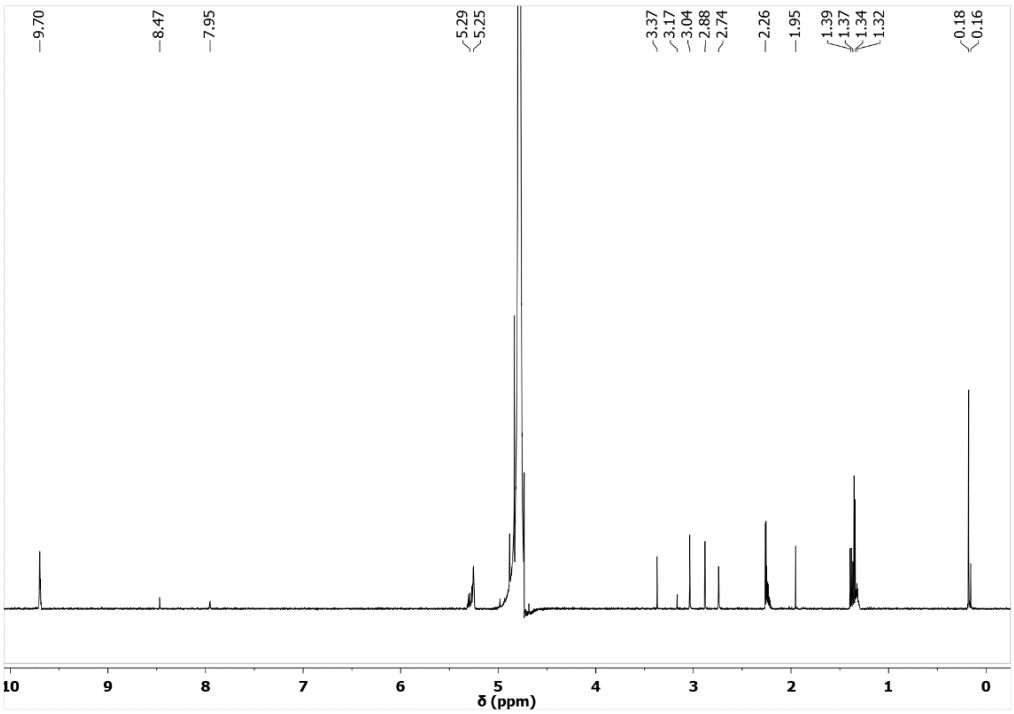

Figure 3.4.2a: ^{1}H-NMR spectrum of TPB-DCM/ASA as a suspension in metaldehyde solution of initial concentration C_0= 103 mg L^{-1}, in D_2O after a 4-day contact time. Recorded using a Bruker AVA500 spectrometer at 500 MHz.

As observed in Figure 3.4.2a, in addition to residual metaldehyde peaks at 1.37 ppm (d, 12H) & 5.3 ppm (q, 4H), a small amount of acetaldehyde is also present at 9.71 ppm (q, 1H) & 2.27 ppm (d, 3H). In accordance with GC-MS results, the presence of paraldehyde is also confirmed by NMR at 1.39 ppm (d, 6H) & 5.3 ppm (q, 3H). With the exception of the acetic acid resonance at 1.95 ppm, corresponding to acetic acid,[335] the remaining resonances could not be assigned.

With reference to relevant literature studies,[336–340] aqueous acetaldehyde has been observed to exhibit diverse reactivity in solution and is present in various different equilibria. Firstly, aqueous solutions of acetaldehyde have been reported to result in the formation of the hydrated form as shown in Figure 3.4.2b.

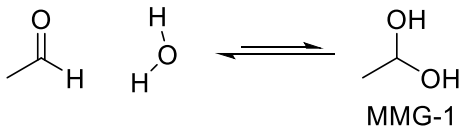

Figure 3.4.2b: Hydration of acetaldehyde to form ethane-1,1-diol (MMG-1).

The presence of hydrated acetaldehyde, MMG1, was confirmed by NMR at 1.35 ppm (d, 3H) & 5.26 ppm (q, 1 H), owing to the acidity of the solution which is known to enhance its formation.[338]

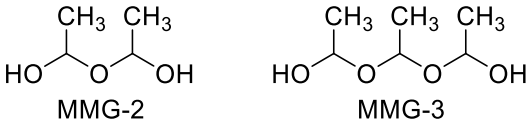

Figure 3.4.2c: Poly(oxymethylene) glycol chains of various lengths, MMG-2 & MMG-3.

Poly(oxymethylene) glycols of different chain lengths (Figure 3.4.2c) have also been commonly reported.[340] However, those could not be unambiguously identified from the spectrum due to resonance overlap, as a consequence of similar chemical shifts in the CH and CH_3 groups of metaldehyde degradation products.

Importantly, a contact time of 46 hrs is generally considered sufficient to achieve equilibration in adsorption processes,[190] and was initially selected in the GC-MS batch-type metaldehyde degradation study. However, the kinetics of metaldehyde degradation were determined by NMR spectroscopy to

be much slower, and significant changes in the consistency of the mixture were observed even after a week of agitation. At an adsorbent dose of 1 mg mL^{-1} and initial concentration of metaldehyde C_0= 103 mg L^{-1}, standardised using a stock solution of dimethylsulfone NMR standard, TPB-DCM/ASA was found by NMR peak integration to result in 80% total degradation, after 2 days of agitation. At contact times longer than 7 days, the degradation efficiency of metaldehyde was found to approach 99%, suggesting that the process may be of catalytic nature, with the degradation kinetics diminishing rapidly when the metaldehyde bulk concentration reduces. As previously, the slow kinetics of degradation are partially attributed to a small average pore size which does not facilitate efficient metaldehyde diffusion across the bulk of the material. Importantly, the presence of various degradation products demonstrated by GC-MS and NMR analyses is also responsible for the declining kinetics of metaldehyde degradation, as these products may compete with metaldehyde for the active catalytic sites. The strong binding of degradation products to the sulfonated surface is thoroughly supported by the TGA profile of TPB-DCM/ASA, recorded after degradation experiments. In summary, at initial degradation stages the metaldehyde bulk concentration is high and no other species are present, therefore the process advances at a moderate rate. As the experiment proceeds the kinetics rapidly diminish due to the simultaneous decrease of metaldehyde bulk concentration, accompanied by the formation of degradation products which may partition into the pores of the polymer.

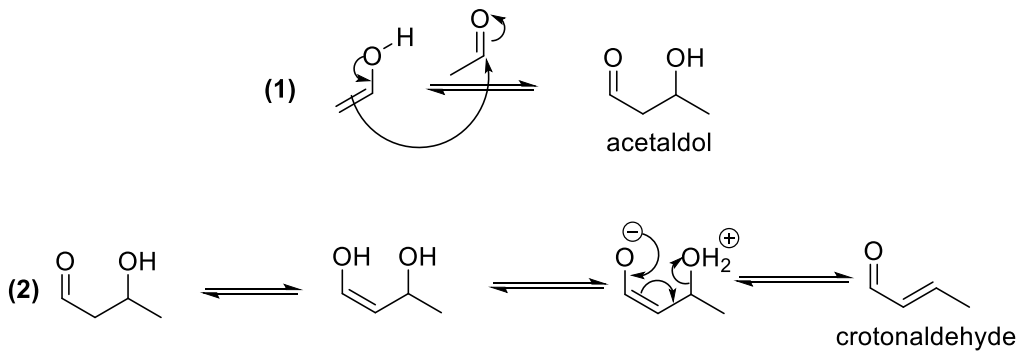

Figure 3.4.2d: **(1)** Acid catalysed aldol condensation of acetaldehyde to from acetaldol. **(2)** Acetaldol dehydration to form crotonaldehyde.

The majority of degradation products is most likely originating from the formation of acetaldol ((1), Figure 3.4.2d), derived from the aldol condensation of acetaldehyde.[337] which then may undergo dehydration to form crotonaldehyde ((2),Figure 3.4.2d).[341] Notably, acetaldol was observed in the ^{1}H-NMR spectrum in trace amounts at the initial stages of degradation. Crotonaldehyde was also observed in small quantities at later stages of the reaction (> 4 days), and was identified based on weak resonances at 6.69 ppm, 6.10 ppm & 1.7 ppm,[342] with the aldehydic proton appearing in the overlapping region 9.68 - 9.76 ppm. The formation of crotonaldehyde has been previously observed to be a main pathway for the conversion of acetaldehyde to other products,[337,343] and it is likely not observed in high quantities due to strong binding to the polymeric active sites, which disallow outward diffusion from the bulk of the solid. This is supported by the ^{1}H NMR spectrum obtained after filtration of the adsorbent and elution of products adsorbed or chemisorbed at the pores of TPB-DCM/ASA, using CD_3OD. Other than a significantly higher presence of crotonaldehyde, other products such as MMG-1, acetone, and acetic acid, were identified amongst a remarkably large number of other unknown products.

The relatively low initial concentration of metaldehyde in combination to the large number of components present in the mixture presented several difficulties in ^{13}C-NMR acquisition, and elucidation of the degradation mechanism would require further investigations using isotopically enriched reagents. Nevertheless, in an attempt to identify some of the products that are formed from acetaldehyde conversion, NMR spectroscopic experiments such Nuclear Overhauser Effect Spectroscopy (^{1}H NOESY), Correlation Spectroscopy (^{1}H-^{1}H COSY), Heteronuclear Single Quantum Coherence (^{1}H-^{13}C HSQC) and ^{2}D-NMR were performed.

The ^{2}D-NMR spectrum confirmed that there exist exchangeable protons at 5.25- 5.28 ppm and 1.30-1.35 ppm, as well as 2.21 ppm, the former associated with MMG1 and the latter with acetaldehyde in which the methyl protons are subject to chemical exchange.[344]

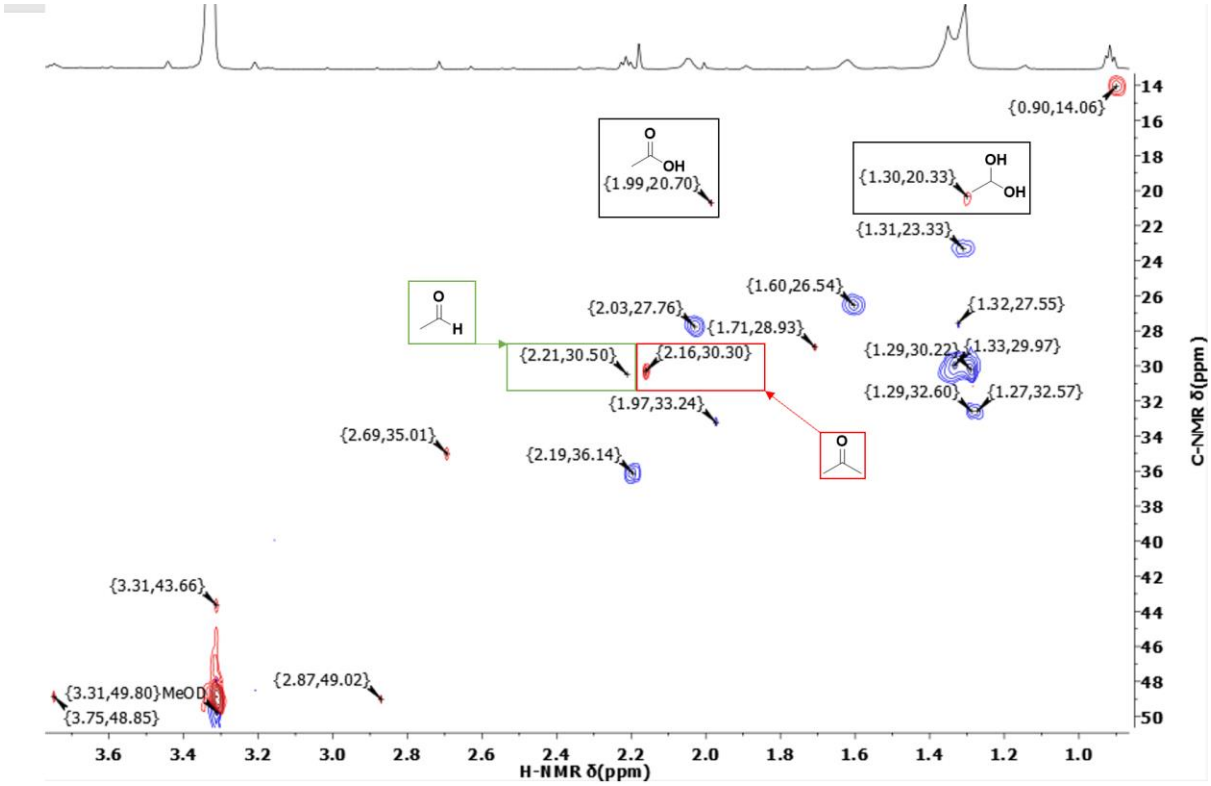

Figure 3.4.2e: ^{1}H-^{13}C HSQC spectrum solvent-extracted TPB-DCM/ASA, in CD_3OD. An additional the resonance pair at δ_H = 5.34 ppm / δ_C= 130.46 ppm was observed. Recorded on a Bruker AVA600 spectrometer, at 600 MHz. Red colour represents CH and CH_3 groups and blue shows CH_2 groups.

In contrast to the problematic ^{13}C-NMR acquisition, the ^{1}H-^{13}C HSQC spectrum of the CD_3OD- extracted TPB-DCM/ASA obtained from the previously described batch-type GC-MS study, reveals that a wide range of degradation products remain adsorbed/chemisorbed into the pores of the solid. The spectrum shows the polymer content after a contact time of 20 days, and products such as acetone, acetic acid and acetaldehyde are present along with of various other species. Specifically, it is suggestive of the presence of linear alkane-based compounds, as demonstrated by the resonance at δ_H = 0.9 ppm / δ_C = 14.06 ppm, as well as alkenes, which are demonstrated by the resonance pair at δ_H = 5.34 ppm / δ_C= 130.46 ppm, and may correspond to ethylene.[335]

Additionally, the ^{1}H-NMR of the particle-suspended solution reveals a highly shielded resonance at 0.18 ppm, which was found to change independently with respect to other signals, was not associated with any other resonances in ^{1}H-^{1}H COSY experiments and appeared as a weak multiplet in the ^{2}D-NMR, spectrum likely due to H-D coupling. A much weaker proximal resonance at 0.16 ppm was also

observed. The chemical shift at 0.18 ppm is consistent with that of methane,[335] and with the resonance shifting to 0.2 ppm in CD_3OD.[345]

Furthermore, the coupling constant with respect to ^{13}C satellite peaks was calculated as J_{H-C} = 119.3 Hz, which is consistent with that of methane, with reference to previous literature.[346] Consistent values of J_{H-C} were obtained from spectra obtained at different contact times.

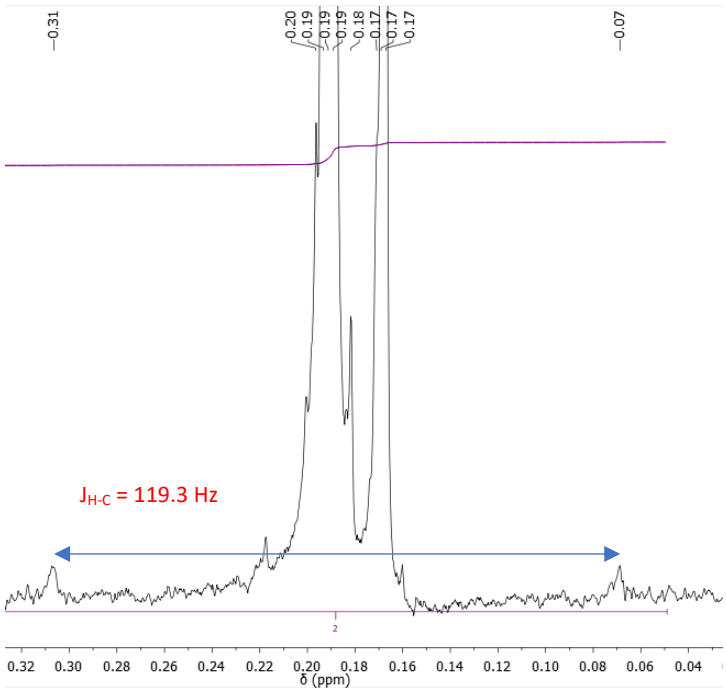

Figure 3.4.2f: The ^1H-NMR resonance at 0.18 ppm showing the ^{13}C satellite peaks used in the calculation of J_{H-C}. Recorded on a Bruker AVA600 spectrometer, at 600 MHz.

As observed in Figure 3.4.2f, there are many overlapping resonances in the region 0.16 - 0.21 ppm, signifying the presence of various compounds containing highly shielded protons. These could be due to the formation of methane clathrates at the confined cavities of the TPB-DCM/ASA, which may host and stabilise such hydrated methane clusters, previously reported to result in significant chemical shift changes.[347–349] It should however be mentioned that methane clathrates are usually observed under high pressure, and further investigations are needed to confirm whether they could form at the micropores of TPB-DCM/ASA.

Additionally, there exist only a few examples of species that resonate at such low chemical shifts, and these are usually nonpolar and highly strained. For instance, cyclopropane produces shifts at δ_H = 0.22 ppm[350] and δ_C = -2.6 ppm,[351] which are in reasonable agreement with the resonance pair of δ_H = 0.19 ppm / δ_C = -1.96 ppm, obtained from the ^{1}H-^{13}C HSQC spectrum (Appendices, Figure 7.2c). Therefore, another possible explanation for the highly populated area at 0.16 - 0.21 ppm, is the formation of cyclopropane-based compounds, with dimethyl cyclopropane also observed in the GC-MS analysis.

Along with the previously mentioned reduced products, oxidised products such as acetic acid and traces of formic acid, observed at 8.22 ppm,[335] are present. Notably, the ^{1}H-^{13}C HSQC spectrum shows a very broad signal in the region 115-150 ppm of the ^{13}C spectrum (Appendices, Figure 7.2b), without any significant proton correlations to account for the size of the resonance. This is likely indicative of the presence of CO_2, which should appear at approximately δ_C = 125 ppm.[352] In addition, dissolved CO_2 may result in the formation of carbonic acid, which may form carbonate species in solution.[353] The formation of formic acid observed in NMR spectra may also be a product of CO_2 and H_2,[354] however the presence of H_2 could not be confirmed due to the broad water peak at 4.79 ppm, or disappearance of the resonance in presat experiments.

It is therefore suggested that a wide range of redox reactions are catalysed at the micropores of TPB-DCM/ASA, which provide a highly polarised and confined environment, which mediates the reduction of chemical reaction activation barriers. The high potential of sulfonated materials in catalysis has therefore recently received significant research attention.[254,266,355]

Previous studies on acetaldehyde and ethanol conversion have reported catalytic cycles yielding similar products to the ones present herein.[343,356–358] Specifically, the authors cited report the formation of methane, alkanes, olefins & CO_2 as products of the catalytic transformations of acetaldehyde. A dependence of those catalytic transformation on the formation of acetone has been observed. In the case of degradation onto TPB-DCM/ASA, acetone which could be originating from the decarboxylation

of the β-keto acid species formed after rearrangement of epoxidized crotonic acid.[359] The mechanism methane has often been associated with the subsequent conversion of acetone to 2-propanol.[356]

3.4.3. Summary, aims and objectives

Conclusively, the sulfonated adsorbent successfully catalyses the depolymerisation of metaldehyde to acetaldehyde, which exists undergoes hydration to form MMG-1, in addition to oxidation to form acetic acid. Paraldehyde is more thermodynamically stable and is present in large amounts at initial degradation stages but is also degraded after contact times longer than 4 days. The slow degradation kinetics are due to the narrow pore size distribution of the sulfonated adsorbent which limits bulk diffusion efficiency to the catalytic sites, in addition to the high occupation of those sites by a plethora of products arising from acetaldehyde conversion.

It is unclear whether the adsorbent TPB-DCM/ASA could be used industrially in metaldehyde degradation, with the major problems being the slow degradation kinetics along with the large number of side reactions based on the acetaldehyde degradation product. The strong ion-exchanging activity of the adsorbent is also likely to cause problems, if real environmental samples were to be used. Nevertheless, the remarkably versatile catalytic activity of TPB-DCM/ASA is recognised and should be further investigated.

4. Conclusions and future work

4.1 Organic pollutant removal: Metaldehyde

HCPs derived from a variety of aromatic units such as DPA, HPB, TP, tryp & TPB were synthesised and tested for aqueous metaldehyde uptake. In preliminary batch adsorption studies the adsorbent TPB-DCM, synthesised from the inexpensive aromatic unit TPB in DCM solvent and in the presence of the Lewis acidic $AlCl_3$, was identified to display exceptional metaldehyde affinity. Synthesis and further testing of TPB-HCPs, derived in the presence of external crosslinking units such as TMOF, TMOC & DMM and solvents such as DCE, DCM, demonstrated that external crosslinking results in significant increases (of up to 15%), in metaldehyde uptake capacities. Analysis of N_2 & CO_2 adsorption data revealed that the presence of external crosslinking units significantly reduces the S_{BET} & V_{micro} of the TPB-HCP, but also introduces higher levels of meso and microporosities, which are important in intraparticle diffusion of metaldehyde. Characterisation using ^{13}C-SS NMR spectroscopy suggests similar network morphologies for all adsorbents synthesized in the presence of external crosslinkers, in addition to a higher level of Scholl coupling linking units for TPB-DCM. Non-linking alkylated and chloroalkylated units were also observed for all networks. Following acid digestion of the HCPs and subsequent ICP-OES analysis, the adsorbent TPB-DCM displaying a moderately high content of 2.3% Al, and that was attributed to its microporosity which resulted in the encapsulation of ions within its structure.

The highest equilibrium uptake was achieved for the adsorbent TPB-DCM/TMOF, which at 1 mg mL^{-1} adsorbent dose and metaldehyde initial concentration of 80 mg L^{-1}, achieved a total removal efficiency of 95% and q_e= 76 ± 2 mg g^{-1}, significantly outperforming the PAC & ST-DV benchmark adsorbents. A solution adsorption isotherm further demonstrated TPB-DCM/TMOF's exceptional affinity for metaldehyde. Statistical analysis and modelling of the experimental dataset using the linear and nonlinear Freundlich and Langmuir models, suggested that the non-linear Langmuir model was the best predictor of the adsorption of metaldehyde onto TPB-DCM/TMOF, and revealed significant

discrepancies in the values of the parameters obtained between the linear and nonlinear methods. A theoretical maximum capacity of q_{max}= 125.00 ± 6.03 mg g^{-1} and Langmuir constant K_L = 0.52 ± 0.06 L mg^{-1} were found to be within the highest values obtained in existing literature, with the separation factor R_L further confirming the favourability of the adsorption process. The adsorption kinetics were very rapid, with 70% of the total metaldehyde removed within 15 s and the equilibrium capacity reached within 10 mins. The calculated PSO rate constant, k_2= 0.15 ± 0.02 mg^{-1} g min^{-1}, demonstrated fast kinetics, attributed to the small particle size of the HCP in addition to its pore size distribution which allows efficient mass transport of the metaldehyde to the adsorption sites. In RSSCTs of the adsorbent TPB-DCE/DMM at lower metaldehyde concentration of C_0= 0.5 mg L^{-1}, flowrate= 0.35 ml min^{-1} & EBCT= 2.4 min, 2500 column volumes were purified before breakthrough, with the effluent concentration being lower than 0.025 µg L^{-1}. TGA showed that metaldehyde can be removed via the application of heat and GC-MS analysis demonstrated that washing with organic solvent results in metaldehyde elution.

In summary, experimental data and overall analysis presented suggests that TPB is an excellent building block for the synthesis of HCPs that could be used in metaldehyde removal. Further investigations should focus on optimising the choice of solvent, crosslinking density and % molar amount of Lewis acid used. Adsorbent recovery after adsorption was determined to be possible, however further studies on performance loss following thermal recovery should be performed. The high packing efficiency of the TPB-DCM/TMOF adsorbent bed resulted in very high backpressures during RSSCTs and controlling the particle size distribution or casting the adsorbent onto a solid support, may both be investigated to address this problem. Finally, the use of TPB-HCPs as industrial adsorbents would necessitate further analytical experiments to assess adsorbent performance using real water samples of various organic and ionic contents. Further assessment on the environmental impact of the TPB synthesis and subsequent polymerisation route should also be performed and compared to the manufacture route of currently used adsorbents.

4.2 Inorganic pollutant removal: Pb (II)

HCPs derived from the TPB, tryp & DBMP aromatic units were sulfonated using two different synthetic routes, a softer ASA method, in the presence of a swelling solvent at 65 °C and using SA-TfA in the absence of swelling solvent at 250 °C. The much higher IECs achieved during SA-TfA modification, were found to significantly enhance Pb^{2+} uptake capacities, as determined from batch studies. Analysis of SS ^{13}C-NMR spectra confirmed successful sulfonation for both routes, with the harsh conditions of SA-TfA modification resulting in oxidation of linking and nonlinking alkyl units to various functionalities including ketones and carboxylic acids, confirmed by the appearance of bands in the region 160-200 ppm and simultaneous disappearance of resonances in the region 10-80 ppm. IR spectroscopy revealed multiple bands originating from sulfonic acid groups, 605 cm^{-1}, 906 cm^{-1}, 1032 cm^{-1}, 1172 cm^{-1}, 1228 cm^{-1}, in addition to oxidised alkyl functionalities in the region 1550-1730 cm^{-1}. Complex hydration shells consisting of water network clusters, were also observed for all sulfonated materials. Although counterintuitive, TGA showed that increases in functionalisation were associated with reduced water uptake, likely due to higher interactions between adjacent groups and pore size reductions which may disfavour intraparticle moisture diffusion. Higher levels of hydration were found to reduce the thermal stability of the ASA-modified polymers and particularly in the case of tryp-DCM/ASA, due to the strongly bound chemisorbed water which allowed the sulfonic acid moieties to remain deprotonated at temperatures approaching sulfonate degradation onset. The N_2 adsorption properties, and in consequence S_{BET}, V_{micro} & V_{total} were generally found dramatically decrease with increasing functionalisation, while CO_2 uptake increased with moderate sulfonation and decreased when high degrees of functionalisation resulted in severely compromised S_{BET}. An anomaly to this trend was observed for sulfonated analogues of tryp-DCM, with the ASA method resulting in lower gas uptake properties compared to SA-TfA, despite the much higher IEC of the latter. This was attributed to a very high binding strength of chemisorbed water in tryp-DCM/ASA, which could not be removed under conditions of drying and degassing, therefore exerting pore-filling effects. The high relative intensity of

the 1165 cm^{-1} band, corresponding to SO_2 symmetric stretching, with respect to 1250 cm^{-1} which corresponds to SO_3^- symmetric vibrations, suggests a high presence of sulfone bridges introduced during sulfonation with ASA. Sulfone crosslinking may be responsible for reducing material pore size, resulting in a pore structure with high hydration enthalpy.

All SA-TfA modified materials demonstrated similar affinities for Pb^{2+} in batch equilibrium studies, with a DBMP-DCM/SA-TfA achieving a slightly higher capacity than TPB-DCM/SA-TfA & tryp-DCM/SA-TfA. This may suggest that the adsorption properties of the network are more dependent on the distribution and number of functional groups, rather than the morphologies of the parent networks. At initial concentration C_0= 160 mg L^{-1} & adsorbent dose 1 mg mL^{-1}, the adsorbent DBMP-DCM/SA-TfA achieved an excellent capacity of 142.1 mg g^{-1}. Studies on the Pb^{2+}-form of DBMP-DCM/SA-TfA, demonstrated a reduced thermal stability upon Pb^{2+} binding, similar to the highly hydrated sulfonated adsorbents, and was therefore attributed to the higher presence of $-SO_3^-$ functionalities which formed upon ion exchange. The IR spectrum of the Pb^{2+}-form shows band splitting, due to the removal of degeneracy originating from asymmetric Pb^{2+} coordination, in addition to significant wavenumber shifts in sulfonic acid and carbonyl-based oxidised linking units, which suggest strong interactions between Pb^{2+} ions and the abundant oscillating functionalities. Modelling and statistical analysis of the experimental solution isotherm dataset obtained for DBMP-DCM/SA-TfA, at pH= 7.4, reveals satisfactory agreement with the nonlinear Langmuir model, with q_{max}= 148.19 ± 3.47 mg g^{-1} & K_L= 1.6 ± 0.19 L mg^{-1} being indicative of remarkable adsorption properties, and R_L approaching zero demonstrating the occurrence of an irreversible chemisorption process. Better fitting characteristics were obtained from the solubility-normalised D-A model, which showed high heterogeneity with n= 6.55 ± 0.4 and with the estimated energy of adsorption, E = 24.3 ± 3 KJ mol^{-1}, showing that Pb^{2+} uptake relies predominantly on chemisorption.

The sulfonated PIMs EA-TB/ASA in H^+-form & PIM-SBF/TMSCS in K^+-form were also found to display significant Pb^{2+} uptake properties, with the latter demonstrating a similar capacity to the SA-TfA HCPs,

despite a much lower IEC. Further investigations are required to explain PIM-SBF/TMSCS's exceptional Pb^{2+} affinity.

Despite the great popularity of sulfonated adsorbents as ion-exchanging materials, there are many aspects of the sulfonation modification that remain unexplored. Experimental data discussed herein suggests that the novel high temperature sulfonation approach based on SA-TfA in the absence of swelling solvent may have a high potential in the production of ion-exchangers for water purification from heavy metals. Future work should focus on determining the overall effect of TfA and whether it plays a role in alkyl linking unit oxidation, optimisation of reaction time, temperature, in addition to the sulfonation mixture: solid ratio. Further characterisation is required to provide information on the types of functionalities that arise during SA-TfA modification, such as the ring-chain tautomerisation of beta-ketoaryl sulfonic acid to form the cyclic tautomer, and the effect of those in the overall network morphology and metal uptake properties.

Assessing the potential of DBMP-DCM/SA-TfA in metal uptake by ion exchange necessitates further analytical experiments including pH dependence, ionic strength dependence, RSSCTs and kinetic experiments. The latter is of particular importance as slow bulk diffusion processes are a primary reason for the frequent preference of macroporous sulfonated resins. It is thought that the SA-TfA method in the absence of solvent is only suitable for sulfonation of adsorbents with small particle size, as the bulk diffusion pathways of the highly polar sulfonation mixture reduce with decreasing particle diameter. In addition to better sulfonation efficiency, a narrow particle size may reduce the requirement for meso and microporosities during the adsorption process. The solvent-free high temperature SA-TfA route should also be performed on adsorbents of different pore size distributions and crosslinking densities, to investigate the overall effects on material morphology and how it is affected by the oxidation of linking units. Modification of rigid multi-alkylated HCPs may also represent an efficient post-polymerisation approach to introduce an abundance of carbonyl-based polar functionalities, overcoming the pre-polymerisation functionalisation problems associated with the formation of Lewis

acid-base pairs during polymerisation. Finally, owing to the excellent CO_2 uptake properties of sulfonated HCPs, further gas uptake experiments should be performed at various temperatures to investigate the heat of CO_2 adsorption. The work presented herein describes highly sulfonated HCPs as excellent materials for the removal of ions; however, their potential for reusability following ion exchange was not investigated. Future work should focus on assessing material reusability by washing with strong acids to test whether lead can be exchanged for hydrogen ions, facilitating material regeneration. Furthermore, the SA-TfA sulfonation synthesis is easy to perform but suffers from extensive use of toxic reagents at high temperature, and the associated hazards and environmental impact should be further assessed.

4.3 Metaldehyde degradation using sulfonated HCPs

The acidic nature of the sulfonated adsorbents TPB-DCM/ASA & TPB-DCM/SA-TfA was found to facilitate the depolymerisation of metaldehyde into a diversity of different products. GC-MS analysis showed that TPB-DCM/ASA was more effective in metaldehyde degradation compared to TPB-DCM/SA-TfA, confirming that the presence of meso and macropores are of particular importance in the case of metaldehyde. A combination of GC-MS and NMR analyses show that TPB-DCM/ASA catalyses the degradation to acetaldehyde, which exists in equilibrium with its hydrated form, MMG-1, and undergoes aldol condensation to form acetaldol. Further dehydration may form crotonaldehyde. During initial stages of the degradation experiment, paraldehyde forms as a side product, but is also degraded at contact times approaching 7 days. During this period, NMR analysis confirmed the presence of oxidised products such as CO_2, acetic acid and formic acid, as well as reduced products, such as olefins and methane. Those are suggestive of the simultaneous occurrence of reduction and oxidation reactions. The conversion of acetaldehyde to such products has been previously reported for heterogeneously catalysed gas phase systems, and the high complexity of the process requires further investigation. The metaldehyde degradation kinetics were found to be slow, due to inefficient diffusion

of metaldehyde to the catalytic sites, in addition to the high occupancy of those sites by the abundance of products originating from acetaldehyde conversion. The high catalytic activity of sulfonated adsorbents, in combination with the versatile reactivity of acetaldehyde, likely present difficulties concerning the implementation of such systems in industrial applications. The strong ion-exchanging performance would also introduce additional problems if environmental water samples were to be used.

Nevertheless, the high catalytic activity of TPB-DCM/ASA should be further investigated. This would require individual examination of the catalytic steps, and the use of ^{13}C-labelled acetaldehyde may provide valuable information on the relevant degradation pathways. Importantly, the presence of solution-suspended TPB-DCM/ASA did not result in NMR spectrum line broadening, owing to its small particle size and hydrophilicity, which favour the formation of a homogeneous aqueous suspension. It is therefore suggested that NMR spectroscopy may be a suitable technique to study adsorption and heterogeneous catalytic processes, therefore providing access to easily obtainable kinetic and thermodynamic data. Research efforts should focus on the optimisation of the spinning rate, to ensure sufficient mixing during spectrum acquisition. Additionally, the described method of sonication of deuterated solvent-polymer suspension, prior to the volumetric addition to the NMR tube, should be evaluated as a reproducible and accurate way of adding miniscule amounts of solid.

The compatibility of the TPB-DCM/ASA with NMR spectroscopy, could additionally allow for the development of pore informative methods by the selection of an appropriate molecular probe. For instance, the formation of methane clathrates in the presence of water and under high pressure conditions, has been previously explored as a method of extracting pore size information, based on chemical shift changes. It is likely that a similar system could produce valuable pore information for TPB-DCM/ASA, in aqueous solutions saturated with methane. This could be particularly useful, as there are no robust methods of pore size characterisation of polymers in their solvent-swollen state, and the inadequacy of gas adsorption data to give pore size information on solution adsorbents of high polarity

is a well-known research problem. Finally, with reference to the wide diversity of products observed in GC-MS and NMR analyses, the catalytic activity observed within the highly polarised and confined micropore environment of TPB-DCM/ASA should be investigated for other types of catalytic conversions.

5. Experimental

5.1 Materials and methods

5.1.1 Materials

Anhydrous aluminium chloride (Alfa Aesar 99%), triptycene (Aldrich 98%), triphenylene (Aldrich 98%), 1,3,5-triphenylbenzene (Alfa Aesar 99%), hexaphenylbenzene (Aldrich 98%), 9,10-diphenylanthracene (Fluka 98%), Powdered Activated Charcoal (DARCORTM, -100 mesh powder, Sigma Aldrich), Granular Activated Carbon (General purpose, Fischer), metaldehyde (Acros 99%), dichloroethane (DCE, Fisher HPLC grade), dichloromethane (DCM; Fisher HPLC grade), chloroform ($CHCl_3$ Fisher HPLC grade), dimethoxymethane (Sigma Aldrich, 99%) tetrahydrofuran (THF, VWR Chemical), methanol (Fisher) and ethanol (VWR Chemical) were all used as received. Silicon tetrachloride, Lead (II) nitrate (99%, VWR Chemical), 2-methoxyacetophenone (98%, Sigma Aldrich), 2-fluoroacetophenone (98%, VWR Chemical), norbornadiene (98%, VWR Chemical), Sulfuric acid (98% wt, Sigma Aldrich) triflic anhydride (98%, Fluorochem), anthracene, amyl nitrite (97%, Alfa Aesar), anthranilic acid (90 %, VWR Chemical), boron tribromide (98%, Fisher) were used as received. Trimethyl orthoformate (Sigma Aldrich, 99%), tetramethyl orthocarbonate (99%, Sigma Aldrich). Isolute ENV+ 6 mL/150 mg (Biotage) and a VacMaster® manifold were used for Solid Phase Extraction. Syringe filters (PTFE, 0.45 µm, Milex-CR) were purchased from Merck and were used as received. Column chromatography was performed over silica gel (pore size 60 Å, particle size 40-63 µm), as the stationary phase.

5.1.2 Characterization methods

^{1}H NMR, ^{19}F NMR and ^{13}C NMR spectra were recorded on a Bruker PRO500 (500MHz) spectrometer. ^{1}H NMR and ^{13}C NMR spectra were referenced to tetramethylsilane and ^{19}F NMR was referenced to BF_3-.Et_2O. All spectra were recorded at temperature T= 300 K. Mass spectroscopy was performed using a Bruker micrOTOF instrument equipped with an EI source. GC-MS analysis was performed on a Shimadzu QP2010 SE, equipped with a single quadrupole mass analyser. Thermogravimetric analysis was performed using a TA Instruments, model SDT Q600 Analyzer. Nitrogen adsorption/desorption (77 K) and CO_2 adsorption (273 K) isotherms were measured using a Quadrasorb Evo instrument. MAS ^{13}C NMR was preformed using a AVA300, at 76 Hz and referenced to adamantane. The spin rate was set to 12000 Hz, and the spinning bands appeared at -40 & 303 ppm. Sample preparation was performed by packing into 3.2 mm rotors (purchased from Bruker). ICP-OES analysis was performed using a a Perkin Elmer Optima 8300 DV, at a RF forward power of 1500 W, with Ar gas flows of 10, 0.2 and 0.6 L min^{-1} for plasma, auxiliary, and nebuliser flows, respectively. Aqueous sample solutions were taken up into a Gem Tip cross-Flow and Scotts spray chamber nebuliser, at a rate of 1.50 mL min^{-1}, using a peristaltic pump. Infrared adsorption spectra were recorded using a Perkin-Elmer 660 plus FT-IR spectrophotometer. Melting points were determined using a Gallenkamp Melting Point apparatus.

5.1.3 Modelling of experimental data

Isotherm experimental nonlinear regression was performed on Origin® 2018 software, using the built-in functions: LangmuirEXT1(x,a,b,c) and FreundlichEXT(x,a,b,c), with fixed c = 0. The D-R model was obtained using the Allometric1 built-in function and the D-A parameters were obtained upon linearisation. Modelling of kinetic data using the PSO & PFO models was performed on MATLAB software, using scripts present in Appendices (section 7.1).

5.2 Synthetic procedures

5.2.1 Monomer syntheses

5.2.1.1 Synthesis of 1,3,5-tris-(2-methoxyphenyl) benzene

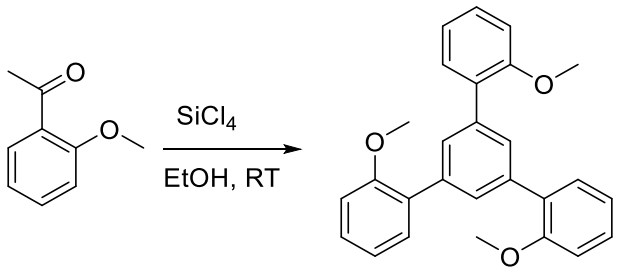

A reaction flask was charged with 2-methoxyacetophenone (2.5 g, 16.65 mmol) and anhydrous ethanol (50 mL). Silicon tetrachloride (5 eq, 14.14 g) was added dropwise at room temperature. The reaction was left to stir for 4 hrs and was quenched using water. The reaction mixture was extracted using DCM (3x 50 mL). The combined extracts were dried using anhydrous magnesium sulphate and the solvent was evaporated under reduced pressure to yield the crude product. Recrystallization from methanol yielded white crystals of 1,3,5-tris-(2-methoxyphenyl) benzene in 67% yield. ^{1}H NMR (500 MHz, Chloroform-d) δ 7.75 (s, 3H), 7.49 (dd, J = 7.5, 1.8 Hz, 3H), 7.37 (ddd, J = 8.2, 7.4, 1.8 Hz, 3H), 7.09 (td, J = 7.5, 1.1 Hz, 3H), 7.04 (dd, J = 8.2, 1.1 Hz, 3H), 3.87 (s, 9H).^{13}C NMR (126 MHz, Chloroform-d) δ 156.77, 137.83, 131.29, 131.10, 129.66, 128.56, 120.89, 111.32, 55.69. mp = 193 °C.

5.2.1.2 Synthesis of 1,3,5-tris-(2-hydroxylphenyl) benzene

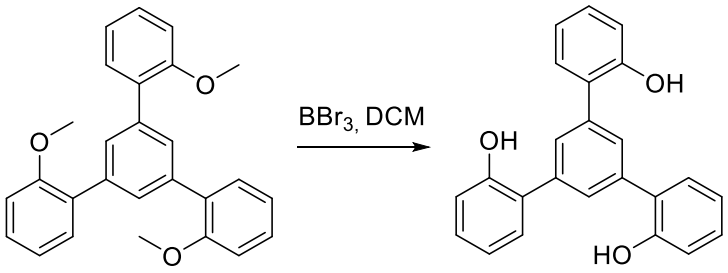

1,3,5-tris-(2-methoxyphenyl) benzene (3 g, 7.57 mmol) was added into a RBF together with anhydrous DCM (60 mL) and BBr_3 (3.2 eq, 5.687 g) was added. The reaction mixture was stirred at reflux for 3 hrs and then was quenched using water and extracted using ethyl acetate (3 x 50 mL). The organic extracts were dried using anhydrous magnesium sulphate and the solvent was evaporated under reduced pressure. The crude product was recrystallized from an isopropanol: water mixture to yield tris-(2hydroxyphenyl) benzene as a white powder in 82% yield. ^{1}H NMR (500 MHz, Acetone-d6) δ 8.21 (s, 3H), 7.78 (s, 3H), 7.43 (dd, J = 7.6, 1.7 Hz, 3H), 7.25 – 7.16 (m, 3H), 7.02 (dd, J = 8.1, 1.2 Hz, 3H), 6.96 (td, J = 7.5, 1.2 Hz, 3H).^{13}C NMR (126 MHz, Acetone-d6) δ 155.11, 139.27, 131.56 , 129.66 , 129.54 , 129.43 , 120.97 , 117.14 . Mp.= 213 °C.

5.2.1.3 Synthesis of 1,3,5-tris-(2-fluorophenyl) benzene

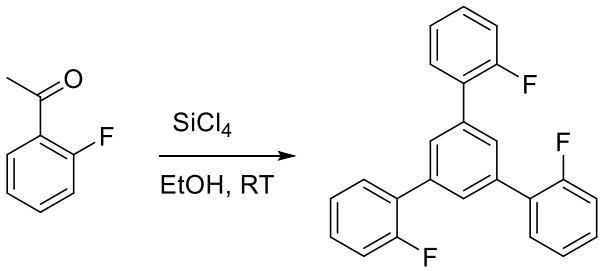

1,3,5-tris-(2-fluorophenyl) benzene was synthesized based on the procedure described in the procedure 2.2.1. The compound was purified by recrystallization from methanol to give white crystals of tris-(2-fluorophenyl) benzene in 69% yield. ^{1}H NMR (400 MHz, Chloroform-*d*) δ 7.75 (q, *J* = 1.1 Hz, 3H), 7.55 (td, *J* = 7.7, 1.8 Hz, 3H), 7.35 (dddd, *J* = 8.2, 7.4, 5.0, 1.8 Hz, 3H), 7.27 – 7.23 (m, 3H), 7.23 – 7.16 (m, 3H).^{19}F NMR (376 MHz, Chloroform-d) δ -117.68 .13C NMR (101 MHz, Chloroform-d) δ 161.07 , 158.61 , 136.20 , 130.91 (d, J = 3.4 Hz), 129.77 – 127.89 (m), 124.44 (d, J = 3.8 Hz), 116.18 (d, J = 22.7 Hz).^{13}C NMR (101 MHz, Chloroform-d) δ 161.07 , 158.61 , 136.20 , 130.91 (d, J = 3.4 Hz), 129.27 (d, J = 8.3 Hz), 129.04 (t, J = 2.9 Hz), 128.64 (d, J = 13.5 Hz), 124.44 (d, J = 3.8 Hz), 116.18 (d, J = 22.7 Hz). Mp.=135 °C.

5.2.1.4 Synthesis of tryp

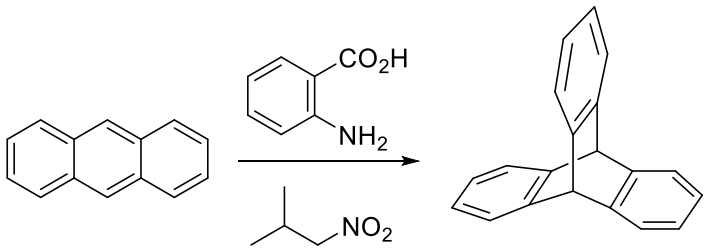

Anthracene (50 g, 0.39 mol) was dissolved in DCE and a solution of amyl nitrite (20.93 g, 0.179 mol) in THF and anthranilic acid (80 g, 0.583) in THF (200 mL) were added simultaneously at *approx.* the same rate over 1 hr. The mixture was refluxed overnight, and the solvent was removed. The residual solid was dissolved in toluene, maleic anhydride was added, and the mixture was refluxed for 6 hr. An aqueous solution of sodium hydroxide was added dropwise, and the mixture was allowed to cool, and the organic layer was separated, dried over $MgSO_4$ and the solvent was removed under reduced pressure. The residual solid was recrystallised from EtOH to obtain white crystals of triptycene (3.1 g, 0.012 mol) in 7 % yield. ^{1}H NMR (400 MHz, Chloroform-*d*) δ 7.47 (dd, *J* = 5.3, 3.2 Hz, 6H), 7.07 (dd, *J* = 5.3, 3.2 Hz, 6H), 5.51 (s, 2H). ^{13}C NMR (101 MHz, Chloroform-*d*) δ 145.40, 125.26, 123.72, 54.23.

5.2.1.5 Synthesis of DBMP

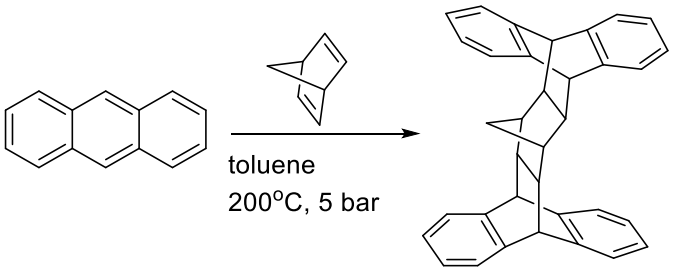

Anthracene (30 g, 168.3 mmol) and norbornadiene (54.4 g, 590.4 mmol) were added to a high pressure reactor vial and were heated to 200°C, with the pressure reaching *approx.* 5 bar. The reaction was heated for 8 hrs and the heat was turned off to allow the reaction mixture to cool overnight. The mixture was extracted using chloroform and the pure product was purified using column chromatography with hexane used as the eluent. ^{1}H NMR (400 MHz, Chloroform-*d*) δ 7.22 (m, *J* = 5.3, 3.2 Hz, 4H), 7.09 (m, *J* = 11.2, 5.4, 3.2 Hz, 8H), 7.03 (m, *J* = 5.3, 3.2 Hz, 4H), 4.21 (s, *J* = 1.3 Hz, 4H), 1.97 (d, *J* = 1.5 Hz, 2H), 1.77 (t, *J* = 1.4 Hz, 4H), -0.90 (s, 2H). ^{13}C NMR (101 MHz, Chloroform-*d*) δ 144.96, 142.34, 125.88, 125.50, 124.07, 123.12, 51.01, 48.47, 43.35, 27.37.

5.2.2 Polymer syntheses

5.2.2.1 General procedure for HCP synthesis: TPB-DCE/DMM

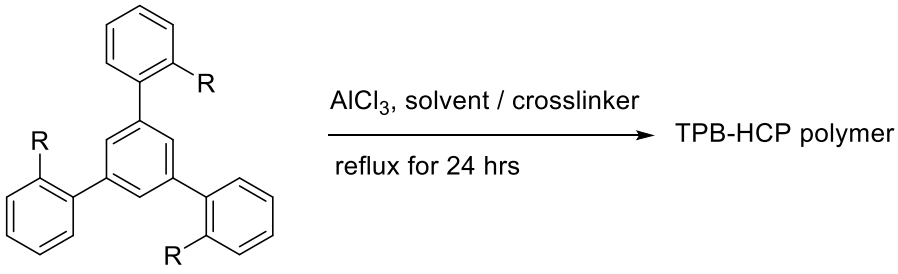

To a flask containing a solution of 1,3,5-triphenylbenzene (1.51 g, 4.9 mmol) and dimethoxymethane (1.72 g, 22.0 mmol, 4.5 eq), in DCE (80 mL), was added anhydrous aluminium chloride (4.9 g, 36.8 mmol, 7.5 eq). The mixture was refluxed for 24 hrs and the resulting polymer was collected by filtration and washed with water followed by ethanol. The polymer was then refluxed sequentially in the following

solvents for 6 hrs: ethanol, $CHCl_3$, THF, acetone and methanol. Yield= 110%. N_2 adsorption (77 K): SA_{BET} = 1399 m^2 g^{-1}, total pore volume = 1.5 ml g^{-1}; CO_2 adsorption at 273 K/1 bar = 2.82 mmol g^{-1} ; Al^{3+} content: 0.09%; TGA: thermal degradation commences at 290 °C.

5.2.2.2 TPB-DCM

Using the general procedure, a polymer was obtained from 1,3,5-triphenylbenzene (1.51, 4.9 mmol), DCM (40 mL), dimethoxymethane (1.72 g, 22.0 mmol, 4.5 eq) and $AlCl_3$ (4.9 g, 36.8 mmol, 7.5 eq). Yield= 107 %, N_2 adsorption (77 K): SA_{BET} = 2082 m^2 g^{-1}, total pore volume = 1.2 ml g^{-1}; CO_2 adsorption at 273 K/1 bar = 4.27 mmol g^{-1}. Al^{3+} content: 2.34%; TGA: thermal degradation commences at 270 °C.

5.2.2.3 TPB-DCM/DMM

Using the general procedure, a polymer was obtained from 1,3,5-triphenylbenzene (1.51, 4.9 mmol), DCM (40 mL), dimethoxymethane (1.72 g, 22.0 mmol, 4.5 eq) and $AlCl_3$ (4.9 g, 36.8 mmol, 7.46 eq). Yield= 109%; N_2 adsorption (77 K): SA_{BET} = 1365 m^2 g^{-1}, total pore volume = 1.1 ml g^{-1} ; CO_2 adsorption at 273 K/1 bar = 3.41 mmol g^{-1}, Al^{3+} content: 0.01%; TGA: thermal degradation commences at 280 °C.

5.2.2.4 TPB-DCM/TMOF

Using the general procedure, a polymer was obtained from 1,3,5-triphenylbenzene (1.51, 4.93 mmol), DCM (40 mL), TMOF (1.57 g, 14.79 mmol) and $AlCl_3$ (4.9 g, 36.8 mmol, 7.46 eq) Yield= 109%, N_2 adsorption (77 K): SA_{BET} = 1308 m^2 g^{-1}, total pore volume = 1.9 ml g^{-1} ; CO_2 adsorption at 273 K/1 bar = 3.4 mmol g^{-1}, Al^{3+} content: 0.02%; TGA: thermal degradation commences at 280 °C.

5.2.2.5 TPB-DCM/TMOC

Using the general procedure, a polymer was obtained from 1,3,5-triphenylbenzene (1.51, 4.9 mmol), DCM (40 mL), TMOC (1.54 g, 11.34 mmol) and $AlCl_3$ (4.9 g, 36.8 mmol, 7.46 eq) Yield= 109%, N_2 adsorption (77 K): SA_{BET} = 1300 m^2 g^{-1}, total pore volume = 1.9 ml g^{-1} ; CO_2 adsorption at 273 K/1 bar = 3.36 mmol g^{-1}; Al^{3+} content: 0.1%; TGA: thermal degradation commences at 290 °C.

5.2.2.6 TPB-NB/DMM

Using the general procedure, a polymer was obtained from 1,3,5-triphenylbenzene (0.21 g, 0.69 mmol), NB (40 mL), DMM (0.235 g, 3.08 mmol) and $FeCl_3$ (0.83 g, 5.12 mmol) Yield= 109%, N_2 adsorption (77 K): SA_{BET} = 1426 m^2 g^{-1}, total pore volume = 1.8 ml g^{-1}; CO_2 adsorption at 273 K/1 bar = 2.46 mmol g^{-1}; Fe^{3+} content: 1.3%; TGA: thermal degradation commences at 280 °C.

5.2.2.7 (TPB-F)-DCE/DMM

Using the general procedure, a polymer was obtained from 1,3,5-tris-(2-fluorophenyl) benzene (1 g, 2.77 mmol) DCE (55 mL), DMM (0.95 g, 12.5 mmol, 4.5 eq) and $AlCl_3$ (2.76 g, 2.07 mmol, 7.46 eq). Yield = 102%, N_2 adsorption (77 K): SA_{BET} = 1510 m^2 g^{-1}, total pore volume = 2.15 ml g^{-1}; CO_2 adsorption at 273 K/1 bar = 2.15 mmol g^{-1}; Al^{3+} content: 1.3 %; TGA: thermal degradation commences at 290 °C.

5.2.2.8 (TPB-OMe)-DCE/DMM

Using the general procedure, a polymer was obtained from 1,3,5-tris-(2-methoxyphenyl) benzene (0.7g, 1.77 mmol), DCE (40 mL), DMM (0.60 g, 7.97 mmol, 4.5 eq) and $AlCl_3$ (1.76 g, 13.27 mmol, 7.46 eq). Yield= 99%, N_2 adsorption (77 K): SA_{BET} = 801 m^2 g^{-1}, total pore volume = 1.52 ml g^{-1}; CO_2 adsorption at 273 K/1 bar = 2.1 mmol g^{-1}. Al^{3+} content: 0.17%; TGA: thermal degradation commences at 280°C.

5.2.2.9 (TPB-OMe)-DCE/DMM

Using the general procedure, a polymer was obtained from 1,3,5-tris-(2-hydroxylphenyl) benzene (0.3 g, 0.85 mmol) DCE (30 mL), dimethoxymethane (0.3 g, 3.94 mmol, 4.5 eq) and $AlCl_3$ (0.85 g, 13.27 mmol, 7.46 eq). Yield = 106% ; N_2 adsorption (77 K): SA_{BET} = 673 m^2 g^{-1}, total pore volume = 0.67 ml g^{-1}; CO_2 adsorption at 273 K/1 bar = 1.83 mmol g^{-1}; Al^{3+} content: 0.07%; TGA: thermal degradation commences at 280°C.

5.2.2.10 tryp-DCM

Using the general procedure, a polymer was obtained from 1,3,5-tris-(2-hydroxylphenyl) benzene (0.3g, 0.85 mmol) DCM (30 mL), dimethoxymethane (0.3 g, 3.94 mmol, 4.5 eq) and $AlCl_3$ (0.85 g, 13.27 mmol, 7.46 eq). Yield = 106% N_2 adsorption (77 K): SA_{BET} = 673 m^2 g^{-1}, total pore volume = 0.67 ml g^{-1}; CO_2 adsorption at 273 K/1 bar = 1.83 mmol g^{-1}.

5.2.2.11 DBMP-DCM

Using the general procedure, a polymer was obtained from DBMP (1.5 g, 3.34 mmol), DCM (30 mL) and $AlCl_3$ (4.5 g, 24.9 mmol, 7.46 eq). Yield = 110% N_2 adsorption (77 K): SA_{BET} = 1398 m^2 g^{-1}, total pore volume = 0.85 ml g^{-1}; CO_2 adsorption at 273 K/1 bar = 2.42 mmol g^{-1}. Al^{3+} content: 0.1%; TGA: thermal degradation commences at 270 °C.

5.2.3 Synthesis of the nanocomposite Fe_3O_4@TPB-HCP

(i) Functionalisation of superparamagnetic iron oxide nanoparticles

Magnetite particles were dispersed in dry DCM and were sonicated for 30 min. The solution was then continuously stirred under sonication and 3-chloropropyltriethoxysilane (0.96 g, 4 mmol) was added dropwise. Sonication was continued for 2 hr and the suspension was left to stir overnight. The particles were collected using a magnet and were washed thrice with DCM then MeOH. The functionalised particles were dried under vacuum and stored under a nitrogen atmosphere.

(ii) Synthesis of a TPB-based magnetic nanocomposite

Functionalised iron oxide nanoparticles were dispersed in nitrobenzene under sonication for 1 hr. Iron (III) chloride (0.83 g, 5.12 mmol) was added and the sonication was continued for 20 mins before a mixture of dimethoxymethane (0.235 g, 3.08 mmol) and TPB (0.21 g, 0.69 mmol) in nitrobenzene (6

mL) was added over 2 hr at 50 °C. Sonication was continued for 30 min after addition and was then turned off and the reaction mixture was stirred at 75 °C overnight. The composite was collected using a magnet, refluxed in methanol and dried. Yield = 106% N_2 adsorption (77 K): SA_{BET} = 673 m^2 g^{-1}, total pore volume = 0.67 ml g^{-1}; CO_2 adsorption at 273 K/1 bar = 1.83 mmol g^{-1}.

5.2.4 Post-polymerisation modifications: ASA

5.2.4.1 General procedure

(i) Synthesis of ASA

Acetylsulfuric acid was generated *in situ* by the dropwise addition of sulfuric acid (8.2 ml, 97 wt.%) to an ice- chilled solution of acetic anhydride (22.8 mL) in DCE (120 mL) with vigorous stirring. The mixture was allowed to phase separate, and the bottom acid layer was obtained and stirred under vacuum to remove excess solvent.

(ii) Surface modification of HCPs using ASA

A dry sample of HCP (0.5 g) was left to swell in DCE (5 mL) for 2h at room temperature. The suspension was heated to 65°C and ASA was added dropwise with stirring. The mixture was heated for 2h and then filtered to recover the polymer which was washed thrice with water followed by acetone and methanol. The modified polymer was refluxed in MeOH overnight, filtered and dried under vacuum.

5.2.4.2 TPB-DCM/ASA

Using the general procedure, a polymer was obtained from TPB-DCM (0.5 g), in DCE (7 mL) & ASA (0.5 mL); Yield = 115%; N_2 adsorption (77 K): SA_{BET} = 1364 m^2 g^{-1}, total pore volume = 0.68 ml g^{-1}; CO_2 adsorption at 273 K/1 bar = 4.93 mmol g^{-1}; IEC = 3.04 ± 0.02 mmol g^{-1}; MAS ^{13}C NMR (76 MHz) δ (ppm): 139.47, 130.9, 125.9, 64.78, 34.45, 12.22; ν_{max} (cm^{-1}): 2962, 2860, 1730, 1674, 1504, 1051, 1007; TGA: thermal degradation commences at 280°C.

5.2.4.3 tryp-DCM/ASA

Using the general procedure, a polymer was obtained from tryp-DCM (0.5 g), in DCE (7 mL) & ASA (0.5 mL); Yield = 110 % N_2 adsorption (77 K): SA_{BET} = 515 m^2 g^{-1}, total pore volume = 0.26 ml g^{-1}; CO_2 adsorption at 273 K/1 bar = 2.75 mmol g^{-1}; IEC = 2.86 ± 0.01 mmol g^{-1}; MAS ^{13}C NMR (76 MHz) δ (ppm): 183.6, 169.04, 138.61, 129.19, 49.34, 35.00, 15.07; IR: ν_{max} (cm^{-1}): 2357, 1713, 1655, 1591, 1402, 1252, 1160, 1034, 862, 573; TGA: thermal degradation commences at 225°C.

5.2.4.4 DBMP-DCM/ASA

Using the general procedure, a polymer was obtained from tryp-DCM (0.5 g), DCE (7 mL) & ASA (0.5 mL); Yield = 106% N_2 adsorption (77 K): SA_{BET} = 1319 m^2 g^{-1}, total pore volume = 0.76 ml g^{-1}; CO_2 adsorption at 273 K/1 bar = 2.8 mmol g^{-1}; IEC = 1.34 ± 0.02 mmol g^{-1}; MAS ^{13}C NMR (76 MHz) δ (ppm): 141.91, 123.63, 72.31, 63.01 48.89, 43.21, 26.29.; IR: ν_{max} (cm^{-1}): 2924, 2158, 1732, 1223, 1184, 1015, 897, 576; TGA: thermal degradation commences at 315°C.

5.2.4.4 EA-TB/ASA

Using the general procedure, a polymer was obtained from EA-TB (0.5 g), DCE (7 mL) & ASA (0.5 mL), the polymer was initially soluble in DCE and precipitated over the course of the modification reaction.; Yield = 106% N_2 adsorption (77 K): SA_{BET} = 0 m^2 g^{-1}, total pore volume = 0.76 ml g^{-1}; CO_2 adsorption at 273 K/1 bar = 2.8 mmol g^{-1}; IEC = 1.34 ± 0.02 mmol g^{-1}; ^1H NMR (400 MHz, DMSO-d_6) δ 8.2—6.6 (m), 5.8- 3.46 (m), 2.5- 0.6 (m).; IR: ν_{max} (cm^{-1}): 2953, 2893, 1450, 1439, 1375, 1371, 1306, 1248, 1209, 1732, 1223, 1144, 1084, 955, 766, 563; TGA: thermal degradation commences at 280°C.

5.2.5 Post-polymerisation modifications: SA-TfA

5.2.5.1 General procedure

(i) Synthesis of SA-TfA

SA/TfA sulphonating agent was generated *in situ* by the dropwise addition of sulfuric acid (2.11 mL, 97 wt.%) to an ice- chilled solution of triflic anhydride (10.6 g) in DCE (20 mL) with vigorous stirring. The mixture was stirred at room temperature overnight and was allowed to phase separate. The bottom acid layer was obtained, washed with DCE and stirred under vacuum to remove excess solvent.

(ii) Surface modification of HCPs

A dry sample of HCP (0.5 g) was added directly to the SA-TfA mixture (10 mL). The suspension was stirred for 30 mins at room temperature and was heated to 250 °C for 2 hrs, was poured into water and filtered. The modified adsorbent was washed with water and then MeOH and was refluxed in water and MeOH overnight and dried under vacuum.

5.2.5.2 TPB-DCM/SA-TfA

Using the general procedure, a polymer was obtained from TPB-DCM (0.5 g), and SA-TfA (10 mL); Yield = 115%; N_2 adsorption (77 K): SA_{BET} = 420 m^2 g^{-1}, total pore volume = 0.21 ml g^{-1}; CO_2 adsorption at 273 K/1 bar = 2.1 mmol g^{-1}; IEC = 6.5 ± 0.13 mmol g^{-1}; MAS ^{13}C NMR (76 MHz,) δ (ppm) 189.7, 166.53, 158.03, 146.24, 133.25, 52.18; ν_{max} (cm^{-1}): 2972, 2353, 1709, 1602, 1217, 1130, 1025, 893, 611; TGA: thermal degradation commences at 335 °C.

5.2.5.3 tryp-DCM/SA-TfA

Using the general procedure, a polymer was obtained from tryp-DCM (0.5 g), and SA-TfA (10 mL); Yield = 115%; N_2 adsorption (77 K): SA_{BET} = 710 m^2 g^{-1}, total pore volume = 0.26 ml g^{-1}; CO_2 adsorption at 273 K/1 bar = 4.15 mmol g^{-1}; IEC = 4.15 ± 0.01 mmol g^{-1}; MAS ^{13}C NMR (76 MHz) δ (ppm) 195.6,

182.63, 167.8, 146.75, 130.33, 51.40; ν_{max} (cm^{-1}): 2974, 2361, 1699, 1672, 1597, 1242, 1257, 1173, 1032, 897, 613; TGA: thermal degradation commences at 335 °C.

5.2.5.4 DBMP-DCM/SA-TfA

Using the general procedure, a polymer was obtained from TPB-DCM (0.5 g), and SA-TfA (10 mL); Yield = 115%; N_2 adsorption (77 K): SA_{BET} = 245 m^2 g^{-1}, total pore volume = 0.15 ml g^{-1}; CO_2 adsorption at 273 K/1 bar = 2.01 mmol g^{-1}; MAS ^{13}C NMR (76 MHz) δ (ppm) 181.03, 167.8, 150.27, 130.27, 49.09.; ν_{max} (cm^{-1}): 1722, 1678, 1593, 1236, 1180, 1032, 903, 635; TGA: thermal degradation commences at 290 °C.

5.2.6 PIM-SBF/TMSCS (K^+-form)

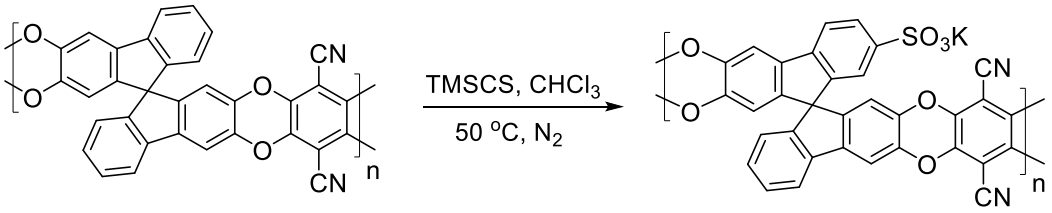

Trimethylsilyl chlorosulfonate (TMSCS, 1.54 mL, 10 mmol) in anhydrous chloroform (5 mL) was added drop-wise to a solution of PIM-SBF polymer (1.0 g, 2.00 mmol) in anhydrous chloroform (30 mL), under inert atmosphere. The mixture was stirred at 50 °C, to form a brown precipitate. After heating for 24 hrs, the mixture was poured in methanol and filtered. The powder was stirred vigorously in aqueous ammonium hydroxide solution (100 mL). Ion exchange in aqueous KCl (1 M) was performed thrice, and the final filtered product was washed thoroughly with deionised water, filtered, and then dried in a vacuum oven at 110 °C for 12h to afford the desired sulfonated PIM-SBF as orange or pale brown powder (1.2 g, 95%). ν_{max} (cm^{-1}): 3400, 2239, 1180, 1030, 663, 623; ^{13}C NMR (600 MHz, solid state): δ (ppm) 147.0, 141.5, 128.1, 121.6, 111.5, 95.3, 67.1; BET surface area = 482 m^2 g^{-1}; Micropore volume = 0.167 cm^3 g^{-1} obtained from N_2 adsorption based on NLDFT model; Ion exchange capacity = 1.86 mmol g^{-1}; TGA analysis (N_2): 356 °C

5.3 Analytical methods: Metaldehyde adsorption

5.3.1 Batch equilibrium experiments for metaldehyde

Polymer samples were ground into a fine powder, passed through a sieve (100 µm) and dried under vacuum at 120 °C overnight. To an incubation tube containing 50 mg of polymer sample, 50 mL of 80 mg L^{-1} metaldehyde solution in ultrapure water was added. The tubes were shaken for 46 hrs at 25 °C and 2500 rpm using an incubator. After removal, 5 mL of each solution was slowly passed through preconditioned styrene-divinyl copolymer SPE ENV+ (6ml/150 mg) cartridges. Preconditioning was performed using DCM (2 column volumes), MeOH (2 column volumes) and water (1 column volume). The cartridges were then air-dried using a vacuum SPE extraction manifold and the analyte was eluted directly into volumetric flasks (25 mL) using DCM (10 mL) and was then made up to the mark using DCM. The solutions were then analysed using Gas Chromatography-Mass spectrometry (GC-MS) using the method parameters described in section 2.5. All adsorbents were tested in triplicate against three controls and a calibration curve containing five standards: 0.1, 1, 5, 10 & 20 mg L^{-1}.

5.3.2 Solution isotherm for the adsorption of metaldehyde onto TPB-DCM/TMOF

The adsorbent TPB-DCM/TMOF was passed through a sieve (100 µm) and dried under vacuum at 120 °C overnight. To incubation tubes containing 25 mg of polymer sample, 25 mL aliquots of metaldehyde-spiked aqueous solutions were added. The experiment was performed in duplicates for various initial metaldehyde concentrations; C_0 = 4, 5, 10, 25, 50, 75, 100 mg L^{-1}. The tubes were shaken for 46 hrs at 25 °C and 2500 rpm using an incubator. After removal by filtration through a 0.22µm syringe filter, 5 mL of each solution was slowly passed through preconditioned styrene-divinyl copolymer SPE ENV+ (6ml/ 150 mg) cartridges. Preconditioning was performed using DCM (2 column volumes), MeOH (2 column volumes) and water (1 column volume). The cartridges were then air-dried using a vacuum SPE extraction manifold and the concentrated analyte samples were eluted directly into volumetric flasks

(25 mL) using DCM (10 mL) and was then made up to the mark using DCM. The solutions were then analysed using Gas Chromatography-Mass spectrometry (GC-MS) using the method parameters described in section 2.5. All metaldehyde initial concentrations used were standardised in triplicate against a calibration curve containing five standards: 0.1, 1, 5, 10 & 20 mg L^{-1}.

5.3.3 Kinetic experiments for the adsorption of metaldehyde onto TPB-DCM/TMOF

The adsorbent TPB-DCM/TMOF was passed through a sieve (100 µm) and dried under vacuum at 120 °C overnight. To separate glass vials each containing 25 mg of polymer sample and equipped with a stirrer bar, 25 mL aliquots of a standard metaldehyde-spiked aqueous solution C_o= 80.7 mg L^{-1} were added. The resulting suspensions were shaken manually for 15 s to ensure good homogeneous mixing of the hydrophobic polymer with the aqueous solution, and then they were stirred magnetically at 1000 rpm. After contact time, t, was reached the polymer samples were removed by filtration through a 0.22 µm syringe filter and 5 mL of each solution were solid phase extracted onto preconditioned styrene-divinyl copolymer SPE ENV+ (6ml/150 mg) cartridges. The cartridges were then air-dried using a vacuum SPE extraction manifold and the concentrated analyte samples were eluted directly into volumetric flasks (25 mL) using DCM and was then made up to the mark using DCM. The solutions were then analysed using Gas Chromatography-Mass spectrometry (GC-MS) using the method parameters described in section 2.5. The experiments were performed in duplicates for several adsorbent-adsorbate contact times, t = 15 s, 30 s, 60 s, 300 s, 600 s, 1800 s, 50000 s & 108000 s, and quantitative analysis was performed against a calibration curve in DCM containing five standards: 0.1, 1, 5, 10 & 20 mg L^{-1}.

5.3.4 RSSCTs

A custom-made Teflon® column (**b**) with internal dimensions h = 10 mm, & d= 6.1mm, was connected via a screw-type connection to a Swagelock® fitting (**a**), and the apparatus was connected to an Agilent HPLC pump. Polymer packing in the column was performed using dried powdered adsorbents (200 mg) sandwiched between frits of 0.22 µm pore size, and the packed bed volume was measured using a micrometer as 0.8 mL. The column was washed with MeOH for 1 hr followed by ultrapure water, before an aqueous solution of metaldehyde-spiked ultrapure water (C_0 = 0.5 mg L^{-1}) was filtered through, at a constant flowrate of 0.35 ml min^{-1}. The effluent water was passed through a pre-conditioned SPE (1g/ 25mL ST-DV) cartridge (**b**) directly. The SPE cartridge was replaced every 24 hrs/ 504 mL of filtration for a period of 9 days. After filtration, the cartridges were air-dried in a vacuum SPE manifold and the analyte samples were eluted into 25 mL volumetric flasks using DCM and analysed using GC-MS against

a calibration curve containing 5 standards: 1, 5, 12.5, 25, 50 µg L^{-1}. The initial metaldehyde-spiked solution was also standardised using quantitative GC-MS analysis.

5.3.5 GC-MS method

GC compartment: Split-less injection at 160 °C was employed at injection volumes of 1µl, unless otherwise state. The oven temperature gradient was as follows: 40 °C for 4 min, heated to 220 °C at a rate of 20 °C min^{-1}, held isothermally for 2 mins. A non-standard chromatographic column was used: Rxi 624 MS (thickness 1.4µm, length 30m, diameter 0.25µm).

MS compartment: Electron ionisation was employed at 70 eV. The ion source & Interface temperatures were set at 150 °C & 160 °C, respectively. Metaldehyde was detected by total ion count (TIC) across m/z = 10-224 & Single Ion Monitoring (SIM) of the peaks: m/z= 45 (target ion), m/z= 89 (reference ion) & m/z=117 (reference ion), in batch equilibrium experiments. For the remainder of the experiments only SIM mode was used. The quadrupole detector analyser voltage was kept at 0 V, unless otherwise stated.

*For RSSCT experiments, higher instrument sensitivity was achieved by increasing the injection volume to 3 µl and the detector voltage to 1.2 V.

5.4 Analytical methods: Pb (II) adsorption

5.4.1 Batch equilibrium experiments

Polymer samples were ground into a fine powder, passed through a sieve (100 µm) and dried under vacuum at 120 °C overnight. To an incubation tube containing 25 mg of polymer sample, 25 mL of 105 mg L^{-1} lead (II) nitrate solution in ultrapure water were added. The tubes were shaken for 46 hrs at 25 °C and 2500 rpm using an incubator. After equilibration, 10 mL of each suspension were filtered through 0.22µm syringe filters to remove the adsorbent particles and the filtered solutions were analysed quantitatively for Pb^{2+}, using ICP-OES against a calibration curve containing 5 standards: 1, 5, 10, 50 & 100 mg L^{-1}.

5.4.2 Solution isotherm for DBMP-DCM/SA-TfA

The adsorbent DBMP-DCM/SA-TfA was passed through a sieve (100 µm) and dried under vacuum at 120 °C overnight. To incubation tubes containing 10 mg of polymer sample, 10 mL aliquots of $Pb(NO_3)_2$-spiked aqueous solutions were added. The experiment was performed in duplicates for various initial Pb^{2+} concentrations; C_0 = 62.3, 80.1, 93.4, 120.7, 141.4, 158.6, 180.1 & 200.3 mg L^{-1}. The solutions were adjusted by addition of small volumes of $NaOH_{(aq)}$ (0.01M) or $HCl_{(aq)}$ (0.01M), if needed. The tubes were shaken for 46 hrs at 25 °C and 2500 rpm using an incubator. After removal by filtration through a 0.22 µm syringe filter, the solutions were subjected to quantitative analysis for Pb^{2+} using ICP-OES against a calibration curve constructed from five standards: 1, 5, 10, 50 & 100 mg L^{-1}, and the initial Pb^{2+} solutions were standardised.

5.4.3 ICP-OES methods

ICP-OES analysis was conducted using a Perkin Elmer Optima 8300 DV, at a RF forward power of 1500 W, with Ar gas flows of 10, 0.2 and 0.6 L min^{-1} for plasma, auxiliary, and nebuliser flows, respectively. Aqueous sample solutions were taken up into a Gem Tip cross-Flow and Scotts spray chamber nebuliser, at a rate of 1.50 mL min^{-1}, using a peristaltic pump.

Axial mode operation was performed for all Al, Fe and Pb. The selected wavelengths for each element were analysed in fully quant mode, using three points per unit wavelength. Three replicate runs per sample were performed.

Calibration standards at concentrations 1 mg L^{-1}, 5 mg L^{-1} 10 mg L^{-1}, 50 mg L^{-1} & 100 mg L^{-1} were prepared by performing appropriate dilutions of single element 1000 mg l^{-1} standard solutions (Fisher Scientific UK LTD Bishop Meadow Road, Loughborough, Leicestershire LE11 5RG) (S, P) for all Fe, Pb & Al, using 18.2 M Deionised water.

Wavelength: The following wavelengths were selected for each element based on the shape of the peaks at that wavelength, background interferences, wavelength sensitivity and linearity of the calibration lines: Pb 220.353 nm, Fe 238.204 nm and Al 308.215 nm.

5.4.4 Determination of IEC

Powdered samples of HCPs (70 mg) were stirred for 3 hr in aqueous NaOH solution (1.3 M, 10 mL). The suspensions were then filtered, and the filtrates were washed with distilled water thrice and were titrated against a standardised aqueous HCl solution (0.125 M) using phenolphthalein as an indicator. All experiments were conducted in duplicates to allow for error calculations.

5.4.5 Analytical methods: Metaldehyde degradation

A saturated solution of metaldehyde was made by the addition of metaldehyde (10 mg) D_2O (99.9% atom D) into a 25 mL volumetric flask. The solution was filtered through a 0.22 µm syringe filter and its concentration was determined as 206 mg L^{-1}, via relative peak integration against dimethylsulfone as an NMR standard. A suspension of TPB-DCM/ASA (2 mg mL^{-1}) in D_2O was prepared and sonicated for 15 mins, using an ultrasonic bath. A volumetric pipette was used to add equal volumes of the metaldehyde solution and TPB-DCM/ASA homogenised suspension to an NMR tube, to afford C_0 = 103 mg L^{-1} metaldehyde & adsorbent dose = 1 mg L^{-1}. ^{1}H NMR were acquired daily using a Bruker 400 MHz spectrometer and high resolution ^{1}H-^{13}C HSQC, ^{1}H NMR, ^{1}H-presat NMR & ^{1}H-^{1}H COSY experiments were recorded after 7 days of agitation, using Bruker AVA600 (600 MHz) and Bruker AVA800 (800 MHz) spectrometers, equipped with TXI/ TCI cryo-probes.

6. References

1 M. T. Amin, A. A. Alazba and U. Manzoor, *Adv. Mater. Sci. Eng.*, 2014, **2014,** 1-24.

2 H. K. Jeswani, H. Gujba, N. W. Brown, E. P. L. Roberts and A. Azapagic, *J. Clean. Prod.*, 2015, **89**, 203–213.

3 T. Gupta, *Carbon: the black, the gray and the transparent*, Springer, New York, 2017.

4 M. Stuart, D. Lapworth, E. Crane and A. Hart, *Sci. Total Environ.*, 2012, **416**, 1–21.

5 S. Kurwadkar, *Water Environ. Res.*, 2017, **89**, 1561–1579.

6 L. Gimsing, J. Agert, N. Baran, A. Boivin, F. Ferrari, R. Gibson, L. Hammond, F. Hegler, R. L. Jones, W. König, J. Kreuger, T. van der Linden, D. Liss, L. Loiseau, A. Massey, B. Miles, L. Monrozies, A. Newcombe, A. Poot, G. L. Reeves, S. Reichenberger, A. E. Rosenbom, H. Staudenmaier, R. Sur, A. Schwen, M. Stemmer, W. Tüting and U. Ulrich, *J. fur Verbraucherschutz und Leb.*, 2019, **14**, 1–93.

7 L. E. Padilla and M. Winchell, *J. of Envin. Qual.*, 2020, **49**, 128–139.

8 J. Yang, B. Hou, J. Wang, B. Tian, J. Bi, N. Wang, X. Li and X. Huang, *Nanomaterials*, 2019, **9**, 39-45.

9 P. B. Tchounwou, C. G. Yedjou, A. K. Patlolla and D. J. Sutton, *EXS*, 2012, **101**, 133–164.

10 M. Schumacher, G. Castle, A. Gravell, G. A. Mills and G. R. Fones, *MethodsX*, 2016, **3**, 188–194.

11 K. S. W. Sing, *Stud. Surf. Sci. Catal.*, 1991, **62**, 1–9.

12 G. D. Castle, G. A. Mills, A. Gravell, L. Jones, I. Townsend, D. G. Cameron and G. R. Fones, *Environ. Sci. Water Res. Technol.*, 2017, **3**, 415–428.

13 C. J. Nicholls, *Agric. Hortic. Dev. Board*, 2014, **79**, 4–9.

14 P. Kay and R. Grayson, *Water Environ. J.*, 2014, **28**, 410–417.

15 H. yan Zhang, C. Wang, H. ze Lu, W. bi Guan and Y. qiang Ma, *Ecotoxicol. Environ. Saf.*, 2011, **74**, 1653–1658.

16 R. Busquets, O. P. Kozynchenko, R. L. D. Whitby, S. R. Tennison and A. B. Cundy, *Water Res.*, 2014, **61**, 46–56.

17 P. Kay and R. Grayson, 2014, **28**, 410–417.

18 A. G. Brutlag and B. Puschner, *Metaldehyde*, Elsevier Inc., Amsterdam, 2012.

19 N. S. Bates, N. M. Sutton and A. Campbell, *Vet. Rec.*, 2012, **171**, 324-329.

20 T. F. Booze and F. W. Oehme, *Fundam. Appl. Toxicol.*, 1986, **6**, 440–446.

21 L. K. Dolder, *Vet. Med.*, 2003, **98**, 213–215.

22 S. Semitsoglou-Tsiapou, M. R. Templeton, N. J. D. Graham, L. Hernández Leal, B. J. Martijn, A. Royce and J. C. Kruithof, *Water Res.*, 2016, **91**, 285–294.

23 Department for Environment, Food & Rural Affairs, https://www.gov.uk/government/news/outdoor-use-of-metaldehyde-to-be-banned-to-protect-wildlife, (accessed March 2021).

24 A. L. Wani, A. Ara and J. A. Usmani, *Interdiscip. Toxicol.*, 2015, **8**, 55–64.

26 H. Delile, J. Blichert-Toft, J. P. Goiran, S. Keay and F. Albarède, *Proc. Natl. Acad. Sci. U. S. A.*, 2014, **111**, 6594–6599.

27 L. L. Bergeson, *Environ. Qual. Manag.*, 2008, **18**, 79–84.

28 D. Busselberg, M. L. Evans, H. Rahmann and D. O. Carpenter, *J. Neurophysiol.*, 1991, **65**, 786–

795.

29 A. R. Cohen, M. S. Trotzky and D. Pincus, *Pediatrics*, 1981, **67**.

30 A. Roy, E. Queirolo, F. Peregalli, N. Mañay, G. Martínez and K. Kordas, *Environ. Res.*, 2015, **140**, 127–135.

31 R. Mamtani, P. Stern, I. Dawood and S. Cheema, *J. Toxicol.*, 2011, **2011,** 43-51.

32 A. L. Clune, H. Falk and A. M. Riederer, *J. Heal. Pollut.*, 2011, **1**, 14–23.

33 C. R. Hayes and O. D. Hydes, *J. Water Health*, 2012, **10**, 337–348.

34 K. Deibler and P. Basu, *Eur. J. Inorg. Chem.*, 2013, **2013**, 1086–1096.

35 T. A. H. Nguyen, H. H. Ngo, W. S. Guo, J. Zhang, S. Liang, Q. Y. Yue, Q. Li and T. V. Nguyen, *Bioresour. Technol.*, 2013, **148**, 574–585.

36 M. Ghorbani, O. Seyedin and M. Aghamohammadhassan, *J. Environ. Manage.*, 2020, **254**, 109814.

37 I. Ali and V. K. Gupta, 2007, **1**, 2661–2667.

38 V. K. Gupta, S. Agarwal and T. A. Saleh, *J. Hazard. Mater.*, 2011, **185**, 17–23.

39 S. Yang, J. Hu, C. Chen, D. Shao and X. Wang, *Environ. Sci. Technol.*, 2011, **45**, 3621–3627.

40 X. Y. Yu, T. Luo, Y. X. Zhang, Y. Jia, B. J. Zhu, X. C. Fu, J. H. Liu and X. J. Huang, *ACS Appl. Mater. Interfaces*, 2011, **3**, 2585–2593.

41 M. S. Tehrani, P. A. Azar, P. E. Namin and S. M. Dehaghi, *J. Environ. Prot. (Irvine,. Calif).*, 2013, **04**, 529–536.

42 Z. H. Huang, X. Zheng, W. Lv, M. Wang, Q. H. Yang and F. Kang, *Langmuir*, 2011, **27**, 7558–7562.

43 X. Deng, L. Lü, H. Li and F. Luo, *J. Hazard. Mater.*, 2010, **183**, 923–930.

44 Y. Ren, N. Yan, J. Feng, J. Ma, Q. Wen, N. Li and Q. Dong, *Mater. Chem. Phys.*, 2012, **136**, 538–544.

45 L. Yang, Z. Li, G. Nie, Z. Zhang, X. Lu and C. Wang, *Appl. Surf. Sci.*, 2014, **307**, 601–607.

46 C. Liu, D. Zhang, L. Zhao, X. Lu, P. Zhang, S. He, G. Hu and X. Tang, *RSC Adv.*, 2016, **6**, 113352–113365.

47 B. Li, F. Su, H. K. Luo, L. Liang and B. Tan, *Microporous Mesoporous Mater.*, 2011, **138**, 207–214.

48 M. P. Tsyurupa, O. G. Tarabaeva, A. V. Pastukhov and V. A. Davankov, *Int. J. Polym. Mater. Polym. Biomater.*, 2003, **52**, 403–414.

49 M. Thommes, K. Kaneko, A.V. Neimark, J.P. Olivier, F. Rodriguez-Reinoso, J. Rouquerol, K. S. Sing, *Pure Appl. Chem.*, 2015, **87,** 9-10.

50 J. Rouquerol, D. Avnir, C. W. Fairbridge, D. H. Everett, J. M. Haynes, N. Pernicone, J. D. F. Ramsay, K. S. W. Sing and K. K. Unger, *Pure Appl. Chem.*, 1994, **66**, 1739–1758.

51 L. J. Gibson and M. F. Ashby, *Cellular Solids*, Cambridge University Press, 1997.

52 N. Issaadi, A. Aït-Mokhtar, R. Belarbi and A. Hamami, *Adv. Multi-Physics Multi-Scale Couplings Geo-Environmental Mech.*, 2018, 243–289.

53 P. S. Liu and G. F. Chen, *Porous Materials*, 2014, **32**, 411-492.

54 J. Weber and Q. B. Meng, in *Encyclopedia of Polymer Science and Technology*, John Wiley & Sons, Inc., Hoboken, NJ, USA, 2014, pp. 1–49.

55 D. Bradshaw, J. B. Claridge, E. J. Cussen, T. J. Prior and M. J. Rosseinsky, *Acc. Chem. Res.*, 2005, **38**, 273–282.

56 B. M. Weckhuysen and J. Yu, *Chem. Soc. Rev*, 2015, **44**, 7022.

57 Y. Yusran, H. Li, X. Guan, Q. Fang and S. Qiu, *EnergyChem*, 2020, **2**, 100035.

58 M. Safaei, M. M. Foroughi, N. Ebrahimpoor, S. Jahani, A. Omidi and M. Khatami, *TrAC - Trends Anal. Chem.*, 2019, **118**, 401–425.

59 P. M. Budd, B. S. Ghanem, S. Makhseed, N. B. McKeown, K. J. Msayib and C. E. Tattershall, *Chem. Commun.*, 2004, **4**, 230–231.

60 W. Wen, P. S. Shuttleworth, H. Yue, J. P. Fernándezfernández-Blázquezblázquez and J. Guo, *Cite This ACS Appl. Mater. Interfaces*, 2020, **12**, 7548–7556.

61 Y. Lu, W. Fang, J. Kong, F. Zhang, Z. Wang, X. Teng, Y. Zhu and J. Jin, *J. Memb. Sci.*, 2020, **603,** 118027.

62 Q. Li, Z. Zhan, S. Jin and B. Tan, *Chem. Eng. J.*, 2017, **326**, 109–116.

63 S. M. Manocha, *Porous carbons*, 2003, vol. 28.

64 R. I. Kosheleva, A. C. Mitropoulos and G. Z. Kyzas, *Environ. Chem. Lett.*, 2019, **17**, 429–438.

65 A. W. Samsuri, F. Sadegh-Zadeh and B. J. Seh-Bardan, *Int. J. Environ. Sci. Technol.*, 2014, **11**, 967–976.

66 O. Ioannidou and A. Zabaniotou, *Renew. Sustain. Energy Rev.*, 2007, **11**, 1966–2005.

67 M. E. Ramos, P. R. Bonelli, A. L. Cukierman, M. M. L. Ribeiro Carrott and P. J. M. Carrott, *J. Hazard. Mater.*, 2010, **177**, 175–182.

68 J. Patrick, *Porosity in carbons : characterization and applications*, Edward Arnold, London, 1995.

69 J. Zhou, A. Luo and Y. Zhao, *J. Air Waste Manage. Assoc.*, 2018, **68**, 1269–1277.

n

70 M. A. Yahya, Z. Al-Qodah and C. W. Z. Ngah, *Renew. Sustain. Energy Rev.*, 2015, **46**, 218–235.

71 Z. Heidarinejad, M. H. Dehghani, M. Heidari, · Gholamali Javedan, I. Ali and M. Sillanpää, 2020, **18**, 393–415.

72 N. Rambabu, B. V. S. K. Rao, V. R. Surisetty, U. Das and A. K. Dalai, *Ind. Crops Prod.*, 2015, **65**, 572–581.

73 G. Z. Kyzas, E. A. Deliyanni and K. A. Matis, *Colloids Surfaces A Physicochem. Eng. Asp.*, 2016, **490**, 74–83.

74 H. Sayğili and F. Güzel, *J. Clean. Prod.*, 2016, **113**, 995–1004.

75 Y. D. Chen, W. Q. Chen, B. Huang and M. J. Huang, *Chem. Eng. Res. Des.*, 2013, **91**, 1783–1789.

76 A. M. Youssef, A. I. Ahmed and U. A. El-Bana, *Carbon Lett.*, 2012, **13**, 61–72.

77 L. Khezami and R. Capart, *J. Hazard. Mater.*, 2005, **123**, 223–231.

78 C. Cheng, H. Liu, P. Dai, X. Shen, J. Zhang, T. Zhao and Z. Zhu, *J. Taiwan Inst. Chem. Eng.*, 2016, **67**, 532–537.

79 L. Mouni, L. Belkhiri, F. Zouggaghe and M. Tafer, *Desalin. Water Treat.*, 2014, **52**, 6412–6419.

80 P. Thitame and S. Shukla, *Int. J. Environ. Sci. Technol.*, 2017, **13**, 1628-1633.

81 V. Fierro, G. Muñiz, A. H. Basta, H. El-Saied and A. Celzard, *J. Hazard. Mater.*, 2010, **181**, 27–34.

82 A. Rodríguez, J. García, G. Ovejero and M. Mestanza, *J. Hazard. Mater.*, 2009, **172**, 1311–1320.

83 A. Reffas, V. Bernardet, B. David, L. Reinert, M. B. Lehocine, M. Dubois, N. Batisse and L. Duclaux, *J. Hazard. Mater.*, 2010, **175**, 779–788.

84 K. Suresh Kumar Reddy, A. Al Shoaibi and C. Srinivasakannan, *Carbon N. Y.*, 2013, **52**, 623.

85 P. Patnukao and P. Pavasant, *Bioresour. Technol.*, 2008, **99**, 8540–8543.

86 S. Altenor, B. Carene, E. Emmanuel, J. Lambert, J. J. Ehrhardt and S. Gaspard, *J. Hazard. Mater.*, 2009, **165**, 1029–1039.

87 A. A. Attia, B. S. Girgis and N. A. Fathy, *Dye. Pigment.*, 2008, **76**, 282–289.

88 B. Wang, C. Zhu, Z. Zhang, W. Zhang, X. Chen, N. Sun, W. Wei, Y. Sun and H. Ji, *Fuel*, 2016, **179**, 274–280.

89 M. Galhetas, A. S. Mestre, M. L. Pinto, I. Gulyurtlu, H. Lopes and A. P. Carvalho, *J. Colloid Interface Sci.*, 2014, **433**, 94–103.

90 A. S. Mestre, J. Pires, J. M. F. Nogueira and A. P. Carvalho, *Carbon N. Y.*, 2007, **45**, 1979–1988.

91 A. S. Mestre, A. S. Bexiga, M. Proença, M. Andrade, M. L. Pinto, I. Matos, I. M. Fonseca and A. P. Carvalho, *Bioresour. Technol.*, 2011, **102**, 8253–8260.

92 R. L. Tseng, *J. Hazard. Mater.*, 2007, **147**, 1020–1027.

93 R. Acosta, V. Fierro, A. Martinez de Yuso, D. Nabarlatz and A. Celzard, *Chemosphere*, 2016, **149**, 168–176.

94 F. Boudrahem, A. Soualah and F. Aissani-Benissad, *J. Chem. Eng. Data*, 2011, **56**, 1946–1955.

95 S. Z. Mohammadi, M. A. Karimi, S. N. Yazdy, T. Shamspur and H. Hamidian, *Quim. Nova*, 2014, **37**, 804–809.

96 J. J. Moreno-Barbosa, C. López-Velandia, A. D. P. Maldonado, L. Giraldo and J. C. Moreno-Piraján, in *Adsorption*, Springer, 2013, vol. 19, pp. 675–685.

97 S. Erdoğan, Y. Önal, C. Akmil-Başar, S. Bilmez-Erdemoğlu, Ç. Sarici-Özdemir, E. Köseoğlu and G. IçDuygu, *Appl. Surf. Sci.*, 2005, **252**, 1324–1331.

98 S. Norouzi, M. Heidari, V. Alipour, O. Rahmanian, M. Fazlzadeh, F. Mohammadi-moghadam, H. Nourmoradi, B. Goudarzi and K. Dindarloo, *Bioresour. Technol.*, 2018, **258**, 48–56.

99 N. B. Singh, G. Nagpal, S. Agrawal and Rachna, *Environ. Technol. Innov.*, 2018, **11**, 187–240.

100 P. Veverka and K. Jeřábek, *React. Funct. Polym.*, 2004, **59**, 71–79.

101 J. Huang and S. R. Turner, *Polym. Rev.*, 2018, **58**, 1–41.

102 L. Tan and B. Tan, *Chem. Soc. Rev.*, 2017, **46**, 3322–3356.

103 Y. Luo, B. Li, W. Wang, K. Wu and B. Tan, *Adv. Mater.*, 2012, **24**, 5703–5707.

104 C. Zhang, P. C. Zhu, L. Tan, J. M. Liu, B. Tan, X. L. Yang and H. B. Xu, *Macromolecules*, 2015, **48**, 8509–8514.

105 G. I. Rosenberg, A. S. Shabaeva, V. S. Moryakov, T. G. Musin, M. P. Tsyurupa and V. A. Davankov, *React. Polym. Ion Exch. Sorbents*, 1983, **1**, 175–182.

106 V. A. Davankov, M. M. Ilyin, M. P. Tsyurupa, G. I. Timofeeva and L. V. Dubrovina, *Macromolecules*, 1996, **29**, 8398–8403.

107 V. A. Davankov, S. V. Rogoshin and M. P. Tsyurupa, *J. Polym. Sci. Polym. Symp.*, 2007, **47**, 95–101.

108 R. Tayebee, M. Jarrahi, B. Maleki, M. Kargar Razi, Z. B. Mokhtari and S. M. Baghbanian, *RSC Adv.*, 2015, **5**, 10869–10877.

109 J. Germain, J. M. J. Fréchet Ab and F. Svec, *Chem. Mater.* 2006, **18**, 4430–4435

110 J. Hradil and E. Králová, *Polymer (Guildf).*, 1998, **39**, 6041–6048.

111 A. V. Pastukhov, M. P. Tsyurupa and V. A. Davankov, *J. Polym. Sci. Part B Polym. Phys.*, 1999, **37**, 2324–2333.

112 V. A. Davankov and M. P. Tsyurupa, *React. Polym.*, 1990, **13**, 27–42.

113 J. Clayden, N. Greeves, S. Warren and P. Wothers, *Organic Chemistry (2nd ed.)*, Oxford

University Press, Oxford, 2012.

114 F. G. Oliveira, F. L. Rodrigues, A. V. B. de Oliveira, D. V. L. M. Marçal and P. M. Esteves, *Struct. Chem.*, 2017, **28**, 545–553.

115 R. Dawson, E. Stöckel, J. R. Holst, D. J. Adams and A. I. Cooper, *Energy Environ. Sci.*, 2011, **4**, 4239–4245.

116 C. D. Wood, B. Tan, A. Trewin, F. Su, M. J. Rosseinsky, D. Bradshaw, Y. Sun, L. Zhou and A. I. Cooper, *Adv. Mater.*, 2008, **20**, 1916–1921.

117 J. M. Chem, G. Jonschker, M. Koch, M. G. Schwab, A. Lennert, I. Senkovska, M. Rehahn and S. Kaskel, 2011, **21**, 2131–2135.

118 Y. Yang, Q. Zhang, S. Zhang and S. Li, *RSC Adv.*, 2014, **4**, 5568–5574.

119 D. Chen, S. Gu, Y. Fu, Y. Zhu, C. Liu, G. Li, G. Yu and C. Pan, *Polym. Chem*, 2016, **7**, 3416.

120 G. Liu, Y. Wang, C. Shen, Z. Ju and D. Yuan, *J. Mater. Chem. A*, 2015, **3**, 3051–3058.

121 F. Alves and I. Nischang, *Chem. - A Eur. J.*, 2013, **19**, 17310–17313.

122 C. Yadav, V. K. Maka, S. Payra and J. N. Moorthy, *ACS Appl. Polym. Mater.*, 2020, **2**, 3084–3093.

123 B. Li, Z. Guan, X. Yang, W. D. Wang, W. Wang, I. Hussain, K. Song, B. Tan and T. Li, 2014.

124 M. Grzybowski, K. Skonieczny, H. Butenschön and D. T. Gryko, *Angew. Chemie - Int. Ed.*, 2013, **52**, 9900–9930.

125 L. Li, H. Ren, Y. Yuan, G. Yu and G. Zhu, *J. Mater. Chem. A*, 2014, **2**, 11091–11098.

126 K. J. Msayib and N. B. Mckeown, *J. Mater. Chem. A Mater. energy Sustain.*, 2016, **4**, 10110-1013.

127 B. Li, R. Gong, W. Wang, X. Huang, W. Zhang, H. Li, C. Hu and B. Tan, *Macromolecules*, 2011,

44, 2410–2414.

128 H. Lim, M. C. Cha and J. Y. Chang, *Macromol. Chem. Phys.*, 2012, **213**, 1385–1390.

129 H. Wang, L. Pan, W. Deng, G. Yang and X. Liu, *Polym. J.*, 2016, **48**, 787–792.

130 L. Tan, B. Li, X. Yang, W. Wang and B. Tan, *Polymer (Guildf).*, 2015, **70**, 336–342.

131 D. Zhang, L. Tao, Q. Wang and T. Wang, *Polymer (Guildf).*, 2016, **82**, 114–120.

132 M. Saleh, H. M. Lee, K. C. Kemp and K. S. Kim, *ACS Appl. Mater. Interfaces*, 2014, **6**, 7325–7333.

133 X. Yang, B. Li, I. Majeed, L. Liang, X. Long and B. Tan, *Polym. Chem.*, 2013, **4**, 1425–1429.

134 Y. Ma, Q. Zhou, A. Li, C. Shuang, Q. Shi and M. Zhang, *J. Hazard. Mater.*, 2014, **266**, 84–93.

135 L. Pan, M. Xu, Z. Liu, B. Du, K. Yang and L. Wu, 2016, **6**, 47530–47535.

136 B. Li, R. Gong, Y. Luo and B. Tan, *Soft Matter*, 2011, **7**, 10910–10916.

137 S. Liu, D. Chen, J. Zheng, L. Zeng, J. Jiang, R. Jiang, F. Zhu, Y. Shen, D. Wu and G. Ouyang, *Nanoscale*, 2015, **7**, 16943–16951.

138 H. Li, B. Meng, S. H. Chai, H. Liu and S. Dai, *Chem. Sci.*, 2016, **7**, 905–909.

139 N. B. Mckeown and P. M. Budd, *Macromolecules*, 2010, **43**, 5163.

140 Y. Jiao, F. H. Stillinger and S. Torquato, *Phys. Rev. Lett.*, 2008, **100**, 245504.

141 A. B. Hopkins, F. H. Stillinger and S. Torquato, *Phys. Rev. E - Stat. Nonlinear, Soft Matter Phys.*, 2009, **79**, 031123.

142 M. Heuchel, D. Fritsch, P. M. Budd, N. B. McKeown and D. Hofmann, *J. Memb. Sci.*, 2008, **318**, 84–99.

143 D. Ramimoghadam, E. M. A. Gray and C. J. Webb, *Int. J. Hydrogen Energy*, 2016, **41**, 16944–

16965.

144 M. M. Khan, G. Bengtson, S. Neumann, M. M. Rahman, V. Abetz and V. Filiz, *RSC Adv.,* 2014, **4**, 32148-32160.

145 Z. G. Wang, X. Liu, D. Wang and J. Jin, *Polym. Chem.*, 2014, **5**, 2793–2800.

146 I. Hossain, S. Y. Nam, C. Rizzuto, G. Barbieri, E. Tocci and T. H. Kim, *J. Memb. Sci.*, 2019, **574**, 270–281.

147 I. Rose, C. G. Bezzu, M. Carta, B. Comesanã-Gándara, E. Lasseuguette, M. C. Ferrari, P. Bernardo, G. Clarizia, A. Fuoco, J. C. Jansen, K. E. Hart, T. P. Liyana-Arachchi, C. M. Colina and N. B. McKeown, *Nat. Mater.*, 2017, **16**, 932–937.

148 C. Winkler, *J. für Prakt. Chemie*, 1887, **36**, 177–209.

149 M. A. Spielman, *J. Am. Chem. Soc.*, 1935, **57**, 583–585.

150 H. Xi, C. X. Yuan, Y. X. Li, Y. Liu and X. T. Tao, *CrystEngComm*, 2012, **14**, 2087–2093.

151 M. Carta, R. Malpass-Evans, M. Croad, Y. Rogan, J. C. Jansen, P. Bernardo, F. Bazzarelli and N. B. McKeown, *Science.*, 2013, **339**, 303–307.

152 C. G. Bezzu, M. Carta, A. Tonkins, J. C. Jansen, P. Bernardo, F. Bazzarelli and N. B. Mckeown, 2012, **24**, 5930–5933.

153 P. Zuo, J. Zhou, Z. Yang and T. Xu, *Chempluschem*, 2020, **85**, 1893–1904.

154 R. Tan, A. Wang, R. Malpass-Evans, R. Williams, E. W. Zhao, T. Liu, C. Ye, X. Zhou, B. P. Darwich, Z. Fan, L. Turcani, E. Jackson, L. Chen, S. Y. Chong, T. Li, K. E. Jelfs, A. I. Cooper, N. P. Brandon, C. P. Grey, N. B. McKeown and Q. Song, *Nat. Mater.*, 2020, **19**, 195–202.

155 B. Satilmis, *J. Polym. Environ.*, 2020, **28**, 995–1009.

156 R. W. Smithwick, *Powder Technol.*, 1982, **33**, 201–209.

157 K. K. Mohanty, *AIChE J.*, 1992, **38**, 1303–1304.

158 M. Naderi, in *Progress in Filtration and Separation*, Elsevier Ltd, 2015, pp. 585–608.

159 R. Kecili and C. M. Hussain, in *Nanomaterials in Chromatography*, 2018.

160 T. S. Khayyun and A. H. Mseer, *Appl. Water Sci.*, 2019, **9**, 1–8.

161 F. Ambroz, T. J. Macdonald, V. Martis and I. P. Parkin, *Small Methods*, 2018, **2**, 1800173.

162 S. Brunauer, P. H. Emmett and E. Teller, *J. Am. Chem. Soc.*, 1938, **60**, 309–319.

163 I. M. K. Ismail, *Carbon N. Y.*, 1990, **28**, 423–434.

164 P. S. Liu and G. F. Chen, *Porous Mater.*, 2014, **2**, 411–492.

165 N. B. McKeown, P. M. Budd and D. Book, *Macromol. Rapid Commun.*, 2007, **28**, 995–1002.

166 G. L Aranovich and M. D. Donohue, *J. Colloid Interface Sci.* 1998, **205**, 121-130.

167 A. F. Al-Rubaye, I. H. Hameed and M. J. Kadhim, *Int. J. Toxicol. Pharmacol. Res.*, 2017, **9**.

168 O. Coskun, *North. Clin. Istanbul*, 2016, **3**, 156.

169 L. M. HimaBindu and A. S. Parameswari, *International Journal of Pharmaceutical Quality Assurance*, 2013, **4**, 42-51.

170 I. Hadi and H. Mashkoor Hussein, *Int. J. Pharmacogn. Phytochem. Res.*, 2016, **8**, 21–37.

171 H. J. Al-Tameme, M. Y. Hadi and I. H. Hameed, *J. Pharmacogn. Phyther.*, 2015, **7**, 238–252.

172 P. T. Palmer, in *Encyclopedia of Analytical Chemistry*, John Wiley & Sons, Ltd, Chichester, UK, 2000.

173 M. A. Geer Wallace, J. D. Pleil, S. Mentese, K. D. Oliver, D. A. Whitaker and K. W. Fent, *J.*

Chromatogr. A, 2017, **1516**, 114–124.

174 J. Sneddon and M. D. Vincent, *Anal. Lett.*, 2008, **41**, 1291–1303.

175 C. G. Novaes, M. A. Bezerra, E. G. P. da Silva, A. M. P. dos Santos, I. L. da S. Romão and J. H. Santos Neto, *Microchem. J.*, 2016, **128**, 331–346.

176 M. He, B. Hu, B. Chen and Z. Jiang, *Phys. Sci. Rev.*, 2017, **2**, 1-37.

177 C. Schierle and M. Otto, 1994, **372**, 357–372.

178 S. Fathalinejad, E. Taarning, P. Christensen and J. H. Christensen, *Anal. Methods*, 2020, **12**, 1975–1987.

179 L. Granquist, A. Carlsson, S. Jonson, K. Andersson, P. Karlsson, J. Dahlén and S. Dunne, *Accredit. Qual. Assur.*, 2019, **24**, 215–226.

180 F. Chiadmi and J. Schlatter, *Anal. Chem. Insights*, 2015, **10**, 17–22.

181 J. Quintana, I. Martí and F. Ventura, *Journal of Chromatography A*, 2001, **938**, 3–13.

182 S. Nakashima and Y. Hayashi, *Mass Spectrom.*, 2016, **5**, 43–44.

183 N. Saadati, P. Abdullah, Z. Zakaria, S. Belin, T. Sany, M. Rezayi and H. Hassonizadeh, *Chem. Cent. J.*, 2013, **7**, 1-10.

184 M. Rezaee, F. Khalilian, M. R. Pourjavid, S. Seidi, A. Chisvert and M. Abdel-Rehim, *Int. J. Anal. Chem.*, 2015, **2015**, 397275–397275.

185 J. Wu, J. Lu, C. Wilson, Y. Lin and H. Lu, *J. Chromatogr. A*, 2010, **1217**, 6327–6333.

186 F. J. Camino-Sánchez, R. Rodríguez-Gómez, A. Zafra-Gómez, A. Santos-Fandila and J. L. Vílchez, *Talanta*, 2014, **130**, 388–399.

187 P. Worsfold, A. Townshend, C. F. Poole and M. Miró, *Encyclopedia of analytical science.*,

Elsevier, Amsterdam, 2019.

188 E. Ibáñez, A. Oca, G. De Murga, S. López-Sebastián, J. Tabera and G. Reglero, *J. Agric. Food Chem.*, 1999, **47**, 1400–1404.

189 J. Xiao, J. Wang, H. Fan, Q. Zhou and X. Liu, *International Journal of Environmental Analytical Chemistry* 2016, **96**, 307-435.

190 A. T. Mohd Din, B. H. Hameed and A. L. Ahmad, *J. Hazard. Mater.*, 2009, **161**, 1522–1529.

191 G. Limousin, J. P. Gaudet, L. Charlet, S. Szenknect, V. Barthès and M. Krimissa, *Appl. Geochemistry*, 2007, **22**, 249–275.

192 R. Hasan, S. N. Bukhari, R. Jusoh, N. S. A. Mutamin and H. D. Setiabudi, in *Materials Today: Proceedings*, Elsevier Ltd, 2018, vol. 5, pp. 21574–21583.

193 K. Y. Foo and B. H. Hameed, *Chem. Eng. J.*, 2010, **156**, 2–10.

194 N. Ayawei, A. N. Ebelegi and D. Wankasi, *J. Chem.*, 2017, **2017**, 1-12.

195 H. N. Tran, S. J. You, A. Hosseini-Bandegharaei and H. P. Chao, *Water Res.*, 2017, **120**, 88–116.

196 C. A. Rolph, B. Jefferson, F. Hassard and R. Villa, *Environ. Sci. Water Res. Technol.*, 2018, **4**, 1543–1552.

197 M. A. Al-Ghouti and D. A. Da'ana, *J. Hazard. Mater.*, 2020, **393**, 122383.

198 N. Ayawei, S. S. Angaye, D. Wankasi and E. D. Dikio, *Open J. Phys. Chem.*, 2015, **05**, 56–70.

199 J. Wang and X. Guo, *J. Hazard. Mater.*, 2020, **390**, 122156.

200 H. Qiu, L. Lv, B.-C. Pan, Q.-J. Zhang, W.-M. Zhang and Q.-X. Zhang, *J Zhejiang Univ Sci A*, 2009, **10**, 716–724.

201 T. R. Sahoo and B. Prelot, *Adsorption processes for the removal of contaminants from*

wastewater, Elsevier Inc., 2020.

202 F. Zietzschmann, J. Müller, A. Sperlich, A. S. Ruhl, F. Meinel, J. Altmann and M. Jekel, *Water Sci. Technol.*, 2014, **70**, 1271-1278.

203 M. Poddar, *IOSR J. Environ. Sci. Toxicol. Food Technol.*, 2013, **3**, 77–85.

204 J. C. Crittenden, J. K. Berrigan, D. W. Hand and B. Lykins, *J. Environ. Eng.*, 1987, **113**, 243–259.

205 J. Hrubec, *The Handbook of Environmental Chemistry Drinking Water Pollution and Water Treatment*, 1995.

206 R. Ocampo-Pérez, R Leyva-Ramos, M Sanchez-Polo, J Rivera-Utrilla, Á. M. Sanchez-Polo, Á. J. Rivera-Utrilla and Á. R. Leyva-Ramos, *Adsorption*, 2013, **19**, 945–957.

207 B. Satilmis and T. Uyar, *Appl. Surf. Sci.*, 2018, **453**, 220–229.

208 E. Lorenc-Grabowska and G. Gryglewicz, *Dye. Pigment.*, 2007, **74**, 34–40.

209 B. Tao and A. Fletcher, *Chem. Eng. J.*, 2016, **284**, 741–749.

210 B. Tao and A. J. Fletcher, *Sep. Purif. Technol.*, 2014, **124**, 195–200.

211 M. J. Iqbal and M. N. Ashiq, *J. Hazard. Mater.*, 2007, **139**, 57–66.

212 K. J. Msayib and N. B. McKeown, *J. Mater. Chem. A*, 2016, **4**, 10110–10113.

213 B. P. Dash, R. Satapathy, E. R. Gaillard, J. A. Maguire and N. S. Hosmane, *J. Am. Chem. Soc.*, 2010, **132**, 6578–6587.

214 R. Qiu, X. Xu, L. Peng, Y. Zhao, N. Li and S. Yin, *Chem. - A Eur. J.*, 2012, **18**, 6172–6182.

215 R. Tayebee and M. Jarrahi, *RSC Adv.*, 2015, **5**, 21206–21214.

216 A. Taheri, X. Pan, C. Liu and Y. Gu, *ChemSusChem*, 2014, **7**, 2094–2098.

217 R. Ghanbaripour, I. Mohammadpoor-Baltork, M. Moghadam, A. R. Khosropour, S. Tangestaninejad and V. Mirkhani, *J. Iran. Chem. Soc.*, 2012, **9**, 791–798.

218 H. R. Safaei, M. Davoodi and M. Shekouhy, *Synth. Commun.*, 2013, **43**, 2178–2190.

219 D. Prasad, A. Preetam and M. Nath, *Comptes Rendus Chim.*, 2013, **16**, 252–256.

220 Y. Zhao, J. Li, C. Li, K. Yin, D. Ye and X. Jia, *Green Chem.*, 2010, **12**, 1370.

221 N. Fontanals, R. M. Marcé, F. Borrull and P. A. G. Cormack, *Polym. Chem.*, 2015, **6**, 7231-7244.

222 B. Tao and A. J. Fletcher, *J. Hazard. Mater.*, 2013, **244**, 240–250.

223 C. Zhang, F. Li, S. X. Wang, Z. S. Liu and H. A. Aisa, *Anal. Methods*, 2015, **7**, 10256–10265.

224 A. M. James, S. Harding, T. Robshaw, N. Bramall, M. D. Ogden and R. Dawson, *ACS Appl. Mater. Interfaces*, **25**, 2019.

225 C. D. Valle, M. Zecca, F. Rastrelli, C. Tubaro and P. Centomo, *Polymers (Basel).*, 2020, **12**, 202-212.

226 X. Xie, J. Wang, J. Zheng, J. Huang, C. Ni, J. Cheng, Z. Hao and G. Ouyang, *Anal. Chim. Acta*, 2018, **1029**, 30–36.

227 A. Ferino-Pérez, J. J. Gamboa-Carballo, Z. Li, L. C. Campos and U. Jáuregui-Haza, *J. Mol. Graph. Model.*, 2019, **90**, 94-103.

228 B. Li, X. Yang, L. Xia, M. I. Majeed and B. Tan, *Sci. Rep.*, 2013, **3**, 1–6.

229 X. Yang, B. Li, I. Majeed, L. Liang, X. Long and B. Tan, *Polym. Chem.*, 2013, **4**, 1425–1429.

230 M. Manyangadze, N. H. M. Chikuruwo, T. B. Narsaiah, C. S. Chakra, M. Radhakumari and G. Danha, *South African J. Chem. Eng.*, 2020, **31**, 25–32.

231 X.-Q. He, Y.-Y. Cui, Y. Zhang, H.-T. Li and C.-X. Yang, *Chem. Eng. J. Adv.*, 2021, **6**, 100092.

232 M. I. El-Khaiary and G. F. Malash, *Hydrometallurgy*, 2011, **105**, 314–320.

233 S. C. Tsai and K. W. Juang, *J. Radioanal. Nucl. Chem.*, 2000, **243**, 741–746.

234 Z. L. Yaneva, B. Koumanova Koumanova and N. V. Georgieva, *J. Chem.*, 2013, **2013**.

235 Y. S. Ho, W. T. Chiu and C. C. Wang, *Bioresour. Technol.*, 2005, **96**, 1285–1291.

236 R. Castaldo, G. Gentile, M. Avella, C. Carfagna and V. Ambrogi, *Polymers (Basel).*, 2017, **9**, 304-310.

237 M. A. Hubbe, S. Azizian and S. Douven, *BioResources*, 2019, **14**, 7582–7626.

238 J. López-Luna, L. E. Ramírez-Montes, S. Martinez-Vargas, A. I. Martínez, O. F. Mijangos-Ricardez, M. del C. A. González-Chávez, R. Carrillo-González, F. A. Solís-Domínguez, M. del C. Cuevas-Díaz and V. Vázquez-Hipólito, *SN Appl. Sci.*, 2019, **1**, 1–19.

239 J. Lin and L. Wang, *Front. Environ. Sci. Eng. China*, 2009, **3**, 320–324.

240 S. Canzano, P. Iovino, V. Leone, S. Salvestrini and S. Capasso, *Adsorpt. Sci. Technol.*, 2012, **30**, 217–225.

241 S. Salvestrini, P. Vanore, A. Bogush, S. Mayadevi and L. C. Campos, *J. Water Reuse Desalin.*, 2017, **7**, 280–287.

242 Z. Li, J. K. Kim, V. Chaudhari, S. Mayadevi and L. C. Campos, *Environ. Sci. Pollut. Res.*, 2017, **24**, 17861–17873.

243 M. A. Hubbe, S. Azizian and S. Douven, *BioResources*, 2019, **14**, 7582–7626.

244 W. Weber and J. C. Morris, *J. Sanit. Eng. Div. Am. Soc. Civ. Eng.* 1963, **89**, 31-59.

245 F. C. Wu, R. L. Tseng and R. S. Juang, *Chem. Eng. J.*, 2009, **153**, 1–8.

246 C. Yao and T. Chen, *Chem. Eng. Res. Des.*, 2017, **119**, 87–92.

247 Y. Yes¸im and Y. Cel Aktay, *Process Biochem.*, 2000, **36**, 157-173.

248 In *Nanotechnology: Basic Calculations for Engineers and Scientists*, Wiley Blackwell, 2005, pp. 55–62.

249 V. J. Inglezakis, M. Balsamo and F. Montagnaro, *Ind. Eng. Chem. Res.*, 2020, **59**, 22007–22016.

250 T. Merle, D. R. U. Knappe, W. Pronk, B. Vogler, J. Hollender and U. von Gunten, *Environ. Sci. Water Res. Technol.*, 2020, **6**, 2742–2751.

251 B. Buszewski and M. Szultka, *Crit. Rev. Anal. Chem.*, 2012, **42**, 198–213.

252 V. Hadadi, *Desalin. Water Treat*.,2020, **193**, 266-273.

253 M. Hart, G. Fuller, D. R. Brown, C. Park, M. A. Keane, J. A. Dale, C. M. Fougret and R. W. Cockman, *Catalysis letters*, 2001, **72**, 135-139.

254 S. K. Sahu, P. Meshram, B. D. Pandey, V. Kumar and T. R. Mankhand, *Hydrometallurgy*, 2009, **99**, 170–174.

255 M. Osińska, *J. Sol-Gel Sci. Technol.*, 2017, **81**, 678–692.

256 Q. Wang, R. Li, X. Ouyang and G. Wang, *RSC Adv.*, 2019, **9**, 40531-40535.

257 A. Demirbas, E. Pehlivan, F. Gode, T. Altun and G. Arslan, *J. Colloid Interface Sci.*, 2005, **282**, 20–25.

258 P. A. Kebets and P. N. Nesterenko, *Mendeleev Commun.*, 2002, **12**, 155–156.

259 M. W. Kim, D. G. Peiffer , A. Tanioka, H. Matsumoto and R. Yamamoto, *J. Phys*, 2018, **42** , 12133.

260 F. Kučera and J. Jančář, *Polym. Eng. Sci.*, 1998, **38**, 783–792.

261 J. E. Coughlin, A. Reisch, M. Z. Markarian and J. B. Schlenoff, *J. Polym. Sci. Part A Polym. Chem.*,

2013, **51**, 2416–2424.

262 V. A. Davankov and M. P. Tsyurupa, *React. Polym.*, 1990, **13**, 27–42.

263 C. Wilson, M. J. Main, N. J. Cooper, M. E. Briggs, A. I. Cooper and D. J. Adams, *Polym. Chem.*, 2017, **8**, 1914–1922.

264 J.-H. Ahn, J.-E. Jang, C.-G. Oh, S.-K. Ihm, J. Cortez and D. C. Sherrington, 2006.

265 B. F. H Rhodes and C. B. Barbour, I*nd. Eng. Chem.*, 1923, **15**, 850-852.

266 E. Yılmaz, E. Sert and F. S. Atalay, *Catal. Commun.*, 2017, **100**, 48–51.

267 Z. Li, G. He, Y. Zhao, Y. Cao, H. Wu, Y. Li and Z. Jiang, *J. Power Sources*, 2014, **262**, 372–379.

268 R. Yu Garlyauskayte, A. N. Chernega, C. Michot, M. Armand, Y. L. Yagupolskii and L. M. Yagupolskii, *Tetrahedron*, 1994, **50**, 6891-6906.

269 V. Ayala, A. P. Herrera, M. Latorre-Esteves, M. Torres-Lugo and C. Rinaldi, *J. Nanoparticle Res.*, 2013, **15**, 1–14.

270 D. G. De Kowalewski, V. J. Kowalewski, E. Botek, R. H. Contreras and J. C. Facelli, *Magn. Reson. Chem.*, 1997, **35**, 351–356.

271 H. Aman, Y. C. Chen, J. W. Tu, C. C. Chang and G. J. Chuang, *ChemistrySelect*, 2020, **5**, 15015–15019.

272 H. Aman, Y. C. Chen, J. W. Tu, C. C. Chang and G. J. Chuang, *ChemistrySelect*, 2020, **5**, 15015–15019.

273 F. Freeman, C. R. Armstead, M. G. Essig, E. M. Karchefski, C. J. Kojima, V. C. Manopoli and A. H. Wickman, *J. Chem. Soc. Chem. Commun.*, 1980, **2**, 65–66.

274 J. E. Coughlin, A. Reisch, M. Z. Markarian and J. B. Schlenoff, *Journal of Polymer Science, Part A:*

*Polymer Chemistr*y, 2013, **51**, 2416-2424.

275 A. H. Alahmed, M. E. Briggs, A. I. Cooper and D. J. Adams, *J. Mater. Chem. A*, 2019, **7**, 549–557.

276 C. Deng, M. Xu, Z. Dong, L. Li, J. Yang, X. Guo, L. Peng, N. Xue, Y. Zhu and W. Ding, *Chinese J. Catal.*, 2020, **41**, 341–349.

277 R. J. Ouellette and J. D. Rawn, in *Organic Chemistry*, Elsevier, 2014, pp. 417–451.

278 M. S. Shashidhar and M. V. Bhatt, *Proc. Indian Acad. Sci. - Chem. Sci.*, 1989, **101**, 319–326.

279 M. Grzybowski, K. Skonieczny, H. Butenschön and D. T. Gryko, *Angew. Chemie Int. Ed.*, 2013, **52**, 9900–9930.

280 C. Amadi-Kamalu, H. Clarke, M. McRobie, J. Mortimer, M. North, Y. Ran, A. Routledge, D. Sibbald, M. Tickias, K. Tse and H. Willway, *ChemistryOpen*, 2020, **9**, 431–441.

281 A. Kusoglu and A. Z. Weber, *Chem. Rev.*, 2017, **117**, 987–1104.

282 L. D. Tran, J. I. Feldblyum, A. G. Wong-Foy and A. J. Matzger, *Langmuir*, 2015, **31**, 2211–2217.

283 W. Lu, D. Yuan, J. Sculley, D. Zhao, R. Krishna and H. C. Zhou, *J. Am. Chem. Soc.*, 2011, **133**, 18126–18129.

284 C. Sci, R. Dawson, D. J. Adams and A. I. Cooper, *Chemical Science*, 2011, **2**, 1173–1177.

285 A. Dąbrowski, Z. Hubicki, P. Podkościelny and E. Robens, *Chemosphere*, 2004, **56**, 91–106.

286 D. Feng, X. Li, X. Wang, J. Li, F. Sun, Z. Sun, T. Zhang, P. Li, Y. Chen and X. Zhang, *Appl. Clay Sci.*, 2018, **155**, 126–138.

287 T. Shimoaka, C. Wakai, T. Sakabe, S. Yamazaki and T. Hasegawa, *Phys. Chem. Chem. Phys*, 2015, **17**, 8843.

288 N. A. M. Nor, J. Jaafar and J. D. Kim, *J. Solid State Electrochem.*, 2020, **24**, 1185–1195.

289 H. Sharghi, P. Shiri and M. A. Review, *Beilstein J. Org. Chem*, 2018, **14**, 2745–2770.

290 T. Ikeda, K. Saito, R. Hasegawa and H. Ishikita, *Angew. Chemie - Int. Ed.*, 2017, **56**, 9151–9154.

291 S. Badilescu and C. Sandorfy, *Canadian Journal of Chemistry*, 2011, **65**, 924-927.

292 K. Singh, K. Kunimatsu, K. Miyatake and T. Tsuneda, *Macromolecules*, 2016, **49**, 6621–6629.

293 D. T. Hallinan and Y. A. Elabd, *J. Phys. Chem. B*, 2009, **113**, 4257–4266.

294 R. M. Blanchard and R. G. Nuzzo, *J. Polym. Sci. Part B Polym. Phys.*, 2000, **38**, 1512–1520.

295 X. Y. Z. Designed Research; B, *PNAS*, 2000, **117**, 15423–15428.

296 N. N. Intan, K. Klyukin, T. J. Zimudzi, M. A. Hickner and V. Alexandrov, *J. Power Sources*, 2018, **373**, 150–160.

297 T. M. Kolev and B. A. Stamboliyska, *Spectrochim. Acta - Part A Mol. Biomol. Spectrosc.*, 2000, **56**, 119–126.

298 Y. Maréchal and Y. Marechal, *J. Chem. Phys.*, 1987, **87**, 886.

299 W. W. Sulkowski, K. Nowak, A. Sulkowska, A. Wolińska, W. M. Bajdur, D. Pentak and B. Mikula, *Pure Appl. Chem.*, 2009, **81**, 2417–2424.

300 K. C. Schreiber, *Anal. Chem.*, 1949, **21**, 1168–1172.

301 G. Zundel, *Angew. Chemie Int. Ed. English*, 1969, **8**, 499–509.

302 H. Zhang, M. Wang and X. Jiang, *Green Chem.*, 2020, **22**, 8238–8242.

303 M. Danilczuk, L. Lin, S. Schlick, S. J. Hamrock and M. S. Schaberg, *J. Power Sources*, 2011, **196**, 8216–8224.

304 N. A. Iglamova, F. N. Mazitova, R. R. Shagidullin, G. M. Doroshkina, V. G. Ivanov and I. S. Kabatskaya, *Chem. Technol. Fuels Oils*, 1991, **26**, 557–558.

305 A. G. Theodoropoulos, V. T. Tsakalos and G. N. Valkanas, *Polymer,* 1992, **34**, 3905-3910.

306 L. Hanková, L. Holub and K. Jeřábek, *React. Funct. Polym.*, 2006, **66**, 592–598.

307 D. D. Jiang, Q. Yao, M. A. Mckinney, C. Wilkie, Q. Yao and C. A. Wilkie, *Chemistry Faculty Research and Publications*, 1999, **63**, 423-434.

308 C. Gong, L. Pinatti, G. Lavigne, M. T. Shaw and D. A. Scola, *J. Appl. Polym. Sci.*, 2018, **135**, 45694.

309 Q. Yao, C. Wilkie and C. A. Wilkie, *Chemistry Faculty Research and Publications*, 1999, **66**, 379-384.

310 C. Bas, L. Reymond, A. S. Danérol, N. D. Albérola, E. Rossinot and L. Flandin, *J. Polym. Sci. Part B Polym. Phys.*, 2009, **47**, 1381–1392.

311 C. Korzeniewski, E. Adams and D. I. Liu, *Applied Spectroscopy,* 2008, **62**, 634-639.

312 E. A. Yurkevich, S. V Drozdovskaya, R. Z. Aleksanyan and Y. Y. Navosha, *Journal of Applied Spectroscopy*, 1981, **34**, 311-136.

313 R. Sigwadi, M. S. Dhlamini, T. Mokrani, F. Ṋemavhola, P. F. Nonjola and P. F. Msomi, *Heliyon*, 2019, **5**.

314 M. Laporta, M. Pegoraroa and L. Zanderighi, *Physical Chemistry Chemical Physics,* 1999, **1**, 4619-4628.

315 Y. H. Li, S. Wang, J. Wei, X. Zhang, C. Xu, Z. Luan, D. Wu and B. Wei, *Chem. Phys. Lett.*, 2002, **357**, 263–266.

316 B. Wang, J. Yu, H. Liao, W. Zhu, P. Ding and J. Zhou, *Int. J. Environ. Res. Public Health*, 2020, **17**.

317 F. Lim, Y. M. Zheng, S. W. Zou and J. P. Chen, *Environ. Sci. Technol.*, 2008, **42**, 2551–2556.

318 Q. Hu and Z. Zhang, *J. Mol. Liq.*, 2019, **277**, 646–648.

319 E. Erdem, N. Karapinar and R. Donat, *J. Colloid Interface Sci.*, 2004, **280**, 309–314.

320 S. Rengaraj, Y. Kim, K. Joo, K. Choi and J. Yi, *Korean Journal of Chemical Engineering*, 2004, **21**, 187-194.

321 S. Rengaraj, J. W. Yeon, Y. Kim, Y. Jung, Y. K. Ha and W. H. Kim, *J. Hazard. Mater.*, 2007, **143**, 469–477.

322 V. J. Inglezakis and A. A. Zorpas, *Desalin. Water Treat.*, 2012, **39**, 149–157.

323 S. Kleineidam, C. Schüth and P. Grathwohl, *Environ. Sci. Technol.*, 2002, **36**, 4689–4697.

324 V. J. Inglezakis, *Microporous Mesoporous Mater.*, 2007, **103**, 72–81.

325 F. Stoeckli, M. Victoria López-Ramón and C. Moreno-Castilla, *Langmuir*, 2001, **17**, 3301-3306.

326 G. O. Wood, *Carbon N. Y.*, 2001, **39**, 343–356.

327 V. J. Inglezakis, M. Stylianou and M. Loizidou, *J. Phys. Chem. Solids*, 2010, **71**, 279–284.

328 F. Helfferich, *Ion Exchange*, Dover, New York, 1962.

329 B. Liu, H. Li, X. Ma, R. Chen, S. Wang and L. Li, *RSC Adv.*, 2018, **8**, 38965–38973.

330 J. R. Couper, W. R. Penney, J. R. Fair and S. M. Walas, *Chem. Process Equip.,* Gulf Professional Publishing, Texas, 2005.

331 NIST Mass Spectrometry Data Centre, https://chemdata.nist.gov, (accessed May 2021).

332 G. Socrates, J. Org. Chem., 1969, **34**, 2958

333 S. Falcinelli, D. Bassi, J. M. Farrar, S. Grande, F. Tampieri, A. Nikiforov, A. Giardina, A. Barbon, P. Cools, R. Morent, C. Paradisi, E. Marotta and N. De Geyter, *Front. Chem.*, 2019, **1**, 344.

334 Y. Lin, M. Zheng, C. Ye and I. M. Power, *J. Therm. Anal. Calorim.*, 2018, **133**, 1429–1437.

335 G. R. Fulmer, A. J. M Miller, N. H. Sherden, H. E. Gottlieb, A. Nudelman, B. M. Stoltz, J. E. Bercaw, K. I. Goldberg and M. Beckman, *Organometallics*, 2010, **29**, 2176-2179.

336 B. A. J Kresge and Y. Chiang, *Journal of the Chemical Society B: Physical Organic*, 1967, 53-57.

337 A. Scheithauer, T. Grützner, C. Rijksen, D. Zollinger, E. Von Harbou, W. R. Thiel and H. Hasse, *Ind. Eng. Chem. Res.*, 2014, **53**, 8395–8403.

338 M.-L. Ahrens and H. Strehlow, *Discussions of the Faraday Society*, 1965, **39**, 112-120.

339 A. Scheithauer, E. von Harbou, H. Hasse, T. Grützner, C. Rijksen, D. Zollinger and W. R. Thiel, *AIChE J.*, 2015, **61**, 177–187.

340 A. Scheithauer, A. Brä, T. Grü, D. Zollinger, W. R. Thiel, E. Von Harbou and H. Hasse, *Ind. Eng. Chem. Res.,* 2014, **53**, 8395-8403.

341 A. Scheithauer, E. von Harbou, H. Hasse, T. Grützner, C. Rijksen, D. Zollinger and W. R. Thiel, *AIChE J.*, 2015, **61**, 177–187.

342 P. Sharma, R. Sailani, A. Meena and C. L. Khandelwal, *Turkish J. Chem.*, 2020, **44**, 950–970.

343 W. E. Taifan, T. Bučko and J. Baltrusaitis, *J. Catal.*, 2017, **346**, 78–91.

344 R. P. Bell and W. C. E. Higginson, *Proceedings of the Royal Society of London. Series A, Mathematical and Physical Sciences*, 1949, **197**, 141-159.

345 P. E. Guzmán, J. D. Roberts and S. L. Manatt, *Polyhedron*, 2020, **189**, 114689.

346 N. Muller and D. E. Pritchard, *Contact Electron-Spin Coupling Nucl. Magn. Moments J. Chem. Phys.*, 1959, **31**, 1216.

347 S. Subramanian, R. A. Kini, S. F. Dec and E. D. Sloan, *Chem. Eng. Sci.*, 2000, **55**, 1981–1999.

348 G. M. Bowers, H. T. Schaef, Q. R. S. Miller, E. D. Walter, SP. D. Burton, D. W. Hoyt, J. A. Horner, J. S. Loring, B. P. McGrail and R. J. Kirkpatrick, *ACS Earth Sp. Chem.*, 2019, **3**, 324–328.

349 J. W. Lee, H. Lu, I. L. Moudrakovski, C. I. Ratcliffe, R. Ohmura, S. Alavi and J. A. Ripmeester, *J. Phys. Chem. A*, 2011, **115**, 1650–1657.

350 M. Baranac-Stojanović and M. Stojanović, *J. Org. Chem.*, 2013, **78**, 1504–1507.

351 R. R. Sauers, *tetrahedron*, 1998, **54**, 337-348.

352 J. Seravalli and S. W. Ragsdale, *Biochemistry*, 2008, **47**, 52-58.

353 S. Moret, P. J. Dyson and G. Laurenczy, 2013, **42**, 4353.

354 S. Moret, P. J. Dyson and G. Laurenczy, *Nat. Commun.*, 2014, **5**, 1-7.

355 C. Yadav, V. K. Maka, S. Payra and J. N. Moorthy, *ACS Appl. Polym. Mater.*, 2020, **2**, 3084–3093.

356 T. Yamamoto, A. Kurimoto, R. Sato, S. Katada, H. Mine, N. Tanima and R. Kamata, *Catal. Sci. Technol*, 2021, **11**, 2047.

357 J. F. Miñambres, A. Marinas, J. M. Marinas and F. J. Urbano, *J. Catal.*, 2012, **295**, 242–253.

358 M. D. Jones, C. G. Keir, C. Di Iulio, R. A. M. Robertson, C. V Williams and D. C. Apperley, *Cite this Catal. Sci. Technol*, 2011, **1**, 267–272.

359 M. Sharma, U. Soni, P. P. Rao, O. Prakash and P. K. Sharma, *Int. J. Chem. Sci.*, 2016, **14**, 1755–1767.

7. Appendices

7.1 MATLAB scripts used for kinetic modelling

Psedofirst order kinetic model:

```
xdata = [15 , 30 , 60 , 300, 600, 1800 , 50000, 108000];      % Data x

y_poutsos= [56.69391759 , 59.79103735, 66.09012439 ,70.2788246,  72.2255333 , 73.9976348 , 75.68342 , 75.79958118];

err = [0.043561, 0.01531, 0.04326, 0.01345631, 0.026560134,  0.126296636, 0.027245818 ,0.002772598];


ydata=y_poutsos;


%Function for non-linear square method

disp('Parameters and minimized resnorm:  ')

[P,resnorm]=lsqcurvefit(@(P,xdata)P(1)*(1-exp(-P(2)*xdata)),[1 1],xdata,ydata)

qe=P(1)

k1=P(2)


%Plotting

hold on

plot(xdata,ydata,'kh');errorbar(xdata,ydata,err,'kh');


X=0.00:0.05:max(xdata);

Y=P(1)*(1-exp(-P(2)*X));

plot(X,Y,'b')


ycal=P(1)*(1-exp(-P(2)*xdata));


SStot = sum((ydata-mean(ydata)).^2);        % Total Sum-Of-Squares
```

```
SSres = sum((ydata(:)-ycal(:)).^2);     % Residual Sum-Of-Squares

Rsq = 1-SSres/SStot;

Rsq
```

Psedosecond order kinetic model:

```
%Non-linear least square method

xdata = [15 , 30 , 60 , 300, 600, 1800 , 50000, 108000];      % Data x

y_panos = [56.69391759 , 59.79103735, 66.09012439 ,70.2788246,  72.2255333 , 73.9976348 , 75.68342 , 75.79958118];

err = [0.043561, 0.01531, 0.04326, 0.01345631, 0.026560134,  0.126296636, 0.027245818 ,0.002772598];


ydata=y_panos;

%Function for non-linear square method

disp('Parameters and minimized resnorm:  ')


[P,resnorm]=lsqcurvefit(@(P,xdata) P(1).*P(2)^2.*xdata./(1+P(1).*P(2).*xdata), [0 100],xdata,ydata)


P(3)=P(1)*P(2)^2

h=P(3)

k2=P(1)

qe=P(2)


%Plotting

plot(xdata,ydata,'kh');errorbar(xdata,ydata,err,'kh');


% end

X=0.00:0.05:max(xdata);

Y=P(1).*P(2)^2.*X./(1+P(1).*P(2).*X);

plot(X,Y,'b')

% R^2 calculation

ycal=P(1).*P(2)^2.*xdata./(1+P(1).*P(2).*xdata);
```

```
SStot = sum((ydata-mean(ydata)).^2);                    % Total Sum-Of-Squares
SSres = sum((ydata(:)-ycal(:)).^2);                     % Residual Sum-Of-Squares
Rsq = 1-SSres/SStot;
```

7.2 Additional NMR spectra

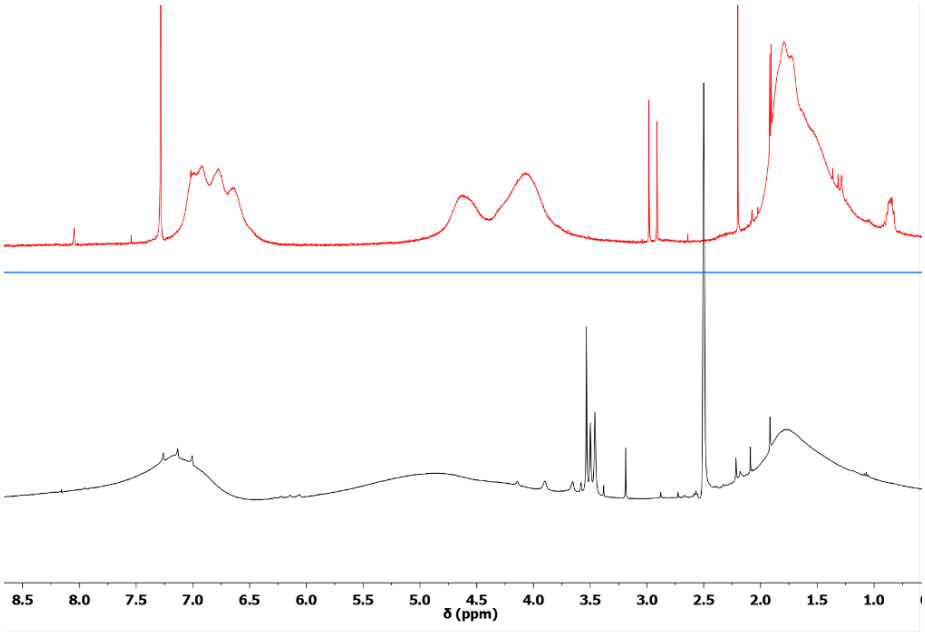

Figure 7.2a: ^{1}H-NMR spectrum of EA-TB (red/top) in $CDCl_3$ & EA-TB/ASA (black/bottom) in deuterated DMSO, Recorded using a Bruker 400 MHz spectrometer.

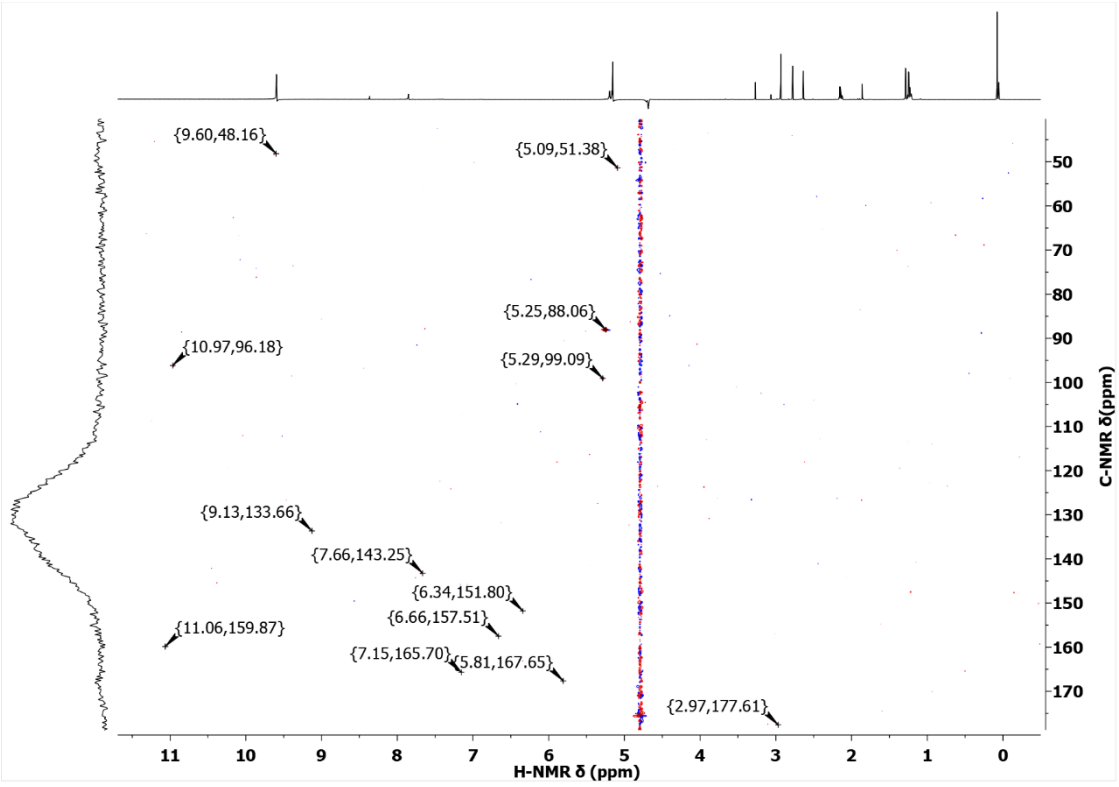

Figure 7.2b: ^{1}H-^{13}C HSQC spectrum of the TPB-DCM/ASA suspension in metaldehyde (C_0 =103 mg L^{-1}, adsorbent dose = 1 mg mL^{-1}) in D_2O. Water signal suppression was achieved using presat. Recorded using a Bruker AVA800 (800 MHz) spectrometers, equipped with TXI/ TCI cryo-probe. ^{13}C-NMR δ= 40 - 180 ppm. Red colour represents CH and CH_3 groups and blue shows CH_2 groups.

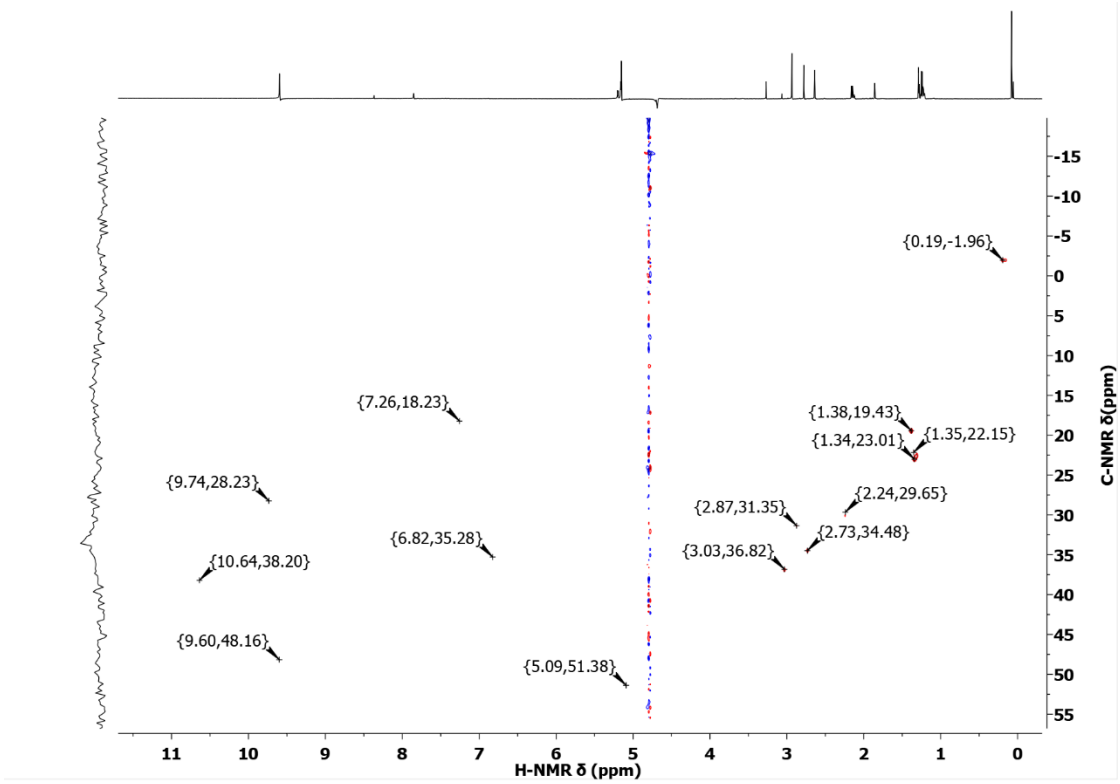

Figure 7.2c: ^{1}H-^{13}C HSQC spectrum of the TPB-DCM/ASA suspension in metaldehyde (C_0 = 103 mg L^{-1}, adsorbent dose = 1 mg mL^{-1}) in D_2O. Water signal suppression was achieved using presat. Recorded using a Bruker AVA800 (800 MHz) spectrometers, equipped with TXI/ TCI cryo-probe. ^{13}C-NMR δ= -20 – 57 ppm. Red colour represents CH and CH_3 groups and blue shows CH_2 groups.